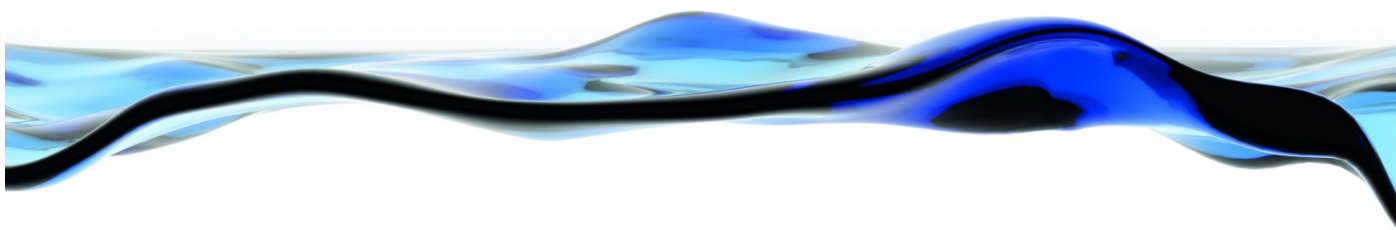


Assessment of Adelaide Plains Groundwater Resources: Appendices Part II – Regional Groundwater Modelling



Goyder Institute for Water Research
Technical Report Series No. 15/33



www.goyderinstitute.org

Goyder Institute for Water Research Technical Report Series ISSN: 1839-2725

The Goyder Institute for Water Research is a partnership between the South Australian Government through the Department of Environment, Water and Natural Resources, CSIRO, Flinders University, the University of Adelaide and the University of South Australia. The Institute will enhance the South Australian Government's capacity to develop and deliver science-based policy solutions in water management. It brings together the best scientists and researchers across Australia to provide expert and independent scientific advice to inform good government water policy and identify future threats and opportunities to water security.



Government
of South Australia

Department of Environment,
Water and Natural Resources



THE UNIVERSITY
of ADELAIDE

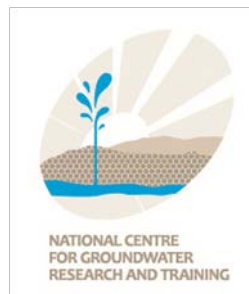


University of
South Australia



Flinders
UNIVERSITY
ADELAIDE • AUSTRALIA

The following associate organisation contributed to the report:



Enquires should be addressed to: Goyder Institute for Water Research
Level 4, 33 King William Street
Adelaide, SA, 5000
tel: 08-8236 5200
e-mail: enquiries@goyderinstitute.org

Citation

Bresciani E, Batelaan O, Banks EW, Barnett SR, Batlle-Aguilar J, Cook PG, Costar A, Cranswick RH, Doherty J, Green G, Kozuskanich J, Partington D, Pool M, Post VEA, Simmons CT, Smerdon BD, Smith SD, Turnadge C, Villeneuve S, Werner AD, White N and Xie Y, 2015, *Assessment of Adelaide Plains Groundwater Resources: Appendices Part II – Regional Groundwater Modelling*, Goyder Institute for Water Research Technical Report Series No. 15/33, Adelaide, South Australia

Copyright

© 2015 Flinders University. To the extent permitted by law, all rights are reserved and no part of this publication covered by copyright may be reproduced or copied in any form or by any means except with the written permission of Flinders University.

Disclaimer

The Participants advise that the information contained in this publication comprises general statements based on scientific research and does not warrant or represent the completeness of any information or material in this publication.

Contents

Appendix K	Regional groundwater modelling	1
K.1	Executive summary	1
K.2	Introduction	2
K.3	Methods	4
	K.3.1 Modelling environment	4
	K.3.2 Model extent and horizontal resolution	4
	K.3.3 Topography, hydrostratigraphy and model layers	6
	K.3.4 Material properties	17
	K.3.5 Flow models (historical conditions)	19
	K.3.6 Flow models (future conditions)	34
	K.3.7 Cl transport models	40
	K.3.8 ¹⁴ C transport model	50
	K.3.9 Structural sensitivity analysis	51
	K.3.10 Calibration	52
K.4	Results and discussion	61
	K.4.1 Reading keys	61
	K.4.2 Structural sensitivity analysis	62
	K.4.3 Calibration	67
	K.4.4 Water balance and its evolution	98
	K.4.5 Uncertainty around model predictions	172
K.5	Conclusions and recommendations	174
	K.5.1 Technical achievements	174
	K.5.2 Model predictions	175
	K.5.3 Model capabilities and limitations	178
	K.5.4 Recommendations	178
K.6	References	181

Figures

Apx Figure K.1 Situation map	5
Apx Figure K.2 T1 top elevation. The eastern and southern limits are based on data interpolation, whereas the northern and western (offshore) limits are characterized by a lack of data.....	9
Apx Figure K.3 Munno Para Clay top elevation. The northern, eastern and southern limits are based on data interpolation, whereas the western (offshore) limit is characterized by a lack of data	10
Apx Figure K.4 T2 top elevation. The northern, eastern and southern limits are based on data interpolation, whereas the western (offshore) limit is characterized a lack of data	11
Apx Figure K.5 Blanche Point Formation top elevation. The northern, eastern and southern limits are based on data interpolation, whereas the western (offshore) limit is characterized by a lack of data a.....	12
Apx Figure K.6 T3-T4 top elevation. The northern, eastern and southern limits are based on data interpolation, whereas the western (offshore) limit is characterized by a lack of data	13
Apx Figure K.7 Bedrock top elevation. The limits are characterized by a lack of data	14
Apx Figure K.8 3D visualisation of the hydrostratigraphic units shown at a 500 m resolution. One or several units are removed (starting from the shallowest) from Figure (a) through to Figure (g), making deeper units visible. The colour bar indicates the 12 units in which hydraulic and transport parameters are taken uniform. Refer to Apx Table K.1 for full unit names. Vertical exaggeration x10	15
Apx Figure K.9 West-east cross section at X = 280000 m showing elevation of layers and hydrostratigraphic units in the numerical model (1,000 m resolution). Refer to Apx Table K.1 for full unit names. Vertical exaggeration x10	16
Apx Figure K.10 West-east cross section at Y = 6160000 m showing elevation of layers and hydrostratigraphic units in the numerical model (1,000 m resolution). Refer to Apx Table K.1 for full unit names. Vertical exaggeration x10	16
Apx Figure K.11 West-east cross section at Y = 6180000 m showing elevation of layers and hydrostratigraphic units in the numerical model (1,000 m resolution). Refer to Apx Table K.1 for full unit names. Vertical exaggeration x10	16
Apx Figure K.12 South-north cross section at X = 280000 m showing elevation of layers and hydrostratigraphic units in the numerical model (1,000 m resolution). Refer to Apx Table K.1 for full unit names. Vertical exaggeration x10	17
Apx Figure K.13 3D contextualisation of the same cross sections shown in Apx Figure K.9 through to Apx Figure K.12 (1,000 m resolution). Refer to Apx Table K.1 for full unit names. Vertical exaggeration x10.....	17
Apx Figure K.14 Eastern (MLR) and coastal boundaries, main surface water features and location of pumping wells.....	21
Apx Figure K.15 Long-term average groundwater level contours in the Mount Lofty Ranges created using all available data, regardless of well screen depth. Interpolation method used: IDW	23
Apx Figure K.16 Specified head for the GHB condition applied to the cells along the eastern boundary (same in all layers).....	24
Apx Figure K.17 Conductance of the eastern GHB cells (3D view) when K equals the preferred value in all units. The distribution of values reflects differences in the area connecting the cells to the external source (product of the cell thickness by the length of boundary line crossing the cell).....	25
Apx Figure K.18 Conceptualization of the coastal boundary	26

Apx Figure K.19 All surface water features, used in winter months. A stream order of -9 indicates an unknown status. ‘Wide streams’ cover only a few areas mostly along streams of order 7 and thus can hardly be differentiated from these streams	27
Apx Figure K.20 Perennial surface water features, used in summer months. ‘Wide streams’ cover only a few areas mostly along streams of order 7 and thus can hardly be differentiated from these streams	28
Apx Figure K.21 Average surface water features tested in the steady-state model. ‘Wide streams’ cover only a few areas mostly along streams of order 7 and thus can hardly be differentiated from these streams	29
Apx Figure K.22 Conductance of RIV cells for all surface water features (including non-perennial).....	31
Apx Figure K.23 Steady-state recharge distribution at its preferred value (0.8 % of rainfall), i.e. before calibration.....	33
Apx Figure K.24 Monthly net pumping rates applied to the entire model domain, T1 and T2 aquifers	34
Apx Figure K.25 Rainfall gauges where downscaled climate projections are available for the AP and MLR (some not shown as outside of extents)	36
Apx Figure K.26 Licensed pumping locations included in model domain of the Adelaide Plains. Note that some allocations for users are larger than shown as some licensees own multiple wells, in which case the total allocation is split equally over these multiple wells	38
Apx Figure K.27 MAR locations for operational and committed schemes.....	39
Apx Figure K.28 Cl versus EC data used to derive the EC-Cl relationship (red) given by $Cl = 0.0558 \times EC1.178$ where Cl and EC are in the units of $mg L^{-1}$ and $\mu S cm^{-1}$, respectively. Upper and lower 95 % confidence bounds (in green) are used to quantify conversion uncertainty	42
Apx Figure K.29 Cl concentrations ($mg L^{-1}$) in the eastern Mount Lofty Ranges used to assign the eastern boundary condition in the Cl transport model.....	43
Apx Figure K.30 Cl concentration ($mg L^{-1}$) assigned to the groundwater inflow across the eastern boundary (same in all layers)	44
Apx Figure K.31 Cl concentrations in the shallow groundwater used to assign the concentration in infiltration from surface water features.....	46
Apx Figure K.32 Cl concentrations assigned to river infiltration from surface water features (including ephemeral)	47
Apx Figure K.33 Cl concentration ($mg L^{-1}$) distribution in recharge when recharge is at its preferred value (0.8 % of rainfall)	49
Apx Figure K.34 Regression of ^{14}C data with depth in the MLR according to equation 12	51
Apx Figure K.35 River network extents for the winter-river and average-river setup.....	52
Apx Figure K.36 Spatial declustering coefficients for head observations in T1 (transient development model).....	55
Apx Figure K.37 Wells selected for hydrograph analysis.....	58
Apx Figure K.38 The impact of grid resolution on the water balance components for horizontal grid resolutions of 2,000 m, 1,000 m, 500 m and 200 m.....	65
Apx Figure K.39 Cumulative change in storage for the development period model (1950–2013) for different river network initialisations (winter-river or average-river)	67
Apx Figure K.40 Evolution of the objective function (Φ) during PEST iterations.....	71
Apx Figure K.41 Parameters normalized composite scaled sensitivity, identifiability and relative uncertainty variance reduction through calibration. Parameter names starting with “hk”, “vk”, “ss” and “sy” are followed by abbreviated zone names defined in Apx Table K.1 and refer to horizontal hydraulic	

conductivity, vertical hydraulic conductivity, specific storage and specific yield, respectively. Other parameters are defined in Apx Table K.12. The specific yield of zones for which the sensitivity was zero is not reported (these zones mostly remain entirely saturated, which is why this parameter has no effect) ...	73
Apx Figure K.42 Simulated mean hydraulic heads (left) and weighted residuals (right) against measured mean hydraulic heads in the transient development model for the entire model (top) and for main units individually (bottom three rows).....	76
Apx Figure K.43 Spatial distribution of weighted residuals for the mean hydraulic heads in Hindmarsh Clay (transient development model).....	77
Apx Figure K.44 Spatial distribution of weighted residuals for the mean hydraulic heads in the T1 aquifer (transient development model)	78
Apx Figure K.45 Spatial distribution of weighted residuals for the mean hydraulic heads in the T2 aquifer (transient development model)	79
Apx Figure K.46 Simulated deviations from the mean head (left) and weighted residuals (right) against measured deviations from the mean head for the entire model (top) and for main units individually (bottom three rows).....	81
Apx Figure K.47 Spatial distribution of weighted residuals for the deviations from the mean head in Hindmarsh Clay (transient development model)	82
Apx Figure K.48 Spatial distribution of weighted residuals for the deviations from the mean head in the T1 aquifer (transient development model)	83
Apx Figure K.49 Spatial distribution of weighted residuals for the deviations from the mean head in the T2 aquifer (transient development model)	84
Apx Figure K.50 Simulated and measured hydrographs in Hindmarsh Clay	85
Apx Figure K.51 Simulated and measured hydrographs in the T1 aquifer.....	86
Apx Figure K.52 Simulated and measured hydrographs in the T2 aquifer.....	87
Apx Figure K.53 Simulated Cl concentrations (left) and weighted residuals (right) against measured Cl concentrations for the entire model (top) and for main units individually (below)	89
Apx Figure K.54 Spatial distribution of weighted residuals for Cl concentrations in Hindmarsh Clay.....	90
Apx Figure K.55 Spatial distribution of weighted residuals for Cl values in T1	91
Apx Figure K.56 Spatial distribution of weighted residuals for Cl values in T2	92
Apx Figure K.57 Simulated ¹⁴ C activities (left) and weighted residuals (right) against measured ¹⁴ C activities for the entire model (top) and for main units individually (below)	94
Apx Figure K.58 Spatial distribution of weighted residuals for ¹⁴ C values in Hindmarsh Clay	95
Apx Figure K.59 Spatial distribution of weighted residuals for ¹⁴ C values in T1.....	96
Apx Figure K.60 Spatial distribution of weighted residuals for ¹⁴ C values in T2.....	97
Apx Figure K.61 Hydraulic head minus topography in the first later for the steady-state historical flow model.....	100
Apx Figure K.62 Hydraulic head minus topography in the T1 aquifer for the steady-state historical flow model.....	101
Apx Figure K.63 Hydraulic head minus topography in the T2 aquifer for the steady-state historical flow model.....	102
Apx Figure K.64 Head contours in the first layer for the steady-state historical flow model	103
Apx Figure K.65 Head contours in the T1 aquifer for the steady-state historical flow model.....	104
Apx Figure K.66 Head contours in the T2 aquifer for the steady-state historical flow model.....	105

Apx Figure K.67 Flux across the top of the T1 aquifer for the steady-state historical flow model	106
Apx Figure K.68 Flux across the bottom of the T1 aquifer for the steady-state historical flow model	107
Apx Figure K.69 Flux across the top of the T2 aquifer for the steady-state historical flow model	108
Apx Figure K.70 Flux across the bottom of the T2 aquifer for the steady-state historical flow model	109
Apx Figure K.71 River leakage in the steady-state historical flow model	110
Apx Figure K.72 Monthly water balance components for the whole model domain (top), T1 aquifer (middle) and T2 aquifer (bottom), for the pre-development model (1900–1950).....	111
Apx Figure K.73 Annual water balance components for the whole model domain (top), T1 aquifer (middle) and T2 aquifer (bottom), for the pre-development model (1900–1950).....	112
Apx Figure K.74 Cumulative changes in storage for the Hindmarsh Clay, Undifferentiated sand, T1 aquifer, and Bedrock upstream, for the pre-development model (1900–1950).	113
Apx Figure K.75 Monthly water balance components for the whole model domain (top), T1 aquifer (middle) and T2 aquifer (bottom), for the development model (1950–2013).....	116
Apx Figure K.76 Annual water balance components for the whole model domain (top), T1 aquifer (middle) and T2 aquifer (bottom), for the development model (1950–2013).....	117
Apx Figure K.77 Cumulative changes in storage for the Hindmarsh Clay, T1 aquifer, Bedrock, T3 and T4 aquifers and the Para Fault, for the development model (1950–2013)	117
Apx Figure K.78 Hydraulic head minus topography in the first layer, October 2012.....	121
Apx Figure K.79 Hydraulic head minus topography in the first layer, April 2013	122
Apx Figure K.80 Hydraulic head minus topography in the T1 aquifer, October 2012.....	123
Apx Figure K.81 Hydraulic head minus topography in the T1 aquifer, April 2013	124
Apx Figure K.82 Hydraulic head minus topography contours in the T2 aquifer, October 2012	125
Apx Figure K.83 Hydraulic head minus topography contours in the T2 aquifer, April 2013	126
Apx Figure K.84 Simulated head contours in the first layer, October 2012	127
Apx Figure K.85 Simulated head contours in the first layer, April 2013.....	128
Apx Figure K.86 Simulated head contours in the T1 aquifer, October 2012.....	129
Apx Figure K.87 Simulated head contours in the T1 aquifer, April 2013	130
Apx Figure K.88 Simulated head contours in the T2 aquifer, October 2012.....	131
Apx Figure K.89 Simulated head contours in the T2 aquifer, April 2013	132
Apx Figure K.90 Simulated vertical flux through the top of the T1 aquifer in October 2012	133
Apx Figure K.91 Simulated vertical flux through the top of the T1 aquifer in April 2013	134
Apx Figure K.92 Simulated vertical flux through the bottom of the T1 aquifer in October 2012.....	135
Apx Figure K.93 Simulated vertical flux through the bottom of the T1 aquifer in April 2013	136
Apx Figure K.94 Simulated vertical flux through the top of the T2 aquifer in October 2012	137
Apx Figure K.95 Simulated vertical flux through the top of the T2 aquifer in April 2013	138
Apx Figure K.96 Simulated vertical flux through the bottom of the T2 aquifer in October 2012.....	139
Apx Figure K.97 Simulated vertical flux through the bottom of the T2 aquifer in April 2013	140
Apx Figure K.98 Monthly water balance components for the whole model domain (top), T1 aquifer (middle) and T2 aquifer (bottom), for the base case scenario (2013–2100)	142

Apx Figure K.99 Annual water balance components for the whole model domain (top), T1 aquifer (middle) and T2 aquifer (bottom), for the base case scenario (2013–2100)	143
Apx Figure K.100 Cumulative changes in storage for the Hindmarsh Clay, T1 aquifer, Bedrock, T3 and T4 aquifers and Para Fault, for the base case scenario (2013–2100)	143
Apx Figure K.101 Hydraulic head change in the first layer between 2013 and 2050 for the base case scenario	145
Apx Figure K.102 Hydraulic head change in the T1 aquifer between 2013 and 2050 for the base case scenario	146
Apx Figure K.103 Hydraulic head change in the T2 aquifer between 2013 and 2050 for the base case scenario	147
Apx Figure K.104 Cumulative changes in storage for the Hindmarsh Clay, T1 aquifer, Bedrock, T3 and T4 aquifers and Para Fault, for the RCP4.5 scenario (2013–2100)	148
Apx Figure K.105 Hydraulic head change in the first layer between 2013 and 2050 for the RCP4.5 scenario	150
Apx Figure K.106 Hydraulic head change in the T1 aquifer between 2013 and 2050 for the RCP4.5 scenario	151
Apx Figure K.107 Hydraulic head change in the T2 aquifer between 2013 and 2050 for the RCP4.5 scenario	152
Apx Figure K.108 Cumulative changes in storage for the Hindmarsh Clay, T1 aquifer, Bedrock, T3 and T4 aquifers and Para Fault, for the RCP8.5 scenario (2013–2100)	153
Apx Figure K.109 Hydraulic head change in the first layer between 2013 and 2050 for the RCP8.5 scenario	155
Apx Figure K.110 Hydraulic head change in the T1 aquifer between 2013 and 2050 for the RCP8.5 scenario	156
Apx Figure K.111 Hydraulic head change in the T2 aquifer between 2013 and 2050 for the RCP8.5 scenario	157
Apx Figure K.112 Cumulative changes in storage for the the Hindmarsh Clay, T1 aquifer, Bedrock, T3 and T4 aquifers and Para Fault, for the Increased pumping scenario (2013–2100)	158
Apx Figure K.113 Hydraulic head change in the first layer between 2013 and 2050 for the Increased pumping scenario	160
Apx Figure K.114 Hydraulic head change in the T1 aquifer between 2013 and 2050 for the Increased pumping scenario	161
Apx Figure K.115 Hydraulic head change in the T2 aquifer between 2013 and 2050 for the Increased pumping scenario	162
Apx Figure K.116 Hydraulic head change in the first layer between 2013 and 2050 for the Decreased pumping scenario	165
Apx Figure K.117 Hydraulic head change in the T1 aquifer between 2013 and 2050 for the Decreased pumping scenario	166
Apx Figure K.118 Hydraulic head change in the T2 aquifer between 2013 and 2050 for the Decreased pumping scenario	167
Apx Figure K.119 Hydraulic head minus topography in the T1 aquifer immediately after injection has ceased, August 2013	170
Apx Figure K.120 Hydraulic head minus topography in the T2 aquifer immediately after injection has ceased, August 2013	171

Apx Figure K.121 Areal recharge to the Adelaide Plains input to the model for the base case, RCP4.5 and RCP8.5.....	172
Apx Figure K.122 Comparison of cumulative storage change between base case, increased pumping, decreased pumping and increased MAR future scenarios in the Hindmarsh Clay, and T3 and T4 aquifers (most significantly affected)	172
Apx Figure K.123 Decadal average water balance components as a percentage of the total balance for pre-development (in 1950), development (in 2012) and future (base-case in 2050) periods. Red coloured pieces of the pie indicate flow out of the system, blue pieces indicate flow into the system, and green indicates storage changes (either gain or loss)	176

Tables

Apx Table K.1 Hydrostratigraphic units (zones) and their abbreviation	8
Apx Table K.2 Hydrostratigraphic units in each layer. Some units (e.g. T1) appear in many layers as they are split by extrapolated layers from other partially-covering units but layer thickness might be negligible	8
Apx Table K.3 Material properties: preferred values, and in parenthesis the allowed ranges of values during calibration. K_H and K_V : horizontal and vertical hydraulic conductivity; S_s : specific storage; S_y : specific yield; θ_E : effective porosity; α_L : longitudinal dispersivity	18
Apx Table K.4 Scenarios summary for Adelaide Plains groundwater modelling.....	35
Apx Table K.5 Performance statistics used to assess the goodness of fit of the model (see Hill <i>et al.</i> (2007) and Barnett <i>et al.</i> (2012)). <i>ois</i> : simulated observation; <i>oim</i> : measured observation; <i>wi</i> : weight associated to the observation (defined here as the inverse of measurement error); <i>n</i> : number of observations; <i>r</i> : number of prior information values; <i>p</i> : number of parameters; ΔO : range of observed values; <i>ms</i> : mean of simulated observations; <i>mm</i> : mean of measured observations.....	57
Apx Table K.6 Net flux matrix between all zones and boundary conditions for the historical steady-state model at grid resolutions of 2,000 m, 1,000 m, 500 m and 200 m. The units of fluxes is GL yr ⁻¹ . Positive values indicate flow from the zone/boundary in a row to a zone/boundary in a column, and negative values indicate the opposite. For example, the net flux between the Coast to Hindmarsh Clay is -9.47 GL yr ⁻¹ , indicating the net flux is from the Hindmarsh Clay to the Coast	64
Apx Table K.7 Change in simulated cumulative storage in Hindmarsh Clay, T1 aquifer, Munno Para Clay and T2 aquifer at the end of the development period (2013) when increasing the numbers of time-steps used per stress period, expressed in percentage of the difference.....	66
Apx Table K.8 Flux (GL yr ⁻¹) matrix based on 10 year average (2002-2012) water balance components (2 time-steps).....	66
Apx Table K.9 Flux (GL yr ⁻¹) matrix based on 10 year average (2002-2012) water balance components (20 time-steps).....	66
Apx Table K.10 Parameters that reached their upper bound (red dots) or lower bound (blue dots) during PEST iterations.....	70
Apx Table K.11 Calibrated material properties, with in parenthesis the factor by which they differ from their preferred value (next to the value) and the post-calibration range of uncertainty (below the value). Values that are at the upper or lower bound of the allowed calibration interval are indicated in red and blue, respectively.....	71
Apx Table K.12 Calibrated parameters (except material properties), with in parenthesis the factor by which they differ from their preferred value (next to the value) and the post-calibration 95% confidence interval (below the value). Values that are at the upper or lower bound of the allowed calibration interval are indicated in red and blue, respectively.....	72
Apx Table K.13 Model performance statistics (definitions are given in Apx Table K.5).....	75
Apx Table K.14 Flux matrix (GL yr ⁻¹) for water balance components in the steady-state historical flow model. Values below 1×10^{-2} are not shown. Colours are indicative of the magnitude, with blue to red colours highlighting small to large fluxes respectively as indicated in the lower table	98
Apx Table K.15 Decadal (1939–1949) average flux matrix (GL yr ⁻¹) for water-balance components in the pre-development transient flow model. The same display threshold and colour scheme as for Apx Table K.14 apply	114

Apx Table K.16 Difference between steady-state flux matrix and decadal average (1939–1949) flux matrix for water-balance components in the pre-development transient flow model. Values below 1×10^{-2} are not shown. Colours are indicative of the magnitude, with blues showing decrease and reds showing increase from steady state fluxes respectively	114
Apx Table K.17 Decadal (1951–1961) average annual flux matrix for water balance components. An additional row of rate of change in storage for all zones is appended to the matrix. The same display threshold and colour scheme as for Apx Table K.14 apply	118
Apx Table K.18 Decadal (2002–2012) average annual flux matrix for water balance components. An additional row of rate of change in storage for all zones is appended to the matrix. The same display threshold and colour scheme as for Apx Table K.14 apply	118
Apx Table K.19 Decadal (2020–2030) average annual flux matrix for water balance components of the base case scenario. An additional row of rate of change in storage for all zones is appended to the matrix. The same display threshold and colour scheme as for Apx Table K.14 apply	144
Apx Table K.20 Decadal (2040–2050) average annual flux matrix for water balance components of the base case scenario. An additional row of rate of change in storage for all zones is appended to the matrix. The same display threshold and colour scheme as for Apx Table K.14 apply	144
Apx Table K.21 Decadal (2020–2030) average annual flux matrix for water balance components of the RCP4.5 scenario. An additional row of rate of change in storage for all zones is appended to the matrix. The same display threshold and colour scheme as for Apx Table K.14 apply	148
Apx Table K.22 Decadal (2040–2050) average annual flux matrix for water balance components of the RCP4.5 scenario. An additional row of rate of change in storage for all zones is appended to the matrix. The same display threshold and colour scheme as for Apx Table K.14 apply	149
Apx Table K.23 Difference between base case and RCP4.5 in the decadal (2040–2050) average annual flux matrix. Values below 1×10^{-3} are not shown	149
Apx Table K.24 Decadal (2020–2030) average annual flux matrix for water balance components of the RCP8.5 scenario. An additional row of rate of change in storage for all zones is appended to the matrix. The same display threshold and colour scheme as for Apx Table K.14 apply	154
Apx Table K.25 Decadal (2040–2050) average annual flux matrix for water balance components of the RCP8.5 scenario. An additional row of rate of change in storage for all zones is appended to the matrix. The same display threshold and colour scheme as for Apx Table K.14 apply	154
Apx Table K.26 Difference between base case and RCP8.5 in the decadal (2040–2050) average annual flux matrix. Values below 1×10^{-3} are not shown	154
Apx Table K.27 Decadal (2020–2030) average annual flux matrix for water balance components of the Increased Pumping scenario. An additional row of rate of change in storage for all zones is appended to the matrix. The same display threshold and colour scheme as for Apx Table K.14 apply	158
Apx Table K.28 Decadal (2040–2050) average annual flux matrix for water balance components of the Increased Pumping scenario. An additional row of rate of change in storage for all zones is appended to the matrix. The same display threshold and colour scheme as for Apx Table K.14 apply	159
Apx Table K.29 Difference between base case and increased pumping in the decadal (2040–2050) average annual flux matrix. Values below 1×10^{-3} are not shown	159
Apx Table K.30 Decadal (2020–2030) average annual flux matrix for water balance components of the Decreased Pumping scenario. The same display threshold and colour scheme as for Apx Table K.14 apply	163
Apx Table K.31 Decadal (2040–2050) average annual flux matrix for water balance components of the Decreased Pumping scenario. The same display threshold and colour scheme as for Apx Table K.14 apply	164
Apx Table K.32 Difference between base case and decreased pumping in the decadal (2040–2050) average annual flux matrix. Values below 1×10^{-3} are not shown	164

Apx Table K.33 Decadal (2020–2030) average annual flux matrix for water balance components of the Increased MAR. The same display threshold and colour scheme as for Apx Table K.14 apply168

Apx Table K.34 Decadal (2040–2050) average annual flux matrix for water balance components of the Increased MAR scenario. The same display threshold and colour scheme as for Apx Table K.14 apply.....168

Apx Table K.35 Difference between base case and increased MAR in the decadal (2040–2050) average annual flux matrix. Values below 1×10^{-3} are not shown169

Apx Table K.36 Scenarios summary for Adelaide Plains groundwater modelling.....177

Appendix K Regional groundwater modelling

Authors: *Bresciani E, Partington D, Xie Y, Post VEA and Batelaan O*

K.1 Executive summary

A new regional groundwater flow and transport modelling platform was developed for the Adelaide Plains region. The model domain extends from the major faults at the foothill of the Mount Lofty Ranges (MLR) in the south and south-east, up to 5 km offshore in the west and it is bounded by the Light River in the north. Compared to previous modelling efforts for the same area, the new platform includes the following key improvements:

- The implementation of boundary conditions relies on stronger physical basis
- The hydrostratigraphy was revised according to newest interpretation of geological data
- A sensitivity analysis was performed on grid resolution, time-step resolution and initial condition for the transient flow model and used as a guide to decide on these structural parameters
- A larger dataset for calibration was collated
- Automatic calibration (as opposed to manual calibration) was achieved; however, while the initial aim was to use hydraulic head and chemistry data as calibration targets, compatibility issues between MODFLOW-NWT and MT3DMS precluded this and thus only hydraulic head data were used
- Calibration performance was extensively assessed using relevant indicators
- Parameters sensitivity, identifiability and uncertainty were analysed
- The model was built using a script based approach, facilitating modifications

The current modelling platform is viewed as an ongoing effort towards achievement of regional-scale predictions of hydraulic heads, fluxes, Cl and ^{14}C . It should not be expected to provide locally accurate predictions. On the basis of the SRMS (2.99 % for hydraulic heads, 28.28 % for Cl and 24.05 % for ^{14}C), the current model can be deemed suitable for regional prediction of hydraulic head but not for Cl and ^{14}C . The uncertainty around flux predictions is unknown and this is considered to be a major limitation.

Furthermore, a number of issues were identified that warrant further work before the model can be deemed capable of providing reliable future predictions:

- Grid resolution (1,000 m) is deemed too coarse to allow accurate estimates of groundwater-surface water exchanges
- The initial condition biases the results of the pre-development period
- A number of parameters deviated significantly from their preferred value during calibration
- Strong biases are observed in the weighted residuals of the calibration dataset

Bearing in mind these limitations, the water balance and flow mechanisms were analysed on the basis of the new model. Under pre-development conditions, the results show that both river leakage and lateral flow from the MLR contribute significantly to the inflows to the Tertiary aquifers. A significant part of the flow from the MLR occurs via lateral flow through the bedrock and subsequent upward flow in the Golden Grove Embayment. This significant groundwater pathway does not seem to have been reported as such before. However, little data is available in deep aquifers to confirm or deny this modelling outcome.

Introduction of pumping changed this balance and caused significant storage depletion, which amounts to 64 % of the inflows to the system for the year 2012. The low calibrated value for the specific storage of both the T1 and T2 aquifers implies that increased pumping draws the head down in these aquifers. In response, the sediments above and below provide large amounts of water. For a business-as-usual predictive scenario, storage loss continues into the future, but at a slightly decreasing rate as other sources start to contribute more water. The coastal boundary switches from net outflow to net inflow by 2050.

K.2 Introduction

A regional groundwater flow and transport modelling platform is needed as a support tool for the management of the groundwater resources in the Adelaide Plains (AP). Such a platform is intended to provide a regional understanding of the water balance and of the impact of extraction/injection on the groundwater system. It is not intended to provide answers to local questions regarding individual wells. It could nonetheless be used to assign the boundary conditions of refined, local models.

A modelling platform was developed previously by RPS Aquaterra (Georgiou *et al.* 2011), which was capable of simulating groundwater flow and salt transport. However, this platform showed a number of important areas for further improvement, namely:

- According to the flow model, almost all of the inflow to the Tertiary aquifers occurred via downward leakage of rainfall recharge in the plains through the Quaternary sediments, both in pre- and post-development regimes. This contradicts the generally accepted conceptualisation of the groundwater flow system according to which a large part of the inflow to the Tertiary aquifers occurs via lateral flow from the western Mount Lofty Ranges (MLR) (Gerges 1999; 2001; 2006; Zulfic *et al.* 2008). The report accompanying the model provided no justification for adopting an alternative conceptual model.
- The model showed groundwater flowing from the plains towards the hills along a significant portion of the MLR boundary, especially in the North Adelaide Plains (NAP). Groundwater should globally flow from the hills towards the plains.
- The hydraulic head and conductance of MODFLOW's general head boundary (GHB) condition used to represent the lateral inflow from the MLR seem to have been chosen arbitrarily. For example, a uniform conductance of $500 \text{ m}^2 \text{ day}^{-1}$ was used all along the boundary and in all model layers, and the sensitivity of model results to these parameters was not reported. Given the importance of this boundary, which is supposed to provide most of the inflow to the Tertiary aquifers, these parameters should be chosen and studied more carefully.
- The base of the T2 aquifer was assumed to be impervious. Upward leakage from underlying layers, while largely unknown, could be significant both in terms of flux and salinity especially where the T2 aquifer is heavily pumped. Hence, it is unsafe to adopt the assumption that no flow occurs across the bottom of T2. A more robust approach would consist of including deeper layers. This approach was already adopted in the numerical model developed by Gerges (1999).
- A constant head boundary condition was used to represent the offshore boundary condition in the first two layers of the model. A more appropriate condition is the use of a GHB package, and in the first layer only. This allows the flow through the Hindmarsh Clay under the seafloor to be modelled. In addition, the head values were not corrected for seawater density, while such a correction has a significant impact for the water depths in the Gulf St Vincent.
- The modelling of surface water features and their exchange with the groundwater did not consider variations of the surface area of the rivers in the calculation of the flux, and no seasonal fluctuations were accounted for.
- Stress periods of 6 months were used. This implies instantaneous transitions of the seasonally-varying stresses such as recharge that may be a poor representation of reality, and may slow down the convergence of the numerical solution.
- The salt concentration of recharge was assumed to be uniform, whereas it should be a function of distance from the coast and of the recharge rate itself, among other factors (Eriksson *et al.* 1969; Bresciani *et al.* 2014).
- The model was calibrated manually. For the number of parameters of the model (>50), manual calibration hardly guarantees the reach of an optimal set of parameters (both in terms of goodness of fit and agreement with prior information on the parameters) and the criteria upon which the final parameters are obtained are unclear. Automatic calibration can assist in addressing these issues and a calibration software like PEST also facilitates sensitivity and uncertainty analysis (see section K.3.10).
- The flow model was calibrated to a limited number of hydraulic head measurements (13697 measurements for 78 wells) compared to the data available. Furthermore, these data covered a limited

range (from about -50 m AHD to 55 m AHD) compared to the range of values observed in the model domain (from about -60 m AHD to 220 m AHD).

- Only a rudimentary sensitivity/uncertainty analysis was carried out, which consisted of testing 6 scenarios corresponding to a single parameter being changed. A rigorous and calibration-constrained uncertainty analysis would provide more reliable results.

A key objective of the current project is to provide a new groundwater flow and transport modelling platform that overcomes the above-mentioned shortcomings as much as possible. Accordingly, many elements of the model conceptualisation have been revised, and the automatic parameter estimation software PEST (Doherty 2013) was used for calibration and uncertainty analysis. The new modelling platform is described in detail in this appendix. For a general introduction to the hydrogeology of the area, the reader is referred to the main document of the project report.

A step further: use of hydrochemistry data for model calibration

Water level data are generally insufficient to constrain groundwater flow parameters such as recharge (Sanford 2002). As recharge is prone to uncertainty, flux-dependent data should also be considered if one wants to effectively constrain recharge and hydraulic conductivity values independently. A number of chemical elements found in groundwater depend on groundwater fluxes and can be used for this purpose. Therefore, in addition to addressing the aforementioned shortcomings, this project aimed at using hydrochemical data for calibrating the model. For this purpose chloride (Cl) and carbon 14 (^{14}C) were selected. A joint calibration exercise including water level, Cl and ^{14}C data was hence attempted. To the best of our knowledge, such a calibration is the first of this kind.

Chloride is an interesting element for three main reasons: (i) groundwater chloride concentrations are inversely proportional to recharge rates, so that it should inform the latter; (ii) chloride can be considered conservative in many subsurface environments since most rocks do not contain Cl, so that it is less subject to uncertainties to which other tracers are prone; (iii) Cl is relatively cheap to analyse, or can be estimated from electrical conductivity (EC) measurements as explained later. Chloride is widely used for estimating recharge using the chloride mass balance method (CMB), especially in semi-arid and arid regions (Scanlon *et al.* 2006). This method was used in the current project as described in appendix C. However, in the context of spatially variable inputs of Cl into the groundwater (due to the spatial variability of chloride deposition and of recharge processes), groundwater flow paths from the water table to the observation wells must be known in order to obtain correct recharge estimates (Ordens *et al.* 2012; Bresciani *et al.* 2014). In practice, simplistic assumptions about groundwater flow paths are often made, whereas a robust approach requires a coupled flow and transport model. This approach is adopted here. The use of a coupled model also avoids biases induced by surface water leakage, as discussed in appendix C, since these are explicitly simulated in the numerical model.

^{14}C provides information about the groundwater age due to its radioactivity decaying with time. Knowing the ^{14}C activity of the recharge, the activity in groundwater at any point downstream indicates how much time the water has spent in the system. Notwithstanding complications due to mixing and chemical reactions, ^{14}C activities are therefore a function of the velocity of groundwater along groundwater flow paths and, because velocity depends on hydraulic properties, they can be used to constrain hydraulic properties.

K.3 Methods

K.3.1 MODELLING ENVIRONMENT

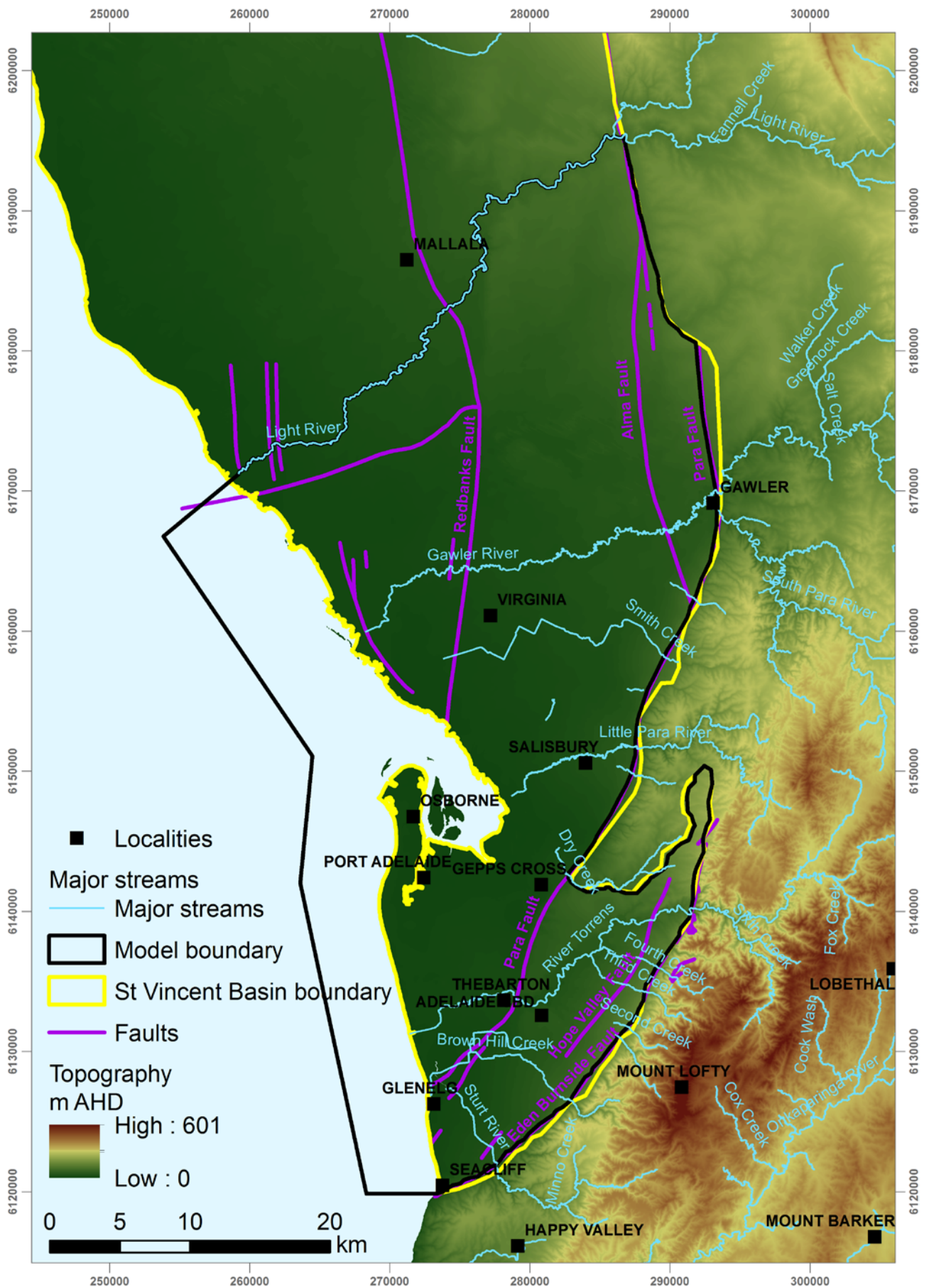
The previous model (Georgiou, Stadter *et al.* 2011) was based on MODFLOW-96, whereas the current model is based on MODFLOW-NWT (Niswonger *et al.* 2011). MODFLOW-NWT is similar to MODFLOW-2005 except that it implements a Newton formulation for solving the non-linear system of equations formed after discretization of the flow equations. This formulation namely allows a more robust handling of dry cells (Hunt *et al.* 2012). The matrix solver GMRES was used and the solver settings were taken as the pre-defined settings under the keyword 'COMPLEX' which qualifies the level of non-linearity of the model.

Apart from the solver, MODFLOW-NWT is otherwise identical to MODFLOW-2005, including the input and output files, so that switching from one to the other is relatively straightforward. The code will be referred to as MODFLOW in the following. The transport model is based on MT3DMS (Zheng *et al.* 1999), which was updated during the project to ensure compatibility with MODFLOW-NWT (unpublished code, USGS).

Of all the steps involved in the modelling process, model construction is the most challenging and time-consuming task. For example, incorporating elements such as hydrostratigraphic units, surface water features and boundary conditions in a model requires numerous steps. Modifying these elements to implement changes to the conceptual model or to incorporate new data can therefore be cumbersome. This difficulty becomes extreme when developing not one but a series of models (steady state model(s), transient model(s), transport model(s)) that should all share the same structure. In order to circumvent this issue, one can automate the model building tasks by scripting them. In this project, the model was built with Matlab (<http://www.mathworks.com/products/matlab/>), which is a high-level scripting language with a robust developing environment. Use was made of a dedicated toolbox called mflab (<https://code.google.com/p/mflab/>) that facilitates the creation of MODFLOW input files with Matlab. Using this environment, versatility such as grid-resolution independent model building has been achieved, i.e., any grid resolution can be tested with almost no additional work. Post-processing of MODFLOW output files was also automated so that plots and final results can directly be obtained after each new model run. In contrast with existing graphical interfaces (e.g. Visual MODFLOW or Groundwater Vistas), there are no limitations for what can be done in pre- and post-processing since any functionality can be programmed. Note that a non-Matlab user can import the model into a graphical interface by loading the MODFLOW files using the import functionality of the interface.

K.3.2 MODEL EXTENT AND HORIZONTAL RESOLUTION

The model extends over 40 km west-east and 76 km south-north, covering an area of 1700 km² (Apx Figure K.1). The boundaries coincide with the Light River in the north-west, fault lines along the foothills of the Mount Lofty Ranges in the east and south-east, and an offshore border 5 km away from the coast in the west. The limits in the east and south-east almost coincide with the limits of the St Vincent sedimentary basin (Apx Figure K.1). Fault lines were taken as limits for the model as this facilitates the construction of a grid that is adapted to the quasi-3D approach used (which will be discussed in the next section).



Apx Figure K.1 Situation map

Sensitivity of the results to grid resolution has been studied, as discussed later. However the grid resolution is in practice limited by computational demand. The critical part in this respect is automated calibration, which requires many model runs (depending on the number of parameters to calibrate). Available computational resources and time allowed the model to be calibrated on a uniform grid with a 1,000 m resolution, and all the results will be presented at this resolution. This grid resolution is significantly coarser than in the previous model by RPS Aquaterra (Georgiou *et al.* 2011) which used a 200 m grid and this is therefore a fundamental limitation. The model grid is deemed suitable for the primary purpose of the model which is to analyse the regional water balance, but not for fine scale analysis of impacts at surface water features or MAR schemes.

K.3.3 TOPOGRAPHY, HYDROSTRATIGRAPHY AND MODEL LAYERS

A 10 m resolution DEM provided by the Department of Environment, Water and Natural Resources of South Australia (DEWNR) was used for the onshore surface topography, which ranges from 0 m AHD to almost 250 m AHD across the model domain. A 500 m resolution bathymetry dataset provided by DEWNR was used for the offshore topography, which goes down to -29 m AHD. The bathymetry dataset was linearly interpolated onto a 10 m resolution grid and merged to the inland topography dataset to form a complete dataset for the model domain. Then, because a resolution of 10 m is finer than the model resolution, the minimum value found in each cell was taken. This choice should honour the elevation of surface water features within the cells, which was then used for groundwater-surface water interaction modelling.

The model implements a simplified but comprehensive hydrostratigraphy of the area based on the description given by Zulfic *et al.* (2008). The following hydrostratigraphic units are considered, from top to bottom:

- Hindmarsh Clay aquitard; Quaternary clay units with inter-bedded sandy aquifers, globally acting as an aquitard in respect to lower units. It extends over the entire domain except in the north-east part of the Golden-Grove embayment where the Undifferentiated Tertiary Sand aquifer outcrops (see below).
- Undifferentiated Tertiary Sand aquifer; non-marine Tertiary sediments constituting a relatively thin unconfined aquifer. It is located north-east of the Golden-Grove embayment where the Hindmarsh Clay is not present. It lies directly upon the bedrock but there may be a low permeability weathered zone between Tertiary sediments and underlying basement.
- T1 aquifer; several sub-unit confined aquifers lumped together. These are the thin Tertiary Carisbrooke Sand, the Tertiary Sand T1a aquifer and the Tertiary Upper Limestone T1b aquifer. Note that in this model we considered that the T1 aquifer extends throughout the model domain while recent work suggests that it might be inexistent in the northeast due to rising basement (the Hindmarsh Clay aquitard would lay directly onto basement). This should be adjusted in future model updates.
- Munno Para Clay aquitard; Tertiary clay acting as an effective aquitard.
- T2 aquifer; Tertiary Lower Limestone constituting a confined aquifer.
- Blanche Point Formation aquitard; Tertiary clay, siltstone and marl sediments acting as an aquitard.
- T3-T4 aquifer; several sub-unit aquifers: the Tortachilla Limestone and the Maslin Sand aquifers.
- Bedrock; Proterozoic and Palaeozoic fractured rocks.

Two major differences with the previous model (Georgiou, Stadter *et al.* 2011) are:

- inclusion of layers below the T2 aquifer – an approach already adopted in the numerical model developed by Gerges (1999) and required because upward leakage from underlying layers, while largely unknown, could be significant both in terms of water balance and salinity especially in the current context where the T2 aquifer is heavily pumped
- the T1 and T2 aquifers are considered continuous across Para fault, in accordance with the findings by Zulfic *et al.* (2008).

Top and bottom elevations of the different hydrostratigraphic units were reinterpreted and interpolated on a 100 m resolution grid by DEWNR during the project using the most recent geological data. Apx Figure K.2 through to Apx Figure K.7 show the elevation and extent of the interfaces between different

hydrostratigraphic units. The hydrostratigraphic units are expected to extend offshore, but no data is generally available. Offshore elevations were therefore extrapolated using the inverse distance weighting (IDW) method. The base of the model is fixed at a constant elevation of -700 m AHD; elevation of the bedrock top at its lowest point is -604 m AHD, so that the bedrock layer is at least about 100m thick everywhere. The choice of the base elevation is considered not to be critical as what matters most for the horizontal flow through this unit is the transmissivity of the layer and hydraulic conductivity is a calibration parameter. Apx Figure K.8 provides a three-dimensional overview of the hydrostratigraphic units.

The quasi-3D approach was used for constructing the numerical model, i.e., the top and bottom elevations of the layers follow the hydrostratigraphy. Hydrostratigraphic units were not vertically discretised due to the additional computational cost involved. Hydraulic heads are not expected to vary much along the vertical within each aquifer, and so this is usually considered reasonable for flow simulations on a regional scale. Concentrations, however, are expected to exhibit a substantial stratification within each aquifer (see e.g. Appendix E). Therefore, comparison of the results from the transport models to measured concentrations has to be considered in view of the limitation induced by the lack of vertical discretisation within each aquifer.

Layers representing a hydrostratigraphic unit that only partially covers the model area (that is most of them) were extrapolated over the rest of the domain using the IDW method, while respecting the constraint of not crossing other layers (limit +/- a minimum thickness of 0.01 m was applied where crossing initially occurred). In the extrapolated areas, the layers take the properties of the different units they intercept. Therefore, a single model layer can contain several hydrostratigraphic units. Likewise, a single hydrostratigraphic unit can be split into several model layers.

According to the latest interpretation of geological data, the sedimentary layers are continuous across all fault zones except for the Blanche Point Formation aquitard and the T3-T4 aquifer across Para fault. Hence, only the Para fault was explicitly represented in the model. A line of cells following Para fault was used to represent the fault zone itself, extending vertically from the Blanche Point Formation (included) down to the Bedrock. Across the Para fault, the upthrown and downthrown sides of the Blanche Point Formation aquitard and of the T3-T4 aquifer were treated as different units. Accordingly, different model layers were created. Across the fault, these layers take the properties of the hydrostratigraphic units they intercept. For example, the layers defining the downthrown sides of the Blanche Point Formation aquitard and of the T3-T4 aquifer take the properties of the bedrock across the fault. Apx Figure K.9 through to Apx Figure K.13 illustrate the assignment of layer properties by showing selected cross-sections.

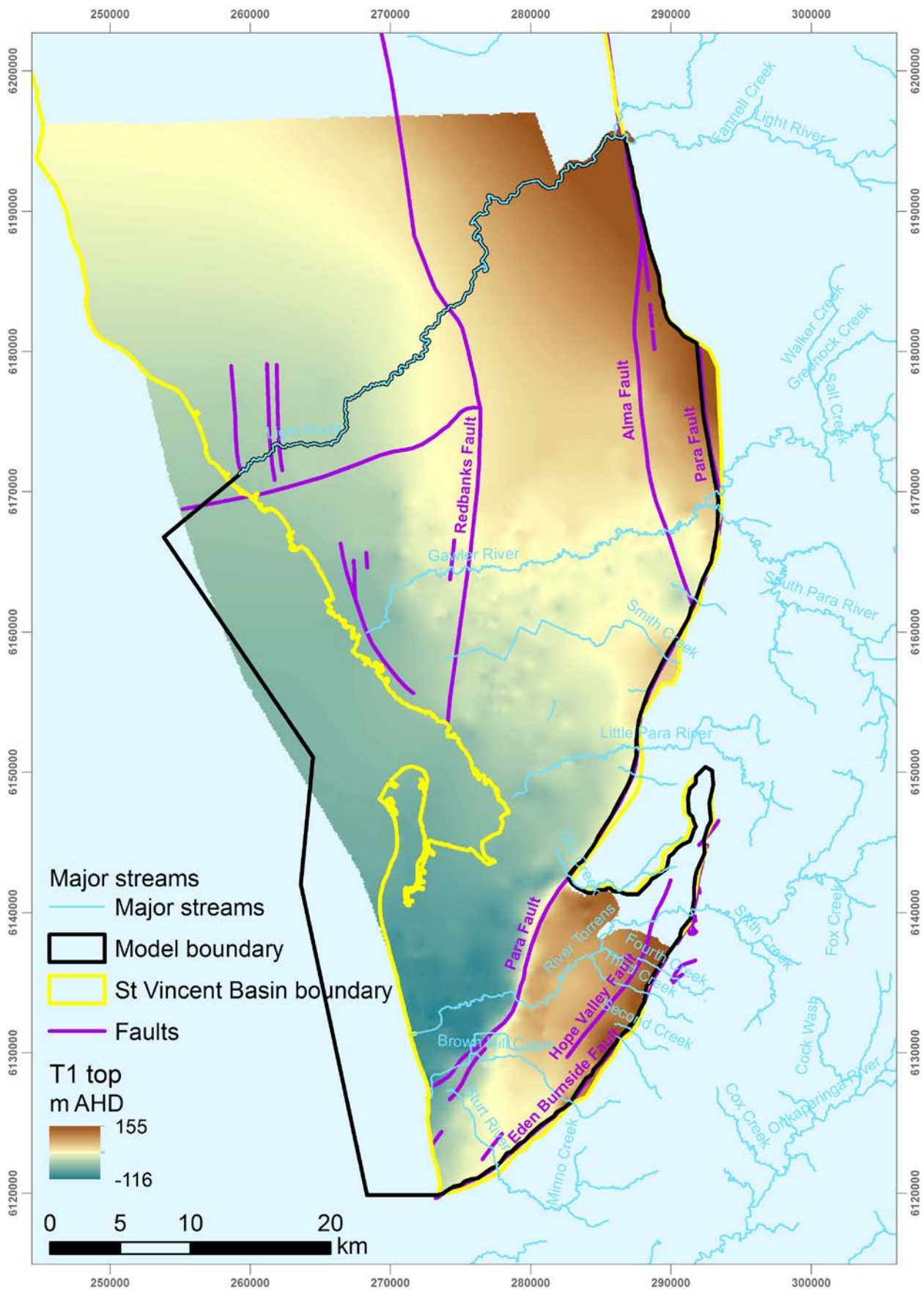
This implementation led to a model that features 10 layers for 12 hydrostratigraphic units (or zones). The hydrostratigraphic units are recapitulated in Apx Table K.1 together with their abbreviation sometimes used for shorter reference (e.g. in figure legends), and their occurrence in each model layer is indicated in Apx Table K.2. Hydraulic properties for each unit are detailed in the next section.

Apx Table K.1 Hydrostratigraphic units (zones) and their abbreviation

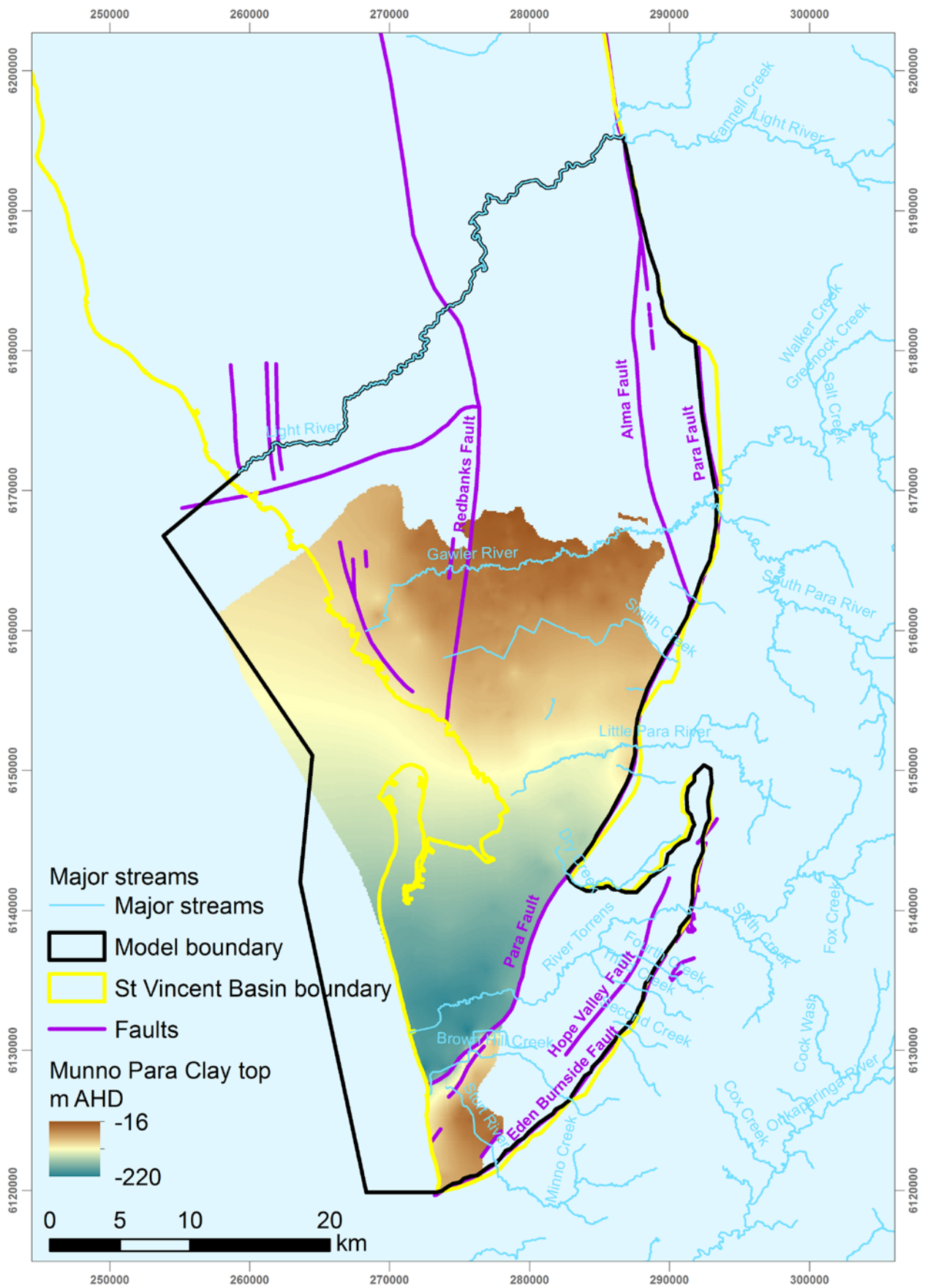
ABBREVIATION	FULL NAME
HClay	Hindmarsh Clay aquitard
UTSand	Undifferentiated Tertiary Sand aquifer
T1	T1 aquifer
MPClay	Munno Para Clay aquitard
T2	T2 aquifer
BPFmnU	Blanche Point Formation aquitard upthrown of Para Fault (i.e., in the Golden Grove Embayment)
T3T4U	T3-T4 aquifer upthrown of Para Fault (i.e., in the Golden Grove Embayment)
BRockU	Bedrock upthrown of Para Fault (i.e., in the Golden Grove Embayment)
BPFmnD	Blanche Point Formation aquitard downthrown of Para Fault (i.e., in the Adelaide Sub-Basin)
T3T4D	T3-T4 aquifer downthrown of Para Fault (i.e., in the Adelaide Sub-Basin)
BRockD	Bedrock downthrown of Para Fault (i.e., in the Adelaide Sub-Basin)
PFault	Para Fault

Apx Table K.2 Hydrostratigraphic units in each layer. Note that some units appear in many layers (e.g. T1). This happens due to the horizontal extrapolation of model layers linked to units that do not cover the entire model. However, layer thickness might be negligible

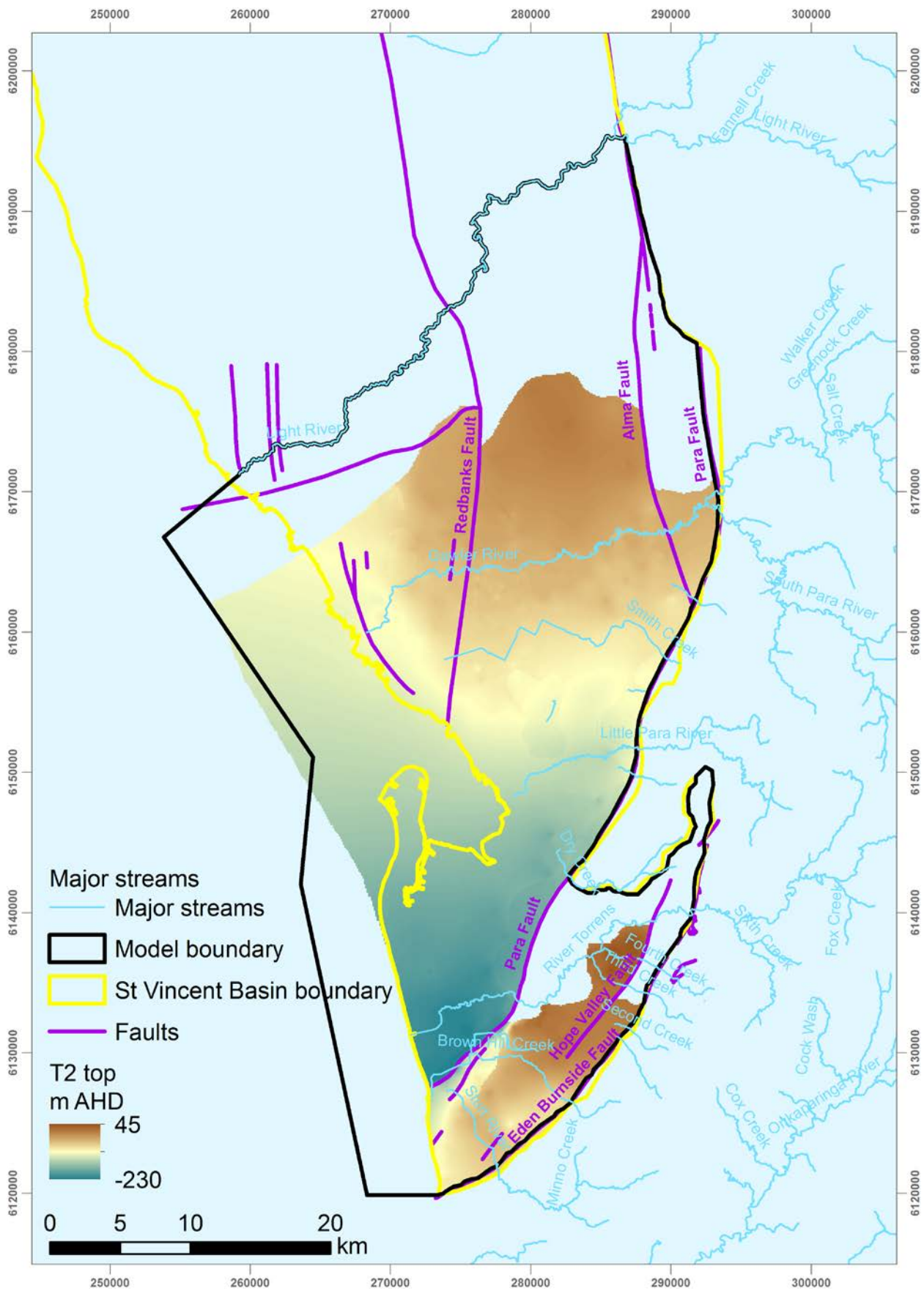
LAYER	HYDROSTRATIGRAPHIC UNITS
1	HClay and UTSand
2	T1 and UTSand
3	MPClay, T1 and UTSand
4	T2, T1 and UTSand
5	BPFmnU, PFault, T2, T1 and UTSand
6	T3T4U, BPFmnU, PFault, T2, T1 and UTSand
7	BRockU, PFault, T2 and T1
8	BPFmnD, BRockU, PFault and T1
9	T3T4UD, BPFmnD, BRockU, PFault and T1
10	BRockU, PFault and BRockD



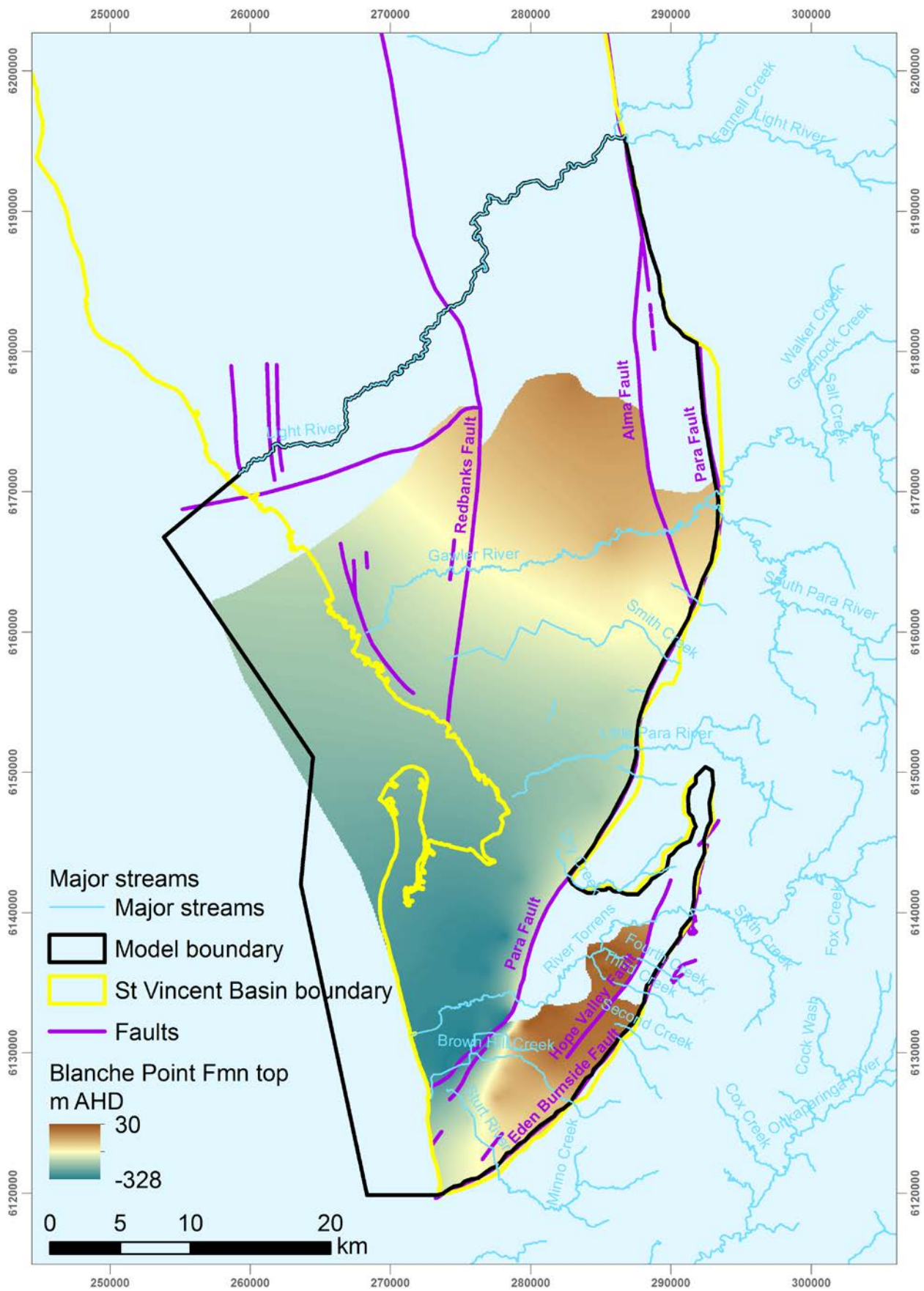
ApX Figure K.2 T1 top elevation. The eastern and southern limits are based on data interpolation, whereas the northern and western (offshore) limits are characterized by a lack of data



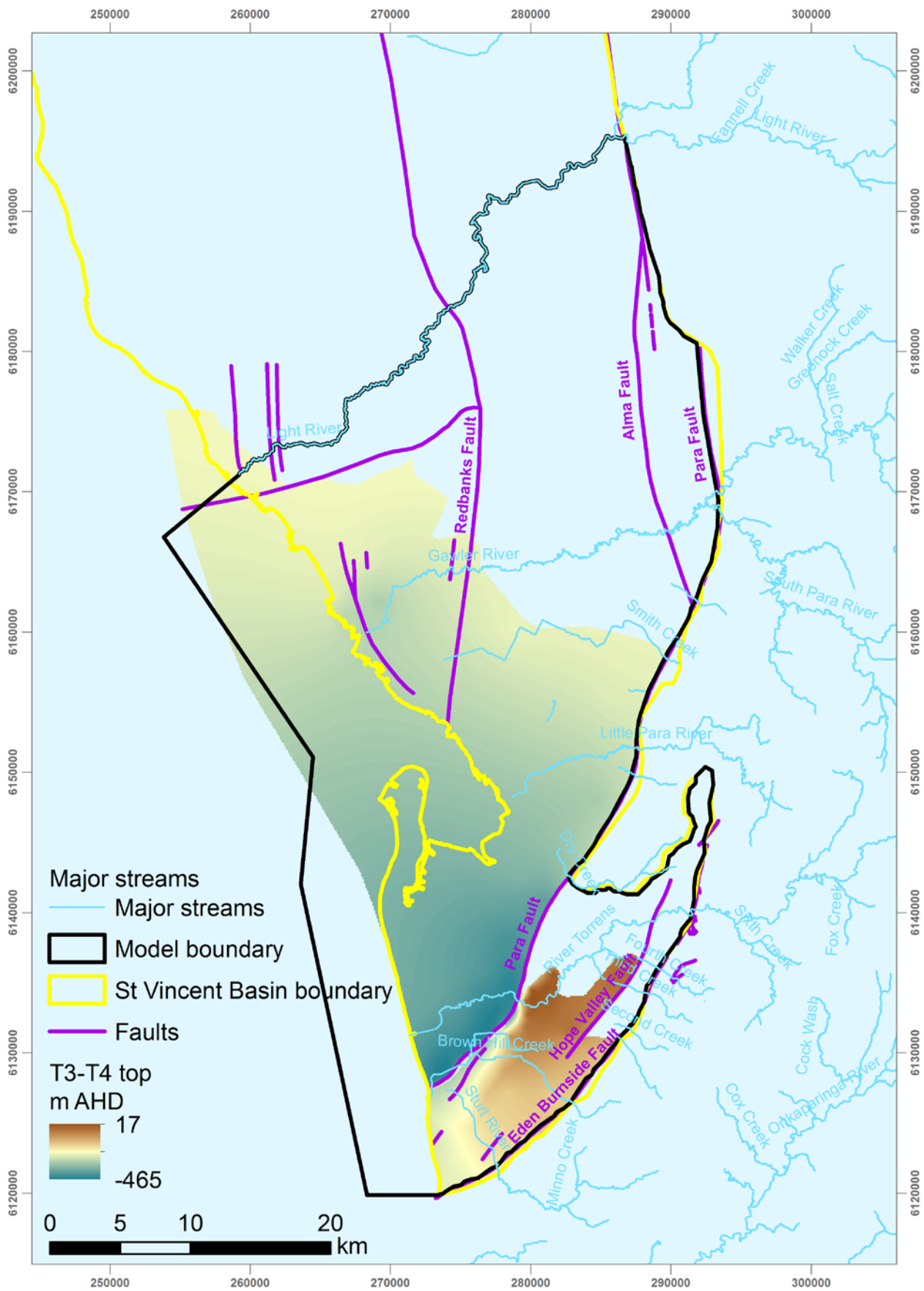
ApX Figure K.3 Munno Para Clay top elevation. The northern, eastern and southern limits are based on data interpolation, whereas the western (offshore) limit is characterized by a lack of data



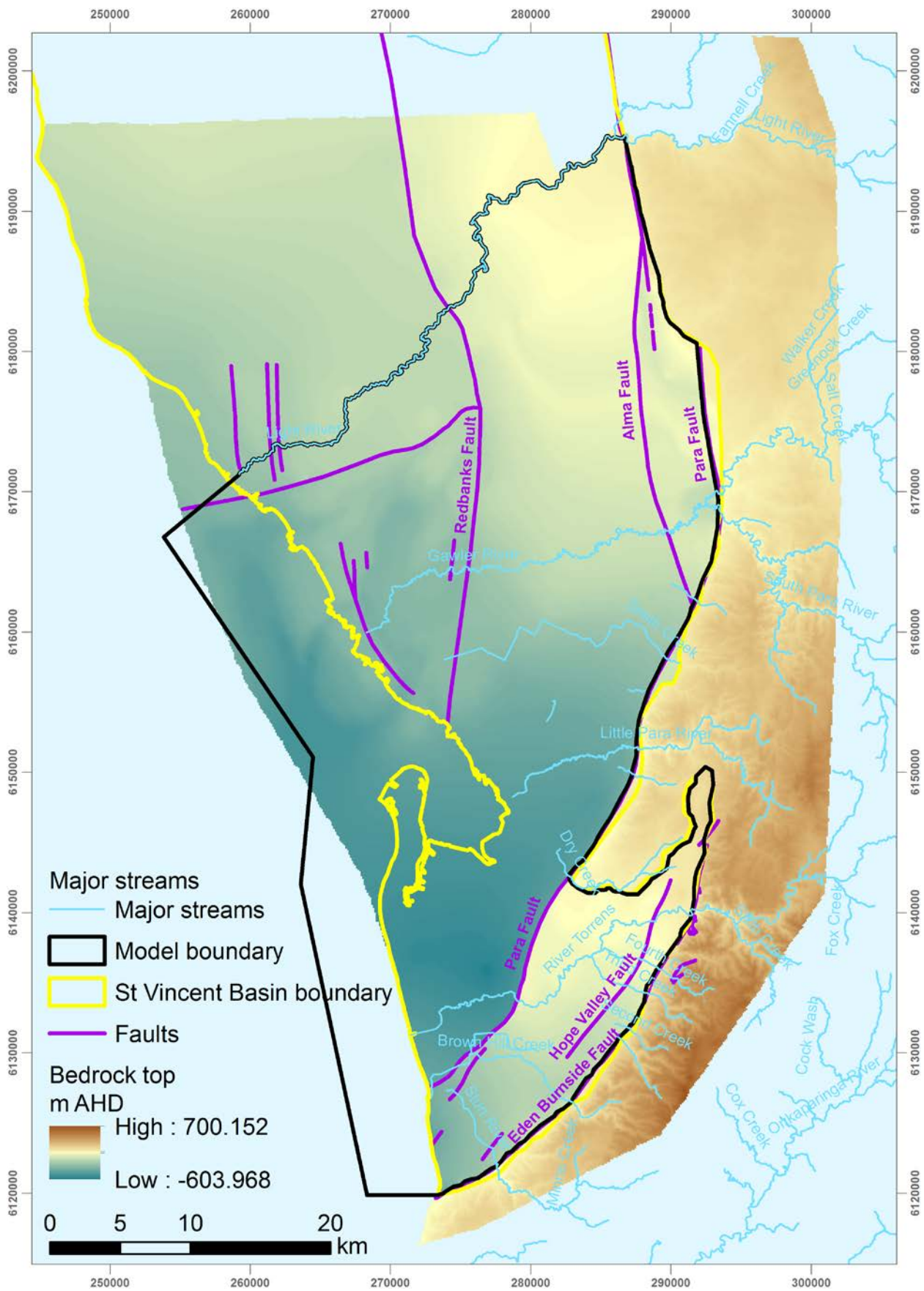
ApX Figure K.4 T2 top elevation. The northern, eastern and southern limits are based on data interpolation, whereas the western (offshore) limit is characterized a lack of data



ApX Figure K.5 Blanche Point Formation top elevation. The northern, eastern and southern limits are based on data interpolation, whereas the western (offshore) limit is characterized by a lack of data a

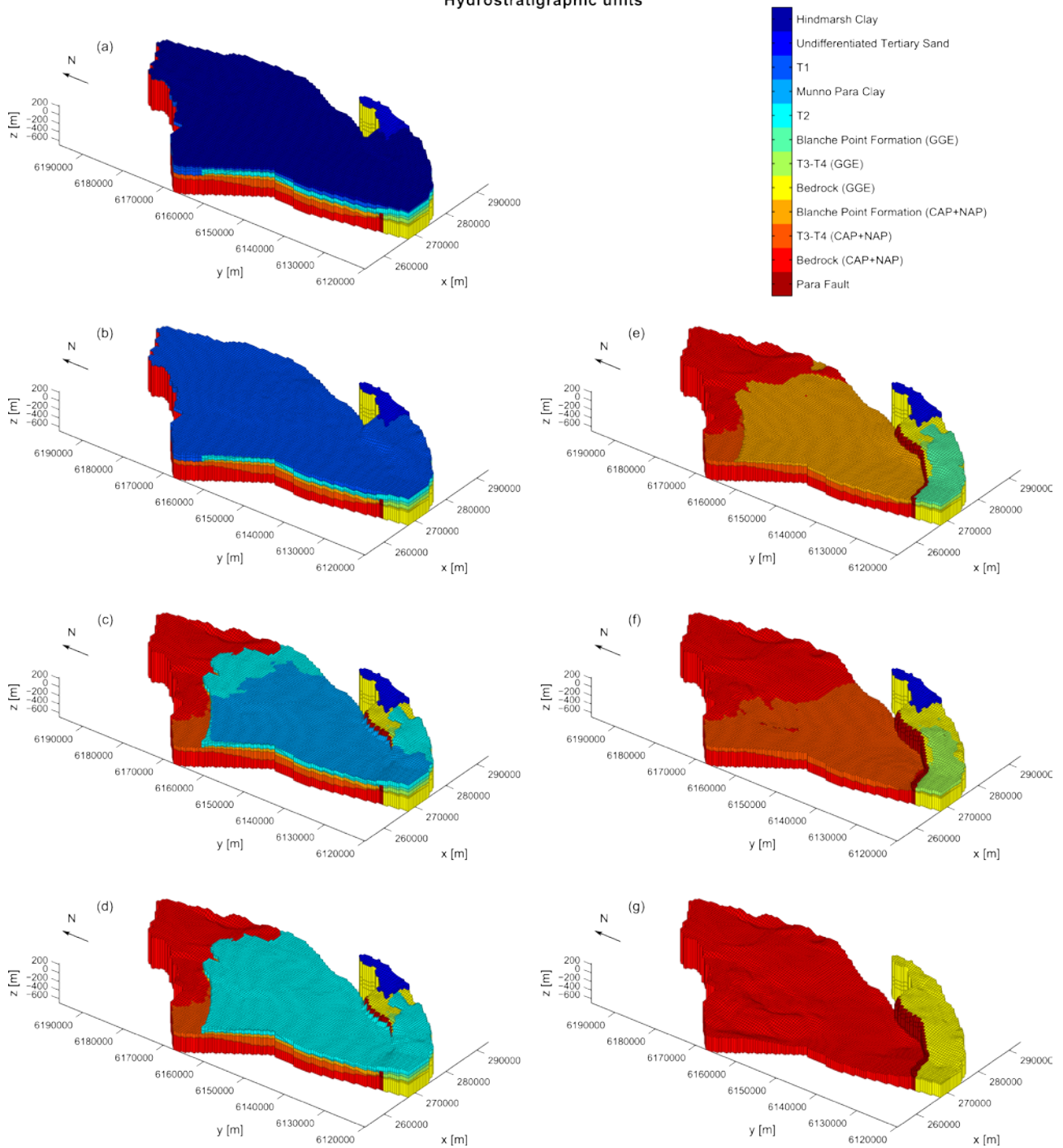


Apx Figure K.6 T3-T4 top elevation. The northern, eastern and southern limits are based on data interpolation, whereas the western (offshore) limit is characterized by a lack of data

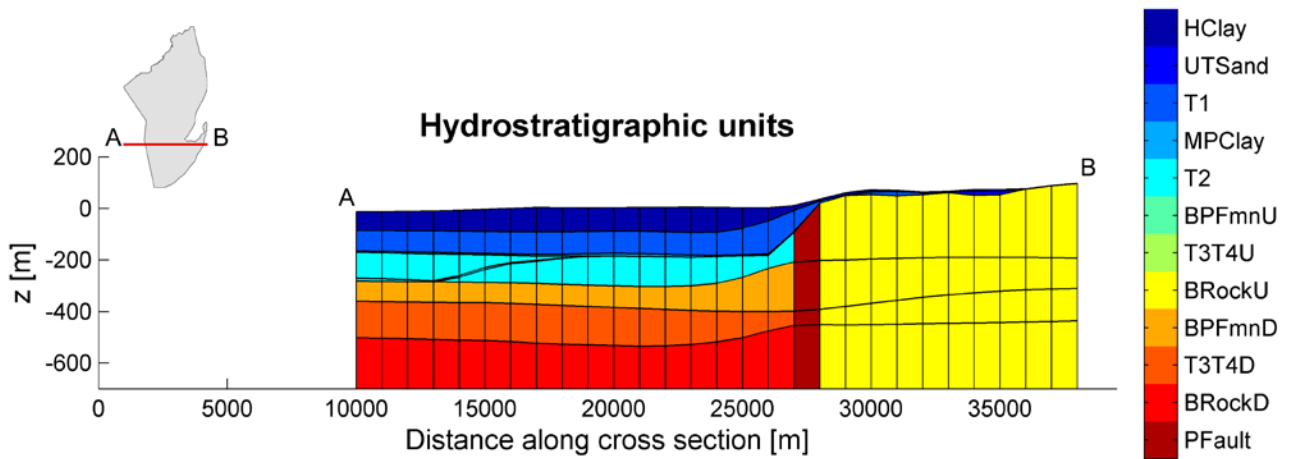


Apx Figure K.7 Bedrock top elevation. The limits are characterized by a lack of data

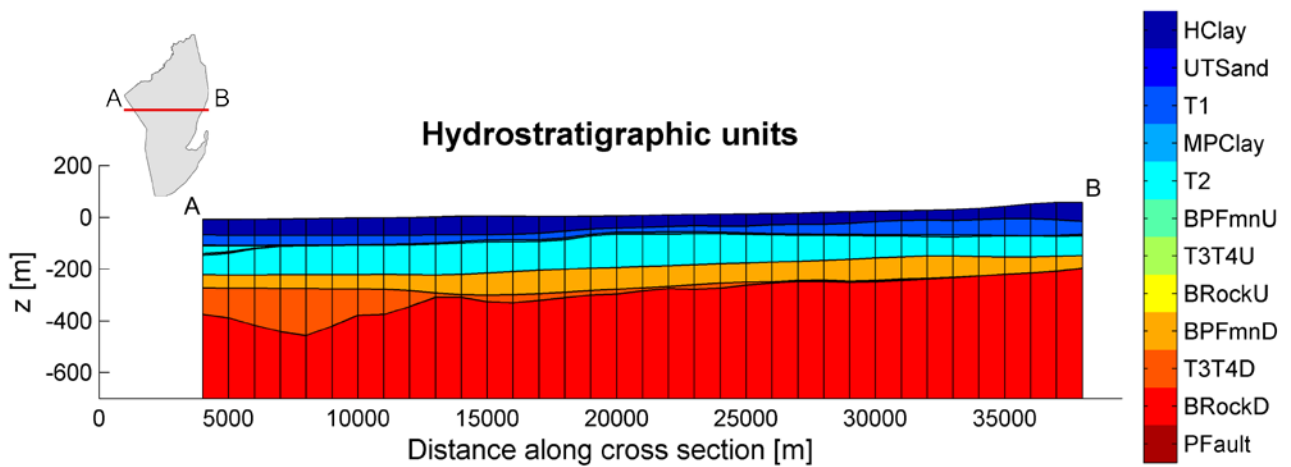
Hydrostratigraphic units



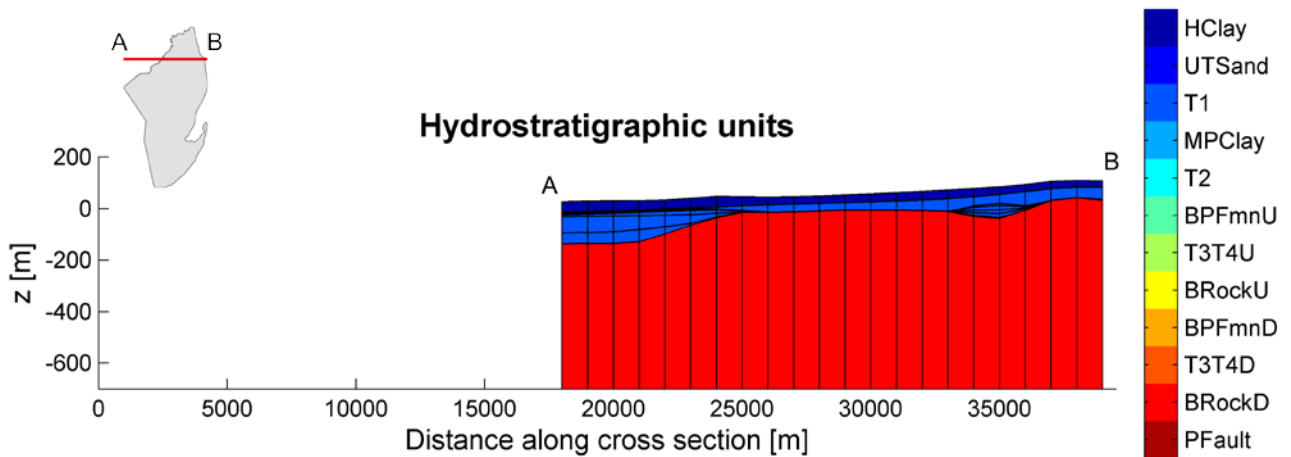
Apx Figure K.8 3D visualisation of the hydrostratigraphic units shown at a 500 m resolution. One or several units are removed (starting from the shallowest) from Figure (a) through to Figure (g), making deeper units visible. The colour bar indicates the 12 units in which hydraulic and transport parameters are taken uniform. Vertical exaggeration x10



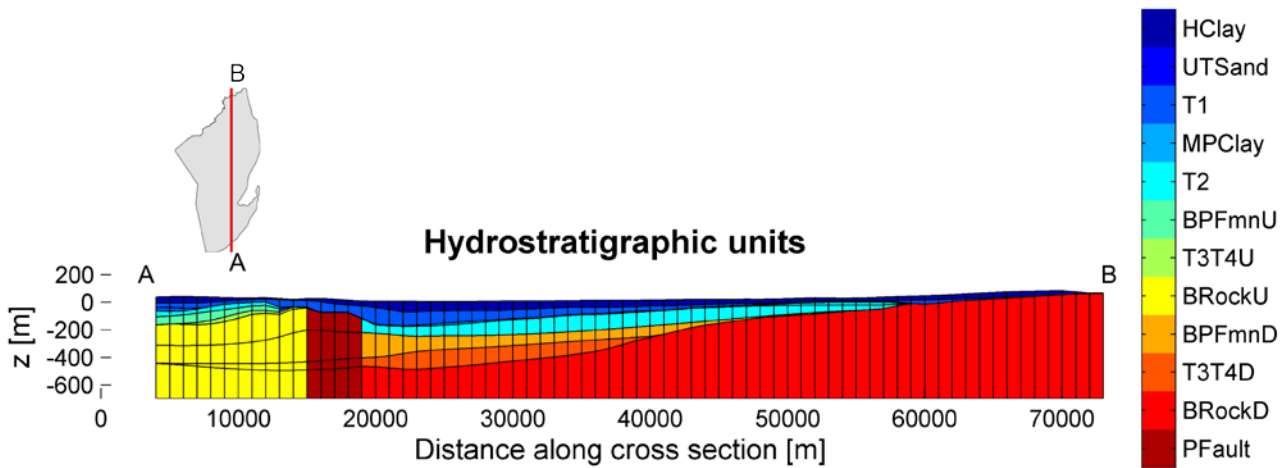
Apx Figure K.9 West-east cross section at Y = 6140000 m showing elevation of layers and hydrostratigraphic units in the numerical model (1,000 m resolution). Refer to Apx Table K.1 for full unit names. Vertical exaggeration x10



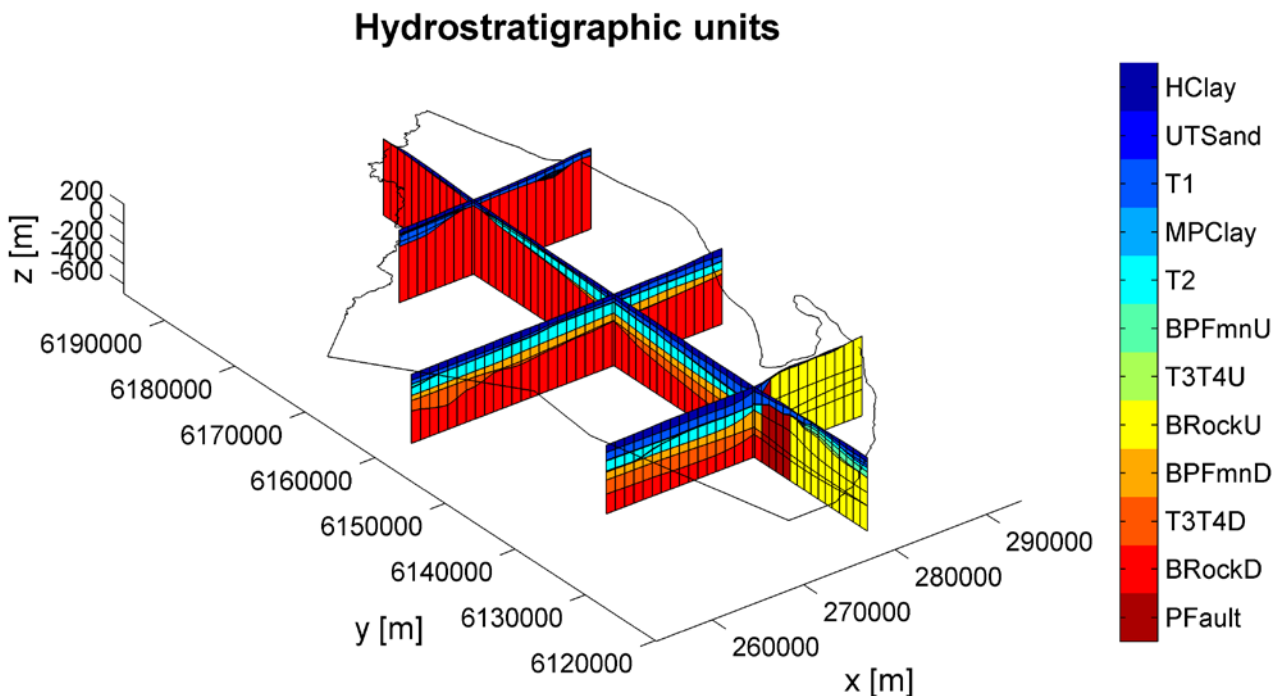
Apx Figure K.10 West-east cross section at Y = 6160000 m showing elevation of layers and hydrostratigraphic units in the numerical model (1,000 m resolution). Refer to Apx Table K.1 for full unit names. Vertical exaggeration x10



Apx Figure K.11 West-east cross section at Y = 6180000 m showing elevation of layers and hydrostratigraphic units in the numerical model (1,000 m resolution). Refer to Apx Table K.1 for full unit names. Vertical exaggeration x10



Apx Figure K.12 South-north cross section at X = 280000 m showing elevation of layers and hydrostratigraphic units in the numerical model (1,000 m resolution). Refer to Apx Table K.1 for full unit names. Vertical exaggeration x10



Apx Figure K.13 3D contextualisation of the same cross sections shown in Apx Figure K.9 through to Apx Figure K.12 (1,000 m resolution). Refer to Apx Table K.1 for full unit names. Vertical exaggeration x10

K.3.4 MATERIAL PROPERTIES

Zonation coinciding with the hydrostratigraphic units was used for assigning hydraulic and transport properties to model cells (i.e., material properties are constant within each zone). The impact of using zones of piecewise constancy, thus disregarding the heterogeneity that exists within each hydrostratigraphic unit, is discussed later.

Material properties were calibrated around their preferred values which were taken as the arithmetic mean of the available estimates found in the literature and determined during this project (Table 2 in the Summary Report). When values vary over several orders of magnitude (typically hydraulic conductivity), the arithmetic mean tends to be of the order of magnitude of the higher values. This bias is deemed appropriate for the purpose of the current model because the scale at which hydraulic conductivity is treated as constant in the model (i.e. the extent of hydrostratigraphic units) is much larger than the scale at which the estimates were obtained. This holds especially for the aquitard properties which were mostly

estimated from core samples. The equivalent hydraulic conductivity is generally expected to increase with scale (Sanchez-Vila *et al.* 2006). The preferred values as well as the allowed ranges of variation during calibration are indicated in Apx Table K.3 for all units, with further justifications given below.

Apx Table K.3 Material properties: preferred values, and in parenthesis the allowed ranges of values during calibration. K_H and K_V : horizontal and vertical hydraulic conductivity; S_s : specific storage; S_v : specific yield; θ_E : effective porosity; α_L : longitudinal dispersivity

HYDROSTRATIGRAPHIC UNIT (ZONE)	K_H (m day ⁻¹)	K_V (m day ⁻¹)	S_s (m ⁻¹)	S_v (-) ¹	θ_E (-)	α_L (m) ²
HClay	3.1E-03 (3.1E-06 – 3.1E+00)	3.1E-04 (3.1E-07 – 3.1E-01)	2.6E-05 (2.6E-08 – 2.6E-02)	tied to θ_E	0.2 (0.1 – 0.4)	50 (5 – 200)
UTSand	9.4E+00 (9.4E-03 – 9.4E+03)	9.4E-01 (9.4E-04 – 9.4E+02)	4.9E-04 (4.9E-07 – 4.9E-01)	tied to θ_E	0.2 (0.1 – 0.4)	50 (5 – 200)
T1	9.4E+00 (9.4E-03 – 9.4E+03)	9.4E-01 (9.4E-04 – 9.4E+02)	4.9E-04 (4.9E-07 – 4.9E-01)	tied to θ_E	0.2 (0.1 – 0.4)	50 (5 – 200)
MPClay	6.4E-05 (6.4E-08 – 6.4E-02)	6.4E-06 (6.4E-09 – 6.4E-03)	1.1E-05 (1.1E-08 – 1.1E-02)	tied to θ_E	0.2 (0.1 – 0.4)	50 (5 – 200)
T2	6.7E+00 (6.7E-03 – 6.7E+03)	6.7E-01 (6.7E-04 – 6.7E+02)	3.3E-04 (3.3E-07 – 3.3E-01)	tied to θ_E	0.2 (0.1 – 0.4)	50 (5 – 200)
BPFmnU	6.4E-05 (6.4E-08 – 6.4E-02)	6.4E-06 (6.4E-09 – 6.4E-03)	1.1E-05 (1.1E-08 – 1.1E-02)	tied to θ_E	0.2 (0.1 – 0.4)	50 (5 – 200)
T3T4U	6.7E+00 (6.7E-03 – 6.7E+03)	6.7E-01 (6.7E-04 – 6.7E+02)	3.3E-04 (3.3E-07 – 3.3E-01)	tied to θ_E	0.2 (0.1 – 0.4)	50 (5 – 200)
BRockU	1.0E-03 (1.0E-06 – 1.0E+00)	1.0E-03 (1.0E-06 – 1.0E+00)	1.0E-05 (1.0E-08 – 1.0E-02)	tied to θ_E	0.01 (0.001 – 0.1)	50 (5 – 200)
BPFmnD	6.4E-05 (6.4E-08 – 6.4E-02)	6.4E-06 (6.4E-09 – 6.4E-03)	1.1E-05 (1.1E-08 – 1.1E-02)	tied to θ_E	0.2 (0.1 – 0.4)	50 (5 – 200)
T3T4D	6.7E+00 (6.7E-03 – 6.7E+03)	6.7E-01 (6.7E-04 – 6.7E+02)	3.3E-04 (3.3E-07 – 3.3E-01)	tied to θ_E	0.2 (0.1 – 0.4)	50 (5 – 200)
BRockD	1.0E-03 (1.0E-06 – 1.0E+00)	1.0E-03 (1.0E-06 – 1.0E+00)	1.0E-05 (1.0E-08 – 1.0E-02)	tied to θ_E	0.01 (0.001 – 0.1)	50 (5 – 200)
PFault	1.0E-03 (1.0E-06 – 1.0E+00)	1.0E-02 (1.0E-05 – 1.0E+01)	1.0E-04 (1.0E-07 – 1.0E-01)	tied to θ_E	0.2 (0.1 – 0.4)	50 (5 – 200)

1. Specific yield is used only in cells containing the water table, but since these are unknown at the beginning of the simulation, a value was assigned to each unit

2. Horizontal and vertical transverse dispersivities were defined by a fixed ratio to the longitudinal dispersivity of 0.1 and 0.01, respectively

Hydraulic conductivity

In general, many more estimates of horizontal hydraulic conductivity (K_H) than estimates of vertical hydraulic conductivity (K_V) were available for the aquifers, whereas the opposite was true for aquitards (Table 2 in the Summary Report). Therefore, the measured K_H (arithmetic mean) was used as a preferred value for aquifers, whereas the measured K_V was used as a preferred value for aquitard. The preferred values of K_V for aquifers and of K_H for aquitards were determined assuming a general anisotropy ratio K_H/K_V of 10. Anisotropy in favour of the horizontal hydraulic conductivity is expected because both aquifers and aquitards must represent a vertical integration of variably conductive, layered sediments disposed on top of another, which generally induces higher conductivity in the horizontal direction than in the vertical direction.

No information was available for the Undifferentiated Sand aquifer, the Blanche Point Formation aquitard, the T3-4 aquifer, the Bedrock and the Para fault. The preferred values for the first three of these units were taken to be equal to the ones of the T1 aquifer, the Munno Para Clay aquitard and the T2 aquifer, respectively. The preferred values for the Bedrock were taken as $10^{-3} \text{ m day}^{-1}$ for both horizontal and vertical hydraulic conductivities, i.e. a rather low value but not extremely low because it must represent an equivalent hydraulic conductivity of the bulk fractured rock. No detailed study of the hydraulic properties associated to Para fault was found. Therefore, the preferred value for the horizontal hydraulic conductivity of the Para fault was taken identical to the one of the Bedrock ($10^{-3} \text{ m day}^{-1}$), whereas the preferred value was taken 10 times higher for the vertical hydraulic conductivity, as fault zones often promote preferential flow in the vertical direction (Bense *et al.* 2013).

Because hydraulic conductivity display high heterogeneity, and because the values incorporated in the model must represent equivalent properties at a scale that can differ significantly from the scale at which the estimates were obtained, a large uncertainty exists a priori. Therefore, hydraulic conductivities of all units were allowed to vary by three orders of magnitude both above and below their preferred value during the calibration process.

Storage parameters

Specific storage (S_s) estimates were available for the Hindmarsh Clay and Munno Para Clay aquitards as well as for the T1 and T2 aquifers. As for hydraulic conductivity, preferred values for the Undifferentiated Sand aquifer, the Blanche Point Formation aquitard and the T3-4 aquifer were taken equal to the ones of the T1 aquifer, the Munno Para Clay aquitard and the T2 aquifer, respectively. The preferred values for the Bedrock and for the Para fault were arbitrarily set to $1.0\text{E-}05 \text{ m}^{-1}$ and $1.0\text{E-}04 \text{ m}^{-1}$, respectively. All the specific storage values were all allowed to vary by three orders of magnitude both above and below their preferred value during calibration.

Specific yield (S_y) is effectively used only in cells containing the water table, but since these are unknown at the beginning of the simulation, a value was assigned to all cells. S_y was taken equal to the effective porosity (θ_E) for all units, i.e., it was tied to θ_E during the calibration process. The values for θ_E are described below.

Transport parameters

An estimate of effective porosity (θ_E) was unavailable for all units. Therefore, θ_E was calibrated within a wide range of possible values. For all units except the Bedrock, the preferred values were taken equal to 0.2, and values were allowed to vary between 0.1 and 0.4 during calibration. This range of values covers most types of sedimentary materials (de Marsily 1986). The Bedrock is expected to have a much lower porosity, mostly formed by fracture porosity, but the range of representative values is unknown. The preferred value was taken equal to 0.01 and values were allowed to vary by one order of magnitude above and below this value.

No estimate was available either for dispersion parameters. The longitudinal dispersivity (α_L) for all units was allowed to take values between 5 and 200 m during calibration with a preferred value of 50 m. Horizontal and vertical transverse dispersivities were defined by a fixed ratio to the longitudinal dispersivity; typical values of 0.1 and 0.01, respectively, were adopted.

K.3.5 FLOW MODELS (HISTORICAL CONDITIONS)

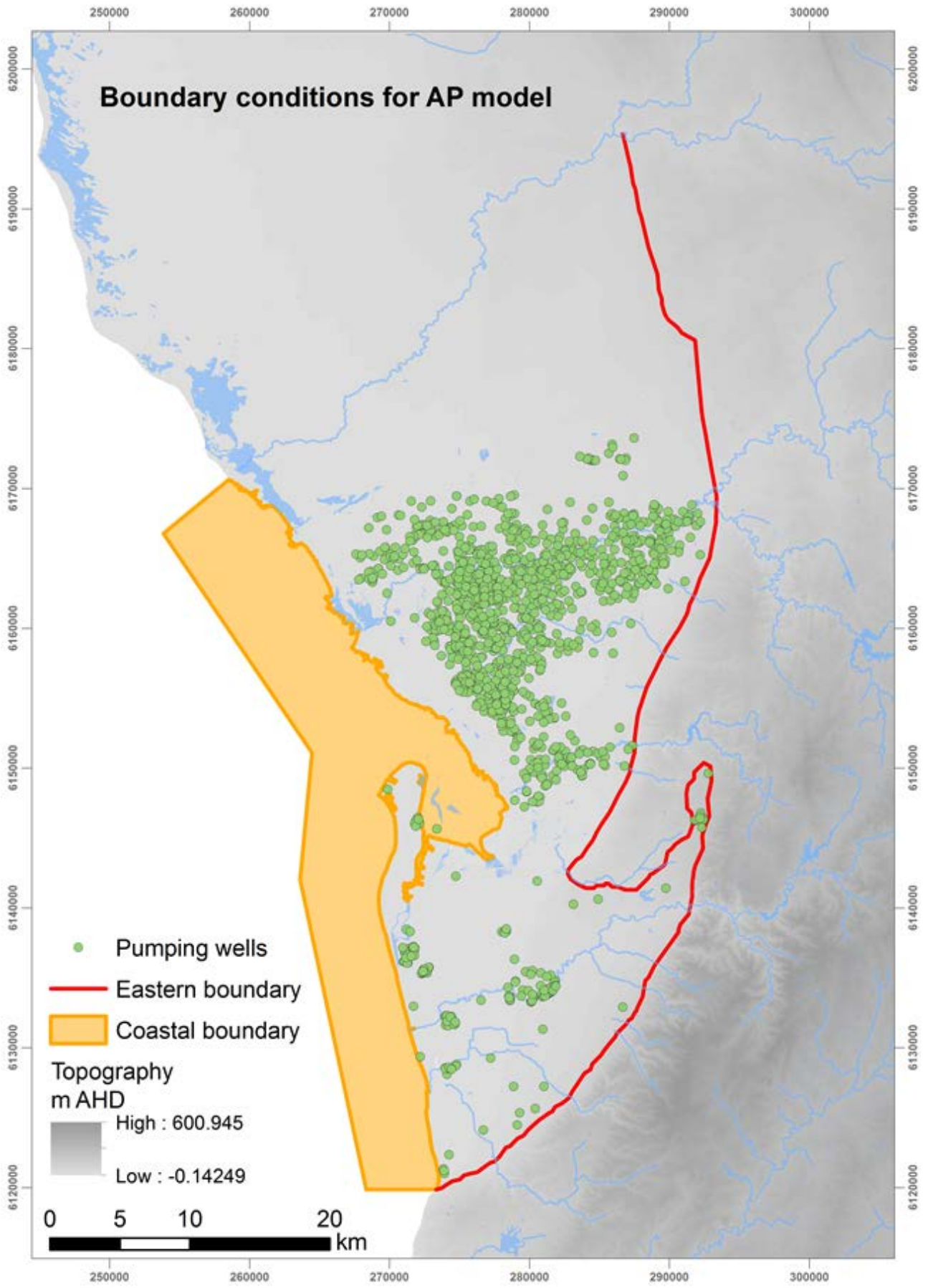
Three flow models representing historical conditions were developed for calibration but also for the analysis of flow mechanisms under both pre-development and development conditions. They consist of:

1. A pre-development steady-state flow model (no pumping).
2. A pre-development transient flow model (May 1900 – April 1950, no pumping).
3. A development transient flow model (May 1950 – April 2013, pumping).

The steady-state model provides the initial heads for the pre-development transient model, which in turn provides initial conditions for the development transient model. The inflows and outflows considered in these models consist of:

- recharge from the Mount Lofty Ranges along the eastern/south-eastern boundary (hereafter referred to as eastern boundary for brevity);
- discharge towards the Gulf St Vincent;
- river-aquifer exchange along the streams and creeks within the model domain;
- diffuse recharge across the top of the model domain;
- pumping (extraction/injection) in various aquifers.

Boundary conditions are schematised in Apx Figure K.14. A description of the implementation for each of these and any assumptions made are provided in detail below. All the boundary conditions were assigned to the model using the mflab package and delineation of the boundaries was based on information stored in GIS shapefiles. Monthly stress periods were used, which is an improvement over the seasonal approach used in the previous model by RPS Aquaterra (Georgiou *et al.* 2011). This allowed refinement of recharge fluctuations on the basis of monthly rainfall data. However, pumping rates and rivers were still varied only on a seasonal (6 month) basis and therefore this represents a possible area for future model improvement.



Apx Figure K.14 Eastern (MLR) and coastal boundaries, main surface water features and location of pumping wells

Eastern boundary (Mount Lofty Ranges)

A general head boundary (GHB) was applied in the model cells along the eastern boundary to simulate the recharge by lateral inflow from the Mount Lofty Ranges (MLR). The hydraulic head in each cell was chosen such that it represents the groundwater level in the MLR formation just outside the boundary and this level was assumed to be constant with depth (i.e. the same hydraulic head was taken in all layers). Groundwater level measurements in the MLR are relatively sparse, especially in the north. But where available, the data show that groundwater levels follow the topography quite closely (Apx Figure K.15). Therefore, the specified head for each GHB cell for the steady-state model was set equal to the elevation of a smoothed version of the topography, created using a 2-km moving average filter. Smoothing was intended to filter the small-scale details of the topography that would not appear in the groundwater levels. Since the resolution at which the topography was available (10 m) was finer than the model grid resolution, the values assigned along the eastern boundary represent the elevation of the closest topography cell crossed by the eastern boundary line, the distances being evaluated between cell centres. The resulting head values (Apx Figure K.16) compare well with the available groundwater level measurements along the eastern boundary (Apx Figure K.15).

The conductance C ($\text{m}^2 \text{day}^{-1}$) for each GHB cell on the eastern boundary was calculated according to:

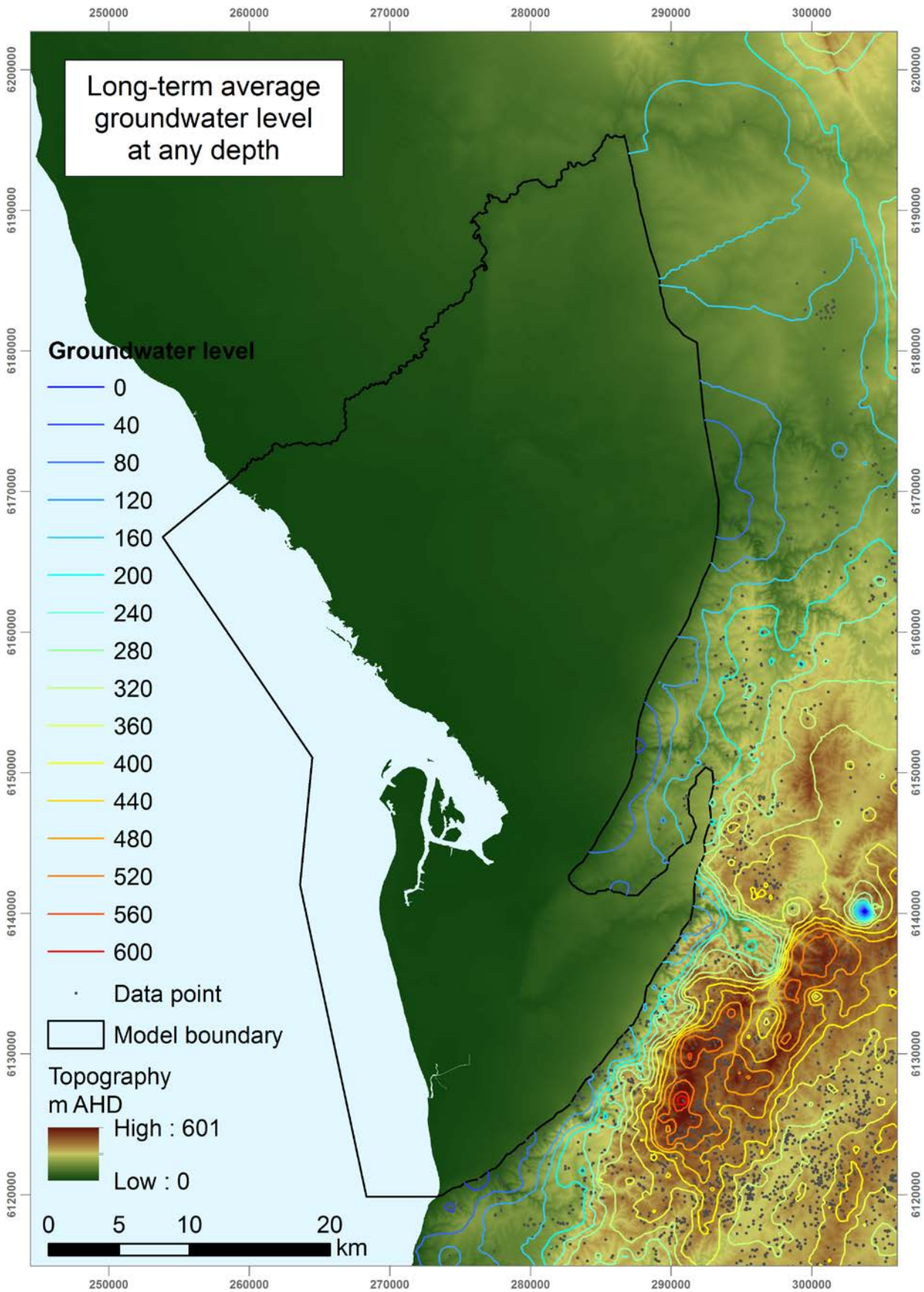
$$C = \frac{K \times A}{L} \quad (1)$$

where K (m day^{-1}) is hydraulic conductivity of the material between the cell centre and the location where the hydraulic head is known, A (m^2) is the area connecting the cell to the external source, and L (m) is the distance over which the head is assumed to vary linearly between the cell and the external source. K is a function of the connectivity of the sedimentary units to the fractured rock of the MLR formation. The magnitude of this parameter is essentially unknown due to the presence of faults (the Eden Burnside fault in the south and the Para fault in the north). Therefore, the current modelling effort aimed at estimating K (named EK in the following as for "Eastern K ") via automated calibration. EK was hence allowed to vary within a large range of values during calibration, i.e. between $1.0\text{E-}06 \text{ m day}^{-1}$ and 1.0 m day^{-1} , with a preferred value of $1.0\text{E-}03 \text{ m day}^{-1}$. A single value was taken along the boundary, thus keeping the level of parameterization commensurate with the zonal approach used otherwise. A was calculated as the product of the cell thickness by the length of boundary line crossing the cell (this differs from the length of the cell side). L was set fixed to 100 m, i.e., the specified head is assumed to hold 100 m from the boundary in the MLR formation. Apx Figure K.17 shows the resulting conductance values when EK equals the preferred value in all units.

The hydraulic head in the MLR is expected to respond to variations in rainfall. Hence, the specified head of the GHB cells in the transient model was variable in time. Temporal variations were modelled by changing the hydraulic head in each stress period by a certain amount h_{shift} calculated as a function of rainfall as:

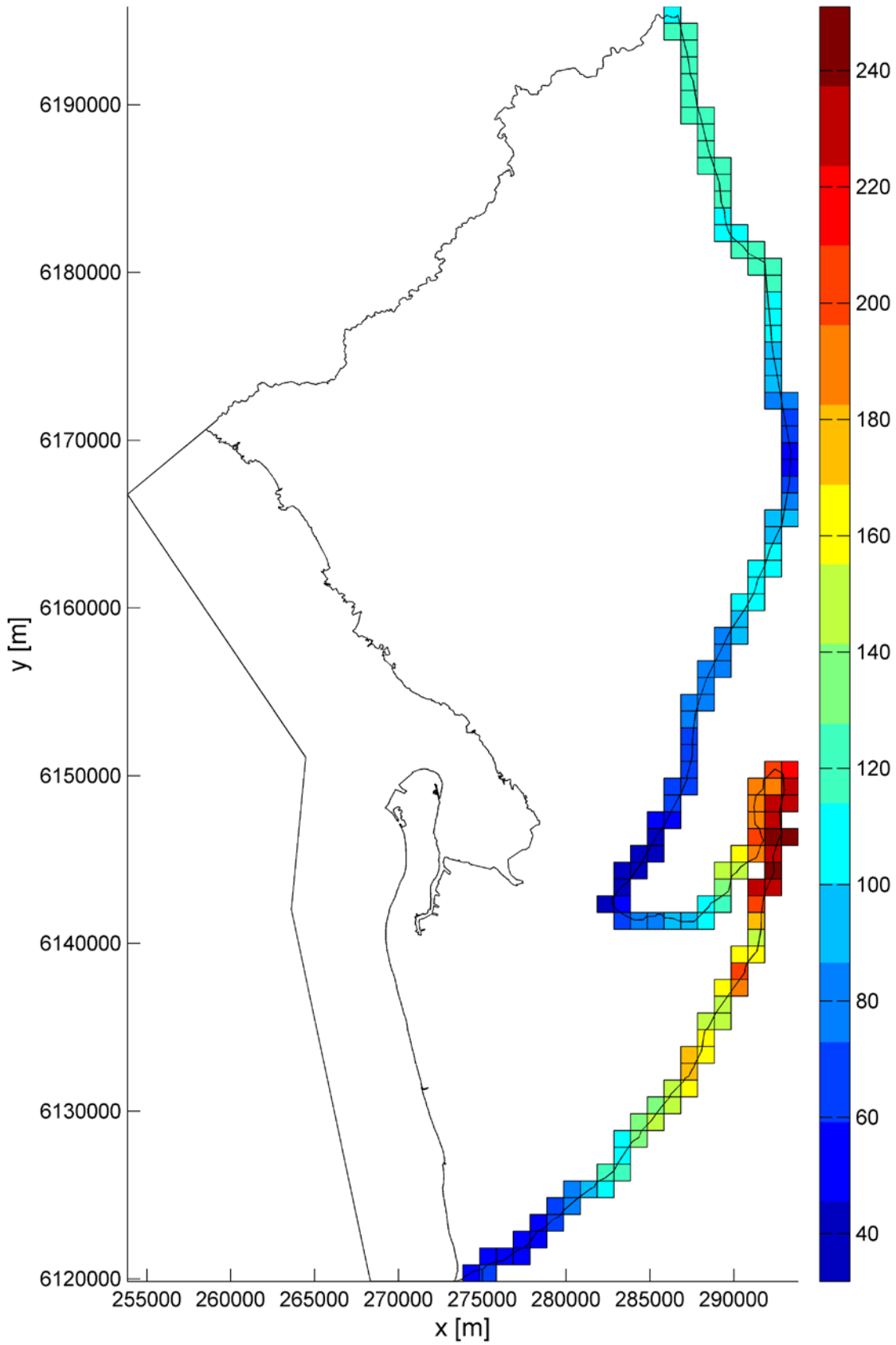
$$h_{shift}(t) = \left(\frac{P_{ave}(t) - P_{min}}{P_{max} - P_{min}} \times 2 - 1 \right) \times HAMP \quad (2)$$

where $P_{ave}(t)$ is the spatially-averaged rainfall across the domain at time t (the rainfall data are described in the Recharge section below), P_{min} and P_{max} are the minimum and maximum spatially-averaged rainfall across the domain and across all times, and $HAMP$ is an amplitude factor. The term in parenthesis takes values between -1 and 1, being -1 when rainfall is at its minimum and 1 when rainfall is at its maximum. Therefore, $h_{shift}(t)$ varies between $-HAMP$ and $HAMP$. $HAMP$ was calibrated with a preferred value of 10 m and was allowed to vary between 1 m and 20 m during calibration.



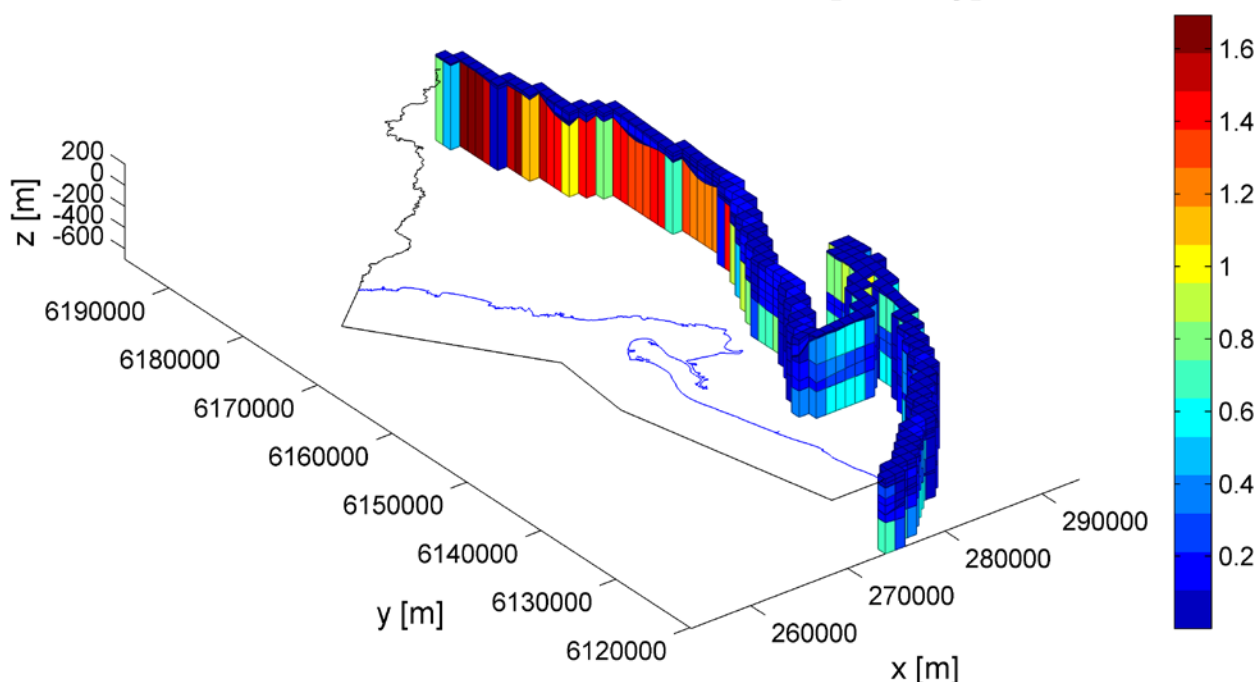
Apx Figure K.15 Long-term average groundwater level contours in the Mount Lofty Ranges created using all available data, regardless of well screen depth. Interpolation method used: IDW

Hydraulic head of eastern GHB cells [m AHD]



Apx Figure K.16 Specified head for the GHB condition applied to the cells along the eastern boundary (same in all layers)

Conductance of eastern GHB cells [m²/day]



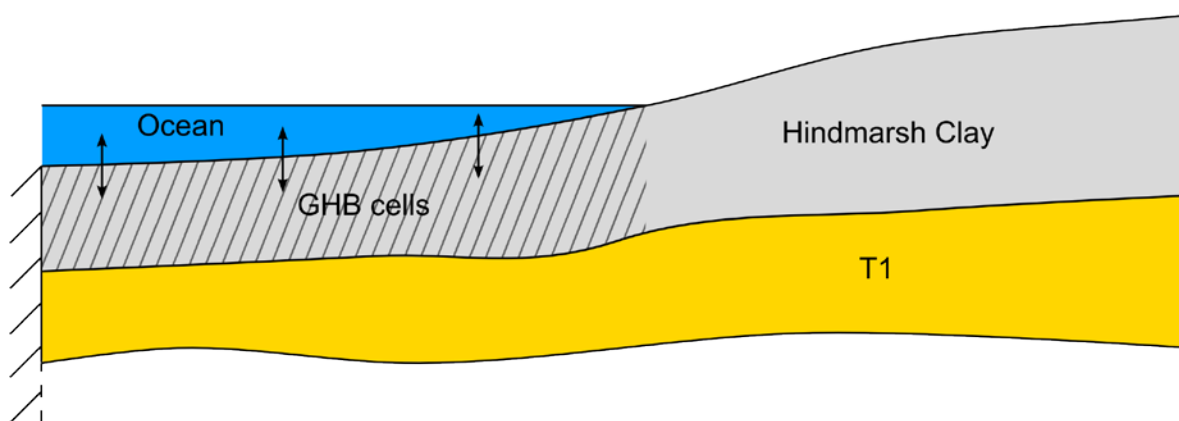
Apx Figure K.17 Conductance of the eastern GHB cells (3D view) when K equals the preferred value in all units. The distribution of values reflects differences in the area connecting the cells to the external source (product of the cell thickness by the length of boundary line crossing the cell)

Coastal boundary

A GHB was implemented at the top model boundary (i.e. layer 1) from the coastline to 5km offshore to allow flow through the ocean floor (Apx Figure K.18). The specified head values were set to the equivalent freshwater head representing mean sea level (0 m AHD) which were calculated using the following formula (Guo *et al.* 2002):

$$h_f = \frac{\rho_s}{\rho_f} h - \frac{\rho_s - \rho_f}{\rho_f} Z \quad (3)$$

where h_f (m AHD) is the equivalent freshwater head, ρ_s and ρ_f (kg L^{-1}) are the densities of seawater ($1,025 \text{ kg m}^{-3}$) and freshwater ($1,000 \text{ kg m}^{-3}$) respectively, h (m AHD) is the seawater head (i.e. 0 m AHD) and Z (m AHD) is the elevation at which the equivalent freshwater head is calculated. Z was obtained from the bathymetry of the seafloor. The conductance used in the GHB, calculated using equation (1), represents the region between the cell centre and the seafloor. Hence, A and L in equation (1) are the surficial area and half-thickness of the cell, respectively, whereas K (named OK in the following as for “Ocean K ”) should be similar to the hydraulic conductivity of the Hindmarsh Clay aquitard that constitutes the first layer under the ocean. Sediments on the seafloor may have a different (and unknown) hydraulic conductivity, and so OK was calibrated independently. The preferred value and the allowed range of values during calibration were nevertheless taken identical to the vertical hydraulic conductivity of the Hindmarsh Clay aquitard.

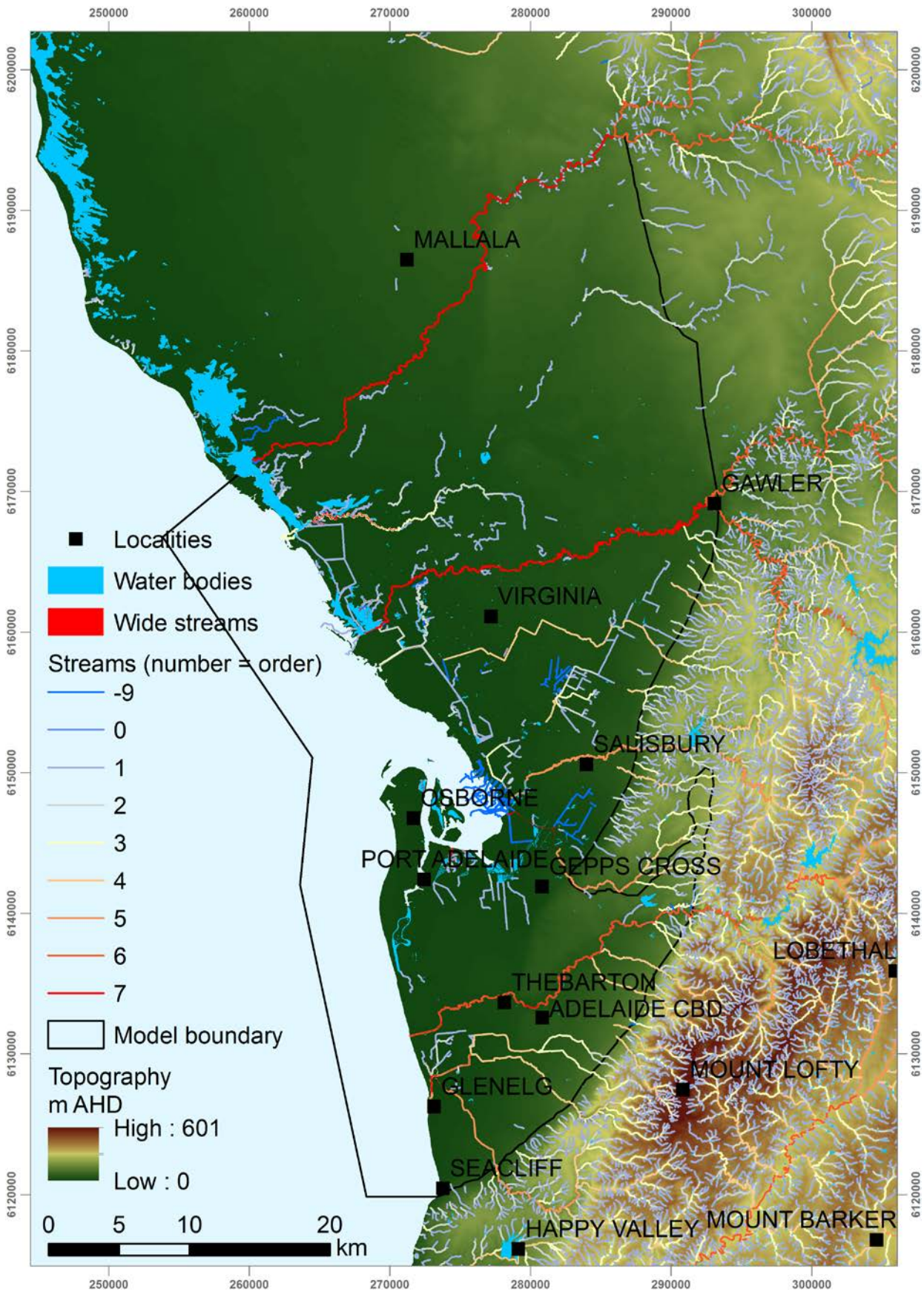


Apx Figure K.18 Conceptualization of the coastal boundary

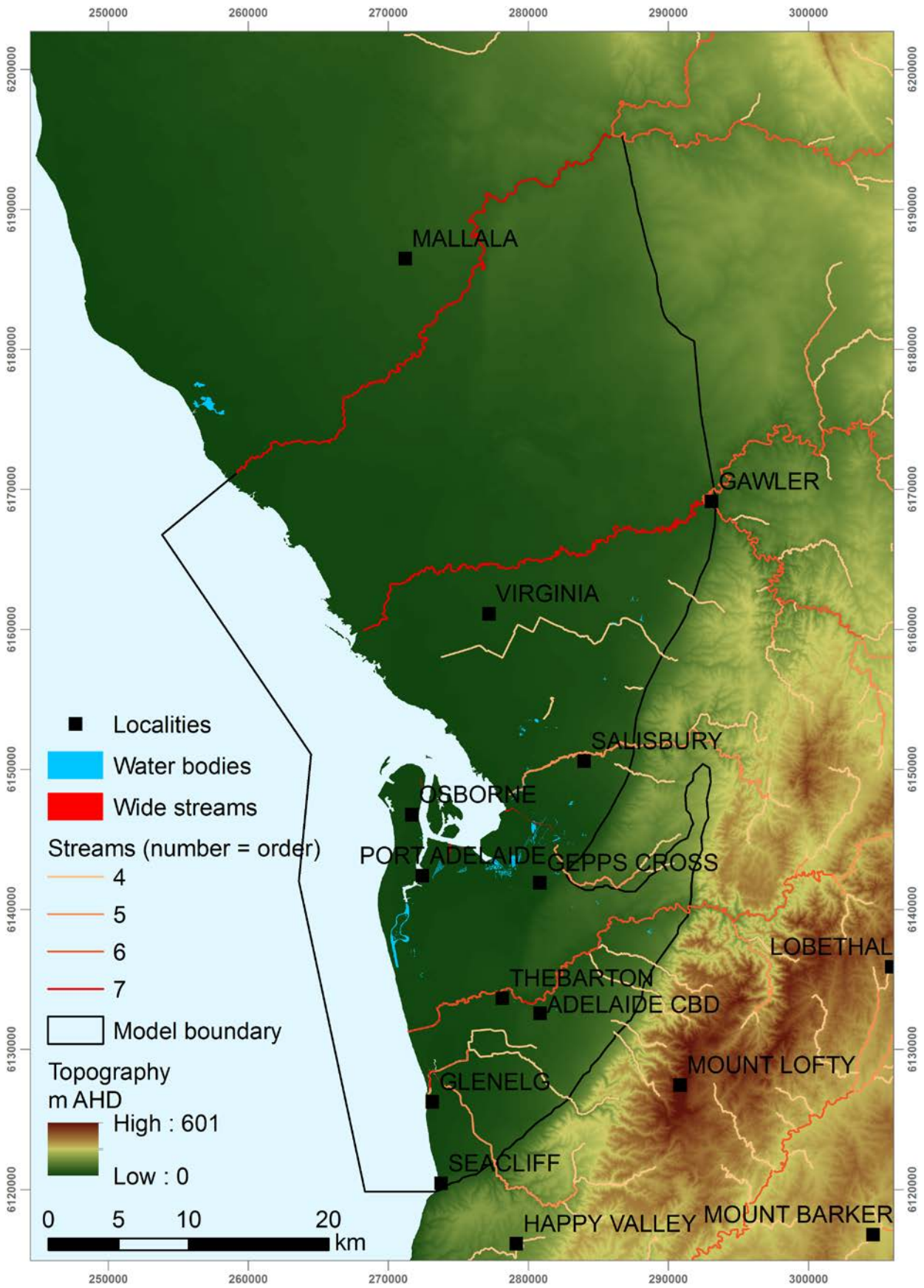
Groundwater-surface water interaction

Surface water features were sourced from three types of data produced by DEWNR: streams (lines), wide streams (polygons) and water bodies (polygons) (Apx Figure K.19). In the transient models, distinction was made between perennial and ephemeral features, the latter being active only during winter months (May to October). Information about seasonal variability was available in the database for some of the wide streams and water bodies. Others were assumed to be ephemeral. No information was available for streams. The stream status was therefore estimated on the basis of the stream order, assuming that a stream order < 4 was indicative of an ephemeral stream as this gave a plausible stream network for summer in the area (Apx Figure K.20).

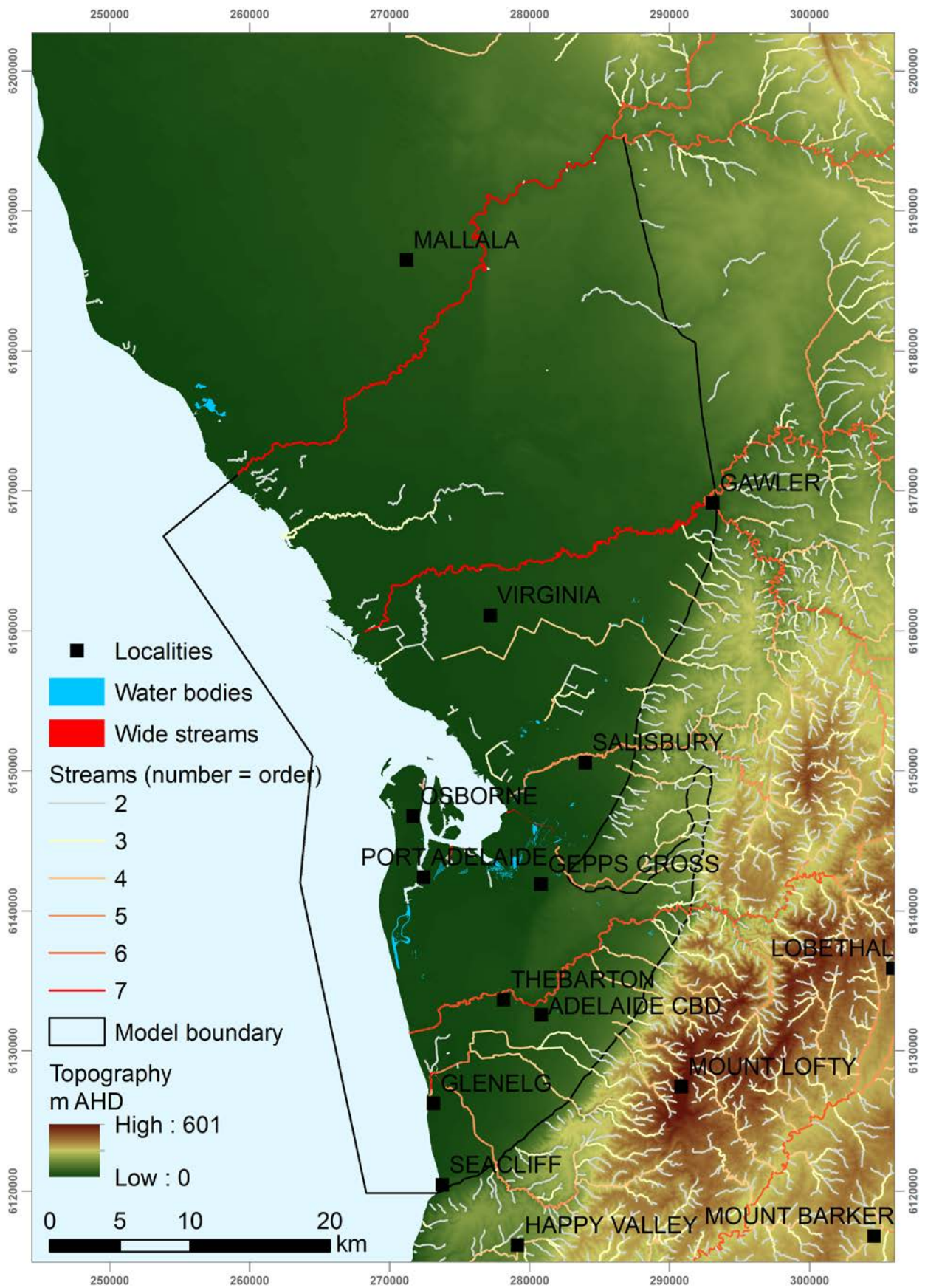
Further difficulties arose concerning the implementation of surface water features in the steady-state model, which ideally requires an equivalent long-term average description of surface water features. As an attempt to approximate such a description, an intermediate set of surface water features was derived, constituted by streams of order > 1 in addition to perennial wide streams and water bodies (Apx Figure K.21). The sensitivity of the results to the implementation of surface water features in the steady-state model was tested as described in section K.3.9.



Apx Figure K.19 All surface water features, used in winter months. A stream order of -9 indicates an unknown status. 'Wide streams' cover only a few areas mostly along streams of order 7 and thus can hardly be differentiated from these streams



Apx Figure K.20 Perennial surface water features, used in summer months. 'Wide streams' cover only a few areas mostly along streams of order 7 and thus can hardly be differentiated from these streams



Apx Figure K.21 Average surface water features tested in the steady-state model. 'Wide streams' cover only a few areas mostly along streams of order 7 and thus can hardly be differentiated from these streams

All surface water features were modelled using the river (RIV) package from MODFLOW. In the absence of river level data, the river level (variable HRIV in MODFLOW) of all surface water features was set equal to

the minimum topographic elevation in the model cell containing a surface water feature. The minimum was chosen as the best option amongst other possibilities (maximum; average; value at the centre of the cell) because the rivers represent incisions of the topography within a cell. Also note that potentially salty surface water features along the coast were not corrected for density effects, as this is expected to have little effect given their small water depth, and information about their salinity is generally not available. In the absence of data, the riverbed bottom (RBOT) was assumed to be 1 m lower than the river stage everywhere. In reality, RBOT is expected to be spatially variable and hence this represents a source of uncertainty of the model. It is noted that the previous model developed by RPS Aquaterra (Georgiou *et al.* 2011) used different RBOT values for different rivers, which should in theory yield a better representation; however, the specified values were not backed-up by any data.

During winter months (May till October), the river package was activated in all cells containing a surface water feature, whereas during summer months (November till April), the river package was activated only in cells containing perennial features. However, all river levels were kept constant throughout the year and therefore this represents a possible area for future model improvement (subject to data availability).

The conductance was calculated as in equation (1), K being here the average river bed hydraulic conductivity of all surface water features contained in the cell, A being the sum of the areas of all surface water features contained in the cell, and L being the average bed thickness of all surface water features contained in the cell. Details on these parameters are given hereafter.

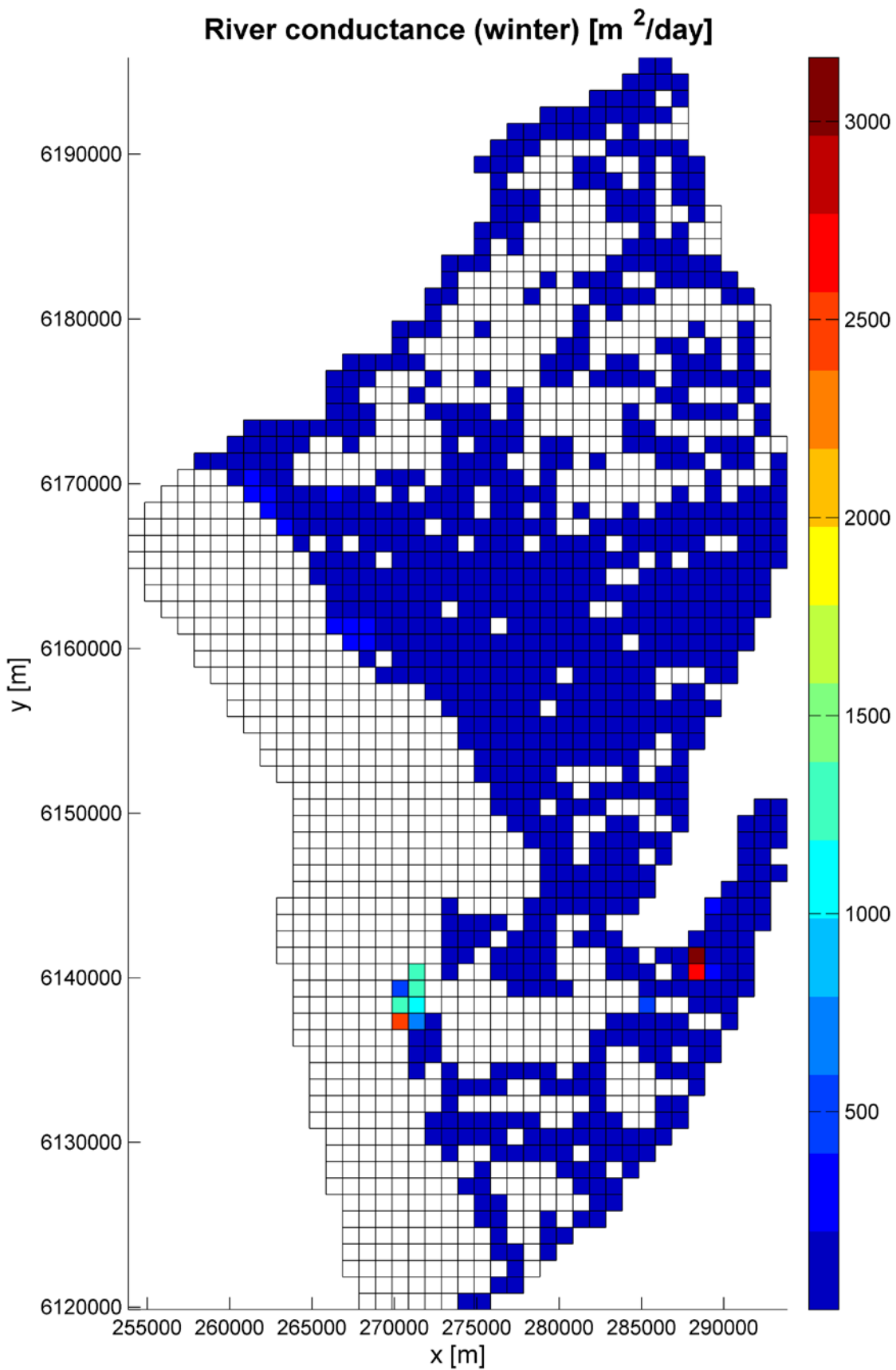
The riverbed hydraulic conductivity (K) was calibrated around a preferred value which was taken as a function of the surficial material upon which the feature lies. Surficial materials were classified into 4 groups based on surface geology data downloaded from <https://sarig.pir.sa.gov.au/Map> on the 02/10/2014: Quaternary sediments, Tertiary sediments, fractured rock and “unclassified”, yielding 4 parameters named $RIVBEDK_Q$, $RIVBEDK_T$, $RIVBEDK_FR$ and $RIVBEDK_Wa$. The preferred values of the first three parameters were taken equal to the preferred value assigned to the vertical hydraulic conductivity of the Hindmarsh Clay aquitard, T1 aquifer and Bedrock, respectively. The preferred value for the “unclassified” was taken equal to the one of the fractured rock. These 4 values were allowed to vary by four orders of magnitude both under and above their preferred value during calibration.

For wide streams and surface water bodies, which were provided as polygons, the area (A) was calculated by finding their intersection with each cell. To apply the same method to streams, which were provided as lines, a transformation into polygons was first performed on the basis of stream width w (m), estimated as:

$$w = 0.5 \times o \tag{4}$$

where o is the stream order. Where a stream order was indicated as < 1 in the available database, it was assumed to be 1. Stream width thus ranges 0.5–3.5 m, which was deemed reasonable for the streams of the area. The resulting cell conductances are shown in Apx Figure K.22 for all surface water features (including ephemeral streams). A large number of cells include a surface water feature (in winter months). This is due both to the large number of surface water features, especially non-perennial (see Apx Figure K.19), and to the use of a relatively coarse grid resolution. Note that some very small water bodies are essentially invisible on that figure but still give rise to cells with groundwater-surface interaction. A finer grid would imply a smaller proportion of cells including a surface water feature. Nevertheless, because the conductance is calculated as a function of the area of the surface water features contained in each cell, the total area of exchange remains the same whatever the grid resolution.

The bed thickness (L) was taken equal to 1 m and was not calibrated since in the definition of the conductance, only the ratio of K to L matters and K was calibrated.



Apx Figure K.22 Conductance of RIV cells for all surface water features (including non-perennial)

Recharge

Here net recharge (i.e., rainfall minus actual evapotranspiration) was modelled using the recharge (RCH) package. The combination of processes leading to net recharge was captured by calculating an effective fraction of the rainfall (*RPMUL*) that was applied uniformly in space and time:

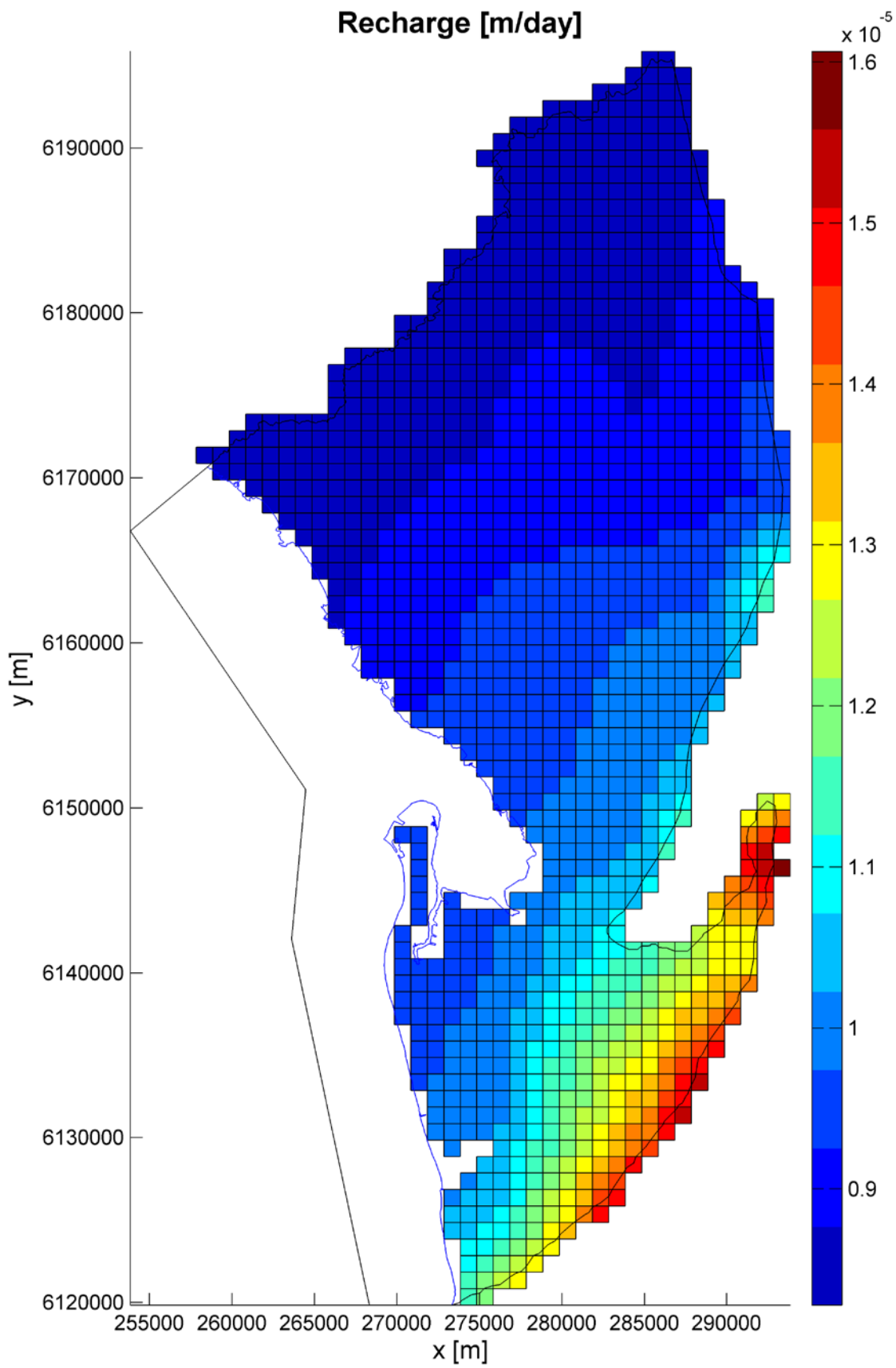
$$R(t) = P(t) \times RPMUL \quad (5)$$

where $R(t)$ is the recharge distribution in each cell of the layer in which the water table resides at time t , and $P(t)$ is the rainfall distribution at time t . The spatial rainfall distribution was obtained from the Scientific Information for Land Owners (SILO) which provided gridded values for rainfall at a 5-km resolution, which were then linearly interpolated onto the model grid. The methodology for generation of this data can be found in Jeffrey *et al.* (2001), with further revisions to the methodology located at: <https://www.longpaddock.qld.gov.au/silo/publications.html>. For the steady-state model, the average annual rainfall distribution calculated for the period 1889–2013 was used.

Note that this is a coarse approach to modelling recharge and that the evapotranspiration package (EVT) could have been used to improve recharge dynamics. The reason for not using it is that the initial idea was to use remote sensing products for estimating actual evapotranspiration, which would then already include direct evapotranspiration from the water table. Unfortunately, time did not allow us to achieve this.

The parameter *RPMUL* was calibrated around a preferred value based on the average recharge to the Quaternary sediments, which was estimated to be 3.6 mm yr⁻¹ based on the CMB method (Appendix C). Using the average rainfall over the model area for the period 1889–2013 (438 mm yr⁻¹) the corresponding value for *RPMUL* is 0.008 (i.e., recharge equals 0.8 % of rainfall). However, a large uncertainty exists in the recharge estimate based on the CI mass balance method (see related discussion in Appendix C). Therefore, *RPMUL* was allowed to vary by one order of magnitude both above and below this value during calibration. The steady-state recharge distribution with *RPMUL* equal to the preferred value (0.008) is shown in Apx Figure K.23.

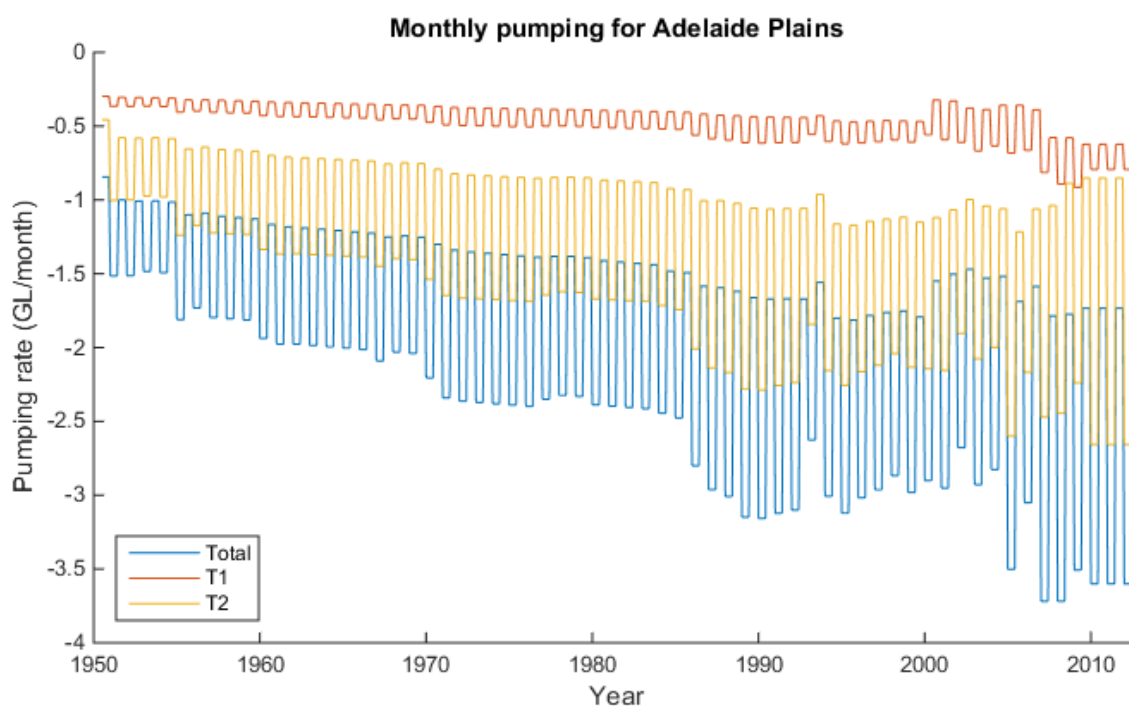
Note that a diffuse recharge rate equal to 5 % of rainfall was applied in the previous model by Georgiou *et al.* (2011). This resulted in a large dominance of diffuse recharge in the water budget, thus contradicting the previous understanding of recharge mechanisms of the aquifers in the area. This recharge rate was based on a former model by REM (2006b) which included the MLR as part of the model domain. In that model, this recharge rate was applied based on recharge estimates for the MLR, and not for the Plains (REM 2006a). As significantly less rainfall occurs in the Plains than in the MLR, a recharge rate of 5 % of rainfall is likely to be an overestimation of diffuse recharge across the Plains.



Apx Figure K.23 Steady-state recharge distribution at its preferred value (0.8 % of rainfall), i.e. before calibration

Pumping and MAR

The effects of both extraction and injection due to production wells and managed aquifer recharge (MAR) schemes is implemented in the model using the wells (WEL) package based on the well data implemented in the previous model (Georgiou *et al.* 2011), with the values and monthly patterns for 2012 and 2013 taken the same as in 2011. The active wells in the model domain are shown in Apx Figure K.14. This includes only licenced production wells (i.e., non-licenced wells are not accounted for) and MAR wells. The total monthly net pumping rates (injection minus extraction) applied across the model domain is shown in Apx Figure K.24. Pumping is seasonally varying with higher pumping in summer (May-October) and less in the winter (November-April). The annual average net pumping level increased by 125 % from 1950 (14.2 GL yr⁻¹) to 2011 (32 GL yr⁻¹).



Apx Figure K.24 Monthly net pumping rates applied to the entire model domain, T1 and T2 aquifers

K.3.6 FLOW MODELS (FUTURE CONDITIONS)

The aquifers of the Adelaide Plains provide a vital supply of groundwater to its many users and a suitable target for storage of captured stormwater following high surface flows. Efficient management of this resource necessitates a critical understanding of the impacts of changes to recharge and usage of the aquifers. Investigating the future status of the resource forms the focus of the scenario analyses, with emphasis on:

- Reductions in rainfall due to a changing climate;
- Increased pumping by existing wells up to full allocations; and
- Increased usage of Managed Aquifer Recharge (MAR).

The nature of scripting of the groundwater flow models provides a powerful tool in developing the scenario models as it allows for several models to be easily deployed and updated as new data becomes available and if the projections are revised.

The hydraulic heads of the final time step of the historical transient development model constitute the initial hydraulic heads for future transient models, which run from May 2013 to April 2100. Investigations into potential future conditions were carried out through modification of the boundary conditions and stresses in transient models as detailed below and summarized in Apx Table K.4. While grounded in reality, the scenario analyses carried out serves only to demonstrate the applicability of the model in investigating

increased stresses on the aquifers of the Adelaide Plains and are by no means exhaustive simulations of possible futures. Bearing in mind the limitations of the model, the simulations are nevertheless indicative of future challenges that must be met in managing the groundwater resources of the Adelaide Plains.

Apx Table K.4 Scenarios summary for Adelaide Plains groundwater modelling

SCENARIO	EFFECT/DRIVER	IMPOSED BY	CHANGE SIMULATED	REFERRED TO AS
Base case	-	-	-	Base
Climate change	Reduced rainfall to the AP&MLR due to emissions	Reduced RCH and GHB	RCP4.5 (See below)	RCP4.5
		Reduced RCH and GHB	RCP8.5 (See below)	RCP8.5
Increased pumping	Increased demand	Increasing WEL pumping fluxes	+10 %	Increased pumping
Decreased pumping	Decreased demand	Decreasing WEL pumping fluxes	-10 %	Decreased pumping
Increased MAR	Increased demand	Increasing MAR schemes in WEL	Increased schemes	Increased MAR

Base case

A base case scenario was developed as a point of comparison for all of the other future scenarios (i.e. climate change, changes to pumping and increased MAR). It is aimed at being representative of what might happen if average conditions from the recent years were to persist. In order to simulate this, an average of the last 10 years of distributed rainfall for each month was implemented as a recurring annual rainfall input (with monthly variations) to the model from 2013 to 2100. This influenced both the areal recharge and the MLR boundary. The choice of 10 years is subjective, but was deemed better than choosing only the last year as representative, or choosing a longer term average which also isn't representative of more recent climatic conditions. The pumping and MAR rates applied were the same as the 2012 year of the development period. These rates were repeated annually without change for the entire base case simulation. The coastal boundary remained unchanged for the base case.

Climate change

The future changes in rainfall directly affect the recharge across the plains and, indirectly, the head values at the eastern boundary of the model. A recent report by Charles *et al.* (2015) details climate projections for South Australia and in particular the Adelaide Plains and Mount Lofty Ranges, and the data for these projections is provided online at: <https://data.environment.sa.gov.au/Climate/SA-Climate-Ready/Pages/default.aspx>. The climate projections based upon fifteen global climate models (GCMs) consider two Representative Concentration Pathways (RCP):

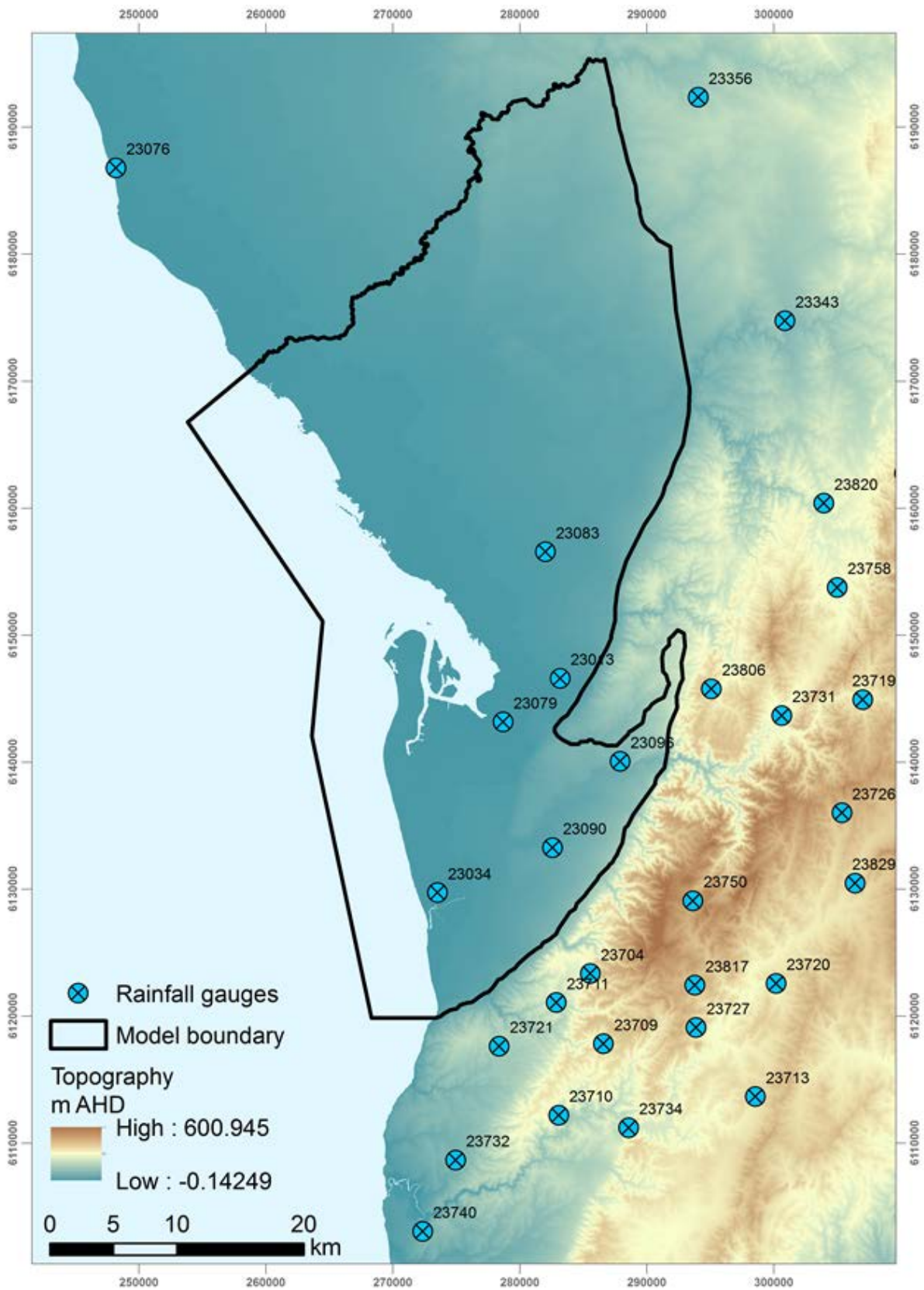
- Intermediate: 4.5 W/m² of radiative forcing (RCP4.5)
- High-emission: 8.5 W/m² of radiative forcing (RCP8.5)

Future climate was simulated by using downscaled monthly-averaged rainfall at the rainfall gauge locations shown in Apx Figure K.25 for the two different emission scenarios (RCP4.5 and RCP8.5) based upon the MRI-CGCM3 model (Charles *et al.* 2015). The point rainfall data was interpolated across the model area from the rainfall gauge stations using inverse distance weighting at a monthly time-step. Finally, maps of the rainfall distribution for each month from 2013-2100 were used to derive the recharge condition.

To account for compounding effects of higher ET etc., a reduction is applied to the parameter *RPMUL* to cause further reduction of the recharge signal over time. This is implemented as follows:

$$RECH(t) = P(t) \times RPMUL \times (1 - r_{red} \times t/NPER) \quad (6)$$

where r_{red} is the final amount by which recharge is further reduced at the end of the climate change scenarios and $NPER$ is the total number of stress periods in the model simulation (equal to 1044).



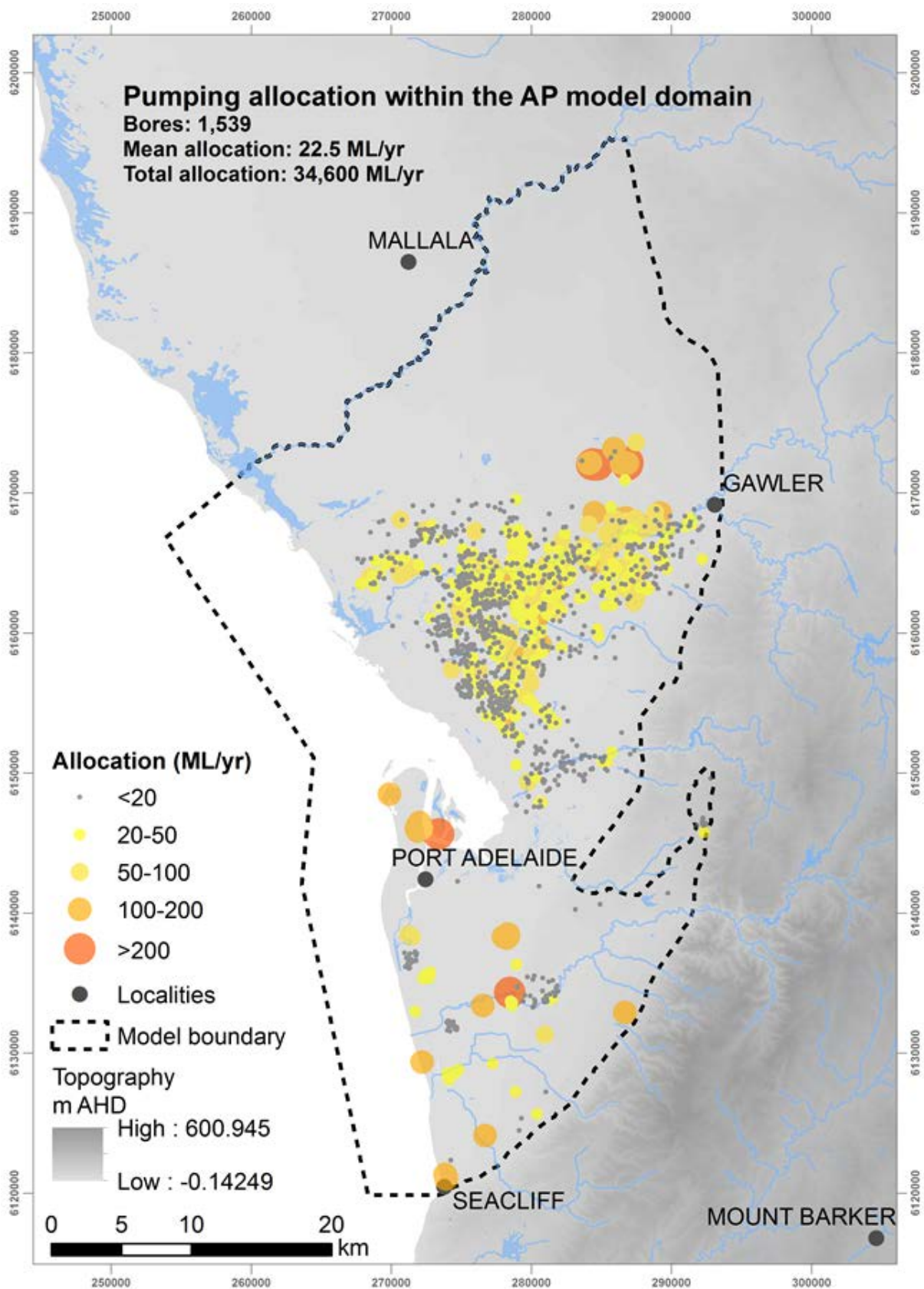
Apx Figure K.25 Rainfall gauges where downscaled climate projections are available for the AP and MLR (some not shown as outside of extents)

Pumping and MAR

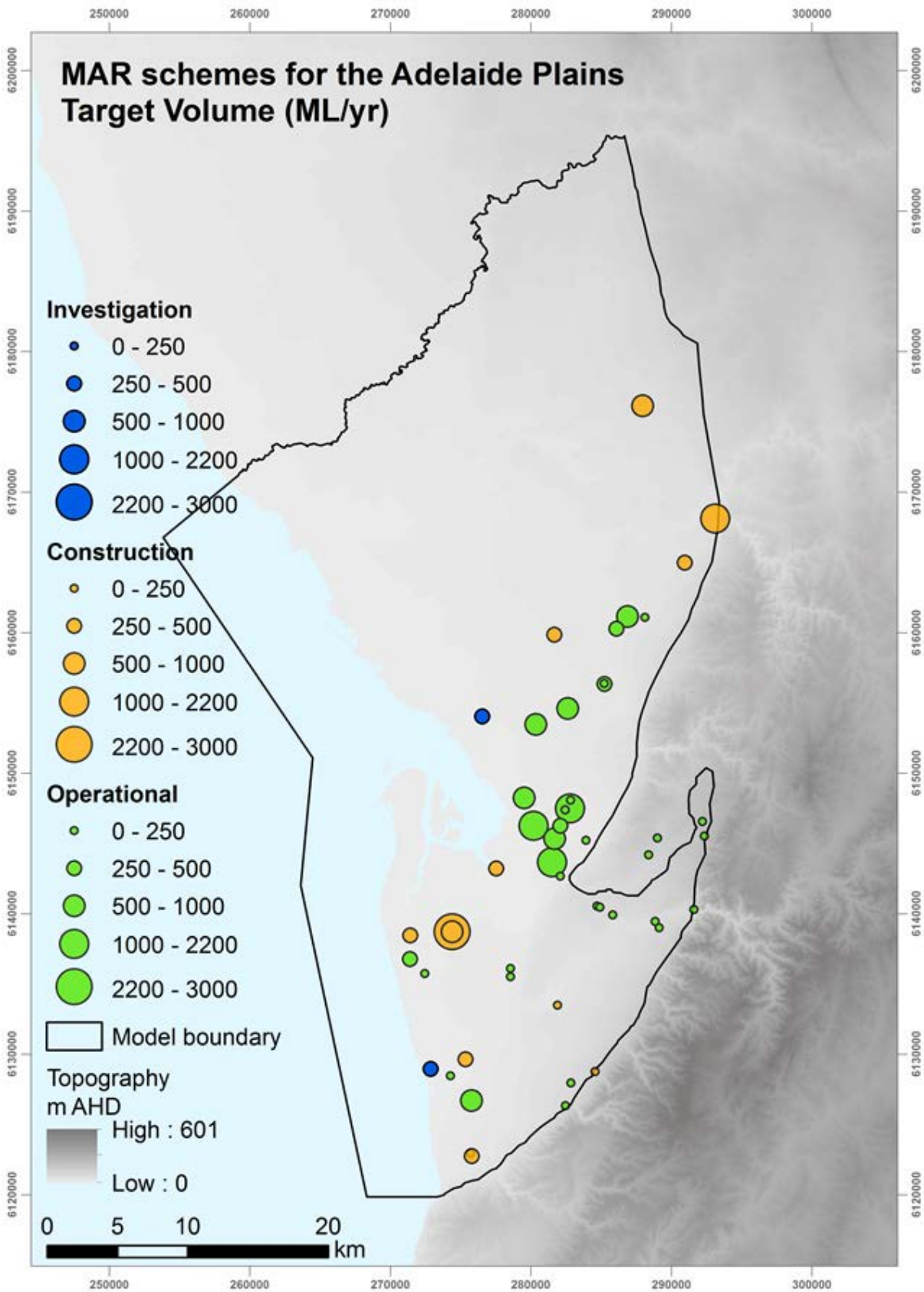
The current total allocation for licensed production bores in the Adelaide plains is approximately 35 GL yr⁻¹ (DEWNR 2015, *pers. comm.*) (Apx Figure K.26), which is 3 GL yr⁻¹ (9%) more than the 32 GL yr⁻¹ of pumping occurring at the end of the transient flow model (1950–2013). To assess the impacts of both increased and reduced total pumping across the Adelaide Plains, the model was perturbed in a simple sensitivity analysis whereby pumping was uniformly adjusted by ±10%, which gives rise to two different pumping scenarios (Increased pumping, Decreased pumping).

Improved utilisation of stormwater runoff as a resource is attractive to many local councils within the AP and there are now numerous plans for implementing MAR schemes. Apx Figure K.27 shows the locations and target volumes for operational schemes, and those that are under construction or under investigation. However, unlimited uptake of MAR on a large scale could have adverse impacts on the aquifers, despite targeting a zero sum change to storage over time (i.e. injection equals extraction). The aim of these particular scenario analyses is to elucidate if seasonal loading and unloading of stormwater to the AP aquifers significantly affects the heads and water balance of the T1 and T2 aquifers and how it compares to the business-as-usual approach. The total number of MAR schemes considered was 50 based on unpublished data supplied by DEWNR, including 36 operational, 12 in construction and 2 under investigation totalling a maximum of 23 GL yr⁻¹ of use. The MAR schemes are implemented by means of the WEL package. Where exact locations of proposed MAR wells for new and planned schemes weren't known, they were estimated based on available information with an expected error of less than 500 m. The rules used in the script for defining the input to the model are as follows:

- Each scheme only has a lifespan of 20 years and is shut off after this period.
- It takes 5 years for each scheme starting to extract as much as is being injected, with recovery rates of 60 %, 70 %, 80 % and 90 % in years 1 to 4 respectively, and 100 % for subsequent years.
- Injection takes place evenly over June, July and August.
- Extraction takes place evenly over November to April, meaning the injection rates are twice as high as the extraction rates.
- The target volume (amount to inject/extract each year) is reached for every scheme.



ApX Figure K.26 Licensed pumping locations included in model domain of the Adelaide Plains. Note that some allocations for users are larger than shown as some licensees own multiple wells, in which case the total allocation is split equally over these multiple wells



Apx Figure K.27 MAR locations for operational and committed schemes

K.3.7 CI TRANSPORT MODELS

In line with the flow models, four CI transport models were developed for simulating (i) pre-development steady-state CI transport, (ii) pre-development transient CI transport (May 1900 – April 1950, no pumping), development transient CI transport (May 1950 – April 2013, pumping) and (iii) future transient CI transport (May 2013 – April 2100). These models serve not only the purpose of estimating salinity movements in groundwater, but also the purpose of calibrating the recharge and hydraulic parameters of the model because CI concentrations are a function of these. Both historical and future transient models implement the same stress periods as the flow models. The number of transport time-steps was not directly specified; instead, it was set to be calculated automatically by MT3DMS.

CI in the Adelaide Plains originates from (i) groundwater recharge from rainfall, (ii) leakage from surface water features and (iii) lateral flow from the MLR. It leaves the system through (i) submarine groundwater discharge, (ii) river discharge and (iii) pumping. Short-term variations in CI input concentrations are generally smoothed before reaching the water table due to mixing occurring in the unsaturated zone, and are further smoothed during transport in the saturated zone. Under these assumptions, groundwater concentrations are only a function of the time-averaged CI input concentration. The current model ignores long-term temporal fluctuations in the inputs that are not smoothed by mixing processes, i.e., CI input concentrations (including along the model boundaries) are assumed constant with time. Details about the concentrations used for the different boundary conditions are given below.

Eastern boundary (Mount Lofty Ranges)

CI concentrations of the lateral inflow across the eastern boundary were derived from interpolation of measured concentration data in the MLR fractured rock aquifers (i.e. outside the model domain) from which the groundwater crossing this boundary is sourced. Data were downloaded from the WaterConnect database maintained by DEWNR on the 19/11/2014. CI concentrations were obtained both from 1,067 direct measurements from 766 wells and from 19,018 EC measurements from 4,545 wells which were converted into CI concentrations using an empirical EC-CI relationship. Even though some degree of uncertainty is introduced by this conversion, it allows significantly more CI concentration estimates to be retrieved because EC is more generally available than direct CI concentration measurements, and the uncertainty induced by the conversion can be quantified. A total of 1,702 EC-CI pairs were used to derive the relationship. Similarly to what was found in Guan *et al.* (2010), the data were best fitted by a power function in the form of $Cl = aEC^b$. A high coefficient of determination ($R^2 = 0.9991$) was obtained with $a = 0.0558$ and $b = 1.178$, where CI and EC are in units of $mg L^{-1}$ and $\mu S cm^{-1}$, respectively (Apx Figure K.28). 95 % confidence intervals were also calculated to estimate the conversion uncertainty.

When several values were available from different sampling times in the same well, the arithmetic average (μ) was taken. The inverse distance weighting (IDW) method was then used for spatially interpolating the average CI concentrations in the MLR fractured rock regardless of sampling depth. The number of neighbours considered in the interpolation algorithm was fixed to 10. Weighting of different neighbours was also used to reflect the confidence of each data point, where the weight was calculated as the inverse of the measurement error. For concentrations obtained from direct measurements, the error on a single measurement was assumed to be 1 % of the value for wells that belong to the observation network managed by DEWNR, and 5 % of the value for other wells. For concentrations derived from EC, the error on a single measurement was estimated on the basis of the conversion uncertainty (i.e. 0.25 times the 95 % confidence interval, assuming a Gaussian distribution of the error). When several measurements were available for the same well, the arithmetic average was calculated. For wells with few or no repetition of measurements, an additional uncertainty arises from the small number of measurements. This uncertainty was estimated on the basis of the temporal standard deviation σ_{time} observed in wells for which at least 5 measurements were available. The uncertainty arising from a small number of measurements, σ_{nb_obs} , was calculated as:

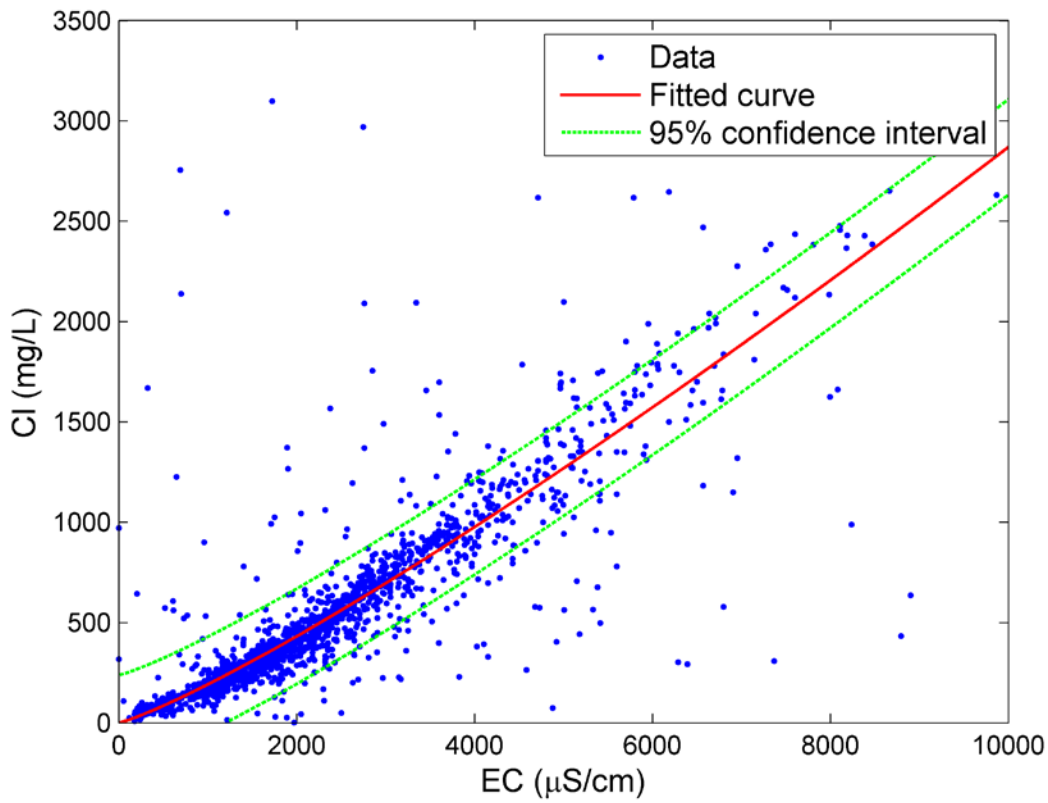
$$\sigma_{nb_obs} = \frac{\sigma_{time}}{\sqrt{n}} \quad (7)$$

where the bar above σ_{time} denotes the geometric average over wells with at least 5 measurements, and n is the number of temporal measurements in the well under consideration. The numerator contains the geometric mean and not the arithmetic mean because of the various orders of magnitude taken by σ_{time} in different wells. This equation defines a standard error, i.e., the error on the average (μ). σ_{nb_obs} was then added to the error associated to single measurements to obtain the final measurement error on μ . As an indication, the estimated measurement error on μ was 82 mg L⁻¹ for concentrations obtained from direct Cl measurements, whereas it was 209 mg L⁻¹ for EC-derived Cl concentrations.

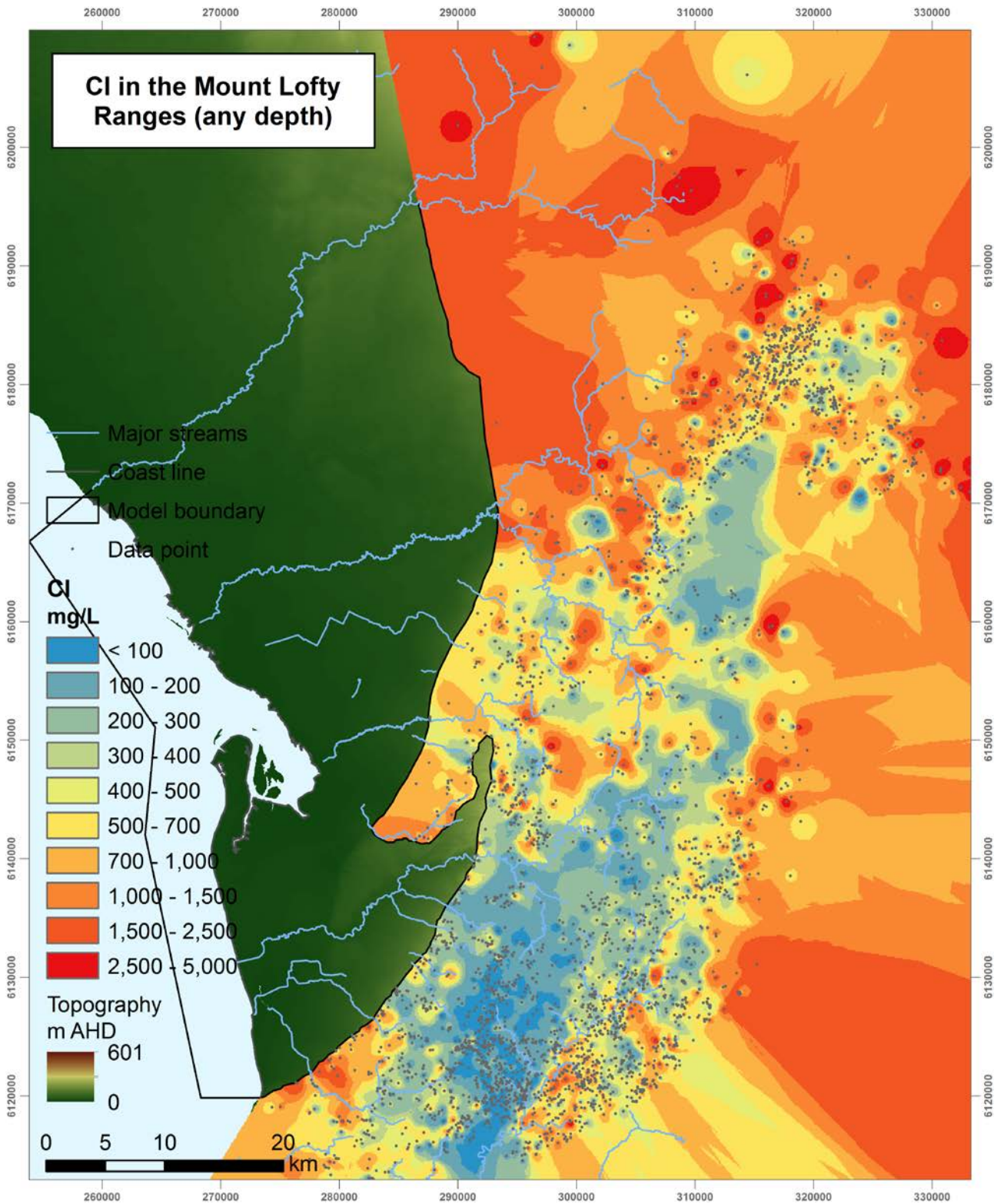
Finally, hydrochemical analysis has suggested that some pockets of very old (probably >> 10,000 years), saline groundwater can be found both in the MLR and in the Plains (see Appendices E and G). Such groundwater must have been recharged under different conditions that are not intended to be captured in the steady state model, which represents contemporary pre-development conditions. Assuming that contemporary recharge is higher than 0.1 % of rainfall (this is likely given the estimation of 0.8 % based on the chloride mass balance) and assuming that rainfall Cl concentration is about 5 mg L⁻¹ (see Appendix C), a maximum Cl concentration in the contemporary groundwater would be 5,000 mg L⁻¹. Therefore, although this limit is somewhat arbitrary, Cl concentrations above 5,000 mg L⁻¹ were excluded from the data before interpolation, assuming they were reflective of quasi immobile pockets of paleo-groundwater. This concerned less than 2 % of the data.

The derived Cl distribution in the MLR is shown in Apx Figure K.29. The concentrations are relatively low east of the Golden Grove Embayment (down to < 100 mg L⁻¹), except in the south close to the coast. This can be explained by a relatively high portion of rainfall transforming into recharge, as can be expected in this area where topography and rainfall are the highest of the region. The concentration increases towards the north along the eastern boundary of the model (up to almost 2,000 mg L⁻¹), which correlates with lower topography and rainfall. Data are quite sparse north east of the model domain, resulting in a relatively high uncertainty.

The chloride values along the eastern boundary were linearly interpolated to the centre of the boundary cells to represent the chloride concentrations of the water flowing in across the boundary. Resulting concentrations are shown in Apx Figure K.30.

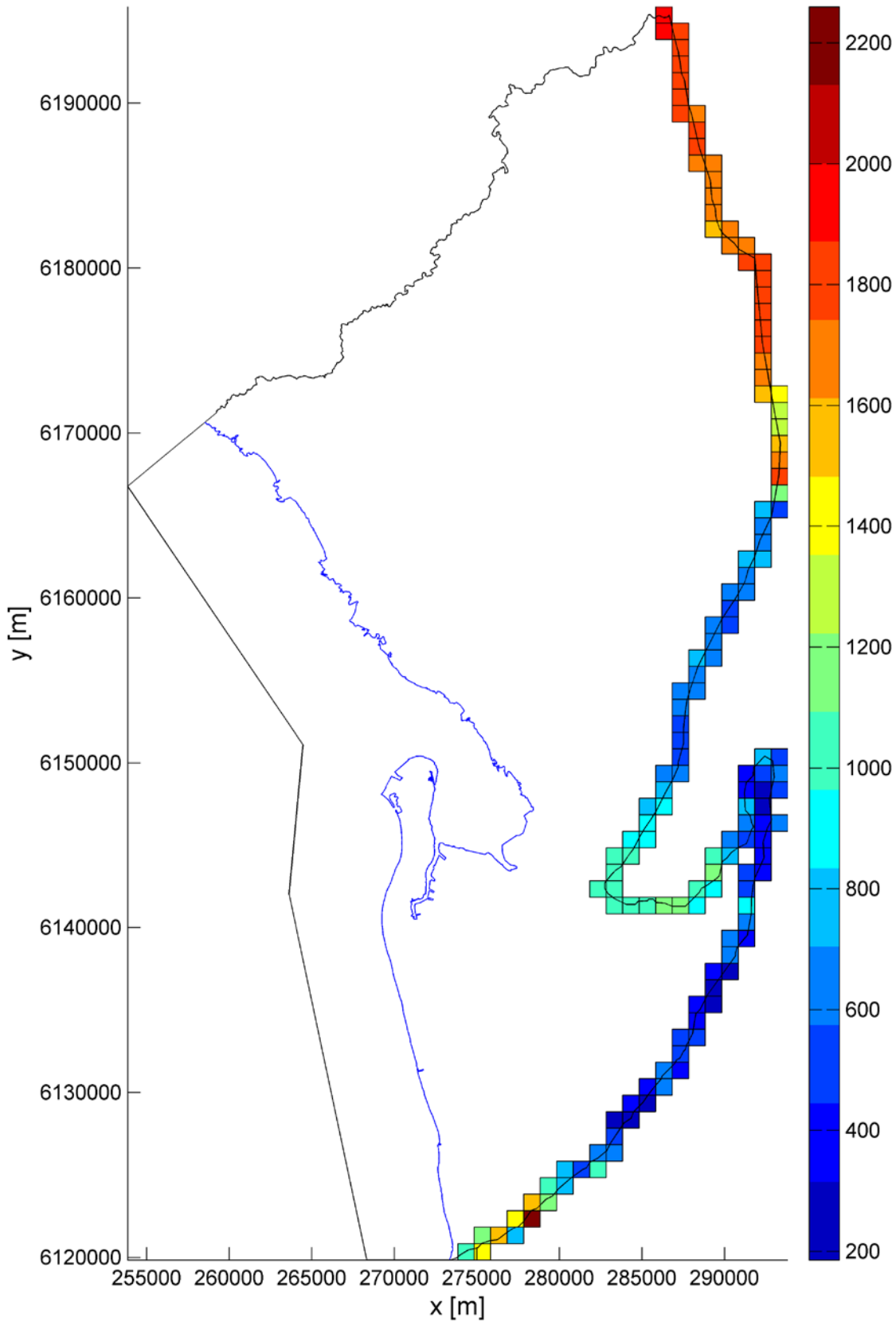


Apx Figure K.28 Cl versus EC data used to derive the EC-Cl relationship (red) given by $Cl = 0.0558 \times EC^{1.178}$ where Cl and EC are in the units of mg L^{-1} and $\mu\text{S cm}^{-1}$, respectively. Upper and lower 95 % confidence bounds (in green) are used to quantify conversion uncertainty



ApX Figure K.29 Cl concentrations (mg L^{-1}) in the eastern Mount Lofty Ranges used to assign the eastern boundary condition in the Cl transport model

Cl concentration in inflow across eastern boundary [mg/L]



Apx Figure K.30 Cl concentration (mg L^{-1}) assigned to the groundwater inflow across the eastern boundary (same in all layers)

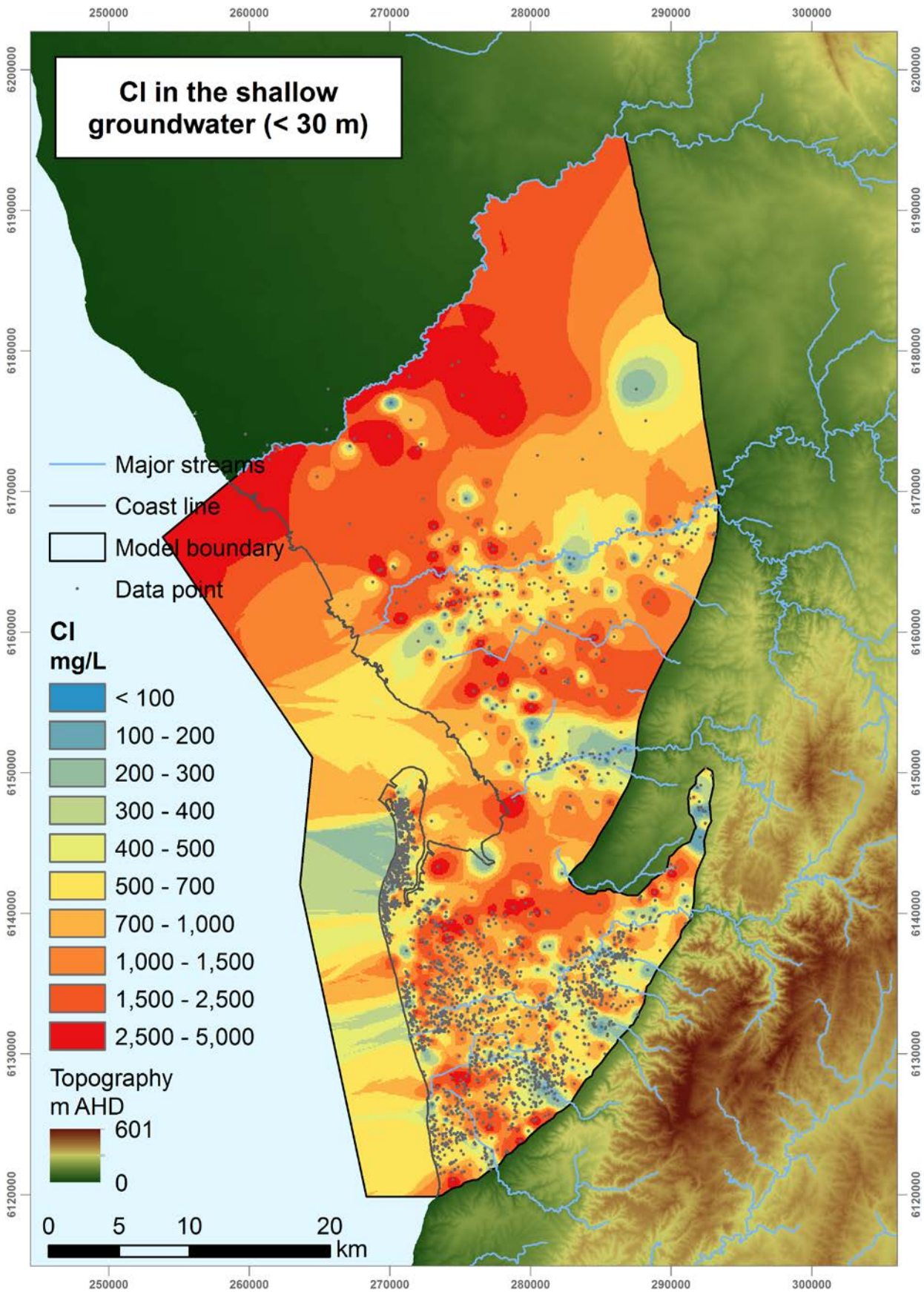
Coastal boundary

A Cl concentration of 19,400 mg L⁻¹ (mean seawater concentration) was used for GHB cells under the ocean floor. This concentration is assigned to any inflow that may occur from the sea into the groundwater system. This should be limited to the natural seawater wedge (not represented in the model) under natural conditions (no pumping), but can be significant when the system is under stressed conditions (pumping).

Groundwater-surface water interaction

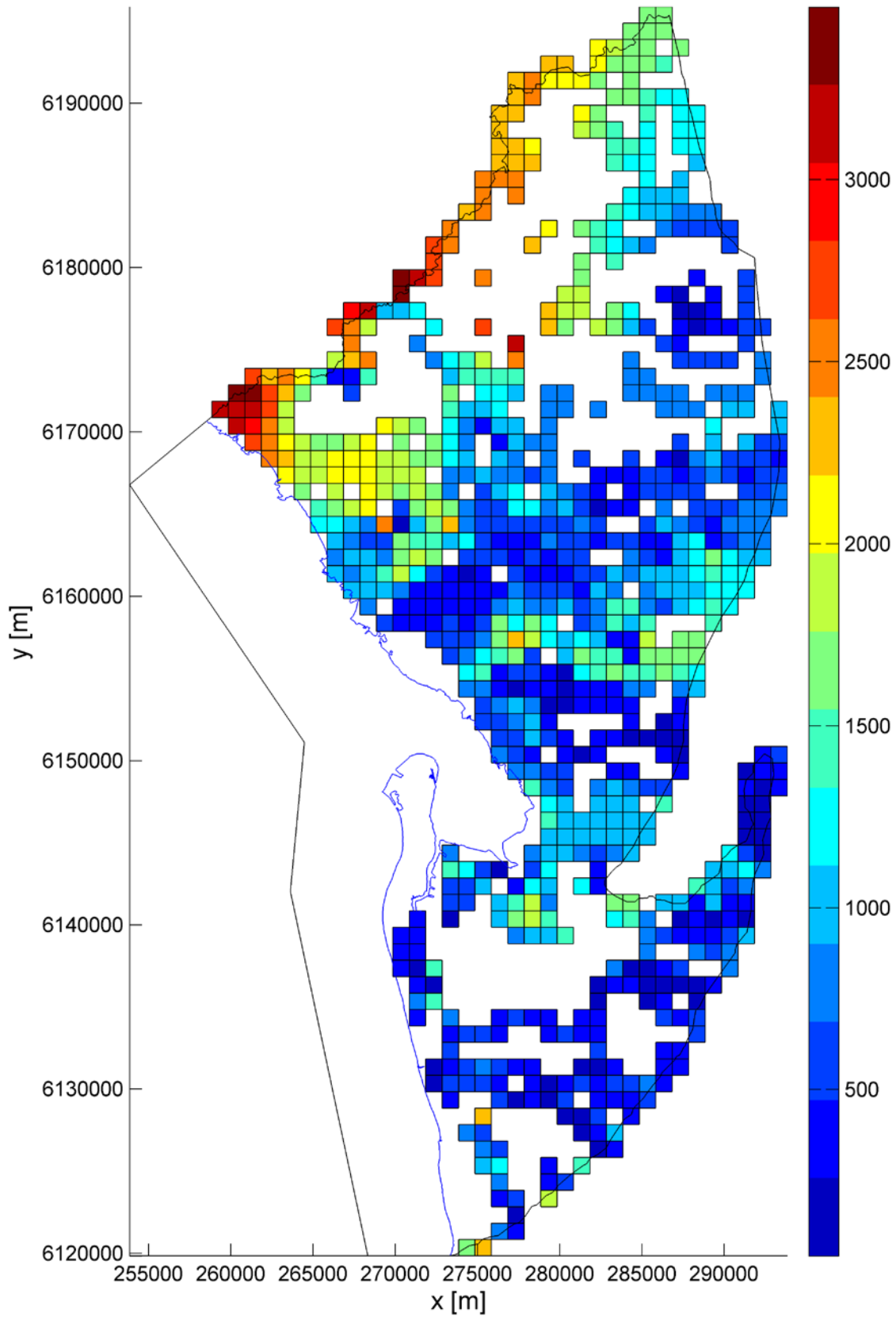
No robust record of surface water Cl concentration was available. The concentration of water infiltrating from surface water features was hence estimated from spatial interpolation of the average concentration data in the shallow groundwater (< 30 m). This approach is valid only if there is no mixing of the infiltrating water with groundwater originating from elsewhere. This assumption is probably not strictly satisfied, but the strong spatial correlation between the location of streams and salinity patterns suggests that it is reasonable. This was done for every cell containing a surface water feature, therefore yielding spatially variable concentration. However, temporal variability was neglected.

The data acquisition and interpolation methodology were the same as when determining the Cl concentration along the eastern boundary (see above). The result of the interpolation shows that the lowest concentrations generally occur below or nearby streams, indicating a significant degree of surface water infiltration (Apx Figure K.31; see also further discussion in Appendix C). Finally, the minimum concentration found in each model cell (model cells are larger than the interpolated map cells) was taken as the infiltration concentration. This is intended to minimize the impact of the mixing of infiltrated water with aquifer water on the estimate of infiltration concentrations, which are expected to be lower than concentrations found otherwise in the aquifer. Resulting values are shown in Apx Figure K.32 for all surface water features (including ephemeral streams).



Apx Figure K.31 CI concentrations (mg L^{-1}) in the shallow groundwater used to assign the concentration in infiltration from surface water features

Cl concentration in river leakage (winter) [mg/L]



Apx Figure K.32 Cl concentrations (mg L^{-1}) assigned to river infiltration from surface water features (including ephemeral)

Recharge

The Cl concentration in recharge was determined based on the Cl mass balance as:

$$C_R = \frac{P \times C_P}{R} \quad (8)$$

where C_R and C_P are the Cl concentrations in groundwater recharge and in rainfall, respectively, R is the groundwater recharge rate and P is the long-term average rainfall. P and R are the same as in the steady-state flow model. Since recharge is taken proportional to rainfall, equation (7) can also be written as:

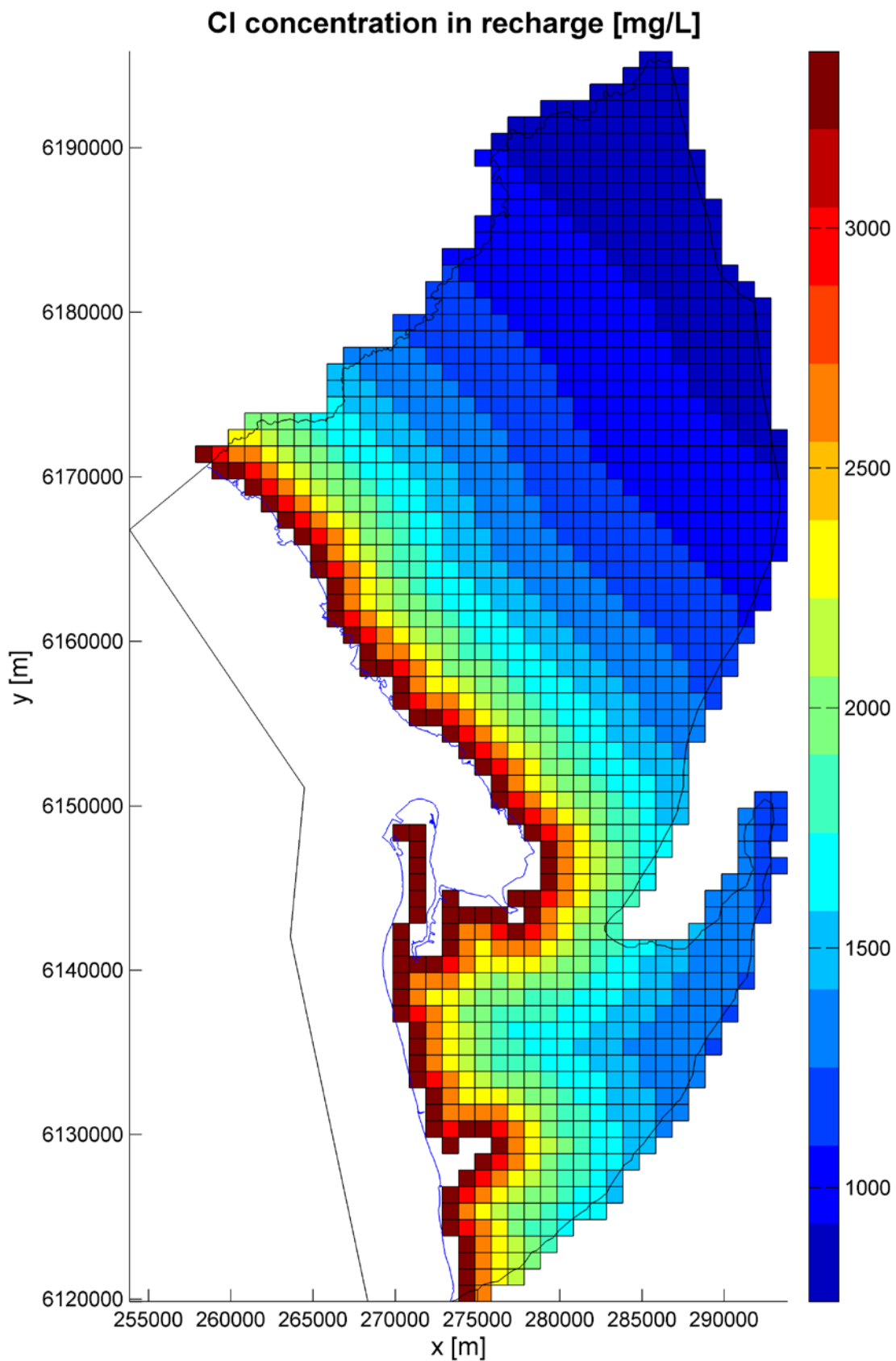
$$C_R = \frac{C_P}{RPMUL} \quad (9)$$

The fact that C_R is taken as a function of R implies that the recharge parameter ($RPMUL$) will be influenced by the concentration observations during the calibration process.

As the Adelaide plains are adjacent to the Gulf St Vincent, C_P is strongly dependent of the distance to the nearest coast according to the empirical formula developed by Hutton (1976). Ordens *et al.* (2012) used this empirical formula to calculate C_P for groundwater recharge estimation in the Uley South Basin, South Australia. The same approach was used here, i.e., C_P is given by:

$$C_P = 35.45 \times \left(\frac{0.99}{\sqrt[4]{d}} - 0.23 \right) \quad (10)$$

where C_P is in mg L^{-1} and d is the distance from the coastline in km. Cl concentration in the groundwater recharge is hence highly dependent on the distance from the coast (Apx Figure K.33). When $RPMUL$ is at its preferred value (0.008), it decreases from 3,370 mg L^{-1} near the coast down to around 760 mg L^{-1} at the furthest distance inland. C_P and therefore the recharge concentration are assumed to be constant with time for reasons mentioned at the beginning of the section.



Apx Figure K.33 Cl concentration (mg L^{-1}) distribution in recharge when recharge is at its preferred value (0.8 % of rainfall)

K.3.8 ¹⁴C TRANSPORT MODEL

A ¹⁴C transport model was developed for serving the purpose of calibration, as ¹⁴C measurements provide an additional constraint to the hydraulic parameters. What differentiates the ¹⁴C transport model from the Cl transport model, apart from the input concentrations as described below, is the simulation of the decay process. This was handled using the RCT package in MT3DMS. Only a steady-state transport model was developed, based on the steady-state pre-development flow model. The steady-state approach for ¹⁴C transport is valid under the assumptions that:

- The flow field is at steady-state over the time scale it takes for a water molecule to exit the model from any entry point. This assumption is of course never satisfied, but if temporal variations can be assumed to appear averaged out in the ¹⁴C activities, the solution would be representative of an average flow field.
- The ¹⁴C activity in the inputs is constant over that same time scale. The ¹⁴C activity in recharge and river leakage can generally be assumed constant with time for waters recharged before 1950 (100 pmC), after which the atmospheric activity increased to over 100 pmC due to nuclear weapons testing (Clark *et al.* 1997). The measured values greater than 100 pmC were not included in the calibration dataset. For the groundwater flowing laterally into the system from the MLR, the assumption of time-constancy is valid only if the groundwater residence times upstream of the eastern boundary are not changing with time over the time scale it takes for a water molecule to travel from any recharge location in the MLR.

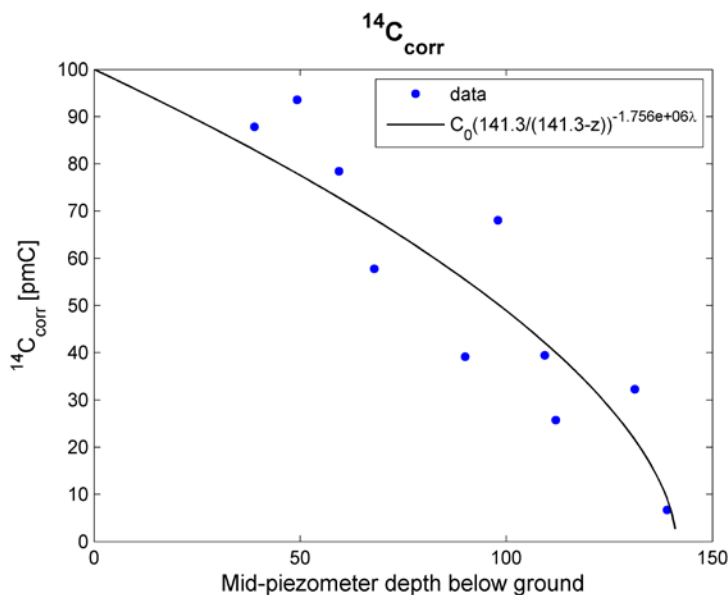
The ¹⁴C activity associated with recharge and with leakage from surface water features or from the ocean was fixed at 100 pmC, as these boundaries are in direct contact with the atmosphere. The ¹⁴C activity of the lateral inflow across the eastern boundary is more difficult to know because it depends on the residence times and transport processes occurring in the MLR. In particular, the residence time along the eastern boundary is expected to increase with depth. Modelling the MLR by an unconfined aquifer receiving uniform recharge, the residence time at the boundary can be expressed as:

$$t = \frac{Hn_e}{R} \ln \frac{H}{H-z} \quad (11)$$

where t is the residence time, H is the aquifer thickness, n_e is the effective porosity, R is the recharge rate and z is the depth (Cook *et al.* 2000). Considering the radioactive decay of ¹⁴C, the ¹⁴C activity as a function of depth is subsequently given by:

$$^{14}\text{C} = C_0 \left(\frac{H}{H-z} \right)^{-\lambda \frac{Hn_e}{R}} \quad (12)$$

where C_0 is the ¹⁴C activity at the water table (100 pmC) and λ is the ¹⁴C decay constant ($3.314 \times 10^{-7} \text{ day}^{-1}$). Using the available ¹⁴C data in the MLR presented in Appendix E (excluding the ones with a corrected activity greater than 100 pmC), it was possible to find H and the ratio Hn_e/R in the above equation by regression analysis. This gave $H = 141.3 \text{ m}$ and $Hn_e/R = 1.756 \times 10^6 \text{ day}$ (see Apx Figure K.34). Equation 12 was then used to assign the ¹⁴C activities as a function of depth along the eastern boundary. A lower threshold of 1 pmC was applied to prevent numerical instabilities.

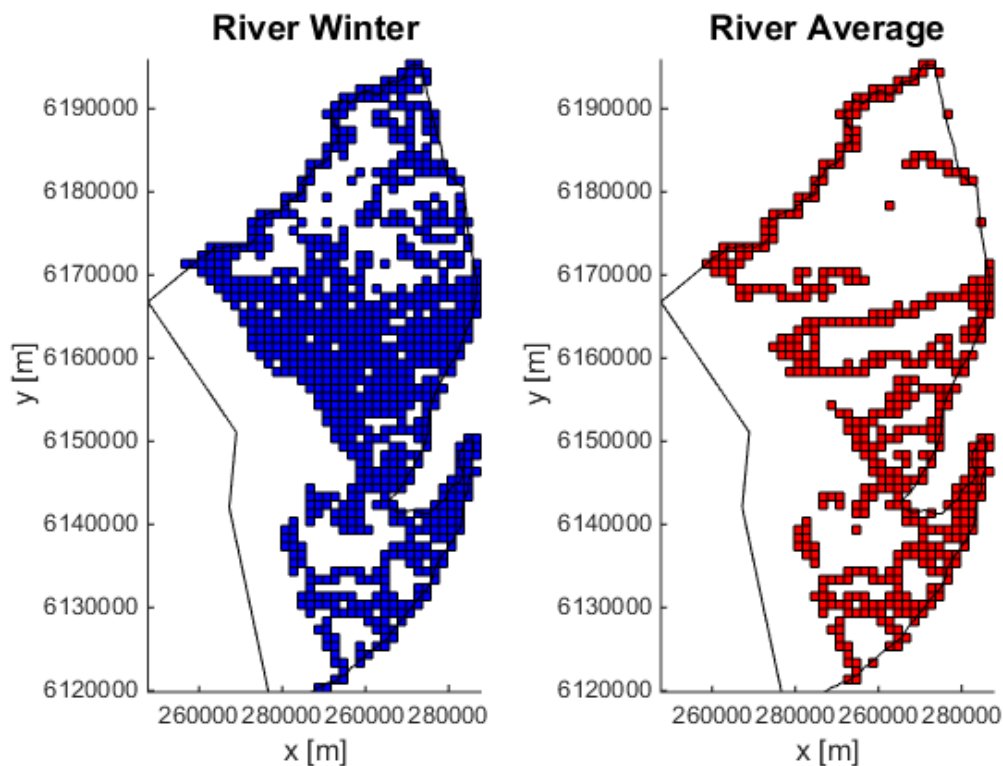


Apx Figure K.34 Regression of ¹⁴C data with depth in the MLR according to equation 12

K.3.9 STRUCTURAL SENSITIVITY ANALYSIS

In order to obtain a robust groundwater simulation model it is important during development of the model to consider structural sensitivities, including grid and time-step resolution and initial and boundary conditions. Complete analysis is not yet achievable due to computational constraints, however, an improved model structure and understanding of this structure can be obtained through systematic testing of the aforementioned aspects. To this end, the model is adjusted and run ideally until both grid resolution and time-step resolution no longer affect the system behaviour significantly within bounds discussed later. All model testing was conducted with the preferred parameter values. The systematic analysis considered the following aspects:

- 1) Several horizontal resolutions (200m, 500m, 1,000m, and 2,000m) were tested to decide on a suitable grid resolution. The steady-state model was used for this purpose.
- 2) The length of stress-periods used in the model were all monthly and a suitable number of time-steps was sought which would provide convergent solutions. The number of time-steps per stress period tested were 1, 2, 5, 10 and 20.
- 3) The solution of the transient models is dependent on the initial conditions specified. In order to test the sensitivity of the transient model to the initial conditions generated by the steady-state model, two variations of initial conditions were chosen based on different stream conditions for the steady-state model: winter-river network (Apx Figure K.19) and average-river network (Apx Figure K.21). Corresponding model cells are shown below in Apx Figure K.35.



Apx Figure K.35 River network extents for the winter-river and average-river setup.

The results of the structural sensitivity analysis are presented in section K.4.2.

K.3.10 CALIBRATION

Strategy

Calibration of the model is essential as a priori parameter values are prone to uncertainty. Hydraulic conductivity, for example, is typically highly heterogeneous and scale-dependent (Sanchez-Vila *et al.* 2006). In-situ estimations based on core analysis or pumping test only gives local information that can hardly be extrapolated. The same applies for storage and transport parameters. Given the number of parameters that need considering, the model was calibrated using the automatic parameter estimation software PEST (Doherty 2013). PEST implements an iterative gradient-search algorithm to minimize an objective function comprised of the sum of squared weighted residuals (i.e., the difference between model outputs and corresponding observations weighted by the degree of confidence associated to these observations). Hydraulic head measurements were used for comparison with simulated heads of the historical groundwater flow models. Attempts were also made to constrain the calibration with Cl and ¹⁴C data conjointly to the transport models. Weights were given to the measurements that reflect the degree of confidence on the data. It is generally recommended that they are taken as the inverse of the standard deviation of the measurement error, if errors are not correlated (e.g. Doherty *et al.* 2010a). Here, this was applied systematically. More details on the data used, estimation of their measurement error and their organization in groups are given below. The PWTADJ1 utility supplied with PEST was used to apply inter-group weighting in such a way that all observation groups have an equal contribution to the objective function at the start of the calibration.

Because groundwater models are often prone to non-uniqueness issues, Tikhonov regularisation was added to the calibration procedure using the preferred-values approach (Doherty *et al.* 2010a). This technique consists of penalizing the objective function when parameters deviate from their a priori estimate. The ADDREG1 utility supplied with PEST was used for this purpose. The weight assigned to the penalization term in the objective function was automatically adjusted during the calibration process such that the target objective function was always one tenth of its value at the beginning of the previous

calibration iteration. This way, a unique solution can generally be achieved. Nevertheless, singular value decomposition was also used to reinforce the numerical robustness of the procedure (Doherty *et al.* 2010a).

Overall, recommended PEST settings were applied as described in the PEST documentation and in the “best PEST settings” document available on PEST website (<http://www.pesthomepage.org/>). All parameters were log-transformed (to base 10). Finally, BEOPEST, which is a parallel version of PEST, was used to achieve a faster calibration (Hunt *et al.* 2010).

Hydraulic head data

Hydraulic head data were retrieved from the WaterConnect database on the 14/07/2014. All wells located within the domain were selected which had at least one water level measurement between 1900 and 2014. The data were filtered to keep only the records for which no anomaly, dryness indicator or pumping at the well at the time of reading was reported, and for which the measurement was not indicated as taken during aquifer test, drilling or well yield. Wells with a single reading were kept as some might be the only information available over some large areas of the model. These wells nevertheless have naturally less influence on the calibration than wells having multiple readings because each observation contributes independently to the objective function (see below). 51,912 hydraulic head data from 4,791 wells remained after filtering.

Steady-state hydraulic head data are commonly used as part of the calibration dataset. However, natural systems are never in steady-state due to seasonal or inter-annual fluctuations (among other reasons). The ongoing introduction of new pumping wells since the early 1900s seems to preclude the use of any period as an approximate steady-state. Therefore, no steady-state observations were derived and included in the calibration dataset. In other words, the model was not calibrated by direct comparison of the steady-state model outputs to field measurements, because the latter do not exist. This does not mean that the steady-state model was not calibrated. The steady-state model gives the starting heads of the transient models, of which the outputs were compared to field measurements (see below). Every time PEST tested a new set of parameters, the steady-state model was first run, followed by the transient models. Therefore, because the steady-state model influences the results of the transient models, the steady-state model influenced the calibration procedure. Because the parameters of the steady-state model are common to those of the transient models, and the latter were calibrated by direct comparison of model outputs to field measurements, the steady-state model was calibrated indirectly.

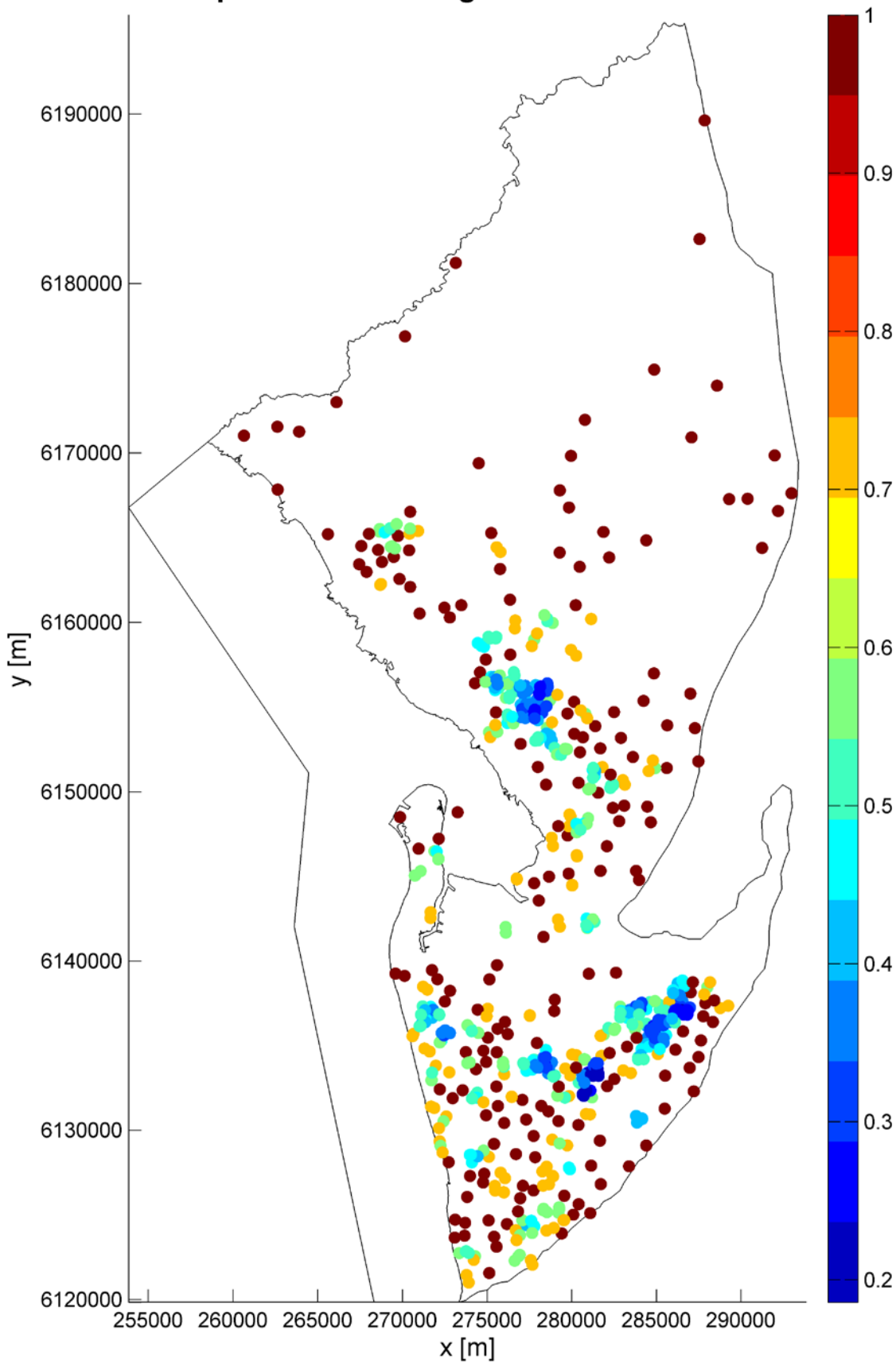
The outputs of the transient models were compared to field measurements in two ways, after having derived two datasets from the raw data. First, the mean hydraulic head measured in each well was calculated. This dataset was compared to the corresponding outputs from the transient models, i.e., mean hydraulic heads in the transient models were calculated at the same locations as the measured values and using the same times as the measurement times. The corresponding dataset encompassed 390 mean hydraulic heads for the pre-development transient model and 4,461 mean hydraulic heads for the development transient model. These values constituted one group of observations. Second, the deviations from the mean hydraulic head in each well were calculated. This dataset was again compared to the corresponding outputs from the transient models. The corresponding dataset encompassed 832 values for the pre-development transient model and 51,080 values for the development transient model, and was treated as a second distinct group of observations. Defining two groups of observations in this manner generally allows better estimation of hydraulic conductivity parameters on the one hand and of storage parameters on the other hand (Doherty *et al.* 2010a; Knowling *et al.* 2015).

Measurement errors used to assign weights to the data were estimated as follows. Hydraulic heads from observation wells belonging to the observation network maintained by DEWNR were assumed to have a standard deviation of 0.5 m. For these wells, the reference elevation would generally have been measured by GPS, implying a small positioning error. The measurement error would hence stem from equipment inaccuracy, operator error, transcription error, barometric fluctuations, unknown tidal variations (ocean and earth tides), poor well construction or possible unknown pumping. The reference elevation for wells that do not belong to the observation network would not generally have been measured by GPS, and would rather have been determined by interpolation of topography data. This could increase significantly the

measurement error. For these wells, the standard deviation was assumed to be 5 m. Additional consideration was given to measurements made before 1950. These had to be compared to outputs of the pre-development model, which does not simulate pumping. However, it is understood that pumping already existed before 1950, as stated in Georgiou *et al.* (2011) and this is confirmed by observations of head measurements below sea level during that period. Therefore, these data were not expected to be matched as accurately as the data used in the development model. Their standard deviation was hence augmented by 5 m, thus becoming 5.5 m for wells belonging to the observation network and 10 m for wells that do not belong to the observation network. It should be noted here that estimating the measurement error is subjective and the adopted values reflect what the authors deemed reasonable.

Spatial density of data varies considerably within the domain. In order for areas with a low data density to be fairly represented in the objective function, spatial declustering was implemented through weighting (Doherty *et al.* 2010a). This was achieved by normalizing the square of the weights in each well by the number of observation wells located within a 1-km diameter circle around the well and in the same aquifer. As an illustration, the normalizing coefficients for observations in the T1 aquifer are shown in Apx Figure K.36. A similar strategy was applied for minimizing the influence of large differences in temporal density of data. Temporal declustering was implemented by normalizing the square of the weight of each observation by the number of observations made within a 6-month time-window in the same well.

Spatial declustering coefficients in T1



Apx Figure K.36 Spatial declustering coefficients for head observations in T1 (transient development model)

Cl data

Cl concentrations in the groundwater are expected to fluctuate much less with time than hydraulic heads. Therefore, time-averaged concentrations measured in observation wells were assumed to be representative of a relatively long-term average transport process, and hence could be compared to the outputs of the pre-development steady-state Cl transport model. The sources of the Cl concentration data are presented in section K.3.7 above. The mean concentration in each well was taken, and the measurement error was estimated as detailed in that same section. Cl concentrations were treated as a distinct group of observations in the calibration. Spatial declustering was also applied in the same way as described for the head data.

¹⁴C data

Similarly to Cl concentrations, ¹⁴C activities in the groundwater are expected to fluctuate little with time. They were therefore also assumed to be representative of relatively long-term average transport process, and were compared to the outputs of the pre-development steady-state ¹⁴C transport model. The 68 ¹⁴C data used in this project (from 68 different wells), corrected for exchange with matrix carbonate, are presented in Appendix E. This dataset was treated as a distinct group of observations. Measurement error was estimated on the basis of the uncertainty related to matrix carbonate exchange, which probably constitutes the main source of error. This uncertainty was estimated based on 1,000 random realisations where correction parameters were modified within plausible ranges. While the mean of the realisations gave the corrected ¹⁴C values, the standard deviation was used as an estimate of the measurement error. Spatial declustering was applied in the same way as described for the head data above.

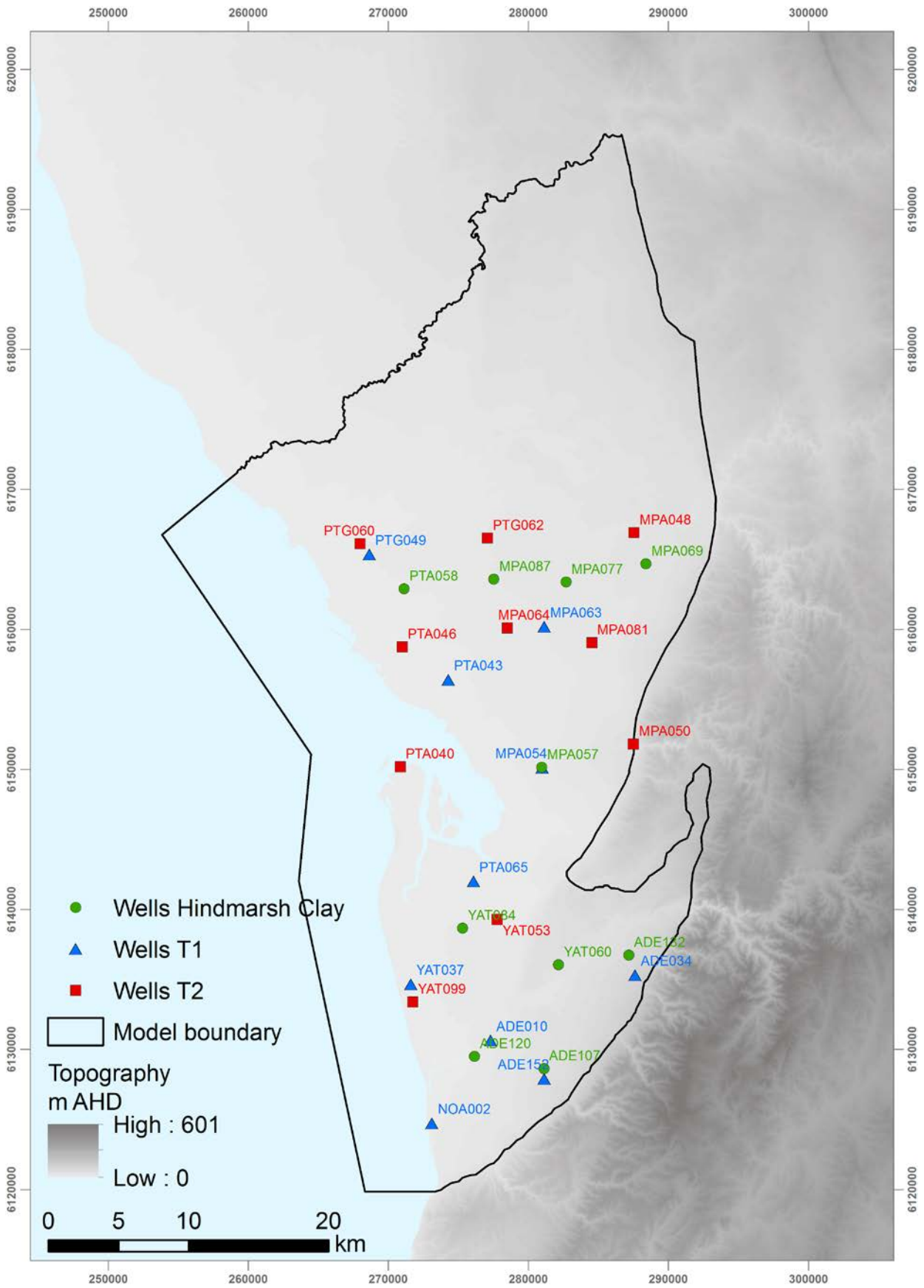
Calibration performance indicators

Calibration performance was analysed with a focus on the entire model as well as on the Hindmarsh Clay aquitard and on the T1 and T2 aquifers. Graphs of simulated versus measured observations were used, on which data points should approach the 1:1 line for an accurate model. Graphs of residuals versus measured observations were also plotted, on which values should be randomly distributed around the zero line for a non-biased model. Next, the spatial distribution of residuals was analysed to see if the model performs better in some areas than others. Finally, hydrographs were analysed to assess the capacity of the model to capture the temporal response to changes in stresses. Not all observation wells are shown as there are too many (4,791). Instead, 10 wells were taken *a priori* in the Hindmarsh Clay aquitard, and similarly 10 wells were taken *a priori* in each of the T1 and T2 aquifers. Wells were selected that had a large number of measurements and such that they together offer a good spatial coverage (Apx Figure K.37).

A number of statistics were also calculated to quantify the goodness of fit. Their definition is given in Apx Table K.5. The first two statistics Root Mean Squared error (RMS) and Scaled Root Mean Squared error (SRMS) are intuitive but do not take into account the different degrees of confidence in the data. Standard Error (SE) is basically equivalent to RMS but weights are used that reflect the degree of confidence in the data. It is dimensionless when weights are defined as the inverse of measurement error, and is expected to be 1 if the model is accurate at a level that is consistent with the level of measurement error (Hill *et al.* 2007). The weights used here are indeed the inverse of measurement error, i.e., the weights are taken before applying spatial and temporal declustering. 95 % confidence intervals around SE were also calculated. Mean Weighted Residual (MWR) allows inspection of the overall bias towards positive or negative values in a dimensionless fashion. Finally, R is the correlation coefficient, which reflects the degree of correlation between weighted simulated and weighted measured observations. Generally, a value of R greater than 0.9 indicates that the weighted simulated observations closely match the weighted measured observations (Hill *et al.* 2007).

Apx Table K.5 Performance statistics used to assess the goodness of fit of the model (see Hill *et al.* (2007) and Barnett *et al.* (2012)). o_i^s : simulated observation; o_i^m : measured observation; w_i : weight associated to the observation (defined here as the inverse of measurement error); n : number of observations; r : number of prior information values; p : number of parameters; ΔO : range of observed values; m^s : mean of simulated observations; m^m : mean of measured observations

ABBREVIATION	FULL NAME	MATH. EXPRESSION	COMMENT
RMS	Root mean squared error	$\sqrt{\frac{1}{n} \sum_{i=1}^n (o_i^s - o_i^m)^2}$	Measure of the degree of misfit. Same unit as o . Inconvenient: does not take into account the different degrees of confidence in the data.
SRMS	Scaled root mean squared error	$100 \times \frac{RMS}{\Delta O}$	Dimensionless measure of the degree of misfit. Values between 0 % and 100 %. Inconvenient: does not take into account the different degrees of confidence in the data.
SE	Standard error	$\sqrt{\frac{1}{n+r-p} \sum_{i=1}^n [w_i(o_i^s - o_i^m)]^2}$	Measure of the degree of misfit. Dimensionless when weights are defined as the inverse of measurement error. Should be close to 1 if measurement error is correctly estimated and if the model is accurate.
MWR	Mean weighted residual	$\frac{1}{n} \sum_{i=1}^n w_i(o_i^s - o_i^m)$	Measure of the degree of bias towards high values (if positive) or low values (if negative). Dimensionless when weights are defined as the inverse of measurement error. Should be between -1 and 1 if measurement error is correctly estimated and if the model is not significantly biased.
R	Correlation coefficient	$\frac{\sum(w_i o_i^s - m^s)(w_i o_i^m - m^m)}{\sqrt{\sum(w_i o_i^s - m^s)^2 \sum(w_i o_i^m - m^m)^2}}$	Measures the degree of correlation between simulated and observed values. A value greater than 0.9 is generally considered to indicate a close match.



Apx Figure K.37 Wells selected for hydrograph analysis

Parameter sensitivity, identifiability and uncertainty

The extent by which the data may inform parameter values can be assessed with a number of methods. Here three methods were used: parameters sensitivity, identifiability and uncertainty reduction.

Sensitivity analysis consists of assessing the effect of a change in parameter on model-simulated observations. To this end, the composite scaled sensitivity (CSS) of the parameters was calculated. CSS is defined as (Hill *et al.* 2007):

$$CSS_j = \frac{1}{n} \sqrt{\sum_{i=1}^n \left[\left(w_i \frac{\partial o_i}{\partial b_j} \right)^2 \right]} |b_j| \quad (13)$$

where o_i and w_j denote an observation and the corresponding weight, respectively, b_j denotes a parameter, and n is the number of observations. In this equation, weights were taken as PEST 'sees' them, i.e., after spatial and temporal declustering was applied and after the PWTADJ1 utility was run. When a parameter was log-transformed, the derivative was calculated with respect to $\log_{10} b_j$, and $|b_j|$ was replaced by $|\log_{10} b_j|$ in the above equation. The CSS were calculated at the calibrated parameter values (the model being non-linear, the derivatives can be different depending on the parameter values at which they are evaluated). The CSS were further normalized by the largest CSS value calculated amongst all parameters, so that they take values between 0 and 1.

CSS is an intuitive metric but it only provides partial information on how much a parameter can be constrained by the data. The main reason is the non-uniqueness that occurs when a parameter has a similar effect as another one (or as the inverse of another one) on simulated observations (i.e., parameters are correlated). In those cases, both parameters can appear sensitive but both cannot be estimated independently (only the product or the ratio of the two parameters can). Singular value decomposition (SVD) of the Jacobian matrix of the model can be used to counter this issue. SVD splits the parameters space into two sub-spaces: the calibration solution space, which contains parameter combinations that can be uniquely estimated on the basis of the data, and the calibration null space, which contains parameter combinations that cannot be uniquely estimated. In PEST, a parameter is said to be identifiable if the magnitude of its projection in the calibration solution space is roughly equal to its magnitude in the original space. In other words, the identifiability of a parameter is a function of how much of the parameter belongs to the solution space. Identifiability varies between 0 and 1, where 0 means that the parameter is not identifiable, whereas 1 means that the parameter is identifiable. The reader is referred to Doherty (2013) for more details on parameter identifiability and its calculation, which was undertaken using the IDENTPAR utility supplied with PEST.

Although identifiability accounts for parameters correlations, it still does not provide complete information on how much a parameter can be constrained by the data. A parameter whose identifiability is equal to 1 cannot necessarily be known with absolute certainty, because identifiability does not account for measurement noise. Measurement noise is referred to as measurement error (as discussed earlier) supplemented by structural noise, which arises from imperfections of the model such as use of a coarse grid or time discretization, errors in boundary conditions or oversimplification of hydraulic properties (Moore *et al.* 2006; Doherty *et al.* 2010b). Uncertainty analysis is required to account for measurement noise and subsequently achieve a complete assessment of how much a parameter can be constrained by the data. The PREDUNC1 utility supplied with PEST can provide such an analysis, i.e., it performs linear predictive uncertainty analysis conditional on the data comprising the calibration dataset. A parameter can be treated as a prediction in such an analysis, and so parameter uncertainty can be calculated. PREDUNC1 requires estimation of pre-calibration parameter uncertainty and estimation of measurement noise. Pre-calibration parameter uncertainty was estimated on the basis of the calibration bounds of the parameters, assuming that the bounds are reflective of the 95 % confidence interval in a Gaussian distribution. Measurement noise is difficult to assess. In the present case where large zones of piecewise constancy are used the system is likely to be oversimplified, and rather over-determined than under-determined (Moore *et al.* 2006; Doherty *et al.* 2010b). In this case, one way to approximate measurement noise is to base it on the post-calibration residuals (i.e., the differences between simulated and measured values). This strategy

was applied here by means of the PWTADJ2 utility supplied with PEST. This utility performs a re-weighting of the measurements such that weights become reflective of the measurement noise as indicated by the residuals, the latter being calculated with parameters taken at their calibrated value. The standard deviation of measurement noise was then assumed to be equal to the inverse of the measurement weights. The results of PREDUNC1 are presented in terms of relative uncertainty variance reduction, which takes values between 0 and 1 and expresses the reduction in parameter uncertainty achieved via calibration. Therefore, a value of 0 means that the post-calibration parameter uncertainty is equal to the pre-calibration parameter uncertainty whereas a value of 1 means that the parameter is known with certainty after calibration. When a parameter was log-transformed, the relative uncertainty variance reduction refers to the log of the parameter.

K.4 Results and discussion

K.4.1 READING KEYS

Simulation results are presented in the form of seven main types of outputs, for which reading keys are given here:

- 1) Tables of water balance components (for all zones and boundaries) for all fluxes, as exemplified below. Fluxes are read from row to column, e.g. the second row (UTSand) shows “1.00” in the T1 column which indicates a flux of 1 GL yr⁻¹ from the UTSand zone to the T1 zone (note: GL yr⁻¹ is the unit used in all flux tables). A flux is also indicated from the UTSand zone to the Streams boundary. Fluxes into the UTSand zone can be identified by looking at the UTSand column, with “0.10” in the first row indicating a flux from the Hclay zone into the UTSand zone. A flux from the Streams boundary into the UTSand zone is indicated in the last line of the UTSand column as 0.6 GL yr⁻¹. Note that there are fluxes both from the Streams boundary into UTSand and from UTSand into the Streams boundary due to spatial variability of the exchanges within a zone. Likewise, the same can occur between zones with flux in one direction in one part of the domain and in the opposite direction in another part. For transient simulations, a final row is added showing the rate of change of storage (in the zones only as the boundaries have no storage associated with them). From the example below, it is apparent that the storage in UTSand is increasing by 0.2 GL yr⁻¹. Summing up the fluxes into and out of a zone also provides the rate of change of storage. Both numbers should be identical unless there is a significant error in the water balance. No such error has been identified when analysing the results. Fluxes that are less than 0.005 GL yr⁻¹ are indicated as blank cells to simplify the table.

	Hclay	UTSand	T1	Streams
Hclay		0.10		0.40
UTSand			1.00	0.50
T1		1.00		
Streams		0.60		
Storage change	-0.40	0.20		

- 2) Tables of water balance components (for all zones and boundaries) for net fluxes, as exemplified below. Net fluxes are directly deduced from the above matrix by subtracting each entry (i,j) by the symmetrical entry (j,i). For example, the net flux from Streams to UTSand in the above example is entry (4,2) minus entry (2,4), which is 0.6 - 0.5 = 0.1 GL yr⁻¹. As opposed to the flux matrix above, there can be negative values as is seen in entry (2,1) of the example below. A positive value indicates that the net flux is in the direction of row to column, whereas a negative value indicates that the net flux is in the direction of column to row. The upper diagonal entries are left empty here as they are just the negative value of the net flux in the other direction, i.e. the same information can be obtained from the lower diagonal part of the table.

Indicates net flux from UTSand to the Hclay
(negative value indicates net flow is from Hclay to UTSand)

NET FLUX

	Hclay	UTSand	T1	Streams
Hclay				
UTSand	-0.10			
T1				
Streams	-0.40	0.10		

Grey cells are left blank to avoid duplication of values

Storage change	-0.40	0.20		
----------------	-------	------	--	--

Indicates net flux from Streams to the UTSand

- 3) Water balance time series for transient simulations (for the entire model, and T1 and T2 aquifers). Such graphs show the fluxes of water into (positive) and out (negative), as well as the rate of change of storage of the entire model, T1 aquifer and T2 aquifer. These figures indicate the dynamics of different fluxes between connected zones and boundary conditions and the net effect, i.e., the storage change.
- 4) Cumulative storage change graphs for transient simulations (for zones with significant change only). Such graphs show the cumulative change in storage over time in zones that have at least 3 % of the maximum change in storage for all zones. On these plots, lines that increase upwardly indicate increases in storage, whereas lines that decrease downwardly over time show decreases in storage. The cumulative change in storage is determined by integrating underneath the rate of change of storage time series from the water balance.
- 5) Maps of hydraulic head, allowing investigation of horizontal flow directions.
- 6) Maps of hydraulic head minus topography, allowing identification of artesian conditions (where positive).
- 7) Maps of vertical fluxes, allowing investigation of inter-aquifer leakage, both in direction and magnitude.

K.4.2 STRUCTURAL SENSITIVITY ANALYSIS

Grid resolution

A comparison was made of the net fluxes from one zone to another and from boundaries for each of the four resolutions tested (2,000 m, 1,000 m, 500 m and 200 m). As the grid resolution changes it is expected that the water balance components change, with the changes becoming less pronounced from one refinement to the next. Results are shown in Apx Table K.6 below for the pre-development steady-state model. The changes between subsequent refinements generally seem to diminish but not always. A few connections can be noted to appear or disappear as the grid is refined (e.g., the connection between zones T3T4D and T2 appears from 1,000 m to 500 m resolution, whereas the connection between zones BRockU and T2 disappears from 2,000 m to 1000 m resolution), which is because the finer grids better resolve the spatial features. Nevertheless, the fluxes associated to these changing connections are minor.

Global changes in boundary fluxes with increasing grid resolution are shown in Apx Figure K.38 for the entire model. Recharge changes only as much as the surface area of the model changes when the grid is refined, with the total area only slightly decreasing with increasing refinement. The impact of grid discretisation is most strongly seen in the river net exchange, although it shows signs of convergence with grid refinement. The river net exchange increases from -3.47 GL yr^{-1} (i.e., a net loss to streams) to 0.95 GL yr^{-1} (i.e., a net gain from streams) as the grid is refined. The flux from the MLR is also substantially affected by the grid resolution and does not show signs of convergence: the net exchange decreases linearly with increasing grid refinement. It drops by 30 % from a 2,000 m resolution to a 200 m resolution. The effect of grid resolution on the exchange flux with the coast is somewhat smaller.

The increase in river net exchange with grid refinement (i.e., a decrease of discharge to streams and/or an increase of recharge from streams) suggests that hydraulic heads in the first layer are overestimated on a

coarse grid. The breakdown into zones (Apx Table K.6) reveals that the changes in river net exchange can be entirely attributed to the changes in the Undifferentiated Sand; in the Hindmarsh Clay, the net exchange with streams appears almost independent of grid resolution. The Undifferentiated Sand is heavily influenced by the specified heads of the GHB (Apx Figure K.16), and is also a thin layer that lies directly on the Bedrock (Apx Figure K.8 f and g), so that a steep hydraulic gradient can be expected. It is likely that in a coarse grid the small number of cells in this zone does not allow accurate simulation of the hydraulic gradient.

The decrease in net exchange with the MLR with increasing grid refinement suggests that hydraulic heads in the eastern boundary cells are underestimated on a coarse grid, as a lower head would induce a larger head gradient across the boundary. This might be induced by the fact that L was fixed in equation (1). Fixing L is valid if the hydraulic conductivity from the boundary to the external source is much lower than the hydraulic conductivity in the model domain. In that case the flow across the boundary would not depend on the distance between the border of the cell and the centre of the cell, whereas in the opposite case it would. Further investigation is warranted to see if adapting L as a function of the grid resolution could reduce the influence of grid resolution on the results.

The influence of grid resolution on the net exchanges with the coast is expected to be a consequence of the influence of grid resolution on the other components of the water balance, as there appears to be no reason for local flow processes along this boundary to be affected by grid resolution.

The fact that grid resolution influences the results suggests a deficient representation of some physical processes, at least on coarse grids. During calibration, some parameters would take a surrogate role to compensate for such deficiencies. Therefore, consequences on model predictions might be relatively insignificant for predictions that are of same nature as the data comprising the calibration dataset. However, consequences on other types of prediction (namely fluxes in this case) remain unknown. In any case, the influence of grid resolution precludes the use of parameters calibrated on a coarse grid for simulations on a finer grid.

In this project, the model was calibrated on a 1,000 m resolution grid. It is expected that calibrating the model on a finer grid would give more realistic groundwater-surface water interactions, especially in the Undifferentiated Sand zone as this shows signs of grid convergence. However it would probably not make a very significant difference on other components of the water balance, as these are less affected by grid resolution or do not show signs of grid convergence (the latter applies to the exchange with the MLR).

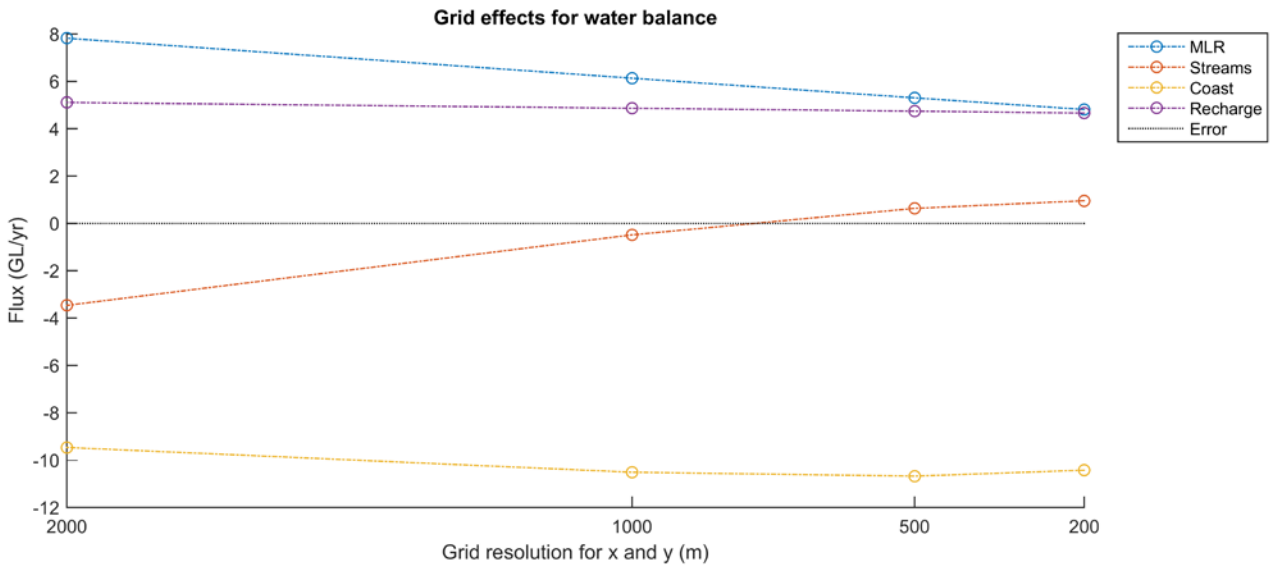
ApX Table K.6 Net flux matrix between all zones and boundary conditions for the historical steady-state model at grid resolutions of 2,000 m, 1,000 m, 500 m and 200 m. The units of fluxes is GL yr⁻¹. Positive values indicate flow from the zone/boundary in a row to a zone/boundary in a column, and negative values indicate the opposite. For example, the net flux between the Coast to Hindmarsh Clay is -9.47 GL yr⁻¹, indicating the net flux is from the Hindmarsh Clay to the Coast

2000m	Hclay	UTSand	T1	MPClay	T2	BPFmnU	T3T4U	BedrockU	BPFmnD	T3T4D	BedrockD	Pfault
Hclay												
UTSand	0.00											
T1	5.61	-0.13										
MPClay			2.92									
T2		-0.01	-1.54	2.91								
BPFmnU		0.00	0.00		0.35							
T3T4U			0.32		0.00	0.16						
BedrockU		1.87	0.85		0.04	0.05	0.48					
BPFmnD			0.00	0.00	0.35							
T3T4D			0.82	0.00					0.00			
BedrockD			1.14						0.24	0.62		
Pfault			0.03		0.06	0.00	-0.01	-0.06	0.00	0.00	0.00	
MLR	0.43	0.05	0.95	0.01	0.55	0.14	0.02	3.34	0.12	0.20	1.99	0.03
Streams	-1.35	-2.12										
Coast	-9.47											
Recharge	4.77	0.33										

1000m	Hclay	UTSand	T1	MPClay	T2	BPFmnU	T3T4U	BedrockU	BPFmnD	T3T4D	BedrockD	Pfault
Hclay												
UTSand	0.00											
T1	6.81	-2.33										
MPClay			2.86									
T2		0.06	-1.73	2.85								
BPFmnU		0.00	0.00		0.19							
T3T4U			0.20			0.08						
BedrockU		1.05	0.53			0.03	0.28					
BPFmnD			0.00	0.00	0.39							
T3T4D			0.74	0.00					-0.01			
BedrockD			0.88		0.00				0.33	0.56		
Pfault			-0.01		0.09	0.00	-0.01	-0.06	0.00	0.01	0.01	
MLR	0.48	0.06	1.01	0.01	0.51	0.08	0.01	1.95	0.07	0.16	1.76	0.03
Streams	-1.40	0.92										
Coast	-10.51											
Recharge	4.62	0.25										

500m	Hclay	UTSand	T1	MPClay	T2	BPFmnU	T3T4U	BedrockU	BPFmnD	T3T4D	BedrockD	Pfault
Hclay												
UTSand	0.00											
T1	6.95	-2.25										
MPClay			2.61									
T2		-0.64	-0.98	2.59								
BPFmnU		0.00	0.00		0.13							
T3T4U			0.20		0.00	0.07						
BedrockU		0.65	0.47			0.00	0.02	0.27				
BPFmnD			0.00	0.00	0.29							
T3T4D			0.66	0.00	-0.04				-0.01			
BedrockD			0.69		0.00				0.26	0.45		
Pfault			0.02		0.07	0.00	-0.01	-0.06	0.00	0.01	0.01	
MLR	0.52	0.08	1.04	0.01	0.51	0.05	0.01	1.46	0.05	0.16	1.38	0.04
Streams	-1.32	1.96										
Coast	-10.68											
Recharge	4.53	0.21										

200m	Hclay	UTSand	T1	MPClay	T2	BPFmnU	T3T4U	BedrockU	BPFmnD	T3T4D	BedrockD	Pfault
Hclay												
UTSand	0.00											
T1	6.79	-2.46										
MPClay			2.37									
T2		-0.59	-0.76	2.36								
BPFmnU		0.00	0.00		0.11							
T3T4U			0.14		0.00	0.06						
BedrockU		0.44	0.36			0.02	0.02	0.21				
BPFmnD			0.00	0.00	0.23							
T3T4D			0.52	0.00	0.04				-0.02			
BedrockD			0.62		0.00				0.22	0.37		
Pfault			-0.02		0.08	0.00	-0.01	-0.07	0.00	0.01	0.02	
MLR	0.55	0.08	1.10	0.01	0.52	0.03	0.01	1.13	0.03	0.16	1.19	0.01
Streams	-1.40	2.35										
Coast	-10.43											
Recharge	4.48	0.18										



Apx Figure K.38 The impact of grid resolution on the water balance components for horizontal grid resolutions of 2,000 m, 1,000 m, 500 m and 200 m

Time-step

The cumulative change in storage in the T1 and T2 aquifers as well as in the Hindmarsh Clay and Munno Para Clay aquitards were compared for different numbers of time-steps per stress period (Apx Table K.7). The difference in cumulative storage change from two to five time-steps per stress period is less than 1 % for all units, which is deemed insignificant. The decadal (2002-2012) average annual fluxes between all zones and the boundary fluxes were also compared. These also show insignificant differences from two to twenty time-steps per stress period (Apx Table K.8 and Apx Table K.9). Based on this analysis, two time steps per stress-period were used for all subsequent transient simulations.

Apx Table K.7 Change in simulated cumulative storage in Hindmarsh Clay, T1 aquifer, Munno Para Clay and T2 aquifer at the end of the development period (2013) when increasing the numbers of time-steps used per stress period, expressed in percentage of the difference

NUMBER OF TIME-STEPS	Hindmarsh Clay	T1 aquifer	Munno Para Clay	T2 aquifer
From 1 to 2	8.65%	0.38%	0.09%	0.22%
From 2 to 5	0.72%	0.16%	0.05%	0.15%
From 5 to 10	-0.24%	0.09%	0.02%	0.06%
From 10 to 20	-0.19%	0.05%	0.01%	0.03%

Apx Table K.8 Flux (GL yr⁻¹) matrix based on 10 year average (2002-2012) water balance components (2 time-steps)

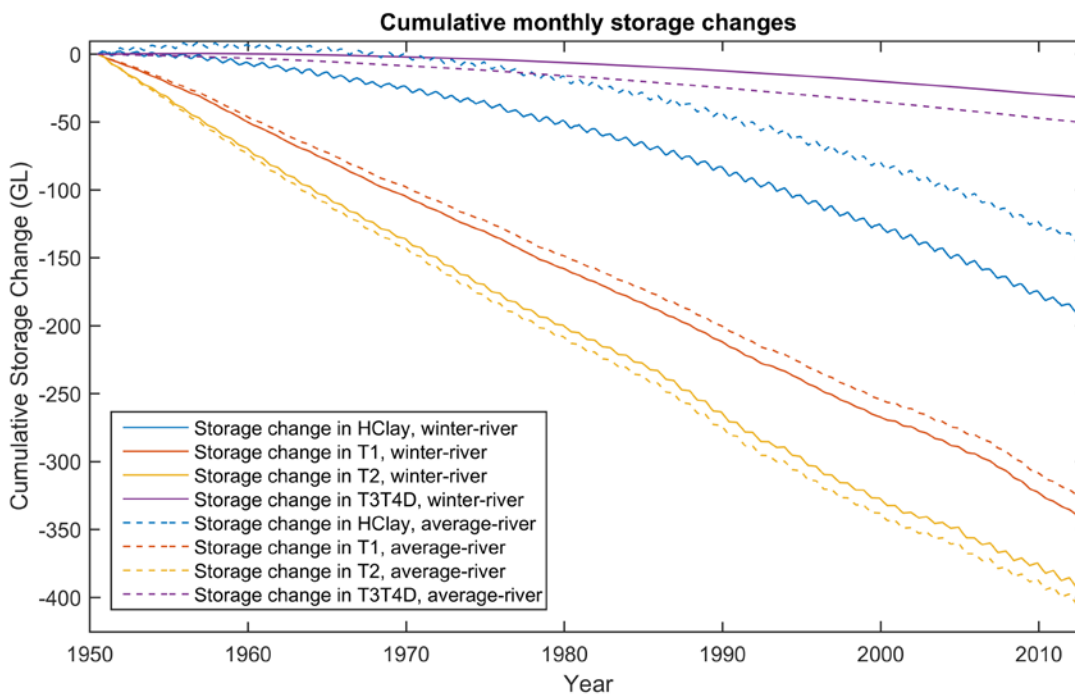
	Hclay	UTSand	T1	MPClay	T2	BPFmnU	T3T4U	BedrockU	BPFmnD	T3T4D	BedrockD	Pfault	MLR	Wells	Streams	Coast	Recharge
Hclay			19.22														
UTSand			2.41					0.20									
T1	10.37	0.05		0.53	20.87		0.58	0.21		0.28	0.05	0.15		7.50		11.36	
MPClay			0.94		0.54												
T2		0.05	7.12	0.93											20.27		
BPFmnU					0.22												
T3T4U			0.29			0.10		0.05							0.72		
BedrockU		0.89	0.53			0.03	0.37					0.06	0.08	0.68			
BPFmnD					0.78					0.02				0.02			
T3T4D			1.80						0.18		0.01						
BedrockD			1.01						0.48	0.61		0.01					
Pfault			0.05		0.21												
MLR	0.47	0.05	1.02	0.01	0.55	0.08		2.04	0.08	0.14	1.69	0.03					
Wells	0.02		0.05		0.26												
Streams	10.80	12.63															
Coast																	
Recharge	5.58	0.22															
Storage change	5.19	0.09	6.14		4.95		0.19	0.16	0.07	0.94	0.36	0.16					

Apx Table K.9 Flux (GL yr⁻¹) matrix based on 10 year average (2002-2012) water balance components (20 time-steps)

	Hclay	UTSand	T1	MPClay	T2	BPFmnU	T3T4U	BedrockU	BPFmnD	T3T4D	BedrockD	Pfault	MLR	Wells	Streams	Coast	Recharge
Hclay			19.22														
UTSand			2.41					0.20									
T1	10.35	0.05		0.53	20.88		0.58	0.21		0.28	0.05	0.15		7.50		11.33	
MPClay			0.94		0.54												
T2		0.05	7.11	0.93											20.27		
BPFmnU					0.22												
T3T4U			0.29			0.10		0.05							0.72		
BedrockU		0.89	0.53			0.03	0.37					0.06	0.08	0.68			
BPFmnD					0.78					0.02				0.02			
T3T4D			1.80						0.18		0.01						
BedrockD			1.01						0.48	0.61		0.01					
Pfault			0.05		0.21												
MLR	0.47	0.05	1.02	0.01	0.55	0.08		2.04	0.08	0.14	1.69	0.03					
Wells	0.02		0.05		0.26												
Streams	10.65	12.56															
Coast																	
Recharge	5.58	0.22															
Storage change	5.23	0.13	6.14		4.94		0.19	0.16	0.07	0.94	0.36	0.16					

Initial condition

The water balances resulting from the different initial conditions of the winter-river and average-river network showed that the development model was sensitive to these, especially for the cumulative storage change in Hindmarsh Clay (Apx Figure K.39). In the average-river network initial condition, the storage in Hindmarsh Clay is seen to initially increase slightly for almost 10 years after pumping is introduced before a decline occurs. This can be explained by an increase in recharge via the seasonally varying river network in the transient model (i.e. summer/winter networks) as compared to the initial condition from the steady-state model that uses an average-river network. However, this behaviour is considered unrealistic because it is expected that storage decrease starts immediately at the initiation of pumping. Based on this analysis, the winter-river network was chosen for the steady-state model and not the average-river network.



Apx Figure K.39 Cumulative change in storage for the development period model (1950–2013) for different river network initialisations (winter-river or average-river)

K.4.3 CALIBRATION

Calibrated parameters

A number of parameter values changed significantly from their preferred values during the PEST iterations, with some of them reaching their upper or lower bound (Apx Table K.10). Given that wide ranges were given to all the parameters, this could be an indication of model structural/conceptual errors. That is, some feature or processes might be missing or be poorly represented in the model so that the only way to match the data is by means of assigning extreme values to the parameters. In this case, calibration is likely biased and adjustment of the parameters to obtain the best fit may in fact compromise the reliability of some model predictions (White *et al.* 2014). In order to minimize this effect, the calibrated parameters adopted were not the ones obtained at the end of the calibration process. Instead, they were chosen to be the ones for which a significant reduction of the objective function was already achieved while not too many parameters had yet reached their bound. This was deemed to occur after PEST iteration 11, at which only 3 parameters had reached their bound, and after which the objective function would not be significantly more reduced (Apx Figure K.40). Another choice would have yielded a different parameters set, and this warrants the need for uncertainty analysis on model predictions.

The calibrated parameters are listed in Apx Table K.11 for material properties and in Apx Table K.12 for other parameters. The parameters that deviate the most notably from their initial value are: K_H in HClay, T1, BRockU, T3T4D and BRockD; K_V in BRockU, BPFmnD and BRockD; S_s in T1, T2, BRockU, BPFmnD and PFault; S_y in UTSand and T1; RPMUL; OK; RIVBEDK_T; RIVBEDK_FR; RIVBEDK_Wa. These are discussed hereafter. It is also noted that the calibrated vertical hydraulic conductivity in T1, BPFmnU, BPFmnD and T3T4D is slightly greater than the horizontal hydraulic conductivity in these layers, which might be unrealistic and thus point towards structural/conceptual errors.

K_H in HClay is $3.4E-01 \text{ m day}^{-1}$ (110 times the initial value). This value is relatively high but still seems reasonable since HClay lumps together sandy aquifers and clay aquitards, while the initial value was in fact based purely on K_V of the clay aquitards multiplied by an anisotropy ratio. This value is also consistent with the calibrated value for the upper Quaternary layers in Georgiou *et al.* (2011) (0.5 m day^{-1}).

K_H in T1 is 0.63 m day^{-1} (0.067 times the initial value). This seems to point towards model structural/conceptual error given that the preferred value was based on 41 aquifer tests from which the smallest value is 1 m day^{-1} . However, other possible explanations for this result include:

- The spatial representation of the aquifer tests is quite limited; namely, no aquifer tests exist along zone 4a (zone in the Golden Grove Embayment and along the Eden-Burnside Fault defined in Gerges (1999)), which was previously suggested as the main groundwater pathway from the MLR (Gerges 1999). This knowledge gap was already reported in Zulfic et al. (2008). Here only one hydraulic conductivity value is assigned to the entire T1 aquifer which covers almost the entire domain and must therefore be an equivalent, regional scale value. Also note that Georgiou *et al.* (2011) used a calibrated value of 1 m day^{-1} in the Golden Grove Embayment, i.e. close to the current value.
- Bias of aquifer test values towards larger values as these are most often performed in areas where yield is expected to be higher as it targets production.
- Misinterpretation of aquifer test data such as underestimation of the activated thickness or similarly underestimation of vertical leakage from layers above/below.

Further work is warranted to investigate these possible explanations. Namely, new pumping tests in strategic locations could be highly beneficial.

K_H in BRockU is $3.8\text{E-}02 \text{ m day}^{-1}$ (37 times the initial value). This value might not be unlikely since the Bedrock layer comprises a weathered zone with a thickness of up to 50 m in the Golden Grove Embayment and this zone might be relatively conductive. Furthermore, the unweathered zone might be significantly fractured (and therefore conductive) as supported by the tectonic activity evidenced by the important faulting in the area. Also note that Georgiou *et al.* (2011) used a calibrated value of $5.0\text{E-}03 \text{ m day}^{-1}$ for an equivalent unit, i.e. a value between 2 and 3 times smaller than here, which is not viewed as a significant difference given the lack of information on this unit.

K_H in T3T4D is $2.1\text{E-}02 \text{ m day}^{-1}$ (0.0031 times the initial value). This value is not deemed unlikely as little information is available on this unit which lumps together different formations.

K_H in BRockD is $9.4\text{E-}06 \text{ m day}^{-1}$ (0.0094 times the initial value). The difference between this value and K_H in BRockU is somewhat surprising. It might be that this area has been less subject to tectonic activity and weathering than the Golden Grove Embayment (this is subject to verification).

K_V in BRockU is $5.3\text{E-}02 \text{ m day}^{-1}$ (53 times the initial value). This value is consistent with the above discussion about K_H in this unit.

K_V in BPFmnD is $1.1\text{E-}05$ (0.011 times the initial value). This value is not deemed unlikely as little information is available on this unit.

S_S in T1 and in T2 are about 1,000 and 100 times smaller than their preferred values, respectively. This is also two and one order of magnitude smaller than the lowest field-based estimates, respectively (Table 2 in the Summary Report). Note that similar calibrated values were reported for previous modelling works (SKM 2009; Georgiou *et al.* 2011). This suggests either model structural/conceptual error such as underestimation of pumping variability (which could be compensated by smaller values of S_S) or misinterpretation of existing aquifer test data. In any case, this warrants further investigation as S_S is an important parameter controlling aquifer dynamics.

S_S in BRockU is $1.3\text{E-}04 \text{ m}^{-1}$ (13 times the initial value). This is consistent with the above discussion about K_H in this unit.

S_S in BPFmnD is $8.7\text{E-}07 \text{ m}^{-1}$ (0.079 times the initial value). This value is not deemed unlikely as little information is available on this unit.

S_S in PFault is $2.6\text{E-}03 \text{ m}^{-1}$ (26 times the initial value). This value is not deemed unlikely as little information is available on this unit.

S_Y in UTSand and T1 reached their upper bound. This seems to indicate that the model creates too large water table fluctuations in the Golden Grove Embayment, where these units outcrop; assigning a larger S_Y

would help to diminish these fluctuations. Too large fluctuations could be due either to an overestimation of recharge fluctuations or to an overestimation of the groundwater-surface water interaction seasonal variability. Further work is warranted to investigate these hypotheses.

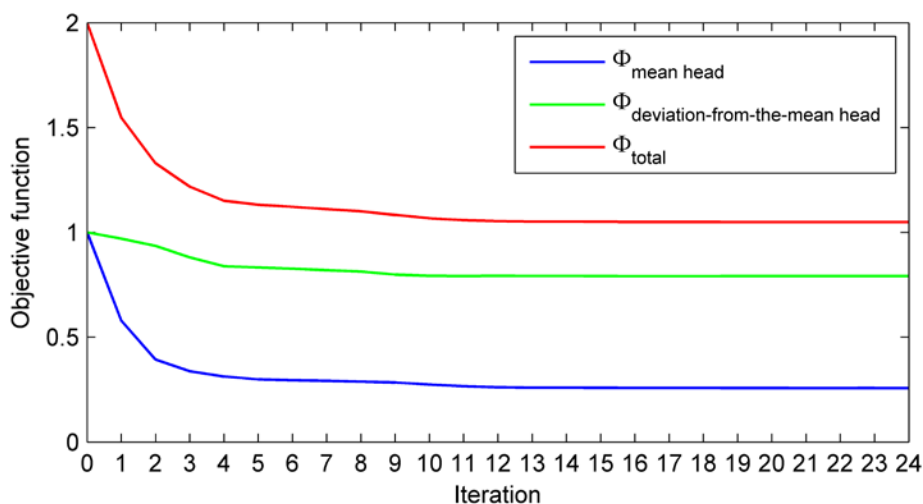
RPMUL (rainfall multiplier in the calculation of recharge) reached its lower bound (0.0008, i.e., recharge would be 0.08 % of rainfall). It is likely that the CMB-derived estimate of diffuse recharge used to assign the preferred value is an overestimation. Indeed, groundwater in the Quaternary aquifers can originate from the MLR in areas where upward flow from the T1 aquifer occurs. Historical groundwater flow (i.e., prior to heavy pumping) was indeed upward over large areas, as suggested by hydraulic heads (Gerges 1999; 2006) and supported by the results of the current model (see below). As groundwater in the MLR is generally fresher than in the Plains, including such groundwater samples when applying the CMB method (as was done) bends the result towards an overestimation of diffuse recharge. Leakage from streams into the aquifer can also bias the CMB method, because corresponding groundwater samples are not representative of diffuse recharge. As stream water would generally be fresher than diffuse recharge, including them (as was done) again bends the result towards an overestimation. Moreover, direct surface runoff was neglected when applying the CMB method and this can also bend the result towards an overestimation. Nevertheless and regardless of these considerations, the observed misfit in hydraulic head, but also (and mostly) in Cl concentration and ^{14}C suggest that the calibrated recharge value could be too small (see below).

OK (vertical hydraulic conductivity used to calculate the conductance of the coastal boundary) is $2.9\text{E-}02 \text{ m day}^{-1}$ (94 times the initial value). This value is significantly higher than K_v in HClay which underlies the ocean floor and therefore could seem unrealistic. It might be that this relatively high value compensates for an inappropriate lateral no-flow boundary used underneath the ocean at 5 km from the coast. The position of the potential seawater wedge which would define an effective no-flow boundary is largely unknown and might be located farther away from the coast. Testing different coastal boundary conditions in future work would be beneficial.

The vertical hydraulic conductivity used to calculate the conductance of surface water features are all fairly different from their initial value and especially RIVBEDK_T, RIVBEDK_FR and RIVBEDK_Wa. This result is not so surprising given the large uncertainty on this parameter but also on riverbed bottom and riverbed thickness parameters for which this parameter play a surrogate role.

Apx Table K.10 Parameters that reached their upper bound (red dots) or lower bound (blue dots) during PEST iterations

ITERATION	S _y in T1	HAMP	RPMUL	S _y in UTSand	Tertiary river conductance	Ocean conductance	S _y in BRockU	K _h in BRockD	S _s in BRockD	S _s in UTSand
1										
2	•	•								
3	•	•								
4	•	•								
5	•	•	•	•						
6	•	•	•	•						
7	•	•	•	•						
8	•		•	•						
9	•		•	•						
10	•		•	•						
11	•		•	•						
12	•		•	•						
13	•		•	•	•					
14	•		•	•	•	•				
15	•		•	•	•	•	•			
16	•		•	•	•	•	•			
17	•		•	•	•	•	•	•		
18	•		•	•	•	•	•	•	•	
19	•		•	•	•	•	•	•	•	
20	•		•	•	•	•	•	•	•	
21	•		•	•	•	•	•	•	•	
22	•	•	•	•	•	•	•	•	•	•
23	•	•	•	•	•	•	•	•	•	•
24	•	•	•	•	•	•	•	•	•	•



Apx Figure K.40 Evolution of the objective function (Φ) during PEST iterations

Apx Table K.11 Calibrated material properties, with in parenthesis the factor by which they differ from their preferred value (next to the value) and the post-calibration range of uncertainty (below the value). Values that are at the upper or lower bound of the allowed calibration interval are indicated in red and blue, respectively

HYDROSTRATIGRAPHIC UNIT (ZONE)	K_h (m day ⁻¹)	K_v (m day ⁻¹)	S_s (m ⁻¹)	S_v (-)	θ_E (-)	α_L (m) ¹
HClay	3.4E-01 (x 110) (3.4E-01 – 3.4E-01)	6.0E-04 (x 1.9) (6.0E-04 – 6.0E-04)	3.6E-05 (x 1.4) (7.6E-06 – 1.7E-04)	tied to θ_E	0.27 (x 1.4) (0.27 – 0.27)	50 (x 1.0) (8 – 316)
UTSand	1.1E+00 (x 0.12) (1.1E+00 – 1.2E+00)	9.1E-01 (x 0.97) (1.7E-02 – 5.0E+01)	9.3E-04 (x 1.9) (4.5E-06 – 1.9E-01)	tied to θ_E	0.4 (x 2.0) (0.23 – 0.70)	50 (x 1.0) (8 – 316)
T1	6.3E-01 (x 0.067) (6.3E-01 – 6.3E-01)	8.7E-01 (x 0.93) (4.7E-03 – 1.6E+02)	8.1E-07 (x 0.0016) (3.4E-07 – 1.9E-06)	tied to θ_E	0.4 (x 2.0) (0.36 – 0.45)	50 (x 1.0) (8 – 316)
MPClay	6.5E-05 (x 1.0) (6.7E-08 – 6.3E-02)	1.4E-05 (x 2.3) (1.4E-05 – 1.4E-05)	6.7E-06 (x 0.61) (1.6E-06 – 2.8E-05)	tied to θ_E	0.2 (x 1.0) (0.10 – 0.40)	50 (x 1.0) (8 – 316)
T2	1.7E+00 (x 0.25) (1.7E+00 – 1.7E+00)	5.8E-01 (x 0.87) (1.4E-01 – 2.4E+00)	3.5E-06 (x 0.011) (3.4E-06 – 3.5E-06)	tied to θ_E	0.2 (x 1.0) (0.10 – 0.40)	50 (x 1.0) (8 – 316)
BPFmnU	3.0E-05 (x 0.47) (5.5E-07 – 1.6E-03)	4.3E-05 (x 6.8) (4.3E-05 – 4.4E-05)	9.8E-06 (x 0.90) (2.1E-07 – 4.6E-04)	tied to θ_E	0.2 (x 1.0) (0.10 – 0.40)	50 (x 1.0) (8 – 316)
T3T4U	2.0E+01 (x 2.9) (1.9E+01 – 2.0E+01)	7.0E-01 (x 1.0) (9.2E-04 – 5.2E+02)	4.0E-04 (x 1.2) (3.3E-05 – 4.7E-03)	tied to θ_E	0.2 (x 1.0) (0.10 – 0.40)	50 (x 1.0) (8 – 316)
BRockU	3.8E-02 (x 37.5) (3.7E-02 – 3.8E-02)	5.3E-02 (x 53) (4.9E-02 – 5.8E-02)	1.3E-04 (x 13) (1.2E-04 – 1.4E-04)	tied to θ_E	0.028 (x 2.8) (0.006 – 0.14)	50 (x 1.0) (8 – 316)
BPFmnD	6.1E-05 (x 0.95) (1.2E-06 – 3.1E-03)	6.5E-04 (x 100) (6.5E-04 – 6.5E-04)	8.7E-07 (x 0.079) (3.9E-07 – 1.9E-06)	tied to θ_E	0.2 (x 1.0) (0.10 – 0.40)	50 (x 1.0) (8 – 316)
T3T4D	2.1E-02 (x 0.0031) (2.2E-03 – 2.0E-01)	6.9E-01 (x 1.0) (1.2E-02 – 3.8E+01)	4.3E-04 (x 1.3) (4.3E-04 – 4.3E-04)	tied to θ_E	0.2 (x 1.0) (0.10 – 0.40)	50 (x 1.0) (8 – 316)
BRockD	9.4E-06 (x 0.0094) (3.5E-07 – 2.6E-04)	1.1E-05 (x 0.011) (4.1E-06 – 2.9E-05)	1.1E-06 (x 0.11) (1.1E-07 – 1.2E-05)	tied to θ_E	0.01 (x 1.0) (0.001 – 0.1)	50 (x 1.0) (8 – 316)
PFault	2.1E-04 (x 0.21) (8.1E-05 – 5.3E-04)	3.8E-02 (x 3.8) (2.7E-02 – 5.3E-02)	2.6E-03 (x 26) (2.4E-03 – 2.7E-03)	tied to θ_E	0.31 (x 1.6) (0.15 – 0.62)	50 (x 1.0) (8 – 316)

1. Horizontal and vertical transverse dispersivities were defined by a fixed ratio to the longitudinal dispersivity of 0.1 and 0.01, respectively

Apx Table K.12 Calibrated parameters (except material properties), with in parenthesis the factor by which they differ from their preferred value (next to the value) and the post-calibration 95% confidence interval (below the value). Values that are at the upper or lower bound of the allowed calibration interval are indicated in red and blue, respectively

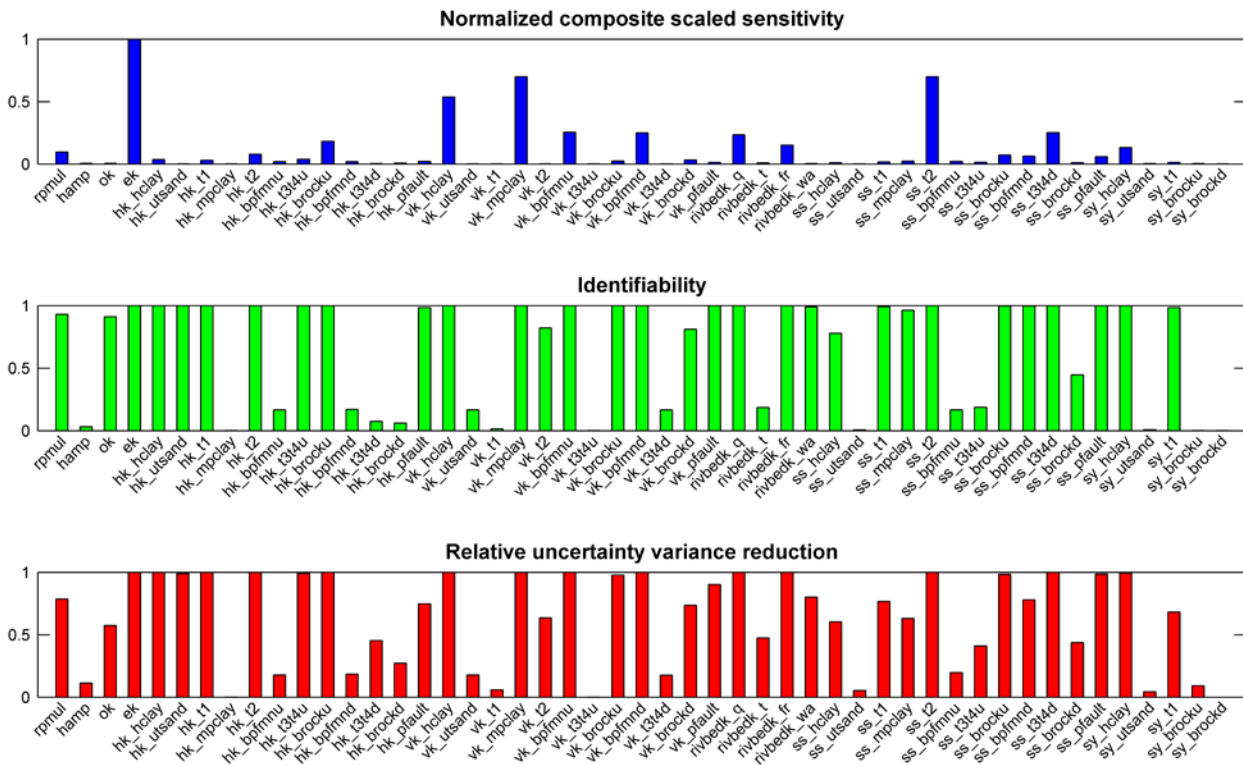
PARAMETER	Definition (unit)	Value
RPMUL	Rainfall multiplier in the recharge calculation (-)	8.0E-04 (x 0.1) (6.2E-04–1.0E-03)
HAMP	Amplitude of temporal fluctuations of the eastern boundary head (m)	5.6 (x 0.56) (2.1–15)
EK	K of eastern boundary conductance (m day ⁻¹)	5.6E-04 (x 0.56) (5.6E-04–5.6E-04)
OK	K of ocean boundary conductance (m day ⁻¹)	2.9E-02 (x 94) (5.5E-03–1.6E-01)
RIVBEDK_Q	K of Quaternary river conductance (m day ⁻¹)	1.5E-03 (x 4.8) (1.5E-03–1.5E-03)
RIVBEDK_T	K of Tertiary river conductance (m day ⁻¹)	2.2E-04 (x 0.00023) (1.2E-05–3.8E-03)
RIVBEDK_FR	K of fractured rock river conductance (m day ⁻¹)	1.8E-01 (x 180) (1.8E-01–1.8E-01)
RIVBEDK_Wa	K of “unclassified” river conductance (m day ⁻¹)	3.8E-02 (x 38) (1.4E-02–9.9E-02)

Parameters normalized composite scaled sensitivity, identifiability and relative uncertainty variance reduction

Parameters normalized composite scaled sensitivity, identifiability and relative uncertainty variance reduction are shown in Apx Figure K.41. The most sensitive parameter is the hydraulic conductivity of the eastern boundary conductance (“ek”). The next most sensitive parameters are the vertical hydraulic conductivity of aquitards (Hindmarsh Clay, Munno Para Clay and Blanche Point Formation) and the specific storage of the T2 and T3T4 aquifers. Some other storage coefficients are also sensitive, such as the specific yield of Hindmarsh Clay. Horizontal hydraulic conductivities are generally less sensitive than vertical hydraulic conductivities for aquitards, whereas the opposite is true for aquifers. The hydraulic conductivities of the conductance of rivers lying upon Quaternary sediments and fractured rock (“rivbedk_q” and “rivbedk_fr”) are also quite sensitive.

Sensitivity does not always correlate to identifiability. The most sensitive parameters are completely identifiable, but so are many less sensitive parameters. A few parameters are almost not identifiable, such as the amplitude of the temporal fluctuations of the eastern boundary head (HAMP, see equation (2)), the horizontal conductivity of MPClay, the vertical hydraulic conductivity of T1 and of T3T4U, the specific storage and specific yield of UTSand, and the specific yield of BRockU and of BRockD. This means that these parameters are quite insensitive or have the same effect on model outcomes as other parameters.

A parameter can be identifiable and yet not be uncertainty-free because of measurement noise. For this reason, a number of parameters that appear identifiable do not have a relative uncertainty reduction equal to 1. That is the case for example for the horizontal hydraulic conductivity of Para fault and for the specific storage of T1, MPCLay and BPFmnd. These nevertheless have a significant uncertainty reduction. Overall, about half of the parameters have a relative uncertainty variance reduction larger than 0.5. The post-calibration 95 % confidence interval of the parameters is given in Apx Table K.11 and Apx Table K.12 above.



Apx Figure K.41 Parameters normalized composite scaled sensitivity, identifiability and relative uncertainty variance reduction through calibration. Parameter names starting with “hk”, “vk”, “ss” and “sy” are followed by abbreviated zone names defined in Apx Table K.1 and refer to horizontal hydraulic conductivity, vertical hydraulic conductivity, specific storage and specific yield, respectively. Other parameters are defined in Apx Table K.12. The specific yield of zones for which the sensitivity was zero is not reported (these zones mostly remain entirely saturated, which is why this parameter has no effect)

Calibration performance (mean hydraulic head)

Apx Figure K.42 shows scatter plots of simulated values and weighted residuals against measured values for the mean hydraulic head (i.e. temporal mean in each well) in the transient development model. Although a large proportion of the points align well with the 1:1 line, there is significant scattering around the line. The absolute values of the weighted residuals are up to 88.8 (dimensionless), i.e., residuals are up to 88.8 times larger than the estimated measurement error. No obvious bias can be distinguished when looking at the results for entire model, but bias exists in individual units. In the Hindmarsh Clay unit, the larger head values are generally underestimated, whereas in T1 and in T2, the smaller head values are generally overestimated. RMS and SRMS for this group of observations are 9.16 m and 3.25 %, respectively (Apx Table K.13). SE is 6.17 with little uncertainty around this value, meaning that the model is not capable of simulating mean hydraulic heads at a level of precision that is commensurate with the estimated measurement error. Possible reasons for and implications of this misfit are discussed later. The mean weighted residual is 0.36, indicating that on average overestimations and underestimations are well balanced. The relatively high value of R (0.95) shows that overall the model captures the distribution of mean hydraulic head values reasonably well.

The spatial distribution of weighted residuals for the mean hydraulic head is shown in Apx Figure K.43, Apx Figure K.44 and Apx Figure K.45 for observation wells in the Hindmarsh Clay, T1 and T2 units, respectively. Note that the colour scales are different between figures to facilitate observation of any spatial bias in each case. Some obvious clustering appears in Hindmarsh Clay, especially in the Golden Grove Embayment along the southeast boundary of the model where hydraulic heads are systematically underestimated. Clusters of negative residuals are also found in the Osborne/Port Adelaide area and near the upper reach of the Little Para River, whereas the largest positive residuals generally appear around the Gawler River. Clustering of similar residuals is a bit less obvious in the T1 aquifer but still exists. Hydraulic heads are typically overestimated in the Waterloo Corner and Mawson Lakes areas and underestimated around the upper reach of the Little Para River. To a certain extent, the spatial distribution of the residuals in the T1 aquifer shows correlation with the spatial distribution of the residuals in Hindmarsh Clay. Residuals also show spatial patterns in T2, being generally negative around the upper reach of the Gawler river and around the upper reach of the Little Para River, whereas being generally positive in the lower reach of the Gawler river and in the Kangaroo Flat and Paradise areas.

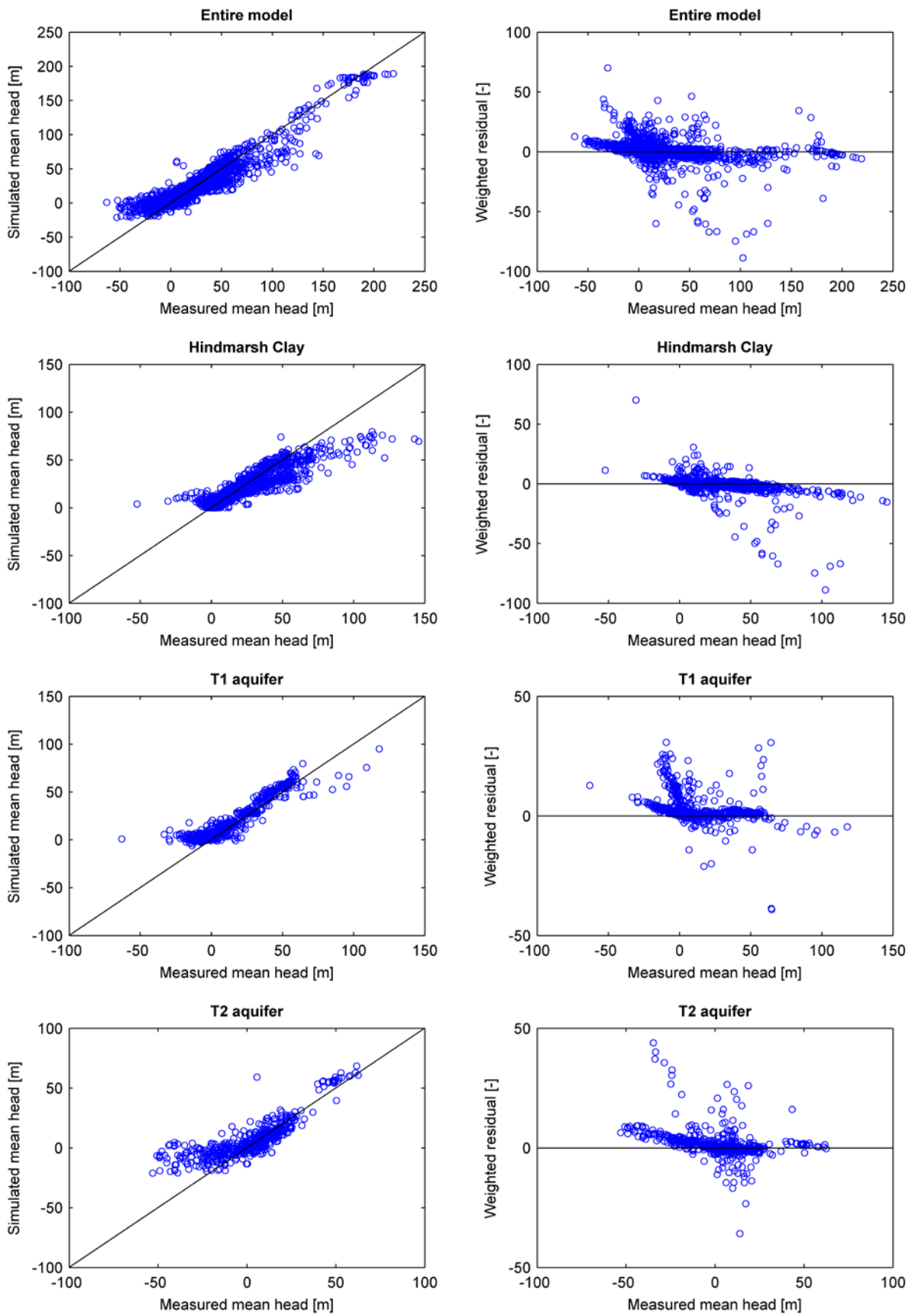
Possible reasons for this misfit in mean head are:

- Underestimation of measurement error. As stated in section K.3.10, estimating measurement error is difficult. The estimated measurement error for wells belonging to the observation network (0.5 m) might be too small.
- Underestimation of pumping. This could explain why low hydraulic heads in T1 and T2 are generally overestimated. This could also explain why RPMUL (the parameter controlling diffuse recharge) reached its lower bound. Indeed, there are a large number of domestic (non-licensed) wells in the Quaternary aquifers that were not included in the model. Individual pumping rates from these wells are relatively small, but together they were estimated to sum up to about 2 GL yr⁻¹ for the sedimentary aquifers (Martin 2011), which is non-negligible in the water balance. Groundwater levels would in reality be affected by these wells, and consequently it is possible that a small calibrated recharge stems from a compensation of the lack of inclusion of these wells in the model.
- Too coarse grid resolution. A finer grid should allow a more accurate variation of hydraulic head especially in areas where the hydraulic gradient is large, as around pumping well. This could also explain why small hydraulic heads in T1 and T2 are generally overestimated. However, a forward simulation on a 500 m-resolution grid using calibrated parameter values showed no qualitative improvement of the fit. Further testing on finer grids including re-calibration is nevertheless warranted to confirm the non-influence of grid resolution on the fit.
- Lack of intra-zone heterogeneity for hydraulic conductivity. The large zones of uniform hydraulic properties are not realistic, and this necessarily implies more uniform hydraulic heads than in reality. Therefore, local variations in hydraulic head cannot be captured by the model. The fact that clear patterns can be identified in the spatial distribution of weighted residuals (Apx Figure K.43, Apx Figure K.44 and Apx Figure K.45) suggests that the lack of intra-zone heterogeneity could be a major reason for the misfit (Moore *et al.* 2006).
- Non-consideration of possible perched water table conditions. If these exist, the vertical leakage from the perched aquifer would be overestimated because in reality the unsaturated zone should be less conductive, and MODFLOW-NWT does not implement such a mechanism. This could explain why large hydraulic heads are underestimated in Hindmarsh Clay. However, if the vertical hydraulic conductivity was allowed to vary locally, it could take smaller values in areas where such conditions exist. Therefore, this problem can be related to the lack of intra-zone heterogeneity mentioned above.
- Poor representation of the spatial variability of recharge or, in other words, lack of spatial variability in RPMUL. It is well known that recharge is not a simple linear function of rainfall (Crosbie *et al.* 2010). Including spatial variability in RPMUL should allow the spatial variability of recharge to be better represented.

Apx Table K.13 Model performance statistics (definitions are given in Apx Table K.5)

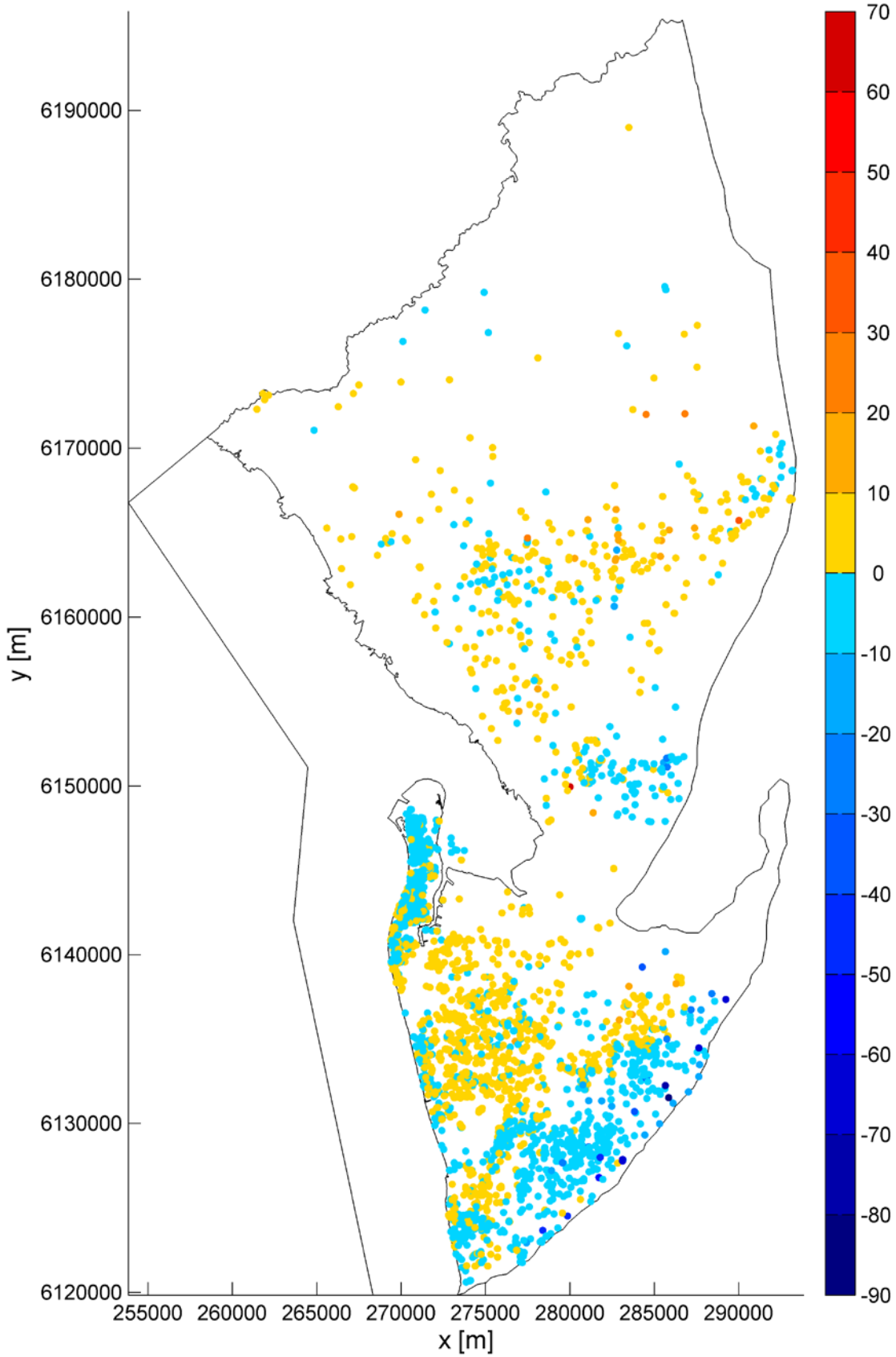
STATISTIC	Mean hydraulic heads	Deviations from the mean hydraulic head	Absolute hydraulic heads ¹	Cl concentrations ¹	¹⁴ C activities ¹
RMS	9.16 m	3.24 m	8.60 m	1410 mg L ⁻¹	22.4 pmC
SRMS	3.25 %	3.90 %	2.99 %	28.28 %	24.05 %
SE	6.17 (6.06–6.27)	6.14 (6.11–6.17)	15.62 (15.54–15.70)	10.58 (10.40–10.77)	34.09 (29.9–39.7)
MWR	0.36	0.00	4.24	7.51	15.07
R	0.95	0.53	0.94	0.25	0.57

1. Not part of the calibration dataset, but compared on the basis of the calibrated model



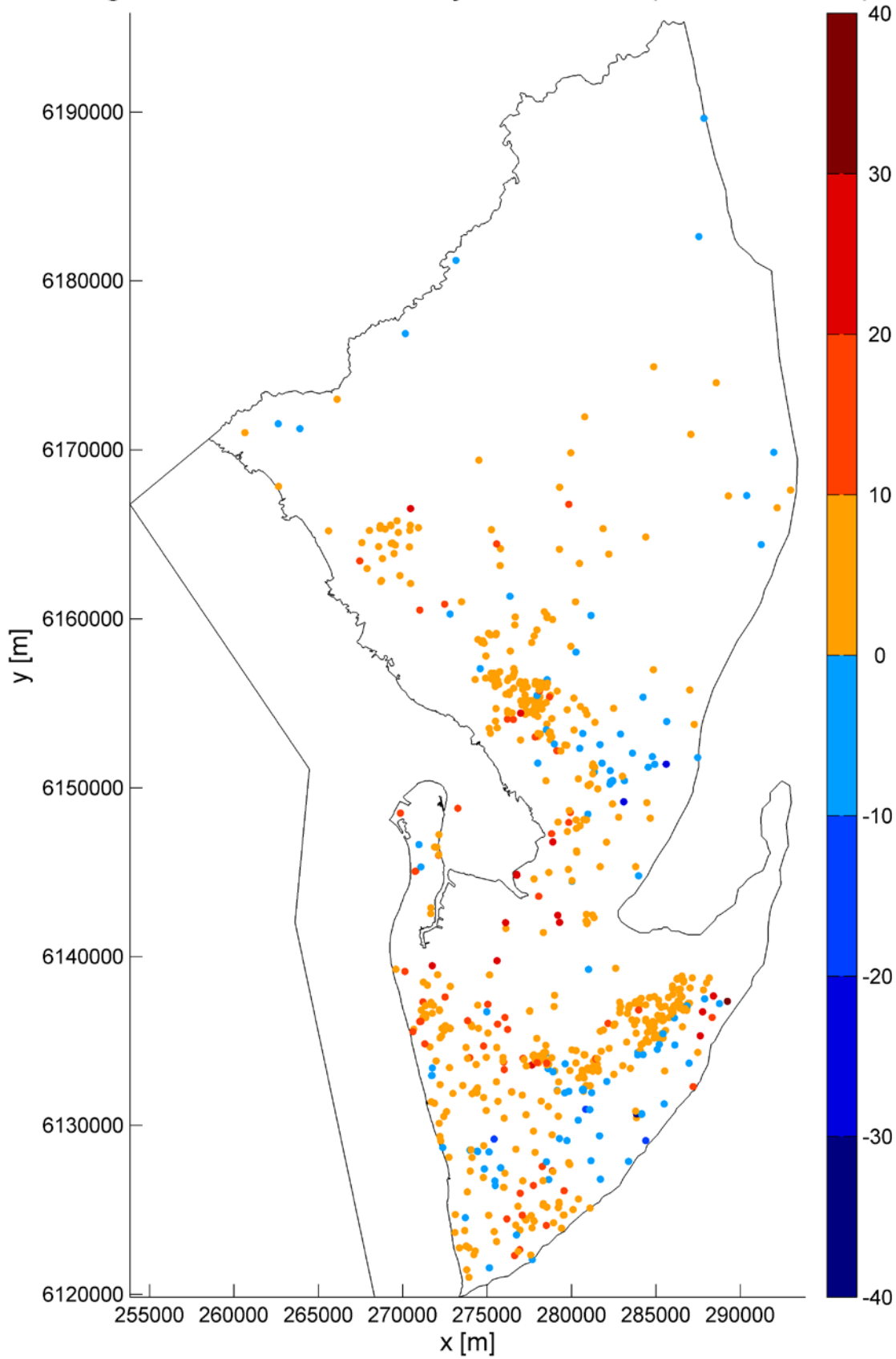
Apx Figure K.42 Simulated mean hydraulic heads (left) and weighted residuals (right) against measured mean hydraulic heads in the transient development model for the entire model (top) and for main units individually (bottom three rows)

Weighted residual of mean hydraulic head (dimensionless)



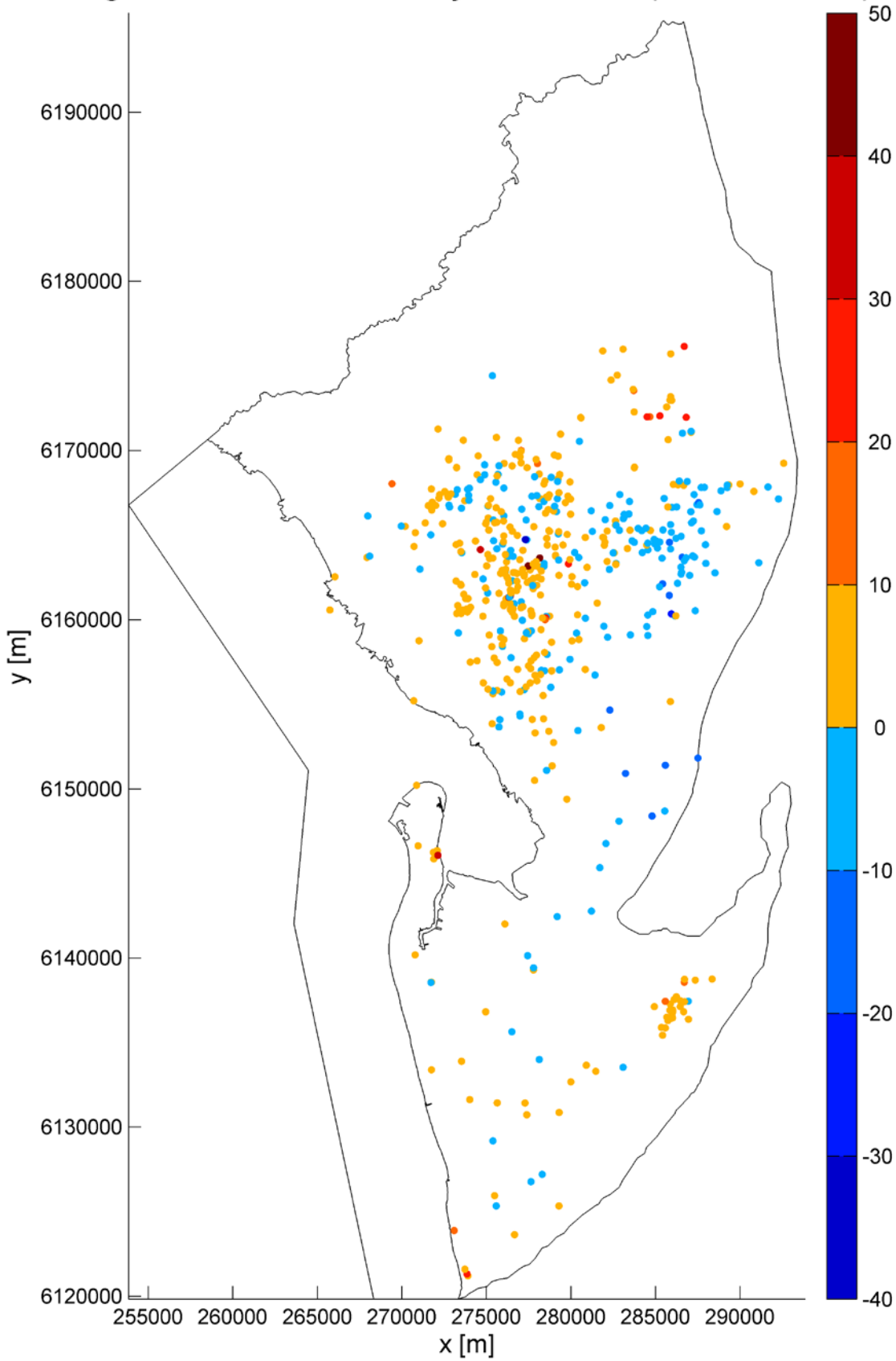
Apx Figure K.43 Spatial distribution of weighted residuals for the mean hydraulic heads in Hindmarsh Clay (transient development model)

Weighted residual of mean hydraulic head (dimensionless)



Apx Figure K.44 Spatial distribution of weighted residuals for the mean hydraulic heads in the T1 aquifer (transient development model)

Weighted residual of mean hydraulic head (dimensionless)



Apx Figure K.45 Spatial distribution of weighted residuals for the mean hydraulic heads in the T2 aquifer (transient development model)

Calibration performance (deviation from the mean head)

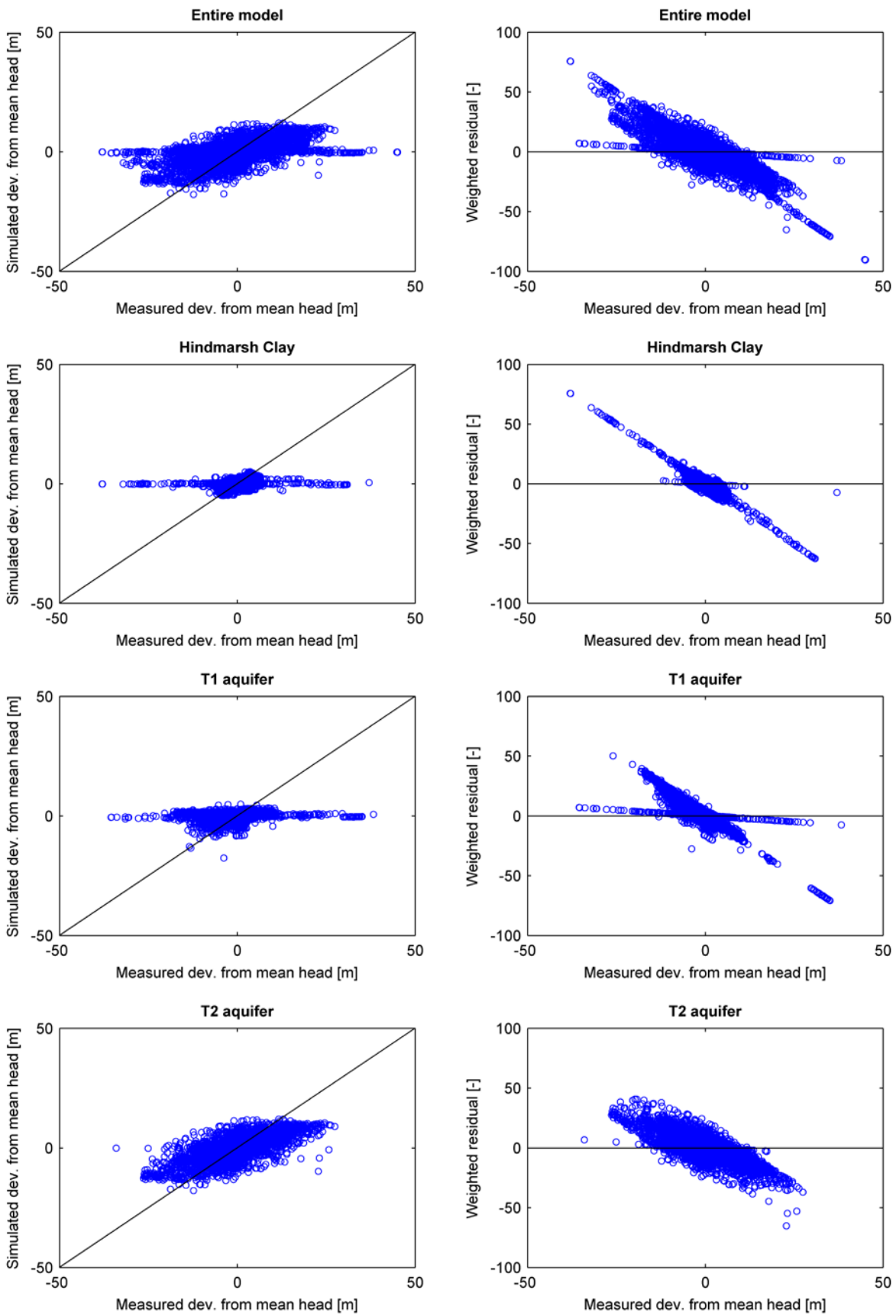
Scatter plots of simulated values and weighted residuals against measured values for the deviations from the mean head in the transient development model are shown in Apx Figure K.46. A strong bias can be noted in the entire model as well as in individual units: the small values are systematically overestimated and the large values are systematically underestimated. This indicates that the transient model does not adequately simulate the temporal variability. The poor performance is also reflected by the small value of R (0.53), despite a small SRMS (3.90 %). The spatial distribution of weighted residuals for the deviations from the mean is shown in Apx Figure K.47, Apx Figure K.48 and Apx Figure K.49 for observation wells in the Hindmarsh Clay, and T1 and T2 aquifers, respectively. Note that the colour scales are different between figures to facilitate observation of any spatial bias in each case. In contrast with what was observed for the mean hydraulic head, there are no obvious signs of spatial correlation.

The selected hydrographs showing simulated and measured hydraulic heads further illustrate some of the aforementioned outcomes of the calibration. All hydrographs in the Hindmarsh Clay show an overall underestimation of the hydraulic head (Apx Figure K.50), whereas hydrographs in T1 and T2 sometimes show underestimation and sometimes show overestimation (Apx Figure K.51 and Apx Figure K.52). Temporal fluctuations are generally poorly captured. However, the seasonal fluctuations appear relatively well simulated and the misfit seems to rather stem from inter-annual fluctuations that are not captured by the model. Observation wells ADE010, PTA043 and PTG049 in T1, and observation wells PTA040, PTA046 and PTG060 in T2 are good examples of that.

Possible reasons for the misfit in deviation from the mean head are:

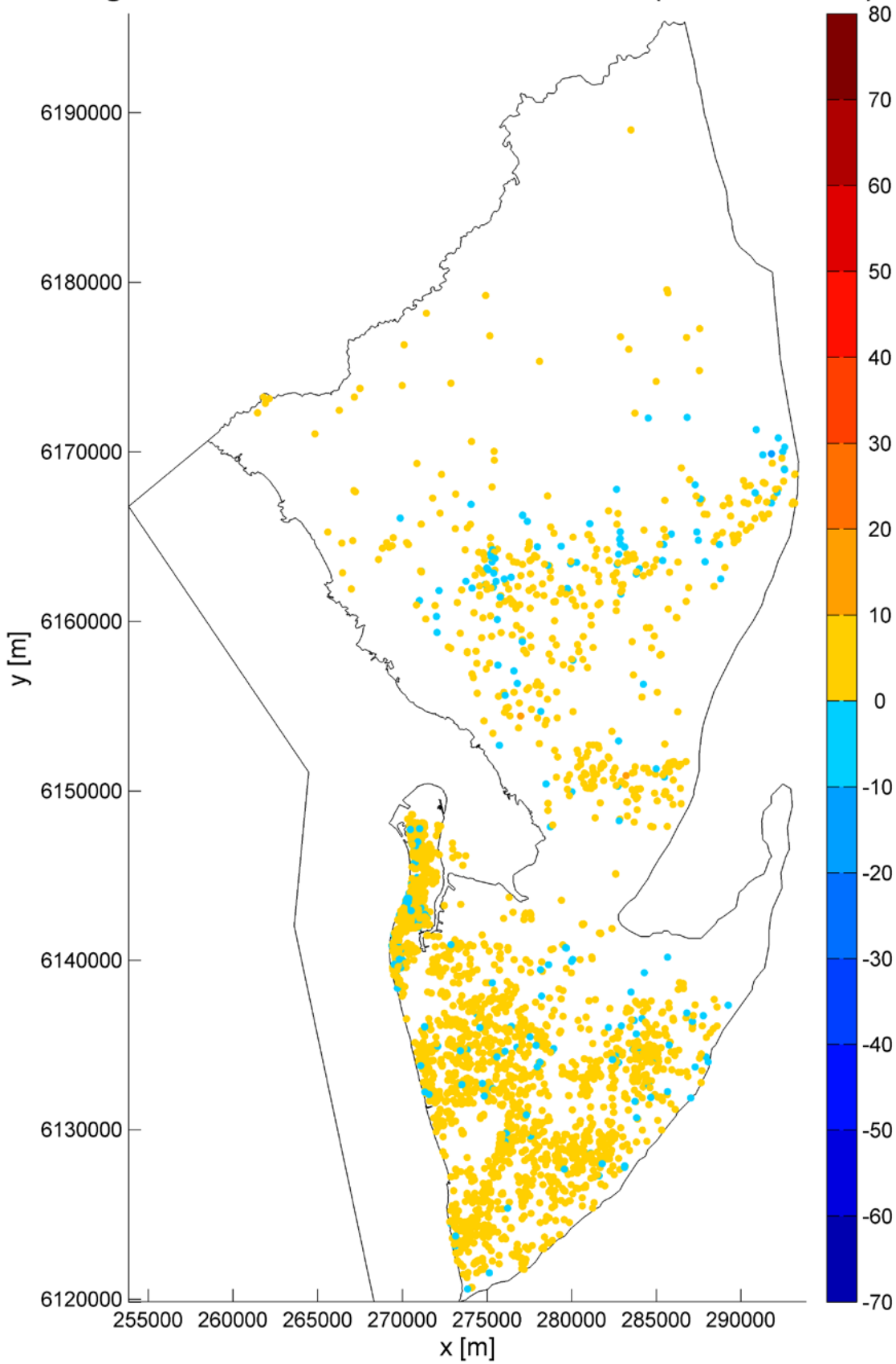
- Underestimation of measurement error. However, some types of error such as positioning-related errors are expected to cancel out in the calculation of the deviations from the mean, whereas here the measurement error associated to the deviations from the mean was assumed to be the same as for the mean heads. Therefore, it seems less likely that underestimation of measurement error can explain the misfit in deviations from the mean head.
- Poor representation of inter-annual fluctuations in recharge and/or pumping. This would explain why especially inter-annual fluctuations are particularly poorly captured (more than seasonal fluctuations). Note that pumping is more likely to be the cause than recharge because the inter-annual fluctuations are poorly captured in T1 and T2, which are confined aquifers and thus less subject to climate-induced fluctuations.
- Too coarse grid resolution. A finer grid should also allow a better resolution of changes in hydraulic head when pumps are turned on/off. However, as noted above a forward simulation on a 500 m resolution grid using calibrated parameter values showed no qualitative improvement of the fit.

Lack of intra-zone heterogeneity for storage coefficients. As mentioned above, the large zones of uniform hydraulic properties are not realistic. Simulated temporal fluctuations could be overestimated or underestimated in areas where the storage coefficient should be larger or smaller, respectively. However, there are no obvious signs of spatial correlation of the weighted residuals. Moreover, as including heterogeneity would imply adjustments in both directions, it seems unlikely that this would correct for the main model defect which is a systematic underestimation of temporal fluctuations.



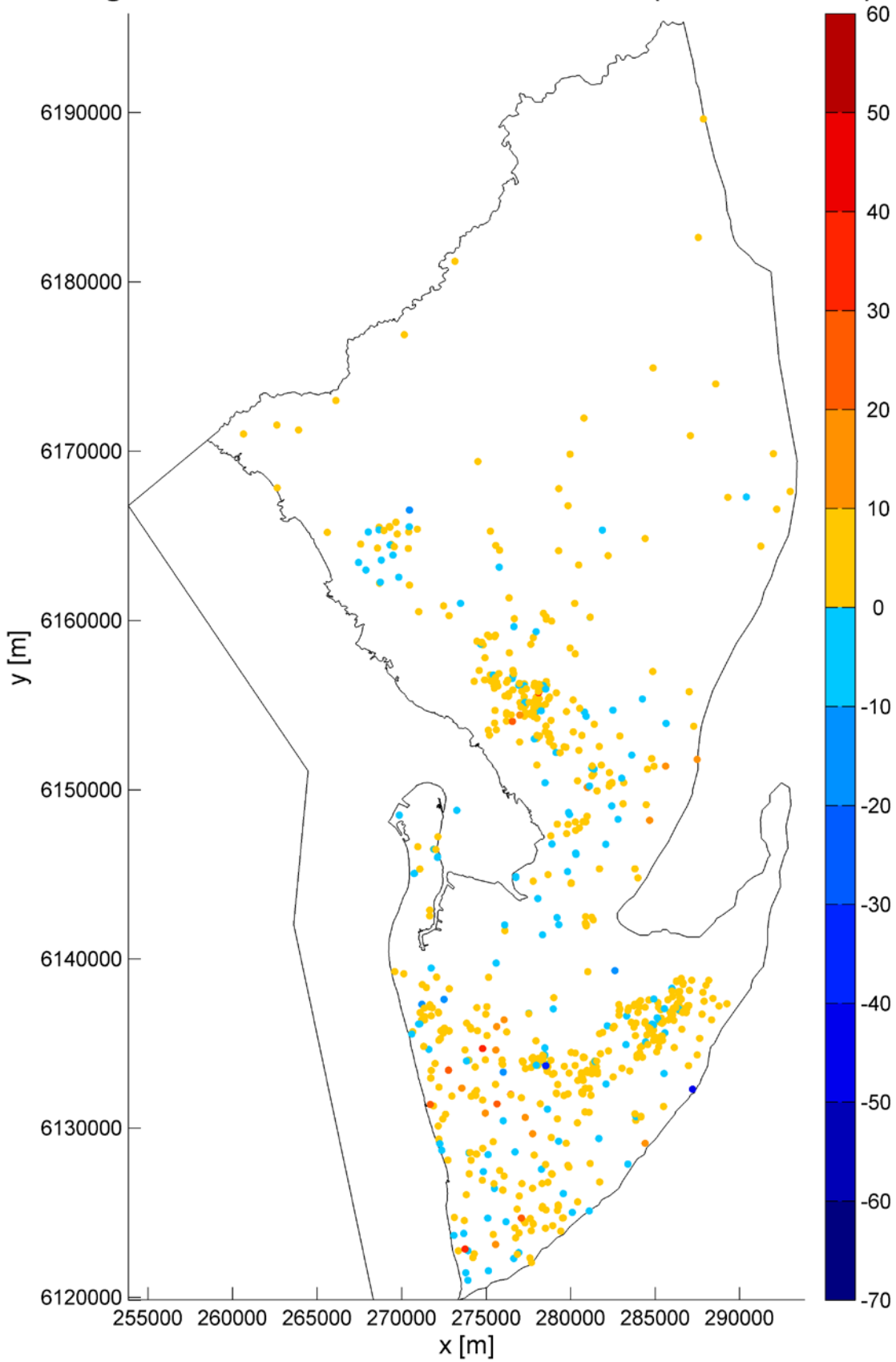
Apx Figure K.46 Simulated deviations from the mean head (left) and weighted residuals (right) against measured deviations from the mean head for the entire model (top) and for main units individually (bottom three rows)

Weighted residual of dev. from mean head (dimensionless)



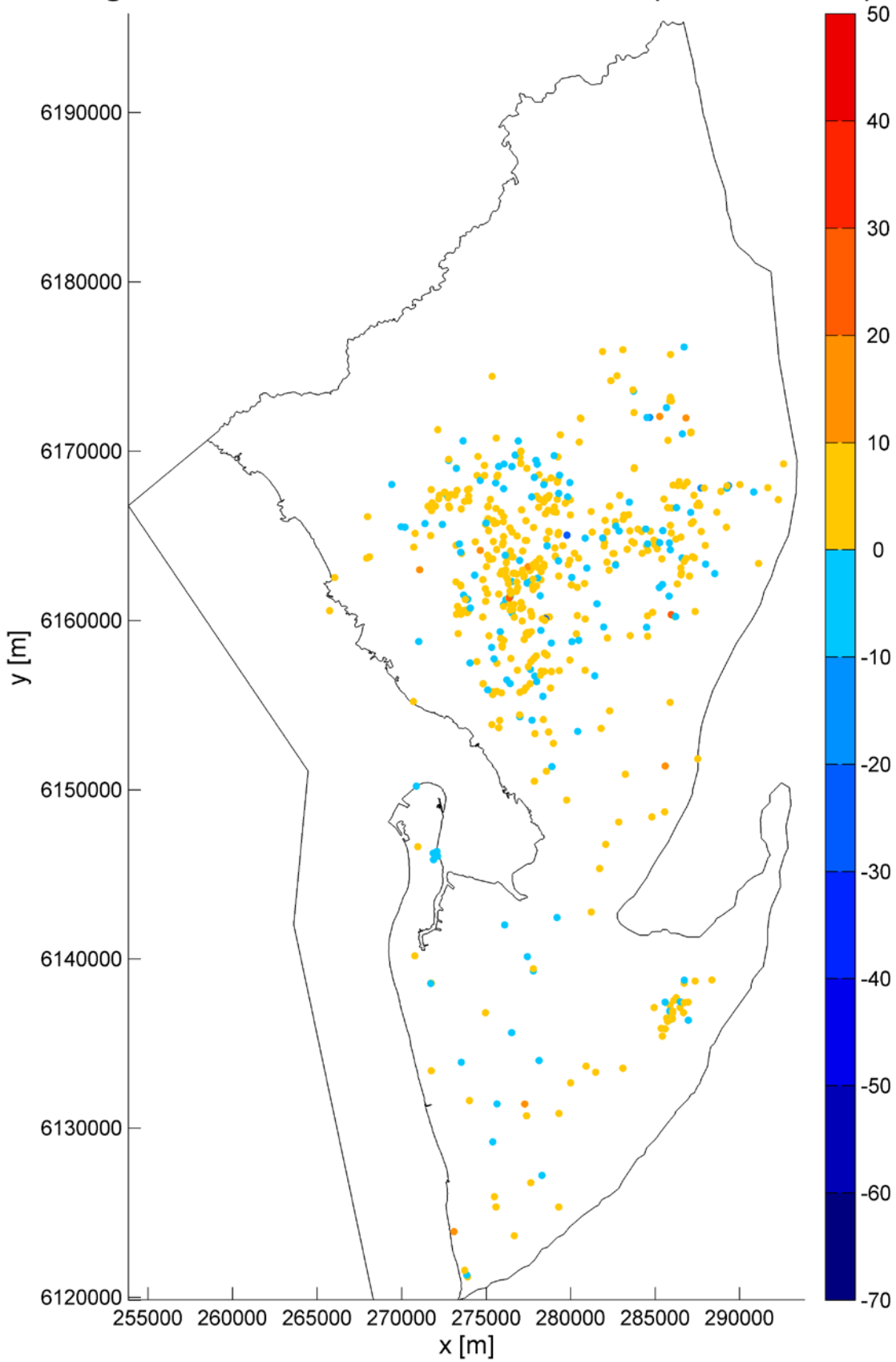
Apx Figure K.47 Spatial distribution of weighted residuals for the deviations from the mean head in Hindmarsh Clay (transient development model)

Weighted residual of dev. from mean head (dimensionless)

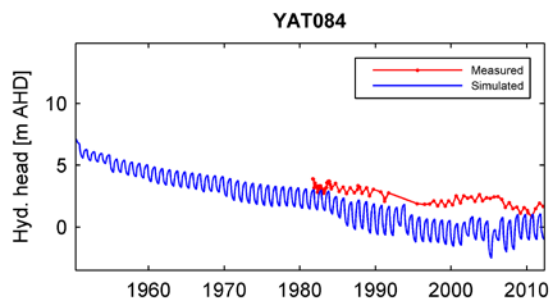
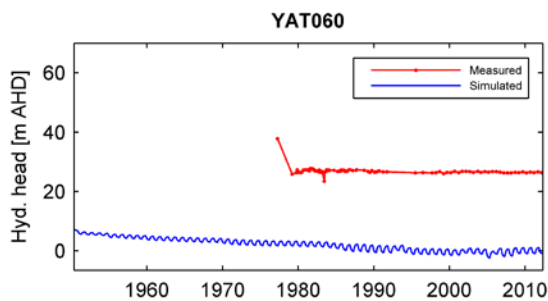
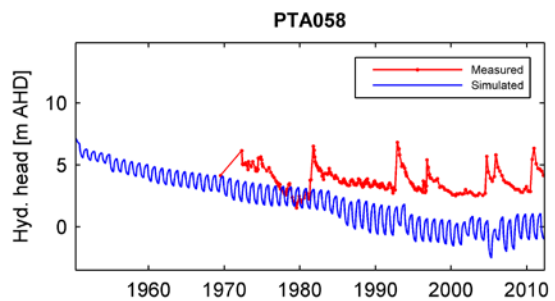
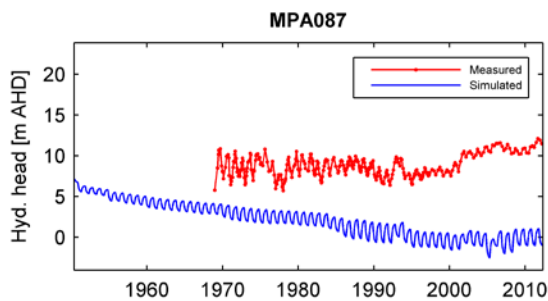
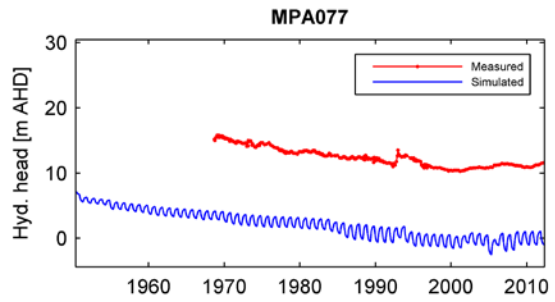
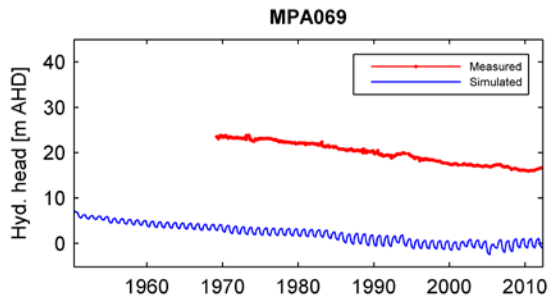
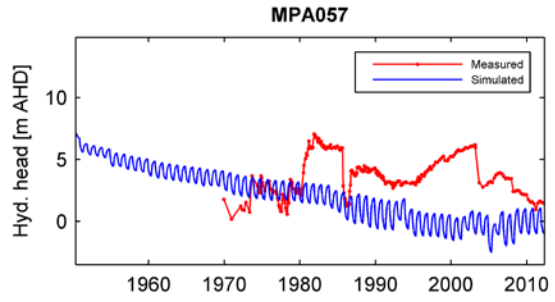
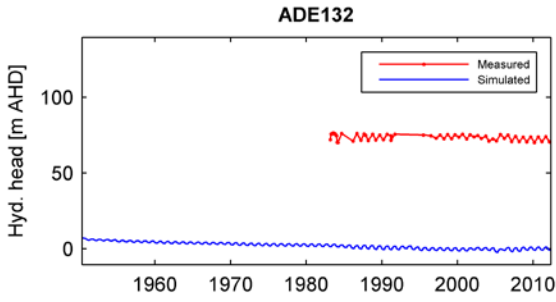
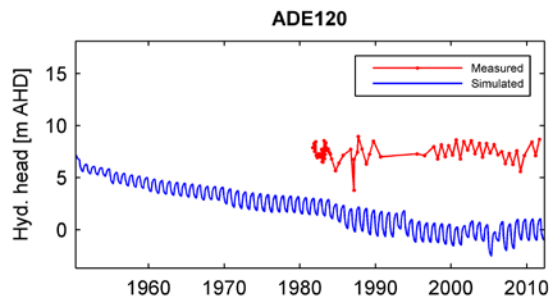
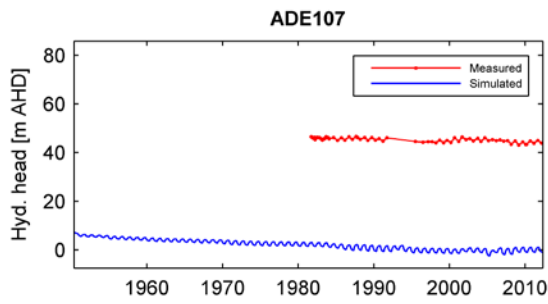


Apx Figure K.48 Spatial distribution of weighted residuals for the deviations from the mean head in the T1 aquifer (transient development model)

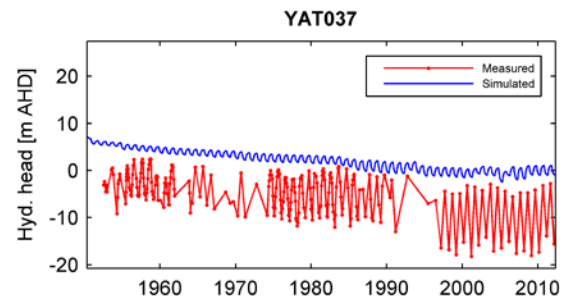
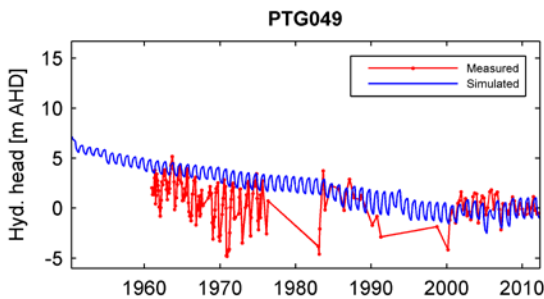
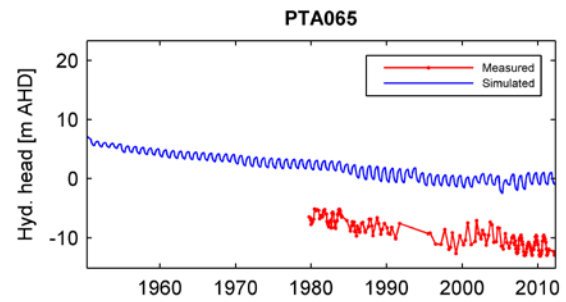
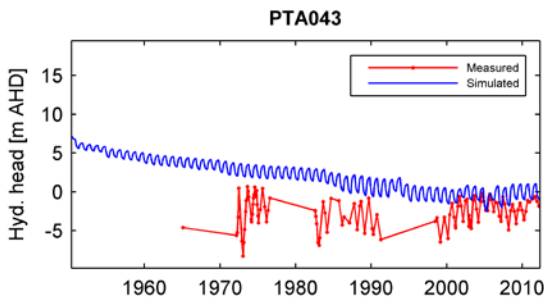
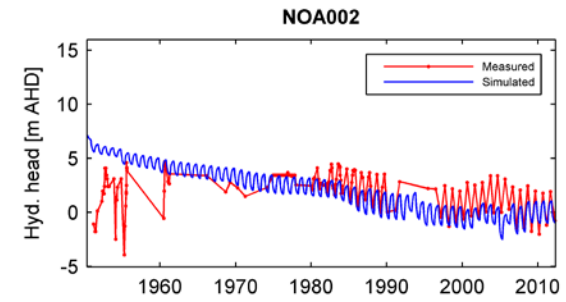
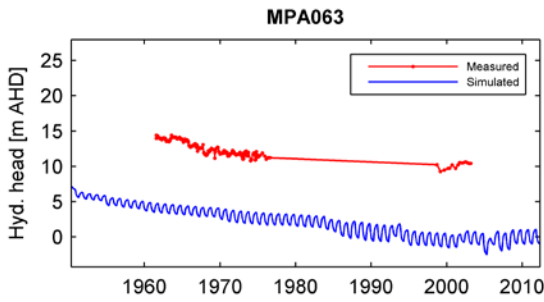
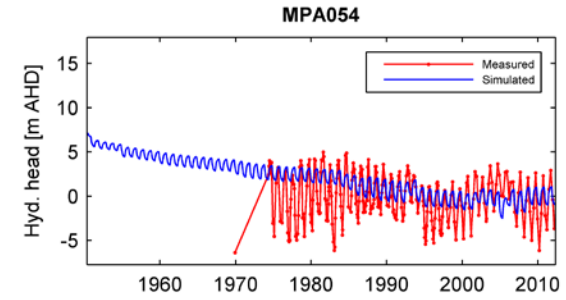
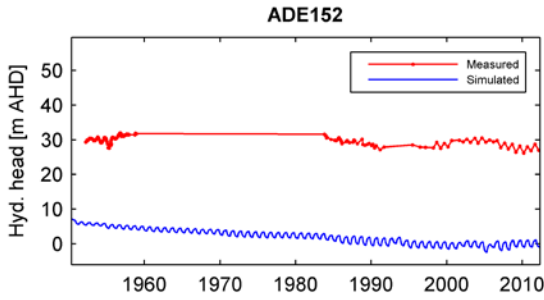
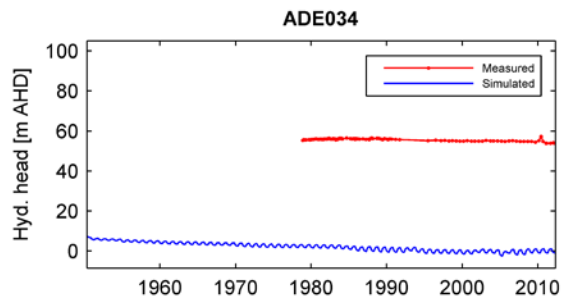
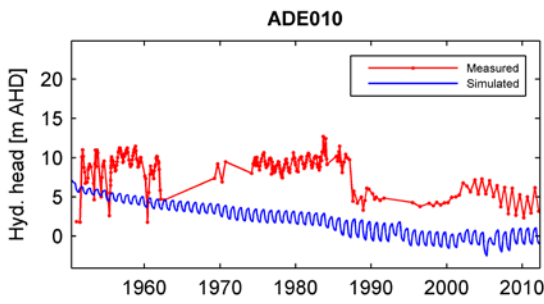
Weighted residual of dev. from mean head (dimensionless)



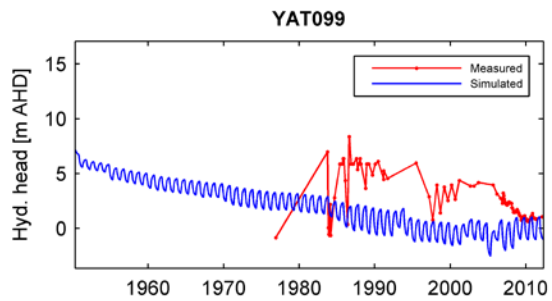
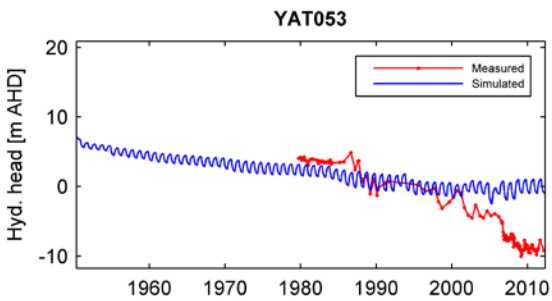
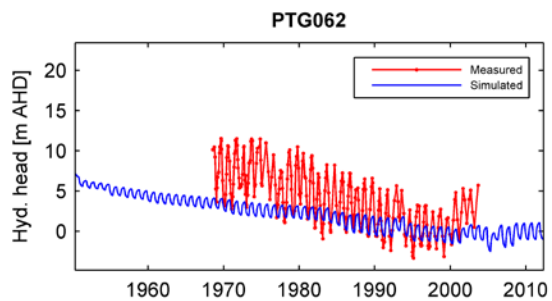
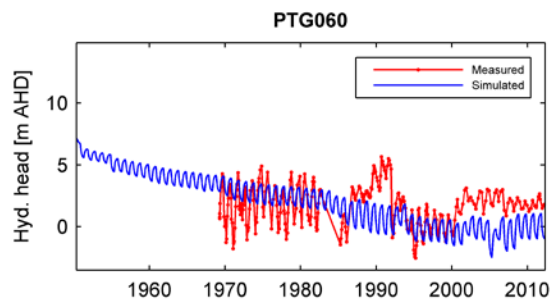
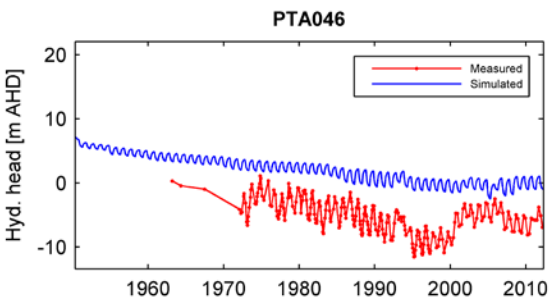
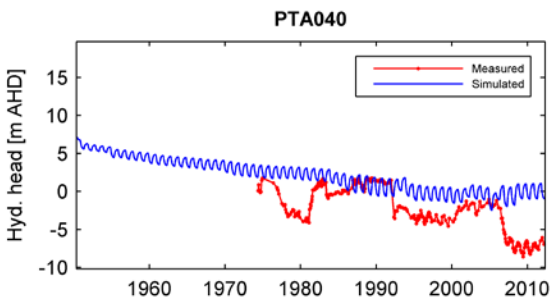
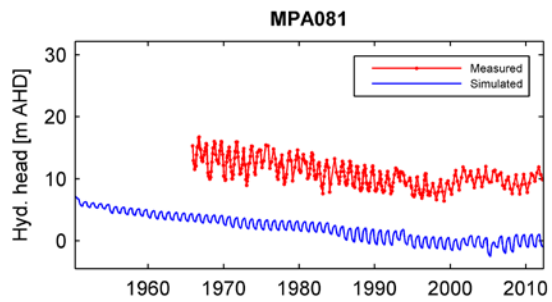
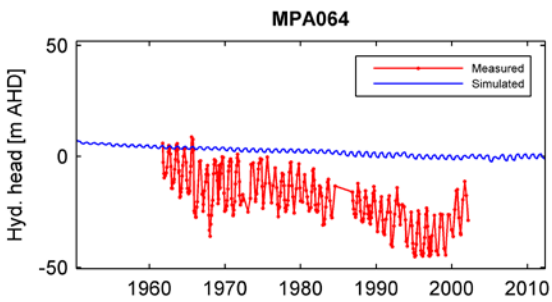
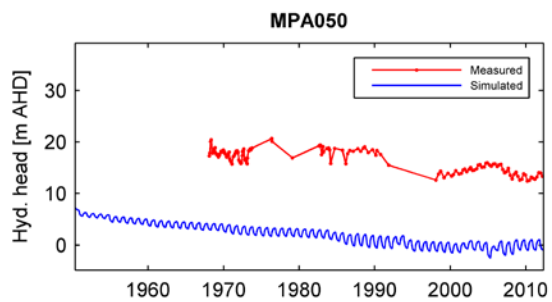
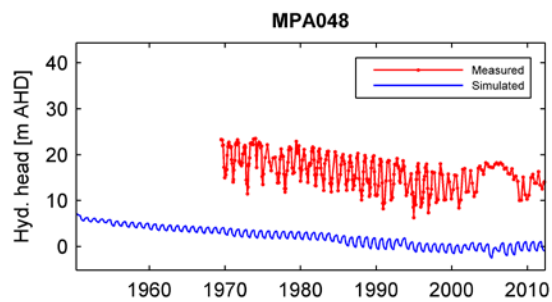
Apx Figure K.49 Spatial distribution of weighted residuals for the deviations from the mean head in the T2 aquifer (transient development model)



Apx Figure K.50 Simulated and measured hydrographs in Hindmarsh Clay



Apx Figure K.51 Simulated and measured hydrographs in the T1 aquifer



Apx Figure K.52 Simulated and measured hydrographs in the T2 aquifer

Calibration performance (Cl)

Originally, the intent was to include Cl measurements in the calibration dataset and calibrate both flow and transport models based on heads and chloride. This strategy had to be abandoned because compatibility issues between MODFLOW-NWT and MT3DMS resulted in erratic behaviour during the PEST runs. Nevertheless, it was possible to run the transport model with the head-calibrated hydraulic parameters and preferred values for non-calibrated parameters (effective porosity and dispersivity). The outputs of this run were compared to the measurements, as described below.

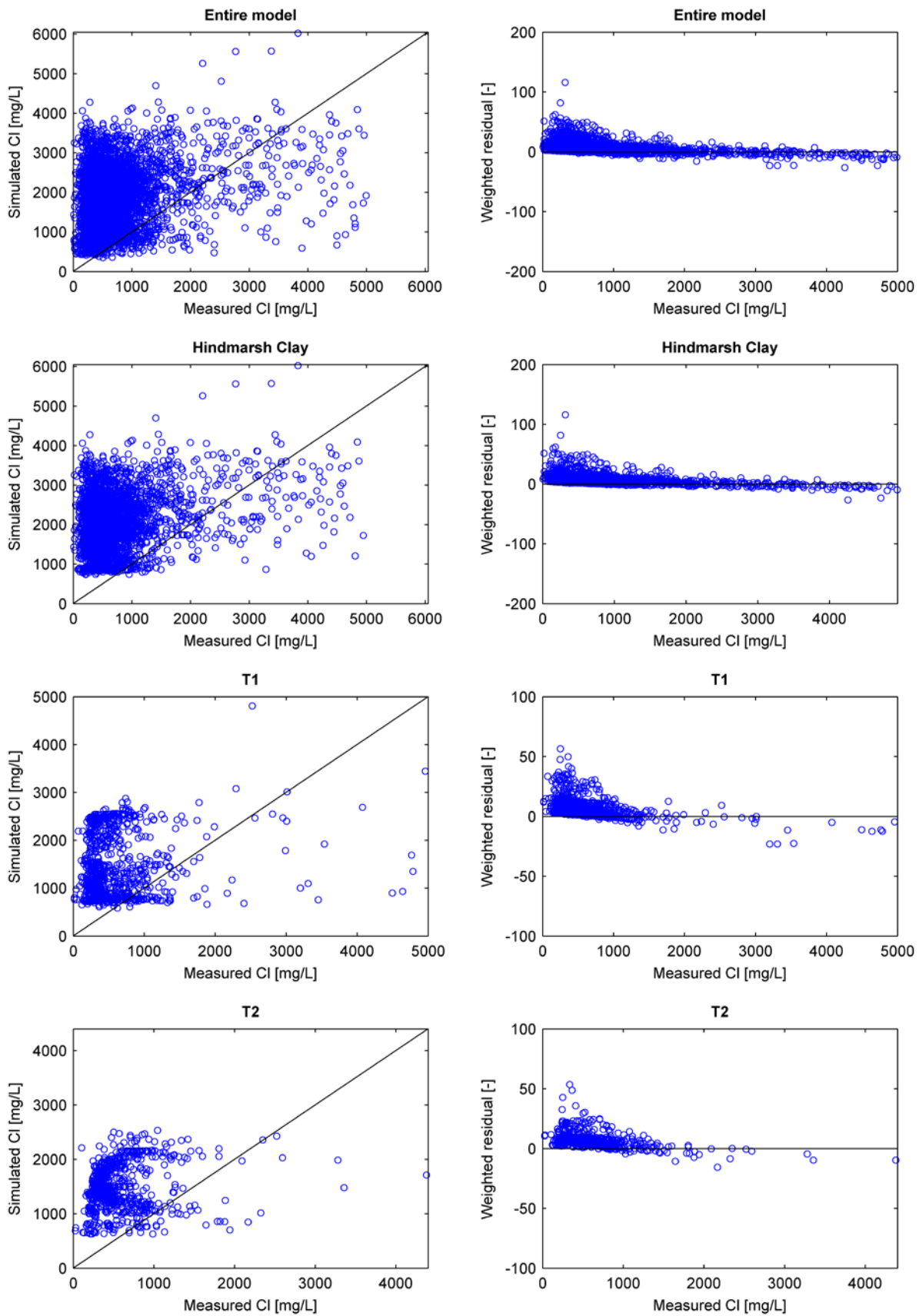
Apx Figure K.53 shows scatter plots of simulated values and weighted residuals against measured values. There is essentially no correlation between simulated and measured chloride concentrations, as also indicated by a small value of R (0.25, see Apx Table K.13). Low values are systematically overestimated and large values are systematically underestimated, with an apparent overall overestimation (MWR = 7.51).

The spatial distribution of weighted residuals in Hindmarsh Clay (Apx Figure K.54) shows some correlation with the weighted residuals of mean hydraulic head (Apx Figure K.43) around the Gawler River. However, in some other areas such as around the upper reach of the Little Para River and in the Osborne/Port Adelaide area, it shows an anti-correlation. The spatial distribution of weighted residuals in T1 (Apx Figure K.55) shows correlation with the spatial distribution of weighted residuals in Hindmarsh Clay, as observed for the mean hydraulic head. The spatial distribution in T2 (Apx Figure K.56) shows a general overestimation of Cl concentrations around the Gawler River and underestimation north of it. Note that the colour scales are different between figures to facilitate observation of any spatial bias in each case.

While the failure of the model to reproduce Cl measurements might be regarded as a fatal shortcoming, the following has to be considered:

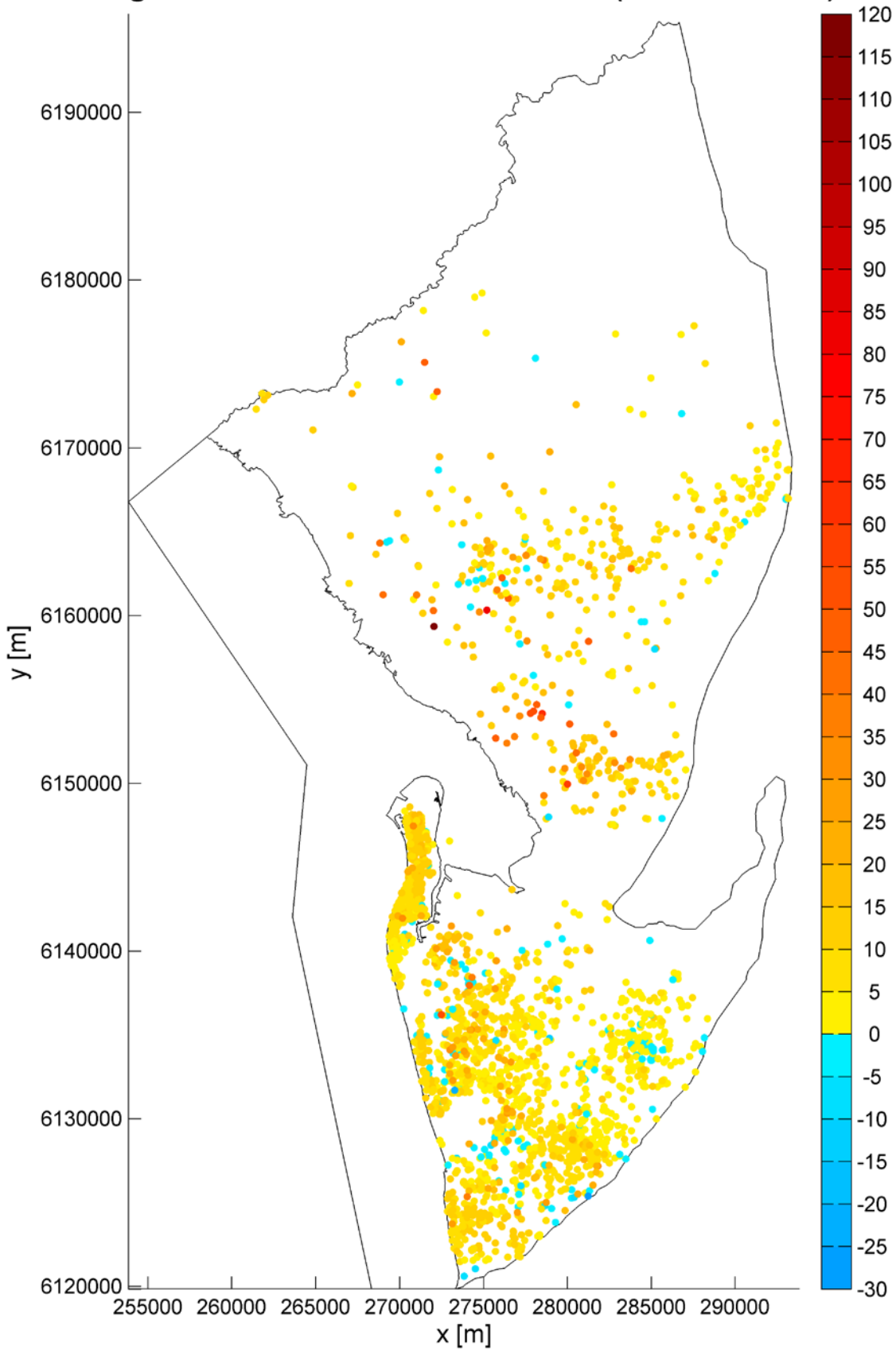
- It is reiterated that the model was not calibrated to the Cl measurements. If the compatibility issue between MODFLOW-NWT and MT3DMS can be resolved, a new calibration could be performed that would include the Cl measurements and the fit would be improved. Namely, the fact that Cl concentrations overall appear overestimated could be an indication of diffuse recharge being too small, as also suggested by the fact that the parameter *RPMUL* reached its lower bound during calibration.
- The spatial correlation (or anti-correlation) between the weighted residuals for Cl concentration and for mean hydraulic head suggests that part of the misfit could be explained by the misfit in heads. Therefore, improving the head fit (by exploring the relevant suggestions above) could have a direct positive impact on the quality of the Cl fit.

The misfit could also be partly due to boundary concentrations being in error. For example, significant uncertainty surrounds the concentration of surface water, which was estimated based on shallow groundwater concentration. Characterising the Cl concentration in rivers could allow adjustment of these values. Also, the concentration of groundwater flowing from the MLR was based on the interpolation of data that are quite sparse along some portions of the boundary.

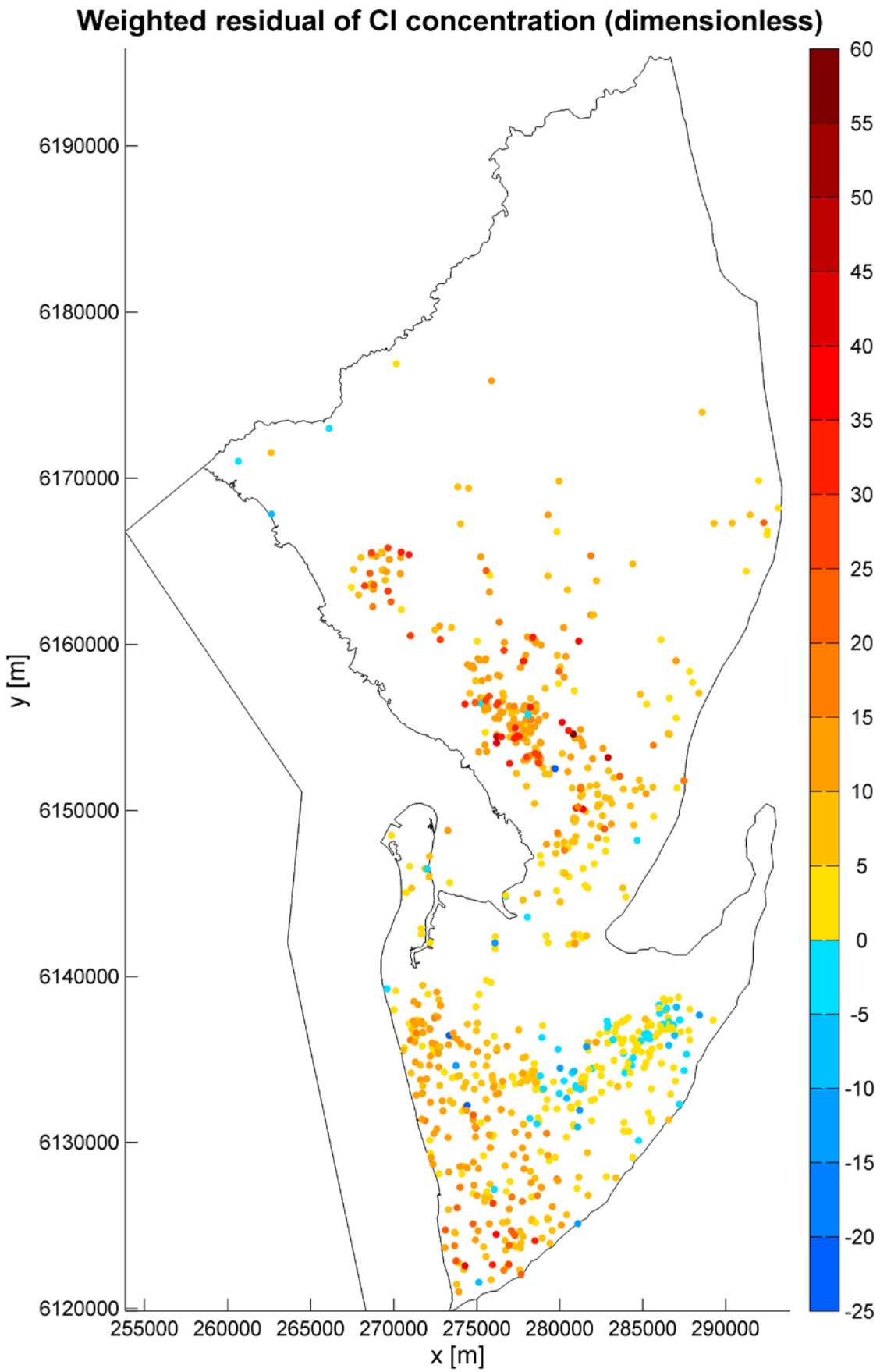


Apx Figure K.53 Simulated Cl concentrations (left) and weighted residuals (right) against measured Cl concentrations for the entire model (top) and for main units individually (below)

Weighted residual of Cl concentration (dimensionless)

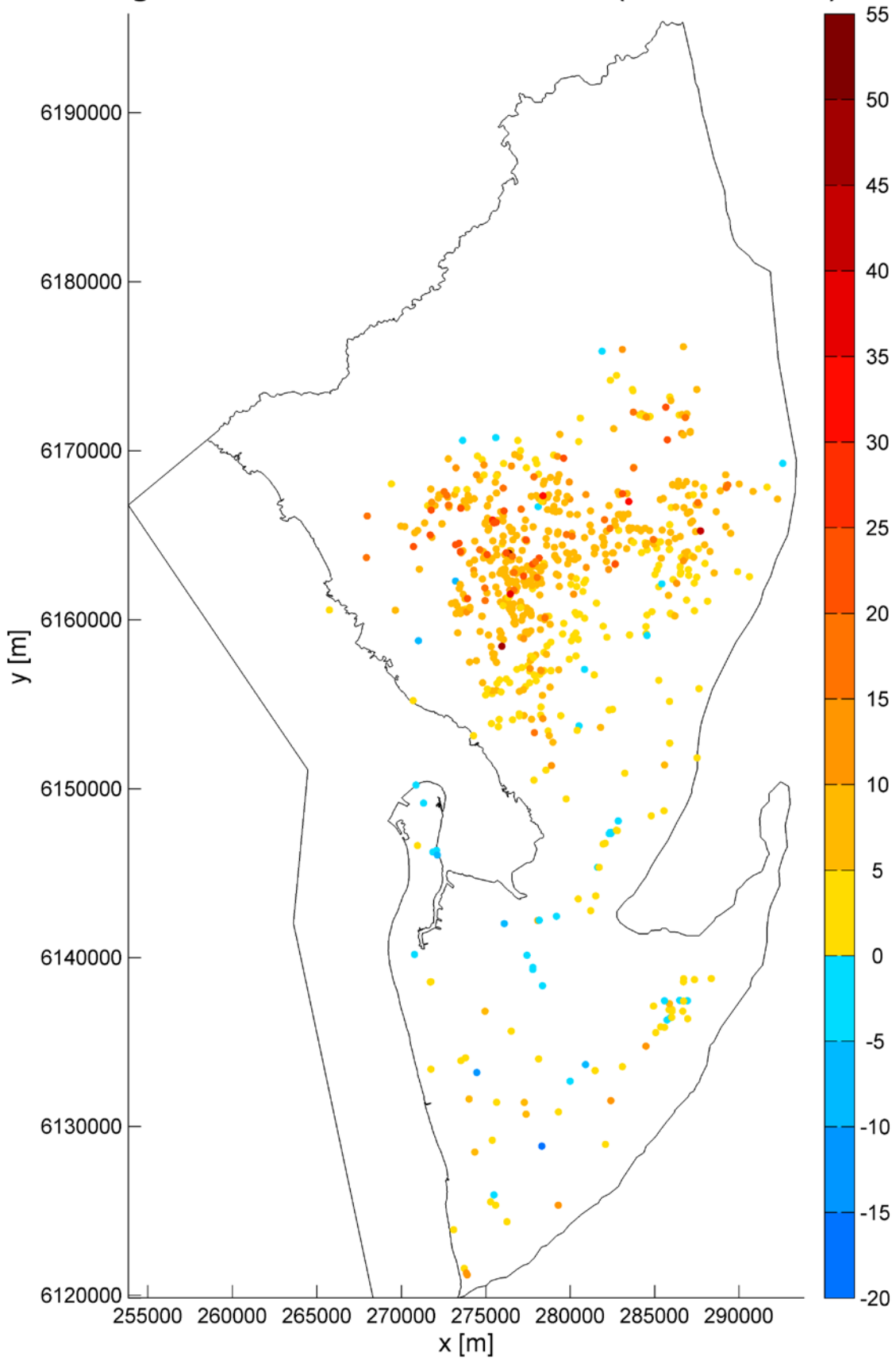


Apx Figure K.54 Spatial distribution of weighted residuals for Cl concentrations in Hindmarsh Clay



Apx Figure K.55 Spatial distribution of weighted residuals for Cl values in T1

Weighted residual of Cl concentration (dimensionless)



Apx Figure K.56 Spatial distribution of weighted residuals for Cl values in T2

Calibration performance (¹⁴C)

Identically as to Cl, ¹⁴C was not included in the calibration dataset due to technical issues. Nevertheless it was possible to run the ¹⁴C transport model with the head-calibrated parameters and preferred values for non-calibrated parameters (effective porosity and dispersivity). The outputs of this run were compared to the measurements, as described below.

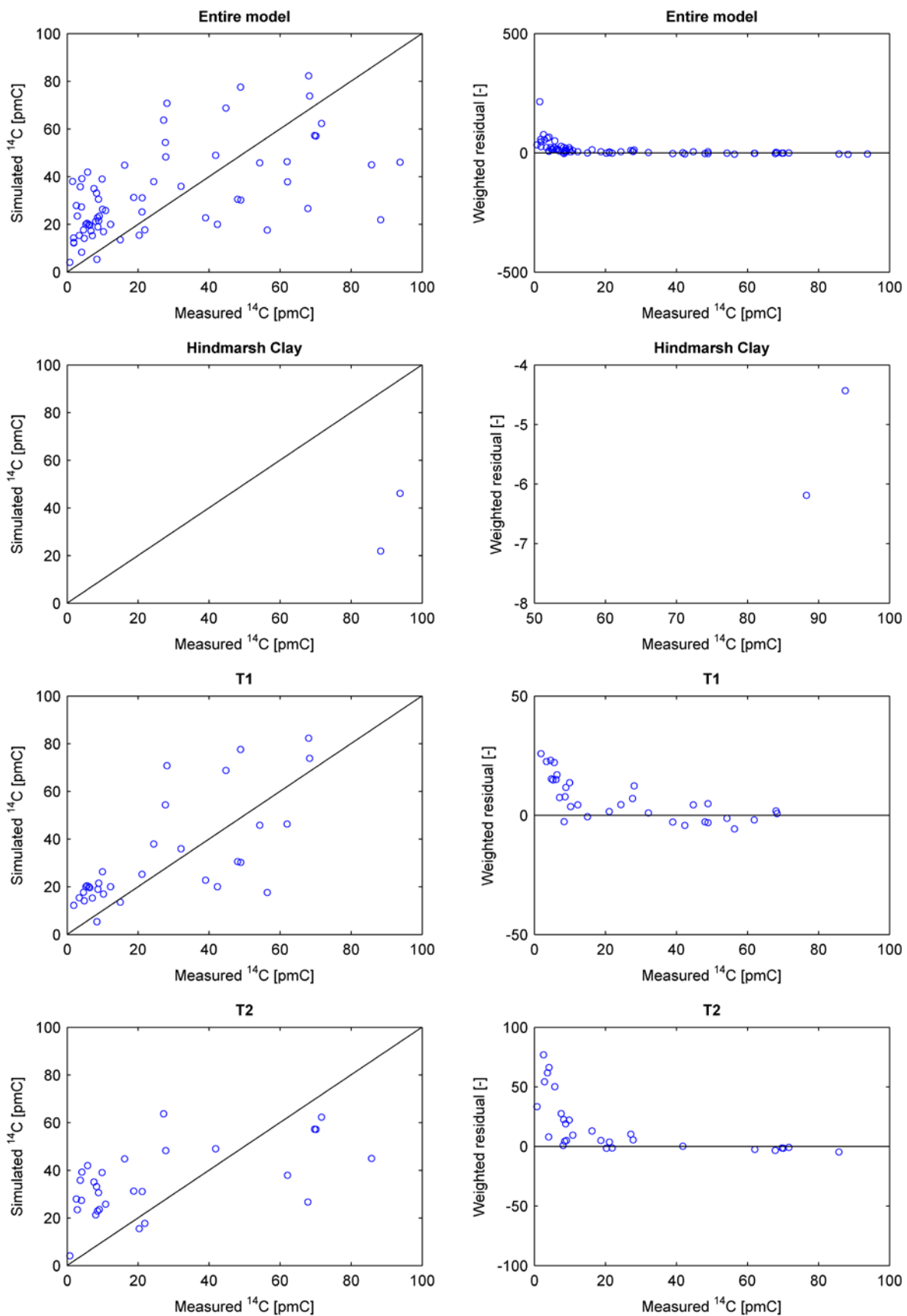
The simulated-versus-observed plots reveal significant scattering (Apx Figure K.57). Some correlation can be seen between measured and simulated ¹⁴C activities and $R = 0.57$ (Apx Table K.13), but the low values are generally overestimated. The results are significantly biased towards an overall overestimation (MWR = 15.07), despite the only two observations available in Hindmarsh Clay are largely underestimated.

The number of observations in Hindmarsh Clay is too small to conclude anything regarding the spatial distribution of residuals (Apx Figure K.57). In the Tertiary aquifers, the spatial distribution of residuals clearly shows that ¹⁴C activities are overestimated towards the west, especially in the T1 aquifer (Apx Figure K.59 and Apx Figure K.60). Note that the colour scales are different between figures to facilitate observation of any spatial bias in each case.

While the failure of the model to reproduce ¹⁴C measurements might also be regarded as a fatal shortcoming, the following has to be considered:

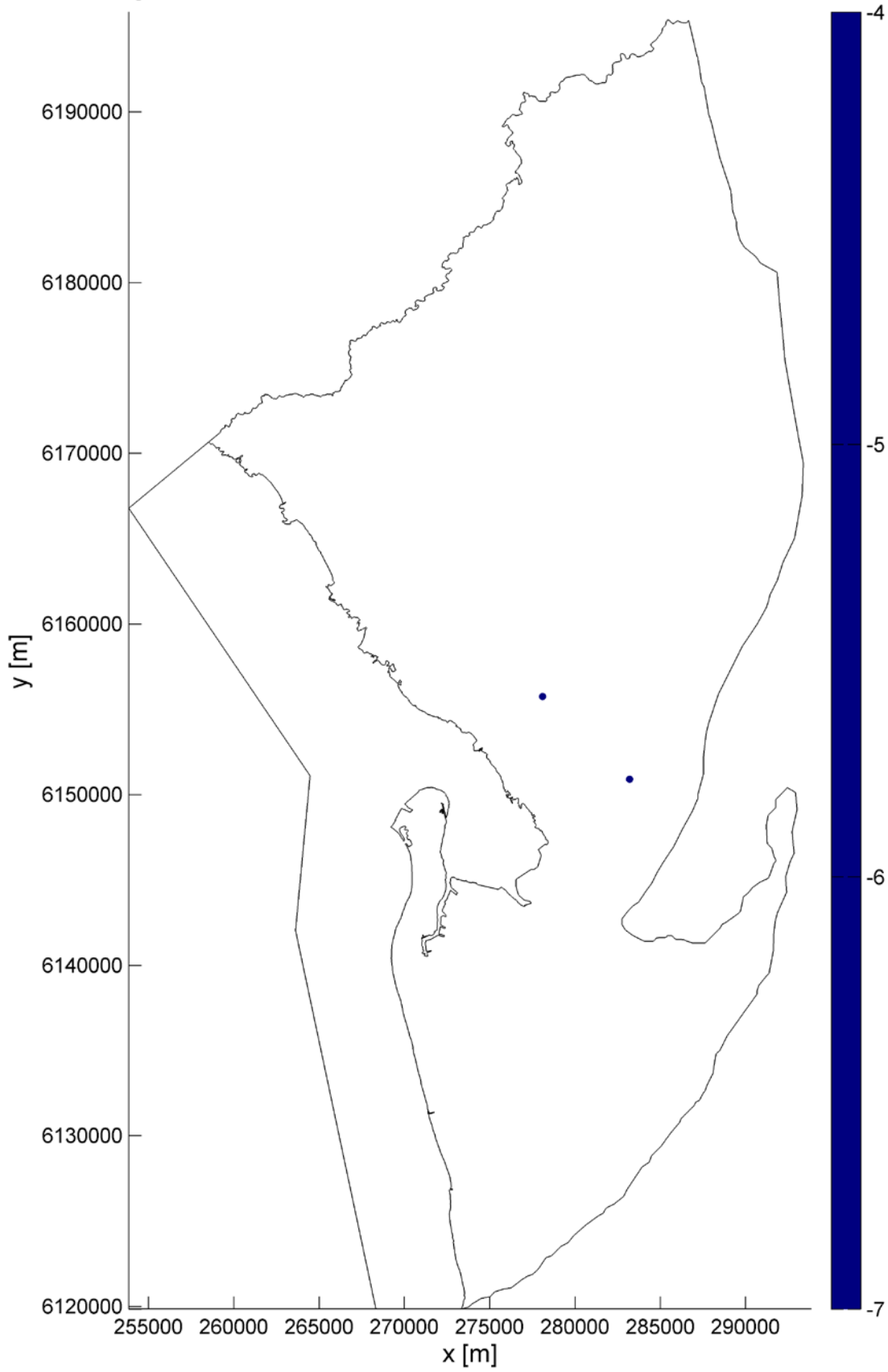
- It is reiterated that the model was not calibrated to the ¹⁴C measurements. If the compatibility issue between MODFLOW-NWT and MT3DMS can be resolved, a new calibration could be performed that would include the ¹⁴C measurements and the fit would be improved. Namely, the fact that ¹⁴C activities are overall overestimated, especially towards the west, could probably be easily corrected by adjusting porosity parameters. Furthermore, the fact that ¹⁴C activities are underestimated in Hindmarsh Clay again suggests that diffuse recharge is too small, therefore corroborating the above findings.

The misfit could also be partly due to the lack of spatial (horizontal) distribution of the ¹⁴C activities along the eastern boundary.

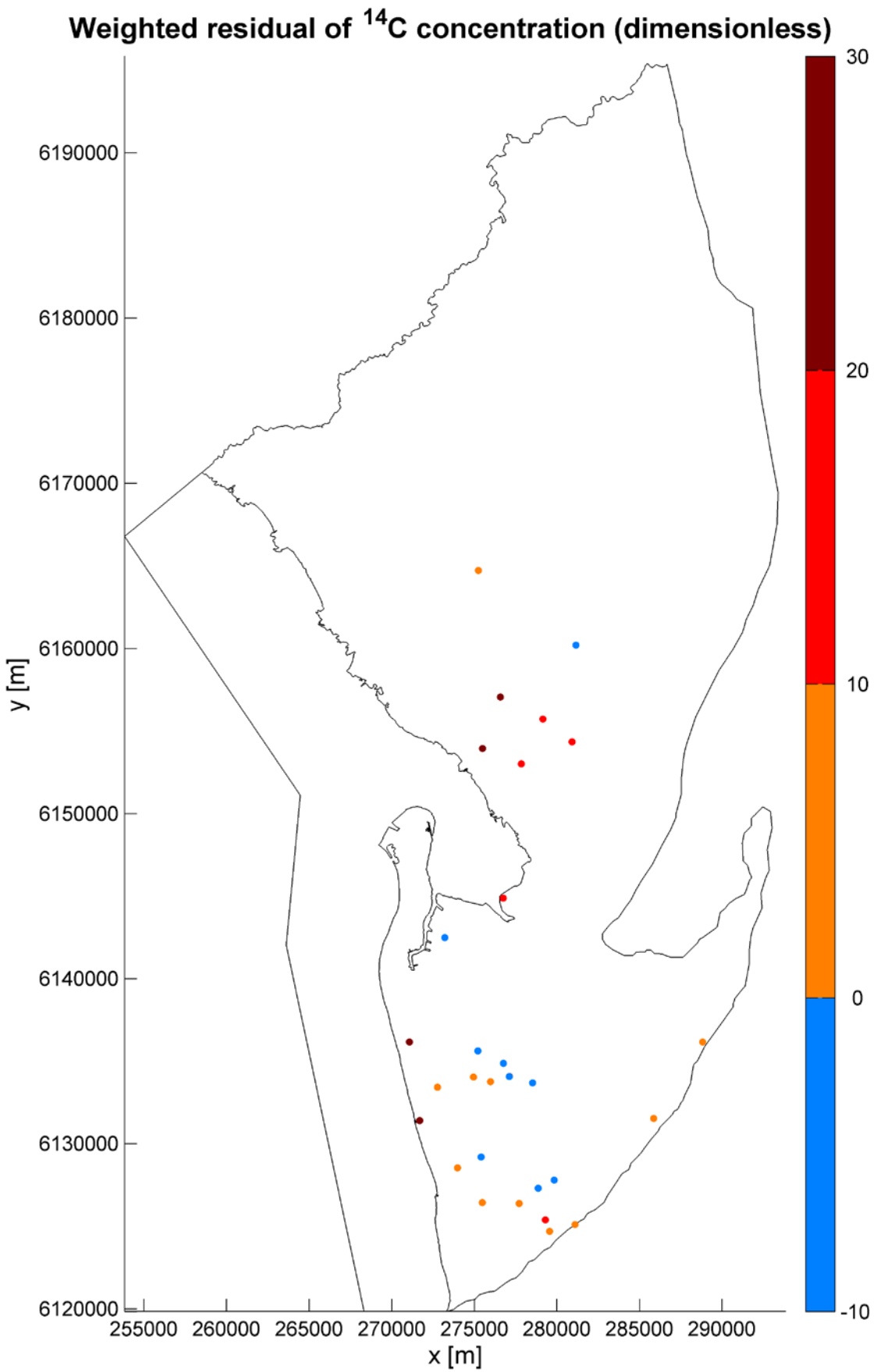


Apx Figure K.57 Simulated ¹⁴C activities (left) and weighted residuals (right) against measured ¹⁴C activities for the entire model (top) and for main units individually (below)

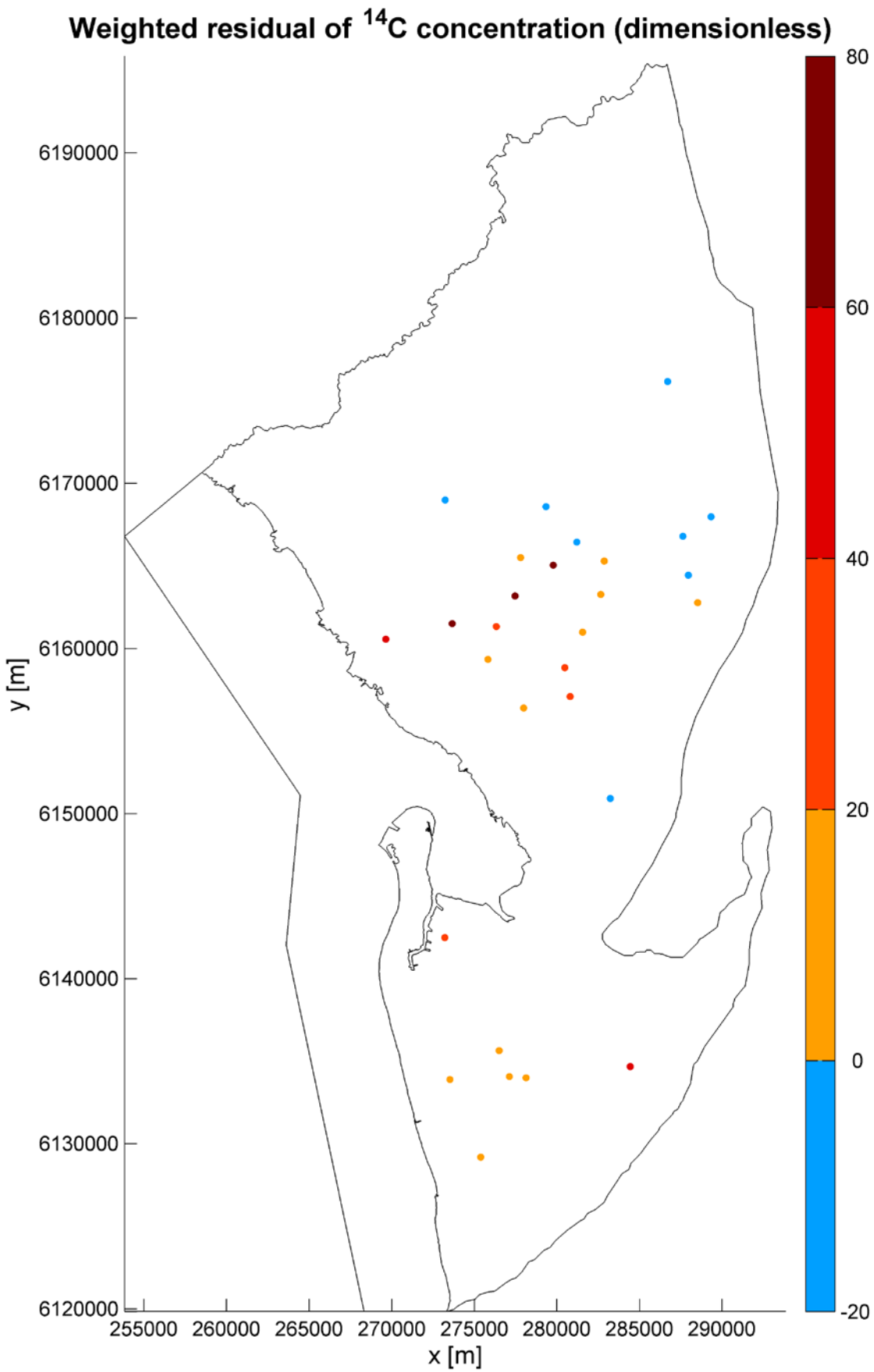
Weighted residual of ^{14}C concentration (dimensionless)



Apx Figure K.58 Spatial distribution of weighted residuals for ^{14}C values in Hindmarsh Clay



Apx Figure K.59 Spatial distribution of weighted residuals for ^{14}C values in T1



Apx Figure K.60 Spatial distribution of weighted residuals for ^{14}C values in T2

K.4.4 WATER BALANCE AND ITS EVOLUTION

This section presents the results of the historical steady-state, pre-development transient and development transient models using the calibrated parameters. Water balances and spatial maps of heads and fluxes are provided for each of the models. Only water balance components that had a value greater than 10^{-2} GL yr⁻¹ are shown. For all transient results presented, only water balance components that had 3% or greater contribution to the maximum component value were deemed significant, with others not shown.

Steady-state water balance

In the steady-state historical model, the simulated behaviour of the system can be inferred from the flux matrix (Apx Table K.14), which shows fluxes from the units listed in the leftmost column to other units listed in the column headings along the first row. So, for example, the flow from Hindmarsh Clay to Undifferentiated sand is 0.01 GL yr⁻¹. Presenting fluxes in this manner elucidates the major connections between units in the model. It is clear from this matrix that most of the recharge into the system is from the streams (7.06 GL yr⁻¹), followed by the MLR (5.34 GL yr⁻¹) and finally a small contribution from areal recharge (0.48 GL yr⁻¹). However, slightly more water is flowing out to the streams (7.23 GL yr⁻¹), resulting in a net loss of groundwater to streams (0.17 GL yr⁻¹). The T1 aquifer receives water from the Hindmarsh Clay (3.47 GL yr⁻¹). Of this flow, a maximum of 0.33 GL yr⁻¹ originates from the MLR via lateral flow into the Quaternary sediments, i.e. at least 3.14 GL yr⁻¹ (the remaining part) originates from infiltration in the Plains (mostly from river leakage as diffuse recharge is about 10 times less than river leakage). The MLR provides lateral recharge to all zones but most prevalently into the Bedrock in the Golden Grove Embayment (3.56 GL yr⁻¹), followed by the T1 aquifer (0.57 GL yr⁻¹), the Hindmarsh Clay (0.33 GL yr⁻¹) and the T2 aquifer (0.31 GL yr⁻¹). After recharge occurs from the streams and MLR, the water flows towards the coast and upward. In the Golden Grove Embayment, most of the water from the Bedrock flows upward into UTSand (2.9 GL yr⁻¹), the T3T4 aquifer (1.53 GL yr⁻¹) and the T1 aquifer (0.74 GL yr⁻¹). There is a large flux from the T2 aquifer to the T1 aquifer through the Munno Para Clay (2.90 GL yr⁻¹) but also a significant component of direct flow from the T1 aquifer to the T2 aquifer (1.41 GL yr⁻¹). The T1 aquifer then discharges into the Hindmarsh Clay (6.81 GL yr⁻¹) and the outflow from the Hindmarsh Clay to the sea is 5.70 GL yr⁻¹.

Comparison with previous water balance estimates is provided in the next section on the basis the pre-development transient model, which should be more realistic as it includes dynamic processes.

Apx Table K.14 Flux matrix (GL yr⁻¹) for water balance components in the steady-state historical flow model. Values below 1×10^{-2} are not shown. Colours are indicative of the magnitude, with blue to red colours highlighting small to large fluxes respectively as indicated in the lower table

	Hclay	UTSand	T1	MPClay	T2	BPFmnU	T3T4U	BedrockU	BPFmnD	T3T4D	BedrockD	Pfault	MLR	Streams	Coast	Recharge
Hclay		0.01	3.47											2.75	5.70	
UTSand			0.14					1.47						4.48		
T1	6.81	0.16		0.23	2.67			0.18				0.01				
MPClay			2.92		0.24											
T2		0.22	1.41	2.91		0.04				0.02						
BPFmnU					1.00		0.06	0.03								
T3T4U			0.76			0.67		0.16								
BedrockU		2.90	0.74			0.19	1.53									
BPFmnD					0.33						0.02					
T3T4D			0.01							0.15						
BedrockD			0.02							0.01	0.02					
Pfault			0.01		0.06											
MLR	0.33	0.04	0.57	0.01	0.31	0.17	0.01	3.56	0.16	0.11	0.05	0.02				
Streams	4.31	2.75														
Coast																
Recharge	0.46	0.02														

Lower	Upper
0.001	0.1
0.1	2
2	4
4	6
6	>6

Apx Figure K.61 shows the spatial pattern of hydraulic head minus topography in the first layer, which for the yellow to red areas shows where conditions were artesian. This highlights areas that were likely wetlands and marshes prior to any development. Apx Figure K.62 and Apx Figure K.63 also show the spatial

pattern of hydraulic head minus topography in the T1 and T2 aquifers which highlights where artesian conditions (yellow to red colours) would have existed prior to significant development. Apx Figure K.64, Apx Figure K.65 and Apx Figure K.66 show the head contours in the Hindmarsh Clay and Undifferentiated sand and the T1 and T2 aquifers, with the heads highest at the eastern boundary and gradually decreasing towards the coast, as expected.

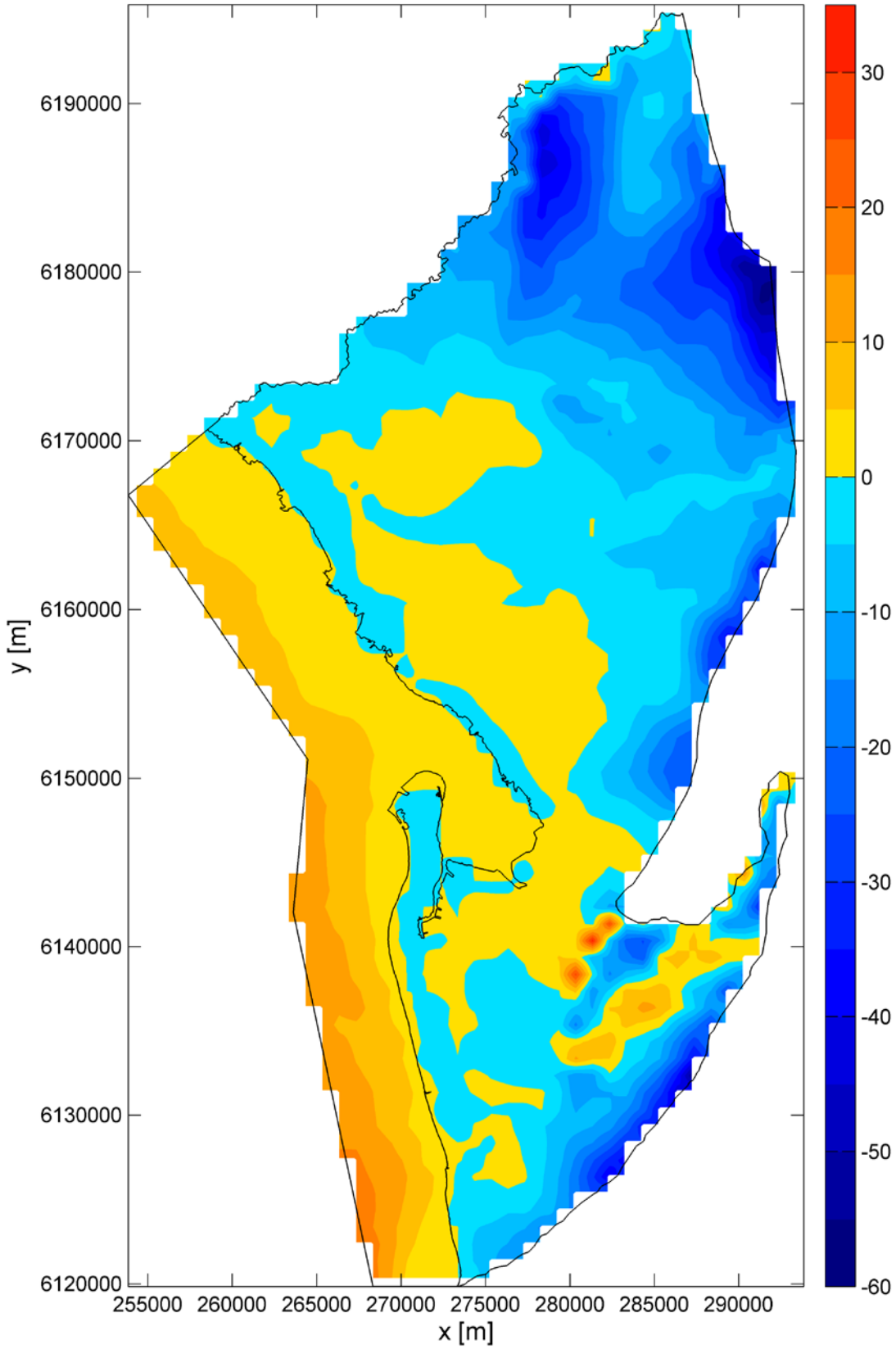
The spatial pattern for the vertical flux through the top and bottom of the T1 aquifer is shown in Figures Apx Figure K.67 and Apx Figure K.68, respectively. In these figures, positive values indicate upward flow and negative values indicate downward flows. It can be seen that the T1 aquifer receives significant water from above near the MLR boundary. Upward flow out of T1 is evident towards the coast and following the line of the Torrens River. The patterns of flow through the bottom of the aquifer are not very different than through the top, although more water is seen to flow down to the T2 aquifer near the southern extent of the eastern boundary.

The spatial pattern for the vertical flux through the top and bottom of the T2 aquifer is shown in Apx Figure K.69 and Apx Figure K.70, respectively. The patterns of the flux through the top of the T2 aquifer follow the ones of the flux through the bottom of the T1 aquifer. The small upward flow across much of the top of the T2 aquifer passes into the Munno Para Clay which subsequently feeds into the T1 aquifer. Flow through the bottom of the T2 aquifer shows all upward flow and reveals that the largest fluxes are concentrated along the eastern boundary and on the upthrown side of Para Fault.

Apx Figure K.71 shows river leakage rates in the steady-state pre-development model. The leakage is generally positive towards the east with large leakage rates found along the boundary. The Torrens River is the main exception with groundwater discharges at a significant rate into it east of the City of Adelaide and up to the eastern boundary.

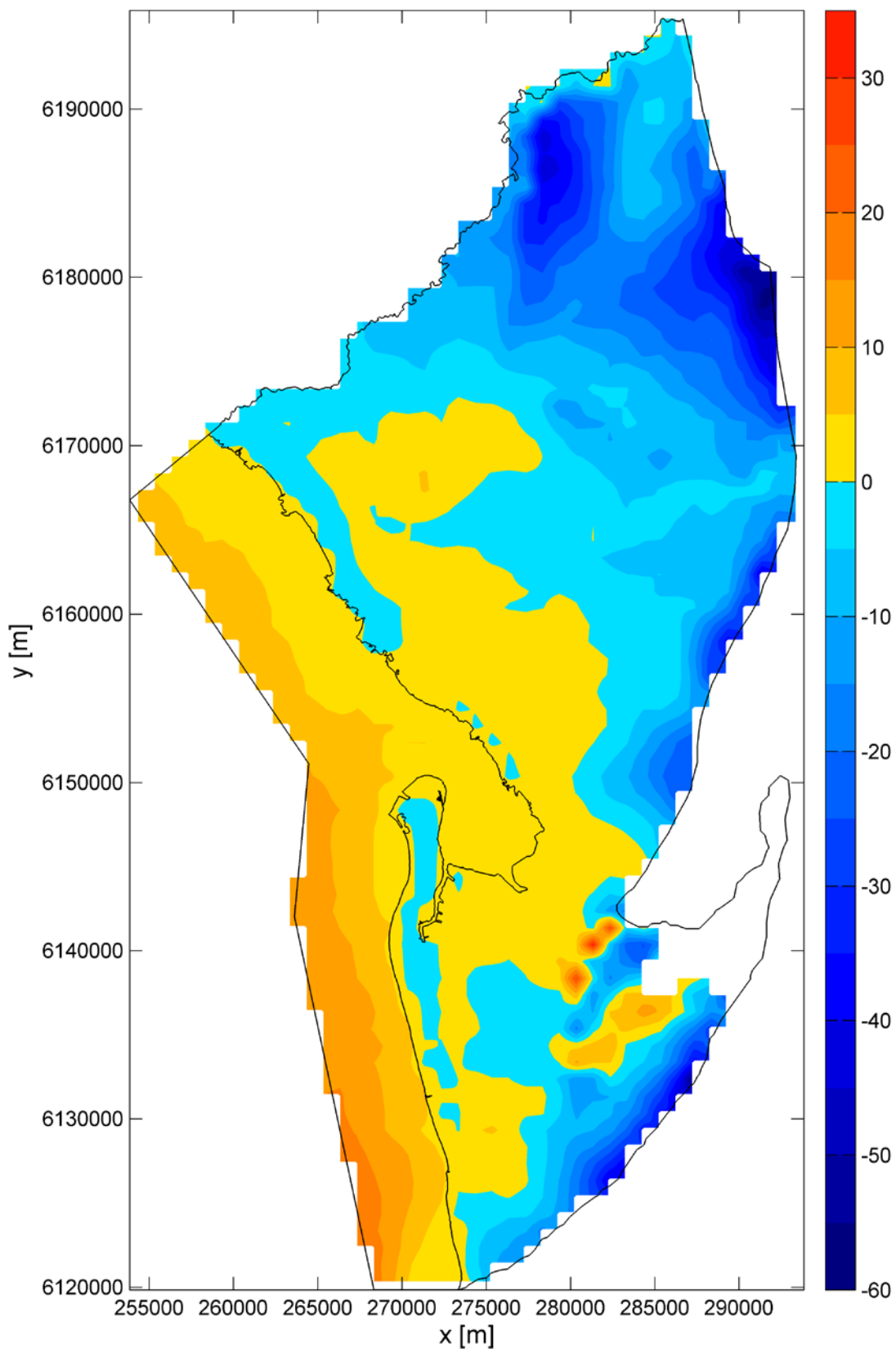
Overall the system in steady state can be summarised as water being sourced mainly from the streams and the MLR especially along the Eden-Burnside Fault and being discharged to streams and the coast. Flow is mainly downward down to the T2 aquifer near the eastern boundary, and upwards elsewhere. Upward flow from the Bedrock in the Golden Grove Embayment is quite high.

Hydraulic head minus topography in first layer [m]



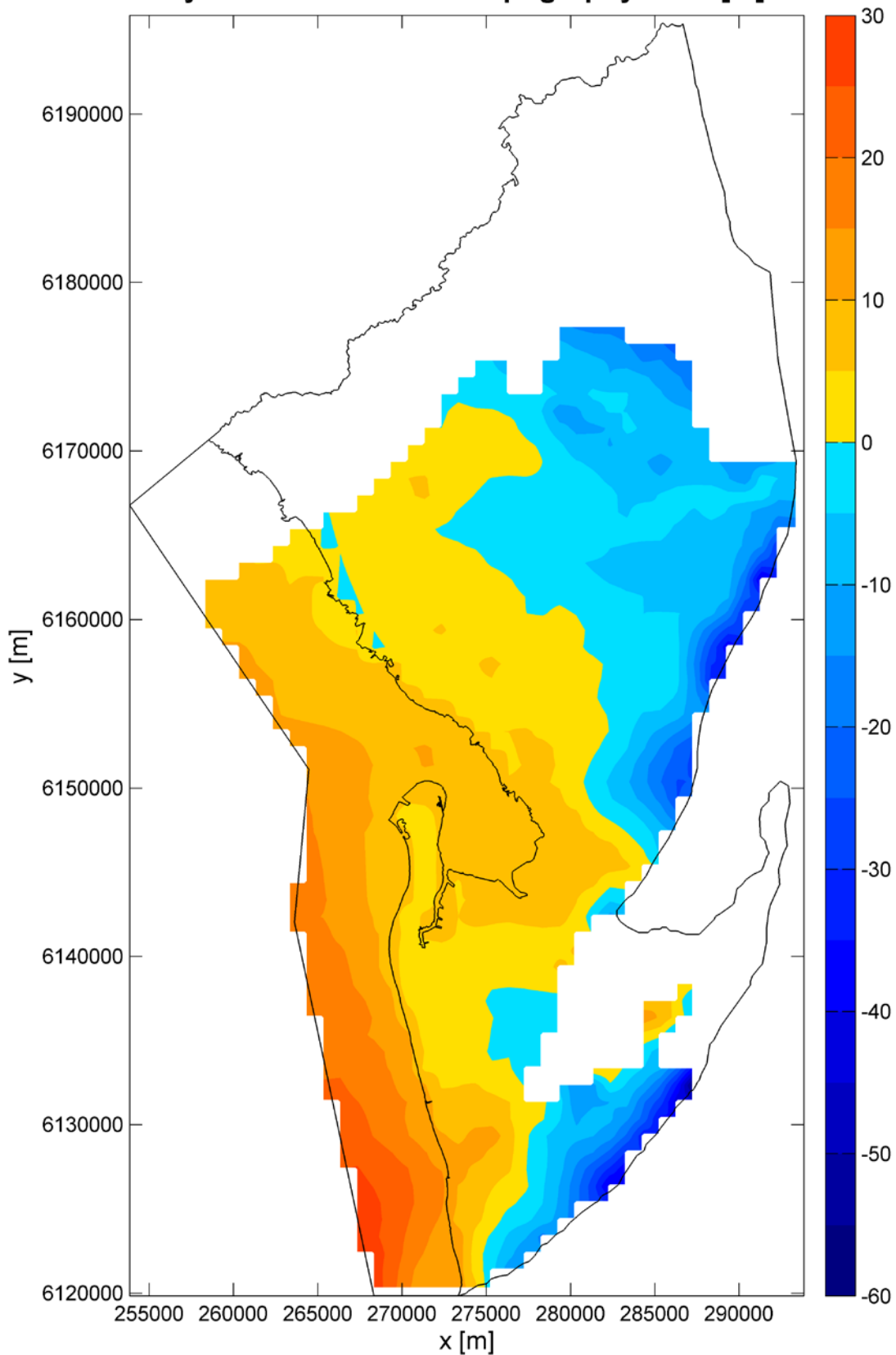
Apx Figure K.61 Hydraulic head minus topography in the first later for the steady-state historical flow model

Hydraulic head minus topography in T1 [m]



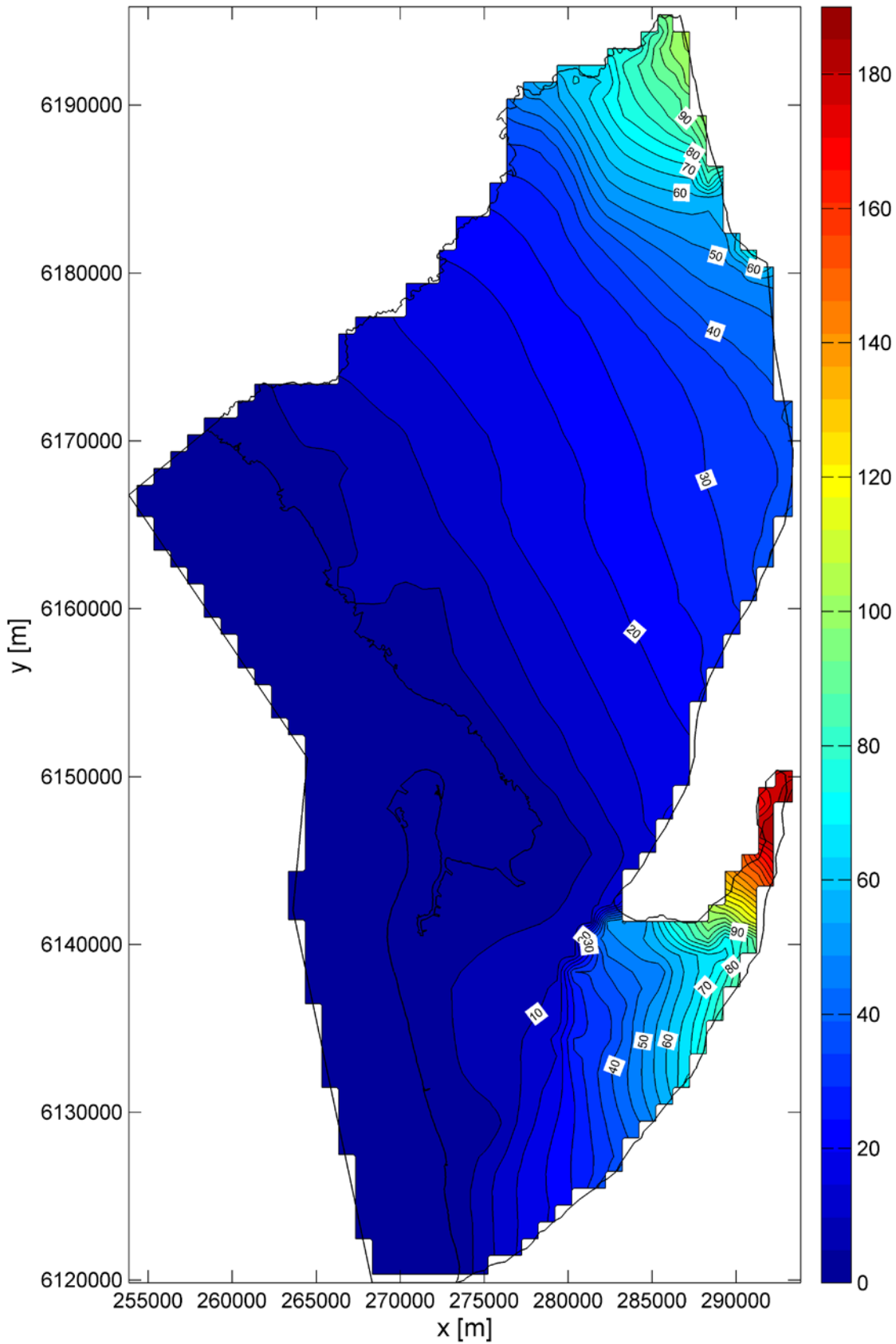
Apx Figure K.62 Hydraulic head minus topography in the T1 aquifer for the steady-state historical flow model

Hydraulic head minus topography in T2 [m]



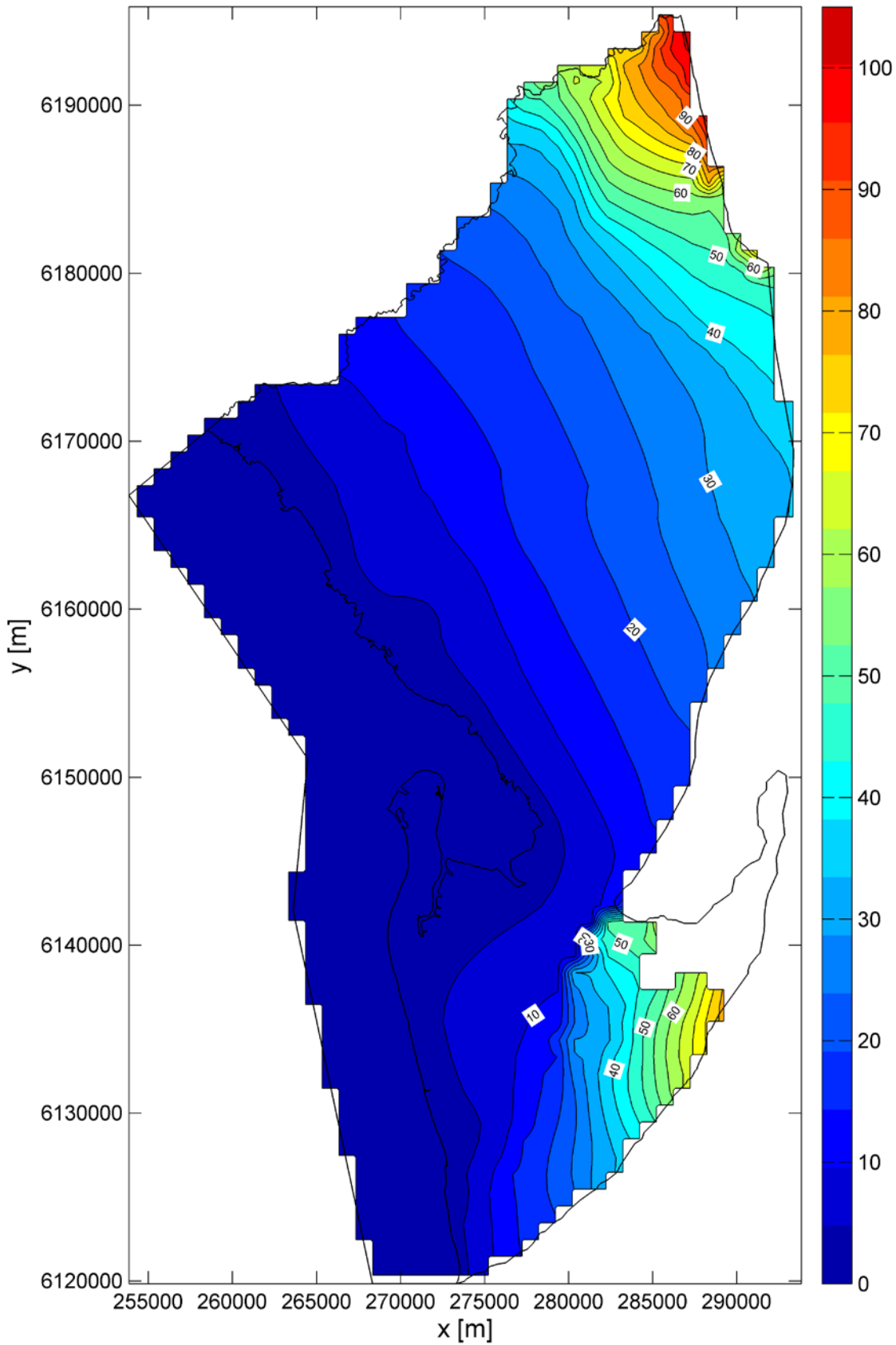
Apx Figure K.63 Hydraulic head minus topography in the T2 aquifer for the steady-state historical flow model

Hydraulic head contours in first layer [m AHD]



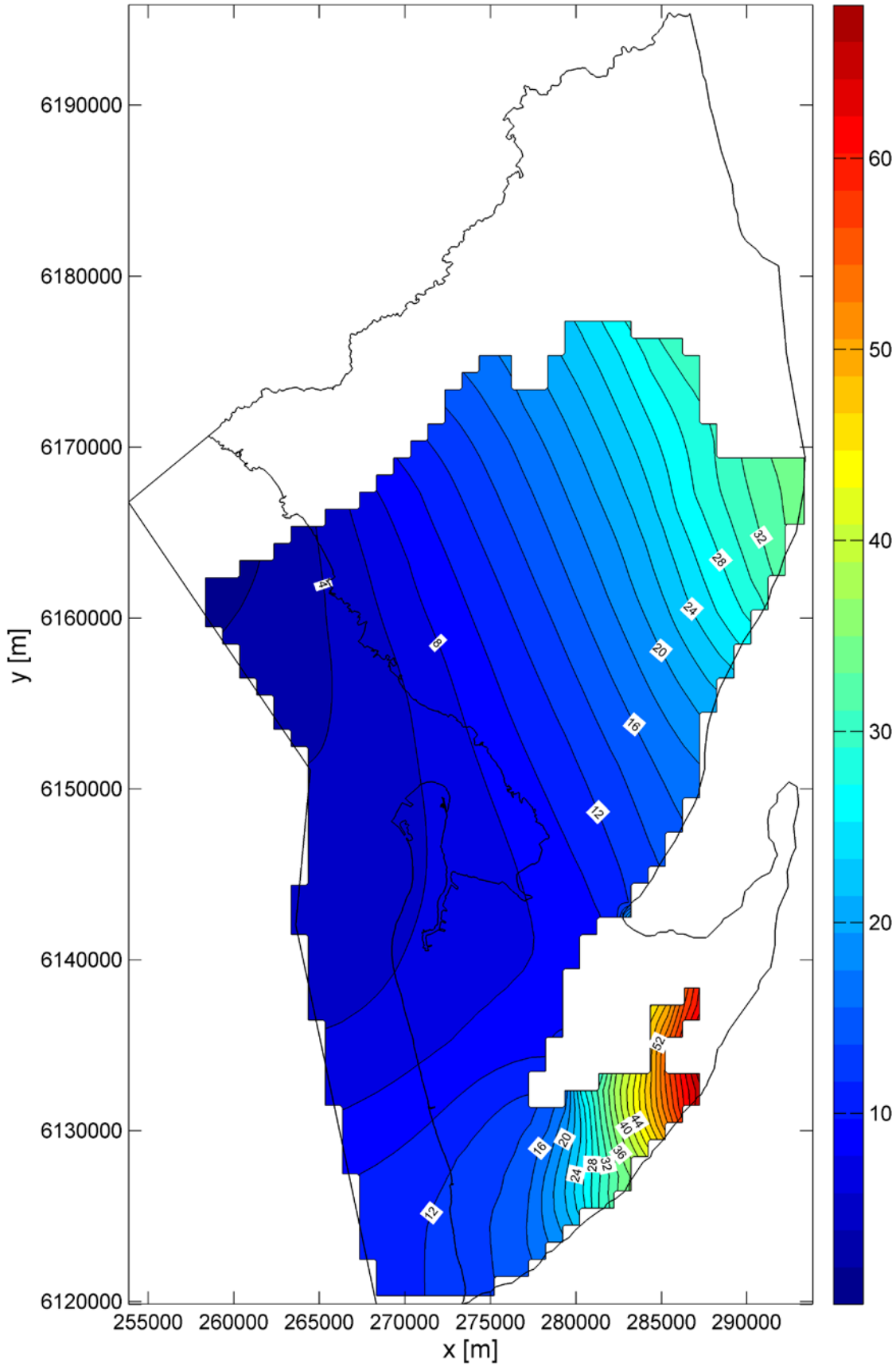
Apx Figure K.64 Head contours in the first layer for the steady-state historical flow model

Hydraulic head contours in T1 [m AHD]

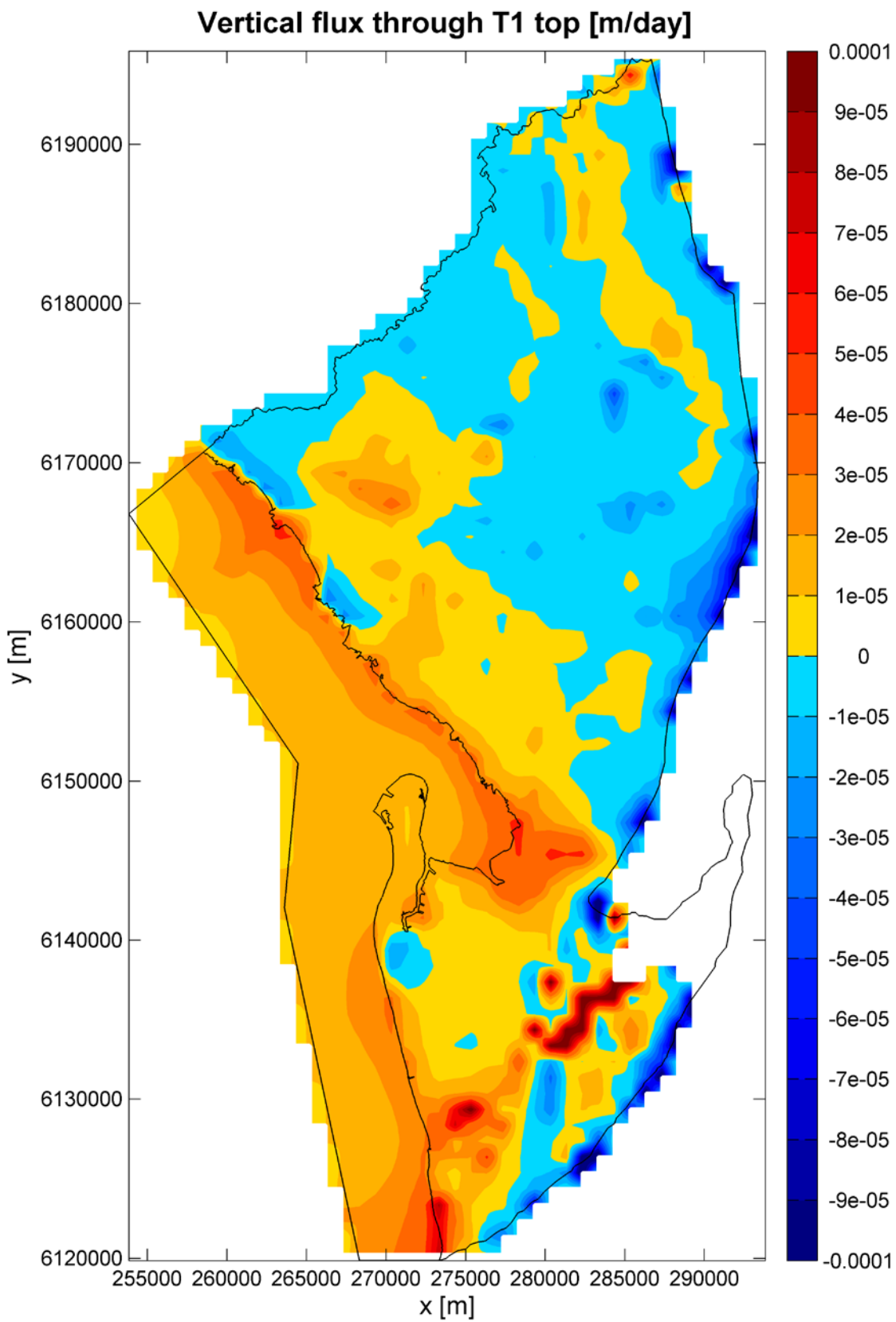


Apx Figure K.65 Head contours in the T1 aquifer for the steady-state historical flow model

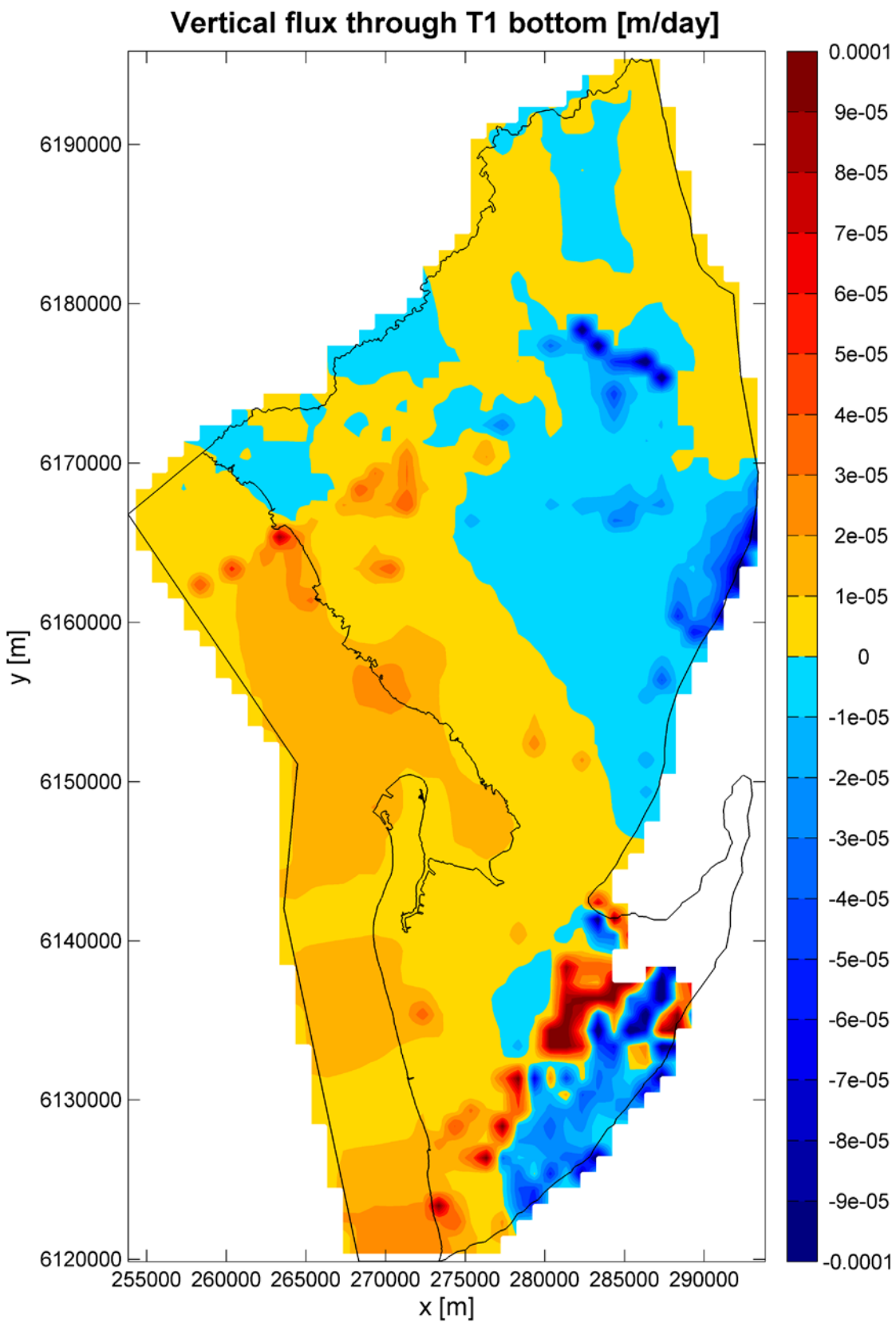
Hydraulic head contours in T2 [m AHD]



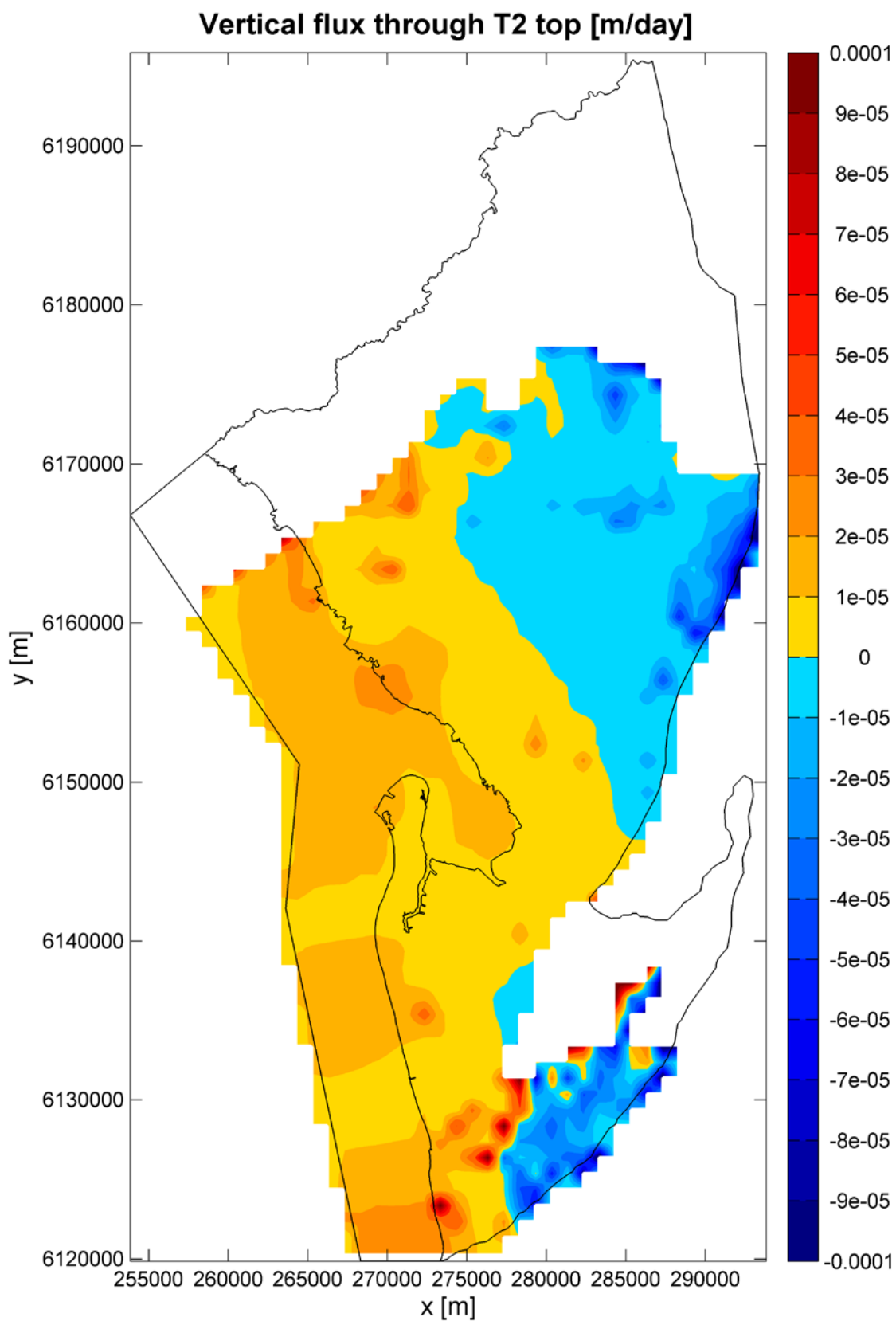
Apx Figure K.66 Head contours in the T2 aquifer for the steady-state historical flow model



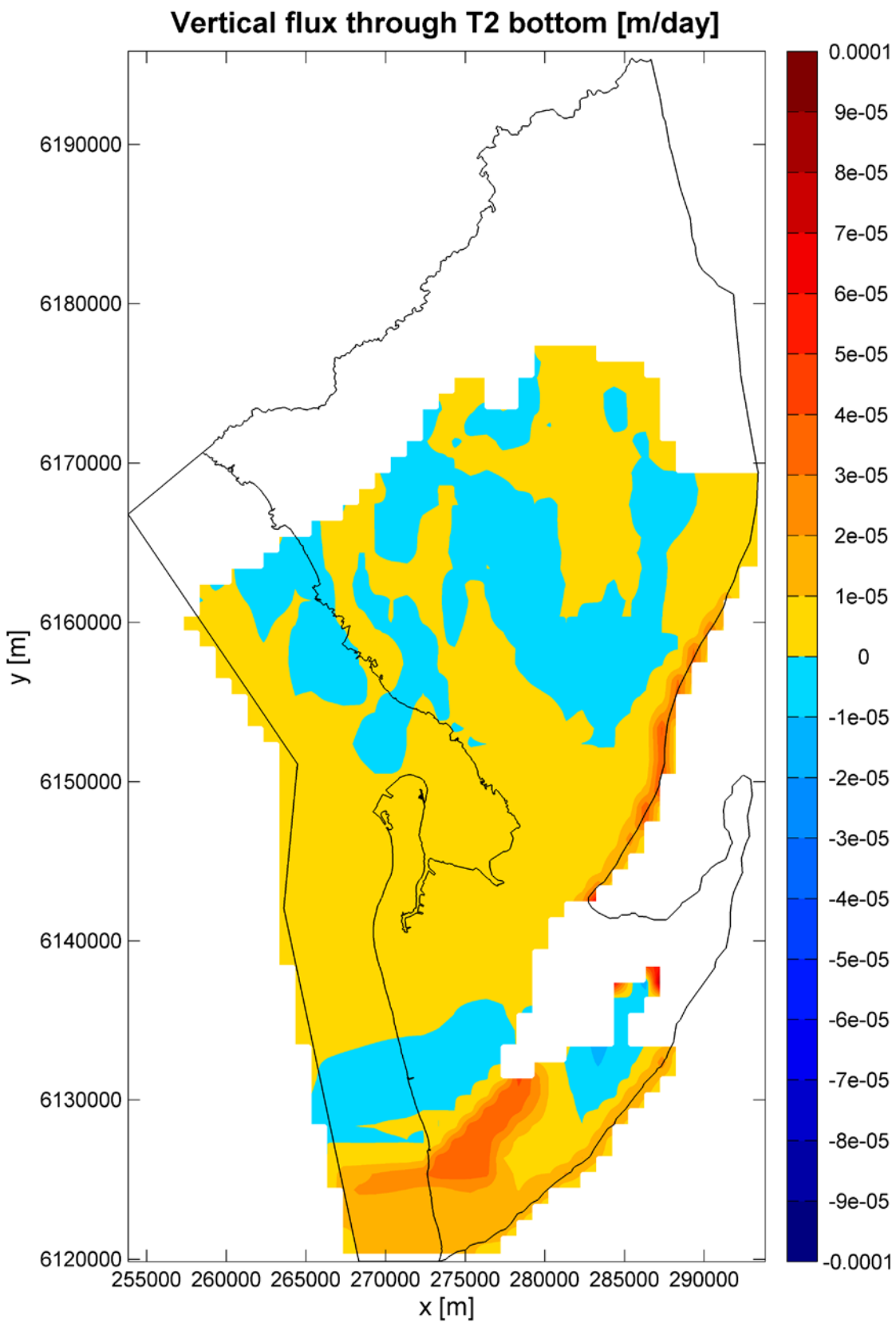
Apx Figure K.67 Flux across the top of the T1 aquifer for the steady-state historical flow model



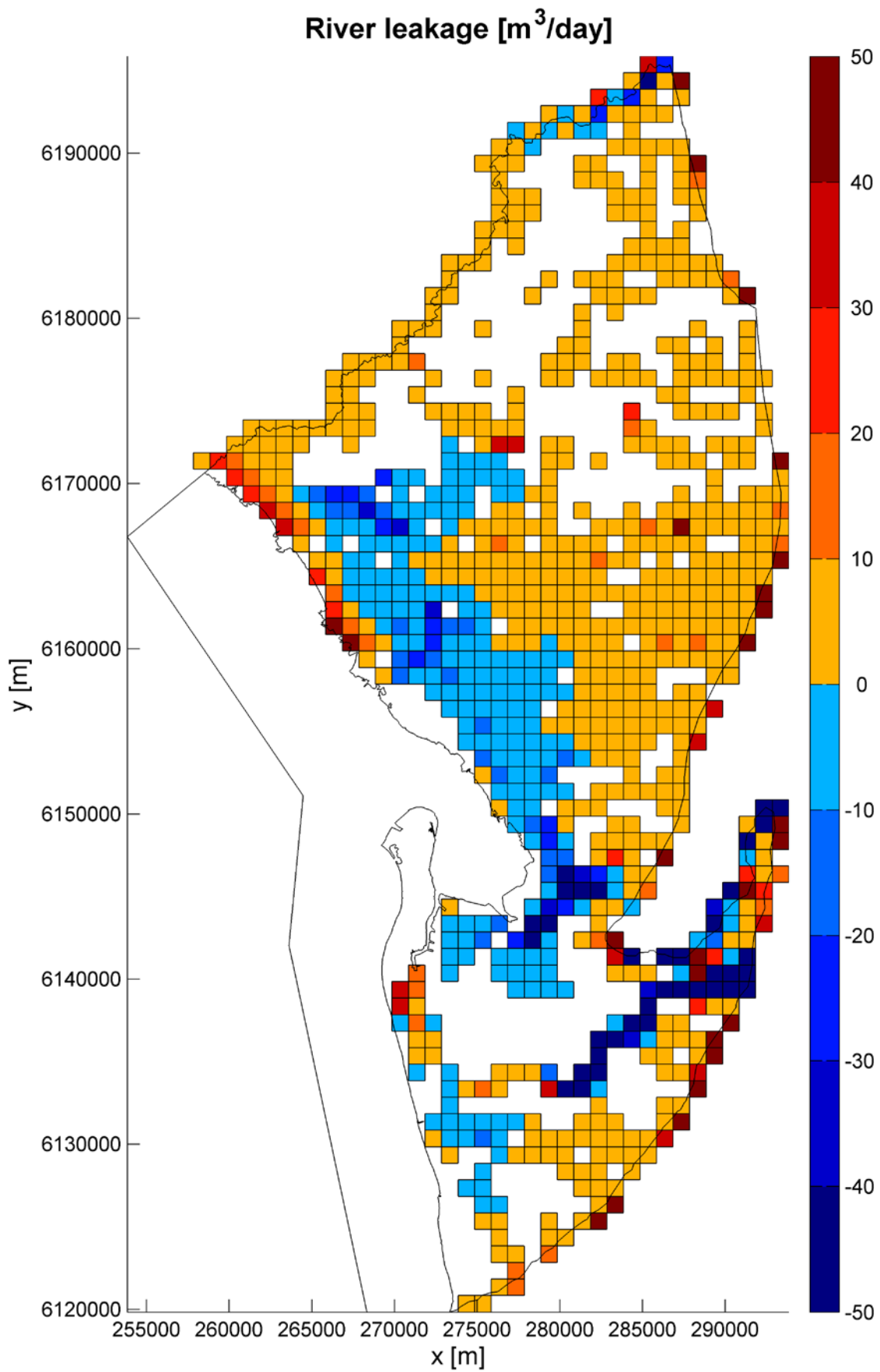
Apx Figure K.68 Flux across the bottom of the T1 aquifer for the steady-state historical flow model



Apx Figure K.69 Flux across the top of the T2 aquifer for the steady-state historical flow model



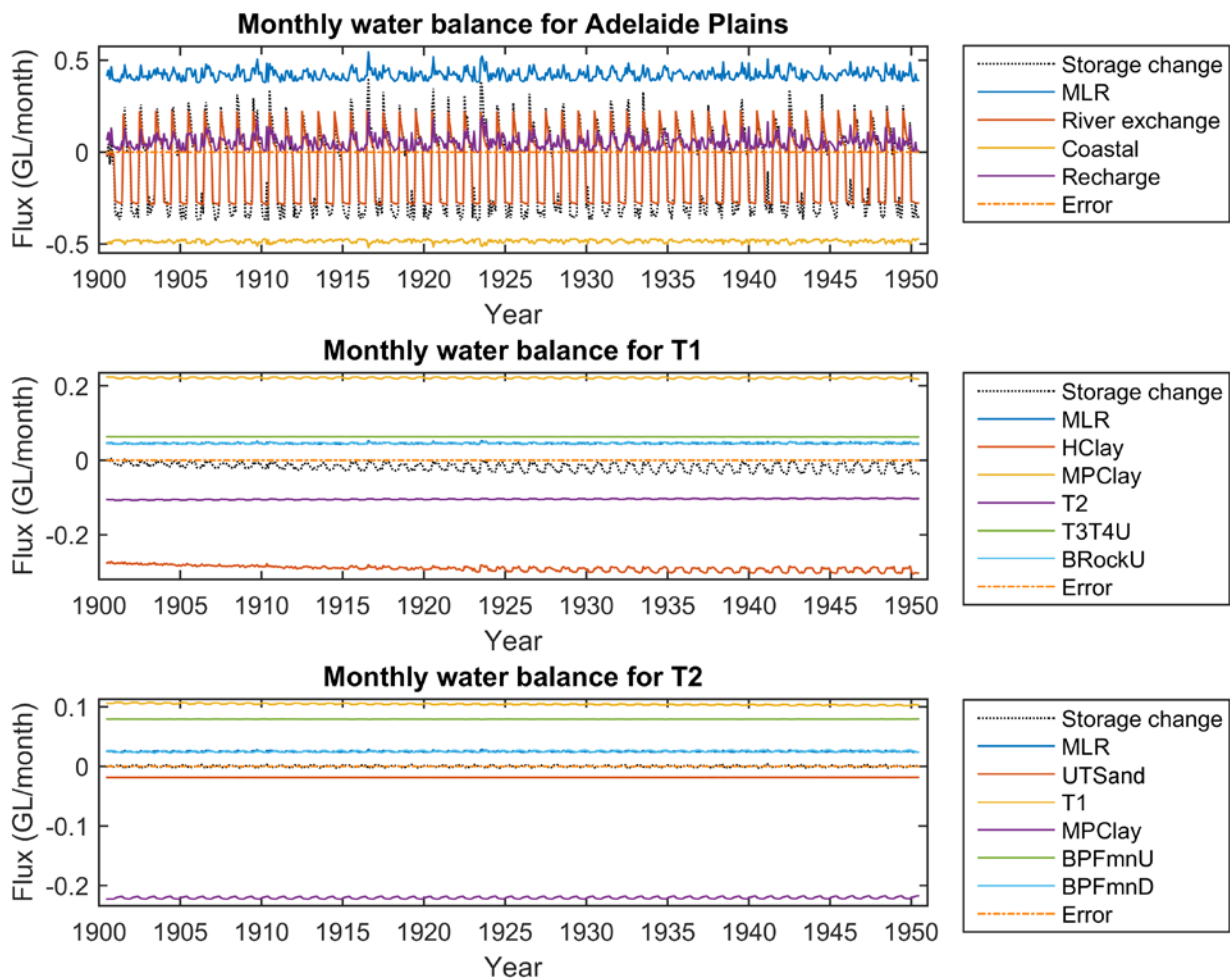
Apx Figure K.70 Flux across the bottom of the T2 aquifer for the steady-state historical flow model



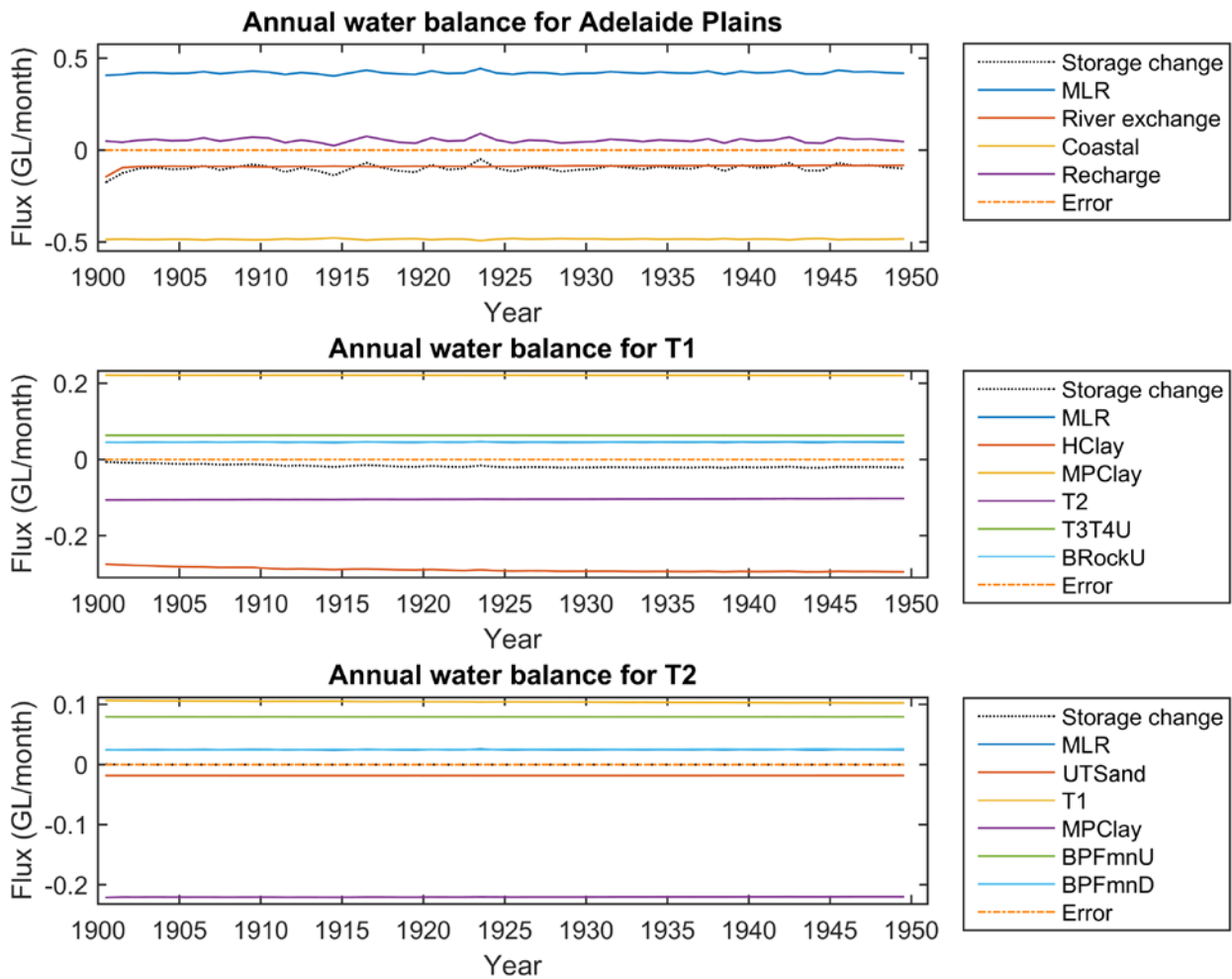
Apx Figure K.71 River leakage in the steady-state historical flow model

Pre-development transient water balance (1900–1950)

The pre-development transient model simulates the period before large scale pumping commenced in the Adelaide Plains. The model does not include pumping. The monthly water balance for the entire Adelaide Plains and for the T1 and T2 aquifers is shown below (Apx Figure K.72). Only components that are more than 3% of the maximum absolute flux from all of the components are shown. The line representing the water balance error (i.e. sum of inflows and outflows) is also included as a visual indicator to ensure that the model is meeting convergence criteria as expected. The magnitude of fluxes is consistent with the steady-state model as expected with seasonal dynamics now evident. In particular, the net river exchange is seen to fluctuate more than any other water balance component, inducing large fluctuations of the rate of storage change from wet to dry periods. There is a clear seasonal variability in the T1 aquifer due to the seasonally changing surface water-groundwater interaction, although of smaller magnitude than for the entire model. It can be seen mostly in the rate of storage change which is correlated to the exchange with the Hindmarsh Clay unit. The rate of change in storage is negative over most of the period (see explanation below). Seasonal fluctuations in the T2 aquifer are small compared to the Hindmarsh Clay and T1 aquifer. Annual water balances are also presented in Apx Figure K.73 to highlight any trends outside of the strong monthly dynamics.

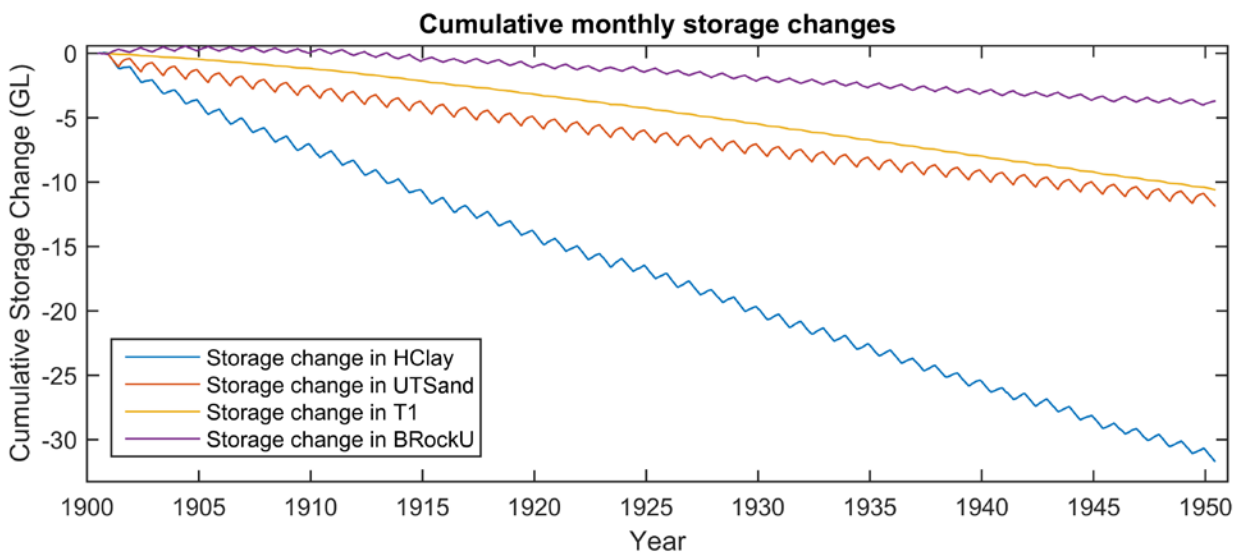


Apx Figure K.72 Monthly water balance components for the whole model domain (top), T1 aquifer (middle) and T2 aquifer (bottom), for the pre-development model (1900–1950)



Apx Figure K.73 Annual water balance components for the whole model domain (top), T1 aquifer (middle) and T2 aquifer (bottom), for the pre-development model (1900–1950)

The cumulative changes in storage are shown in Apx Figure K.74 for zones which had a change of at least 2 % of the maximum change in storage (which was Hindmarsh Clay). The T1 aquifer can be seen to have decreased its storage by around 10 GL over the 50 year period, while the Hindmarsh Clay shows a storage decrease of just over 30 GL over the 50 year period (i.e. around 0.6 GL yr⁻¹). These storage declines are caused by the transition from the initial condition (which is based on a steady-state featuring winter river network, implying that groundwater gains more water than on average) towards a naturally fluctuating transient state (i.e. alternating summer and winter river network). A dynamic equilibrium is not reached at the end of the pre-development period, thus inducing a potential bias in the results.



Apx Figure K.74 Cumulative changes in storage for the Hindmarsh Clay, Undifferentiated sand, T1 aquifer, and Bedrock upstream, for the pre-development model (1900–1950).

The positive fluxes in the model after the 50 year pre-development period is shown in Apx Table K.15 for a decadal average (1939–1949). The rate of storage change is generally small compared to inflows/outflows. When compared to the steady-state model positive fluxes (Apx Table K.16), differences in fluxes are mainly observed at the boundaries with a slight decrease in gain from the streams and a slight increase in recharge. A decrease in discharge to the coast is also observed.

Specifically, the main source of inflow into the system is equivalently from the streams (5.38 GL yr^{-1}) and the MLR (5.11 GL yr^{-1}), and a relatively small contribution comes from areal recharge (0.66 GL yr^{-1}). Groundwater outflow to the streams is 6.41 GL yr^{-1} , resulting in a net loss of groundwater to streams (1.03 GL yr^{-1}). The T1 aquifer receives water from the Hindmarsh Clay (3.09 GL yr^{-1}). Of this flow, a maximum of 0.32 GL yr^{-1} originates from the MLR via lateral flow into the Quaternary sediments, i.e. at least 2.77 GL yr^{-1} (the remaining part) originates from infiltration in the Plains (mostly from river leakage as diffuse recharge is about 10 times less than river leakage). The MLR provides lateral inflow to all zones but most prevalently into the Bedrock in the Golden Grove Embayment (3.37 GL yr^{-1}), followed by the T1 aquifer (0.55 GL yr^{-1}), the Hindmarsh Clay (0.32 GL yr^{-1}) and the T2 aquifer (0.30 GL yr^{-1}). After recharge occurs from the streams and MLR, the water flows towards the coast and upward. In the Golden Grove Embayment, most of the water from the Bedrock flows upward into UTSand (2.71 GL yr^{-1}), the T3T4 aquifer (1.51 GL yr^{-1}) and the T1 aquifer (0.74 GL yr^{-1}). There is a large flux from the T2 aquifer to the T1 aquifer through the Munno Para Clay (2.88 GL yr^{-1}) but also a significant component of direct flow from the T1 aquifer to the T2 aquifer (1.37 GL yr^{-1}). The T1 aquifer then discharges into the Hindmarsh Clay (6.62 GL yr^{-1}) and the outflow from the Hindmarsh Clay to the sea is 5.81 GL yr^{-1} .

The spatial patterns of vertical fluxes are similar as for the steady-state and so the description is not repeated here.

Apx Table K.15 Decadal (1939–1949) average flux matrix (GL yr⁻¹) for water-balance components in the pre-development transient flow model. The same display threshold and colour scheme as for Apx Table K.14 apply

	Hclay	UTSand	T1	MPClay	T2	BPFmnU	T3T4U	BedrockU	BPFmnD	T3T4D	BedrockD	Pfault	MLR	Streams	Coast	Recharge
Hclay		0.01	3.09											2.49	5.81	
UTSand			0.13					1.39						3.92		
T1	6.62	0.15		0.23	2.60			0.17		0.01		0.01				
MPClay			2.88		0.24											
T2		0.22	1.37	2.88		0.04			0.02							
BPFmnU					0.99		0.06	0.02								
T3T4U			0.75			0.68		0.15								
BedrockU		2.71	0.74			0.20	1.51					0.03				
BPFmnD					0.33					0.02						
T3T4D			0.01						0.16							
BedrockD			0.02						0.01	0.02			0.02			
Pfault			0.01		0.07											
MLR	0.32	0.04	0.55	0.01	0.30	0.16	0.01	3.37	0.15	0.10	0.08	0.02				
Streams	3.28	2.10														
Coast																
Recharge	0.64	0.02														
Storage change	0.54	0.20	0.24				0.01	0.08		0.01		0.02				

Apx Table K.16 Difference between steady-state flux matrix and decadal average (1939–1949) flux matrix for water-balance components in the pre-development transient flow model. Values below 1x10⁻² are not shown. Colours are indicative of the magnitude, with blues showing decrease and reds showing increase from steady state fluxes respectively

	Hclay	UTSand	T1	MPClay	T2	BPFmnU	T3T4U	BedrockU	BPFmnD	T3T4D	BedrockD	Pfault	MLR	Streams	Coast	Recharge
Hclay		0.00	-0.38											-0.26	0.12	
UTSand			-0.01					-0.09						-0.56		
T1	-0.19	-0.01		0.00	-0.06			0.00				0.00				
MPClay			-0.03		0.00											
T2		0.00	-0.04	-0.03		0.00			0.00							
BPFmnU					0.00		0.00	0.00								
T3T4U			-0.01			0.00		-0.01								
BedrockU		-0.19	-0.01			0.00	-0.02					0.00				
BPFmnD					0.00					0.00						
T3T4D			0.01						0.00							
BedrockD			0.00						0.00	0.00						
Pfault			0.00		0.01											
MLR	-0.01	0.00	-0.02	0.00	-0.01	-0.01	0.00	-0.19	-0.01	-0.01	0.03	0.00				
Streams	-1.04	-0.65														
Coast																
Recharge	0.18	0.00														

Comparison with previous water balance estimates

Gerges (1999) performed a flow net analysis west of the MLR boundary together with estimated hydraulic parameters from aquifer tests to calculate the pre-development lateral fluxes from the MLR into Quaternary, T1 and T2 aquifers. He studied an area extending from the same southern limit as in this model and up to roughly 3 km north of Little Para River (i.e. about the southern half of the current MLR boundary). In total these fluxes were estimated to be 11.6 GL yr⁻¹. This is twice the current estimate of the total lateral flux from the MLR (5.11 GL yr⁻¹) while the area assessed was smaller than here and did not consider deep lateral flow through the Bedrock. Likely reasons to explain this discrepancy are:

- The calibrated horizontal hydraulic conductivity in T1 here (0.63 m day⁻¹) is 4 times lower than the one used by Gerges (1999) (2.5 m day⁻¹). Possible explanations for this difference in hydraulic conductivity are discussed in section K.4.3 and should be investigated in future work.
- Gerges (1999) used a single transmissivity estimate while transmissivity can be expected to vary significantly along the eastern boundary (this is subject to further analysis).
- In his flow net analysis, Gerges (1999) assumed that all the horizontal flow within the Tertiary aquifers originated from lateral flow from the MLR. However, it might be that a significant part of the horizontal flow originates from focused vertical leakage near the fault zone (from above and/or below). This mechanism is namely suggested to occur by Apx Figure K.67 and Apx Figure K.70 which respectively show focused downward flow into T1 and focused upward flow into T2 along the MLR boundary. It is also in line with the findings from Green *et al.* (2010) who suggested that focused river leakage near the fault zone might be a significant contributor to the Tertiary aquifers.

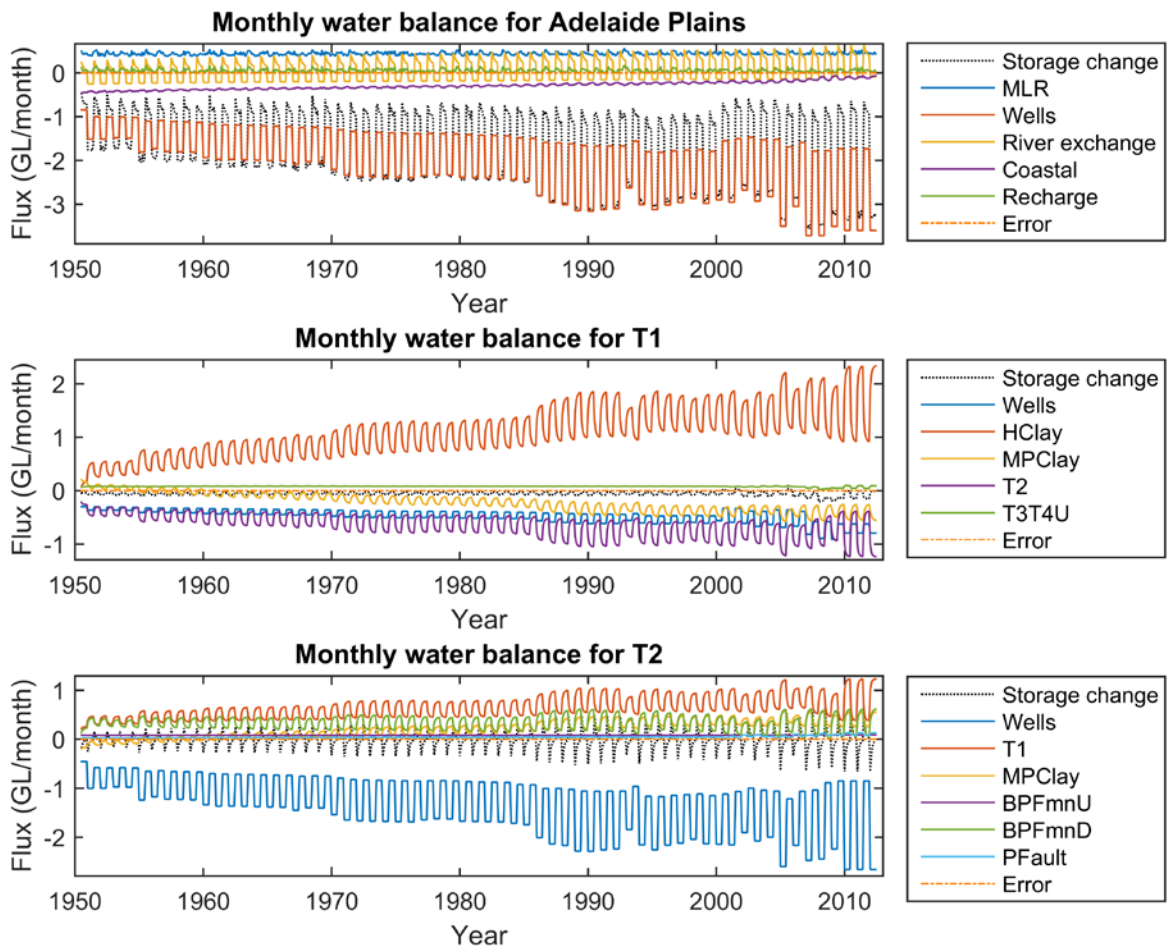
Zulfic *et al.* (2008) used a calibrated groundwater model to estimate the lateral fluxes from the MLR into T1 and T2 in the same area as in Gerges (1999). Under pre-development conditions, the sum of T1 and T2 inflow from the MLR was estimated to be 3.32 GL yr⁻¹. This value is more in line with current results in terms of amount of inflow from the MLR, although here only 0.55 and 0.30 GL yr⁻¹ flow directly into the T1 and T2 aquifers, respectively (and over a larger area), while 4.26 GL yr⁻¹ first flows deeper (mostly through the Bedrock in the Golden Grove Embayment) before flowing upward into the T1 and T2 aquifers. But note that if it exists, such a deeper pathway could not have been simulated in Zulfic *et al.* (2008) as the T2 aquifer was the last layer of the model. Besides and unfortunately, Zulfic *et al.* (2008) did not report the calibrated hydraulic conductivity values.

Finally, in this project the total flow across the faults (i.e., across both Para Fault and Eden-Burnside Fault) from the MLR to the T1 and T2 aquifers was estimated to be 2 – 4 GL yr⁻¹ based on a simple ¹⁴C cross-sectional model along a transect in the North Adelaide Plains (Appendix E). As above, this value is more in line with current results in terms of amount of inflow from the MLR, although here the model suggests a significantly smaller direct inflow into the T1 and T2 aquifers and suggests instead a deeper groundwater path especially in the Golden Grove Embayment. Note that the estimate based on the simple ¹⁴C cross-sectional model is likely to be prone to major uncertainty as the ¹⁴C values might not be representative of current flow conditions and it ignores the spatial variability of flow rates along the faults.

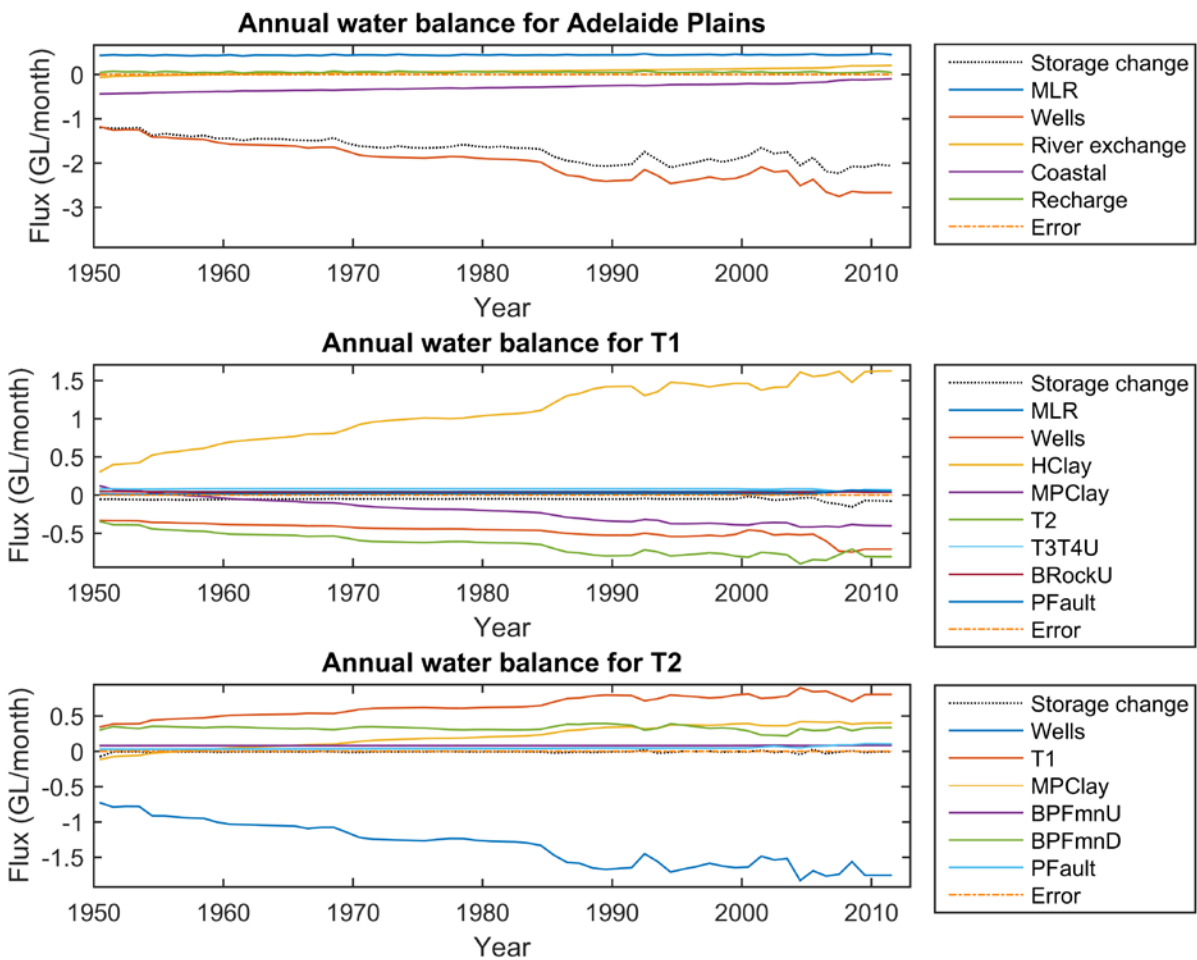
Development transient water balance (1950–2013)

The development period of the model simulates the effect of the introduction of large scale pumping across the Adelaide Plains. The impact of pumping is immediately apparent in the monthly water balance (Apx Figure K.75), in which the overall rate of storage loss is continually increasing on a yearly average in response to a continual increase of pumping (Apx Figure K.76). The rate of change in storage is smaller in the T1 and T2 aquifers than in the Hindmarsh Clay, which is also apparent from the cumulative change in storage in Apx Figure K.77. This is due to the small calibrated specific storage values of the T1 and T2 aquifers (8.1E-07 m⁻¹ and 3.5E-06 m⁻¹, respectively) in comparison with the one of Hindmarsh Clay (3.6E-05 m⁻¹). It can be noted that the average rate of storage loss in Hindmarsh Clay is roughly 12 GL yr⁻¹, i.e. 20 times more than during the pre-development period (0.6 GL yr⁻¹) for which the storage loss was explained to be due to the initial condition. Therefore, it can be concluded the initial condition does not affect significantly the results of the development transient model.

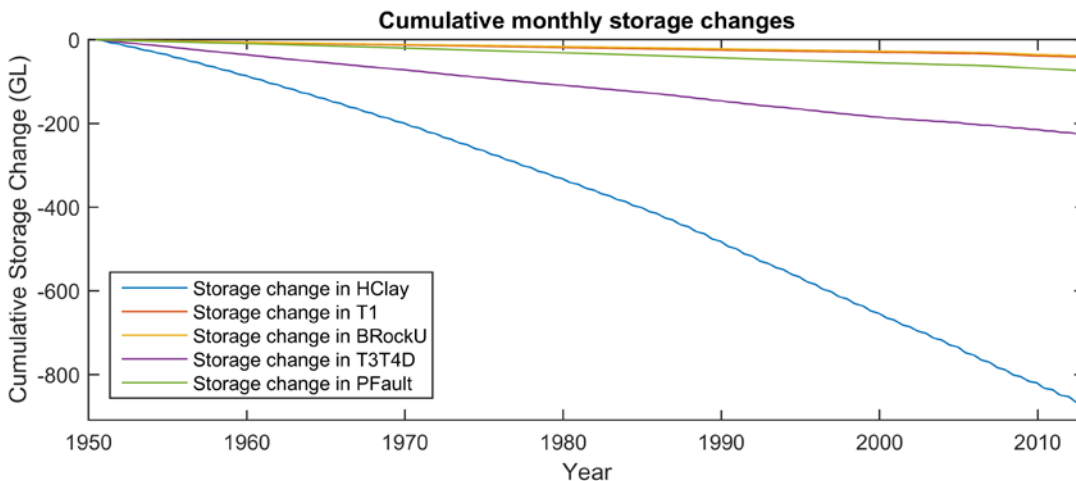
The large flux from the Hindmarsh Clay seems to balance the pumping in the T1 and T2 aquifer, although it is clear that the T1 aquifer is losing a noticeable volume whereas the storage decrease in the T2 aquifer seems to be compensated from the T1 and other units. This is of particular interest, because the T2 aquifer experiences nearly three times the amount of pumping in comparison to the T1 aquifer and has twenty times the amount of pumping than in the Hindmarsh Clay.



Apx Figure K.75 Monthly water balance components for the whole model domain (top), T1 aquifer (middle) and T2 aquifer (bottom), for the development model (1950–2013)



Apx Figure K.76 Annual water balance components for the whole model domain (top), T1 aquifer (middle) and T2 aquifer (bottom), for the development model (1950–2013)



Apx Figure K.77 Cumulative changes in storage for the Hindmarsh Clay, T1 aquifer, Bedrock, T3 and T4 aquifers and the Para Fault, for the development model (1950–2013)

A summary of the water balance for the Adelaide Plains near the start (1951–1961) and at the end of the development period (2002–2012) is captured by the decadal average flux matrix in Apx Table K.17 and Apx Table K.18 respectively. The decadal average annual flux highlights how the system shifted from the pre-development behaviour to a stressed system under widespread pumping across the plains. Firstly, the introduction of pumping wells is seen in the boundaries, which extracts around 30 GL yr⁻¹ from the water balance. The majority of pumping takes place in the T1 (7.5 GL yr⁻¹) and T2 (20.27 GL yr⁻¹) aquifers. This significant pumping reduces the head in these aquifers and hence modifies the internal flow dynamics. The

general upward flow of water from the bottom to the top is reversed in direction over large areas of the model domain, with T2 pulling water from above through the T1 directly (10.59 GL yr⁻¹, around the Gawler and Golden Grove Embayment areas) and through the Munno Para Clay (5.67 GL yr⁻¹). At its bottom the T2 is pulling significant water from the Blanche Point Formation (5.22 GL yr⁻¹). The Blanche Point Formation is in turn receiving water from the T3 and T4 aquifers (4.61 GL yr⁻¹). It is noteworthy that the change in storage for each of the zones (shown in the bottom row of Apx Table K.18) shows only small rates of change in the T1 and T2. This is due to the fact that the specific storage values are low, resulting in large head decreases and consequently increased head gradients, which draws water from surrounding zones. Storage is clearly available in the Hindmarsh Clay and T3 and T4 aquifers and this is being depleted at a large rate when compared to the total freshwater recharge rates.

The pumping stress reduces the heads in the system which then shifts the streams to net losing (spatiotemporal average), which means the groundwater system is net gaining from the streams. The MLR contribution also increases as a consequence of the increased gradient along the boundary, thus drawing more water into the system. Finally, the discharge to the coast is halved, and a small amount of water is flowing from the coast into the Hindmarsh Clay (0.40 GL yr⁻¹).

Apx Table K.17 Decadal (1951–1961) average annual flux matrix for water balance components. An additional row of rate of change in storage for all zones is appended to the matrix. The same display threshold and colour scheme as for Apx Table K.14 apply

	Hclay	UTSand	T1	MPClay	T2	BPFmnU	T3T4U	BedrockU	BPFmnD	T3T4D	BedrockD	Pfault	MLR	Wells	Streams	Coast	Recharge
Hclay			10.95											0.74	1.95	4.88	
UTSand			0.13					1.39							3.91		
T1	4.59	0.14		1.89	6.49			0.21				0.02		4.28			
MPClay			2.13		1.90												
T2		0.22	1.20	2.12		0.04			0.08						10.70		
BPFmnU					1.02		0.06	0.02									
T3T4U			0.99			0.69		0.14							0.14		
BedrockU		2.69	0.72			0.20	1.85								0.26		
BPFmnD					4.18					0.04					0.05		
T3T4D			0.05						3.99								
BedrockD			0.02						0.03	0.04							0.04
Pfault			0.18		0.37												
MLR	0.33	0.04	0.57		0.32	0.17		3.43	0.16	0.11	0.09	0.02					
Wells																	
Streams	3.50	2.11															
Coast																	
Recharge	0.63	0.03															
Storage change	-9.48	-0.20	-0.70		-0.10		-0.04	-0.56	-0.02	-3.84	-0.03	-0.98					

Apx Table K.18 Decadal (2002–2012) average annual flux matrix for water balance components. An additional row of rate of change in storage for all zones is appended to the matrix. The same display threshold and colour scheme as for Apx Table K.14 apply

	Hclay	UTSand	T1	MPClay	T2	BPFmnU	T3T4U	BedrockU	BPFmnD	T3T4D	BedrockD	Pfault	MLR	Wells	Streams	Coast	Recharge
Hclay			20.35											0.99	1.03	2.28	
UTSand			0.14					1.51							3.79		
T1	1.95	0.14		5.66	10.59		0.13	0.22		0.02		0.02		7.50			
MPClay			0.94		5.67												
T2		0.21	1.05	0.94		0.05			0.65						20.27		
BPFmnU					1.07		0.07	0.03									
T3T4U			0.95			0.75		0.13							0.72		
BedrockU		2.57	0.65			0.19	2.21					0.03			0.68		
BPFmnD					4.15					0.58					0.02		
T3T4D			0.04						3.86								
BedrockD			0.02						0.03	0.06							0.03
Pfault			0.47		0.98												
MLR	0.34	0.04	0.59		0.35	0.17		3.48	0.19	0.13	0.08	0.02					
Wells	0.02		0.05		0.26												
Streams	4.61	2.17															
Coast																	
Recharge	0.56	0.02															
Storage change	-16.76	-0.28	-0.97		-0.10		-0.13	-0.97	-0.01	-3.10	-0.06	-1.54					

The modelled head contours for the Hindmarsh Clay and Undifferentiated sand, the T1 aquifer and the T2 aquifer at the end of the winter (October 2012) and summer periods (April 2013) are shown in Apx Figure K.84, Apx Figure K.85, Apx Figure K.86, Apx Figure K.87, Apx Figure K.88 and Apx Figure K.89 respectively. The impacts of pumping are clearly apparent at both the end of winter and end of summer, with the drawdown more pronounced in at the end of summer. The cone of depression in both the T1 and T2 aquifers in the Northern Adelaide Plains is clearly visible in the simulated head distribution.

The hydraulic head minus topography for the first layer, T1 and T2 aquifers is shown in Apx Figure K.78, Apx Figure K.79, Apx Figure K.80, Apx Figure K.81, Apx Figure K.82 and Apx Figure K.83. These show clearly the widespread disappearance of the artesian condition that existed in the pre-development model with only limited areas showing artesian conditions.

The spatial distribution of vertical fluxes through the top and bottom of the T1 and T2 aquifers is shown in Apx Figure K.90, Apx Figure K.91, Apx Figure K.92, Apx Figure K.93, Apx Figure K.94, Apx Figure K.95, Apx Figure K.96 and Apx Figure K.97. The fluxes appear to be mainly downward through the top and bottom of the T1, and this occurs over a larger area at the end of summer which is explained by the pumping in the T2 aquifer, forcing water to flow down.

Comparison with previous water balance estimates

Gerges (1999) performed a flow net analysis to calculate the lateral fluxes from the MLR into the T1 aquifer only along the Para Fault boundary with the MLR (i.e. from roughly 10 km south of Little Para River to 3 km north of it) for year 1999. This flux was estimated to be 1.71 GL yr⁻¹. This is almost 3 times the current estimate of direct lateral inflow into the T1 aquifer (0.59 GL yr⁻¹) while the assessed portion is much smaller. Possible reasons for this discrepancy are the same as mentioned above for the pre-development water balance.

On the basis of a calibrated groundwater model, Zulfic *et al.* (2008) estimated the sum of T1 and T2 inflow from the MLR to be 2.67 GL yr⁻¹ in 2009 over the southern half of the current model (as mentioned earlier). This value is lower than their estimate for the pre-development period, which is surprising because intensive pumping has lowered the groundwater levels in these aquifers and so one would expect to see a larger inflow from the MLR boundary (which they treated as a constant head boundary). No possible explanation was given for this result. Nonetheless comparing it to current work, this value is larger than current estimates of inflow to the T1 and T2 aquifers over a larger area (0.94 GL yr⁻¹). However and as mentioned above for the pre-development water balance, Zulfic *et al.*'s (2008) model neglected a potential deep groundwater pathway below the T2 aquifer.

Georgiou *et al.* (2011) provided model-based water balance estimates at year 1988, 2000, 2005 and 2010. The total lateral inflow across the MLR boundary was hence estimated to be 5.2–5.9 GL yr⁻¹. This is in agreement with the current estimate of 5.39 GL yr⁻¹ of the average total lateral inflow across the MLR boundary over the period 2002–2012. However, the break down into different aquifers is not the same. In Georgiou *et al.* (2011), the Quaternary aquifers receive 0.1–0.2 GL yr⁻¹ (here 0.34 GL yr⁻¹), the T1 aquifer receives 0.9–1.3 GL yr⁻¹ (here 0.59 GL yr⁻¹), the T2 aquifer receives 4.0–4.4 GL yr⁻¹ (here 0.35 GL yr⁻¹) and the Bedrock receives 0.0 GL yr⁻¹ (here 3.56 GL yr⁻¹). In addition, here other aquifers (non-existing in Georgiou *et al.* (2011)) receive a total of 0.55 GL yr⁻¹. Hence, in Georgiou *et al.* (2011) most of the lateral inflow occurred through the T2 aquifer whereas in the current model most of the inflow occurs through the Bedrock (most of it in the Golden Grove Embayment). This difference can be partly explained by the fact that in Georgiou *et al.* (2011) the T2 aquifer was assumed to cover entirely the Golden Grove Embayment whereas here the revised hydrostratigraphy implies that the T2 aquifer is absent over a significant portion of the Golden Grove Embayment and namely along the MLR boundary (Apx Figure K.4). Also, Georgiou *et al.*'s (2011) model neglected a potential groundwater pathway below the T2 aquifer elsewhere that in the Golden Grove Embayment, and in this area the T2 aquifer was assumed to lie directly on the Bedrock which had a relatively low horizontal hydraulic conductivity of 5.0E-03 m day⁻¹. Here the T2 aquifer is considered to lie on other sedimentary layers before the Bedrock, and the calibrated horizontal hydraulic conductivity of the Bedrock is higher (3.8E-02 m day⁻¹).

Pritchard *et al.* (2006) performed a flow net analysis in the Northern Adelaide Plains (i.e. the part of the model area north of Dry Creek) on the basis of March 2003 hydraulic head measurements. This yielded estimates for the lateral inflows from the MLR into the T1 and T2 aquifers of 1.5 GL yr⁻¹ and 3.4 GL yr⁻¹, respectively. For the T1 aquifer, the larger value than here (0.59 GL yr⁻¹ over a larger area) could be explained by the larger hydraulic conductivity used (2.0 m day⁻¹ compared with 0.63 m day⁻¹). However, for the T2 aquifer, the larger value than here (0.35 GL yr⁻¹ over a larger area) could not be explained by a difference in hydraulic conductivity as both are similar (2.0 m day⁻¹ compared with 1.7 m day⁻¹). The most likely explanation for the difference is then the fact that in the current model a significant part of the

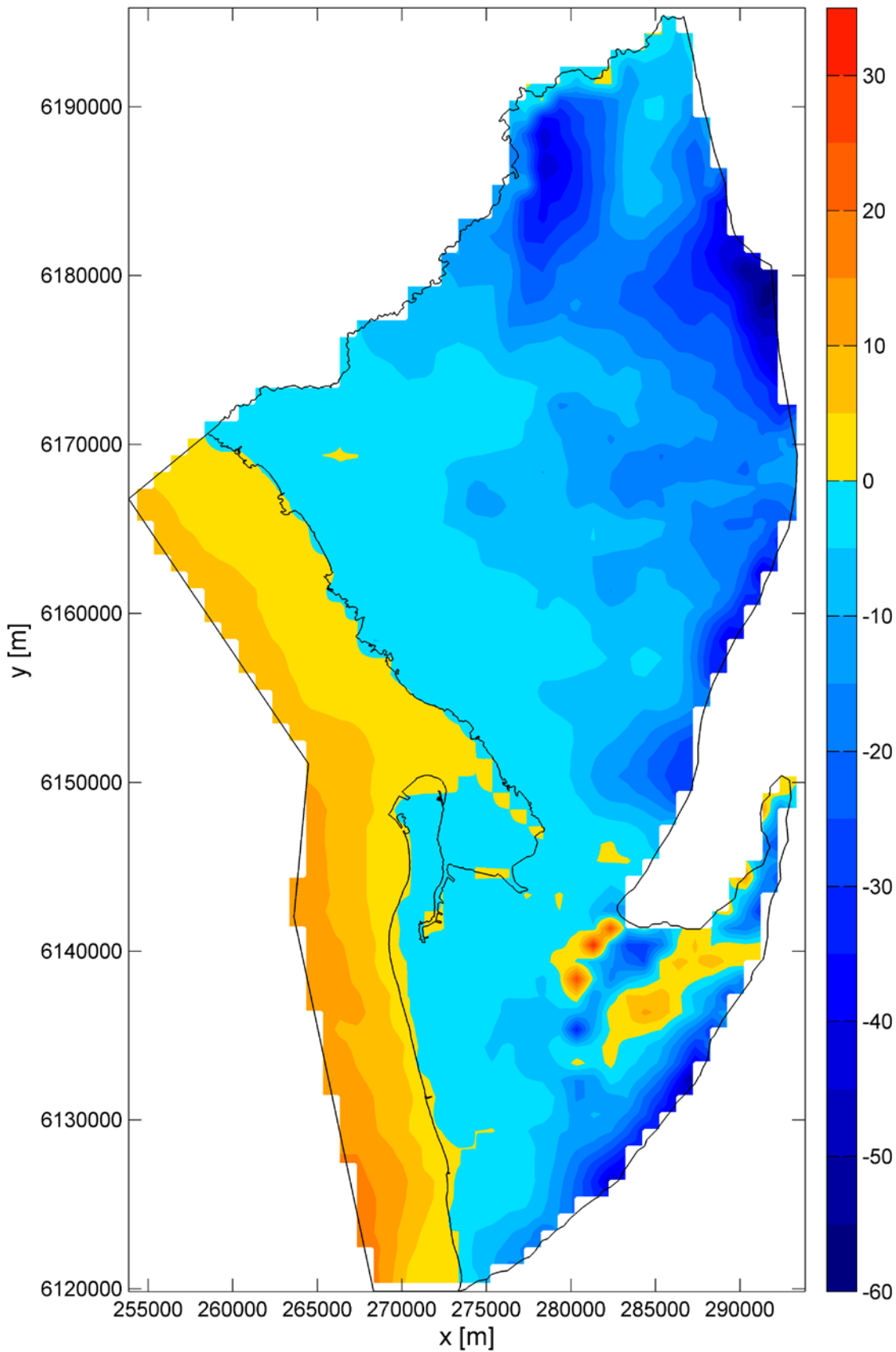
horizontal flow originates from focused vertical leakage around the fault zone; if it exists, such a focused leakage would bias the interpretation of the flow net analysis, as already mentioned earlier about Gerges' (1999) estimates.

Jeuken (2006) developed a groundwater model for the Northern Adelaide Plains targeting the same area as in Pritchard *et al.* (2006) and presented the calculated water balance on the basis of the same period (March 2003). This yielded estimates for the lateral inflows from the MLR into the T1 and T2 aquifers of 2.6 GL yr⁻¹ and 3.7 GL yr⁻¹, respectively, in line with the estimates from Pritchard *et al.* (2006). Accordingly, the same comments as above apply.

In this project river leakage was estimated independently on the basis of a differential stream gauging approach performed in 2014–2015 for creeks flowing across the Eden Burnside Fault (Appendix D). Extrapolating the results to the entire modelled region yielded an estimate of 4.7 GL yr⁻¹. This is only 30 % less than the current model-based 2002–2012 estimate (6.78 GL yr⁻¹). Given the uncertainty surrounding both approaches, this relatively good agreement is quite remarkable.

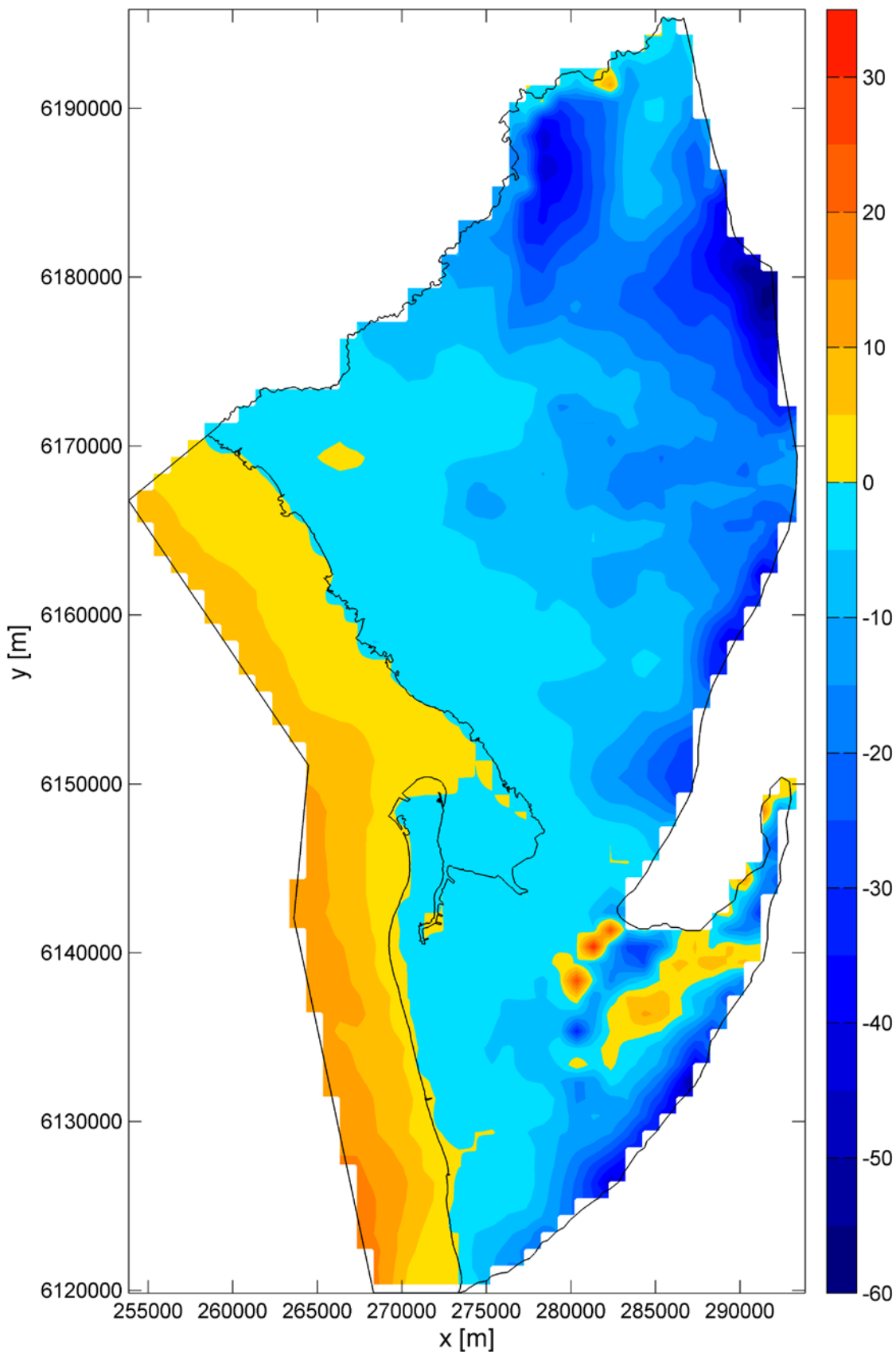
Finally, in this project two core-based estimates of vertical hydraulic conductivity were used conjointly with a year 2014 head-gradient map between the T1 and T2 aquifers to estimate current leakage through the Munno Para Clay at regional scale (Appendix F). This resulted in an upward leakage of 0.36 GL yr⁻¹ in the Central Adelaide Plains and a downward leakage of 1.19 GL yr⁻¹ in the Northern Adelaide Plains. In contrast, here an average total upward leakage of 0.94 GL yr⁻¹ and downward leakage of 5.67 GL yr⁻¹ for the average 2002–2012 is obtained. These differences can be mostly attributed to the 4 times larger K_v calibrated here (1.5E-05 m day⁻¹) than found in Appendix E (3.4E-06 m day⁻¹). This difference in K_v could easily be explained by the fact that core-based estimates are not likely to be representative of the regional scale hydraulic conductivity.

Hydraulic head minus topography in first layer [m]



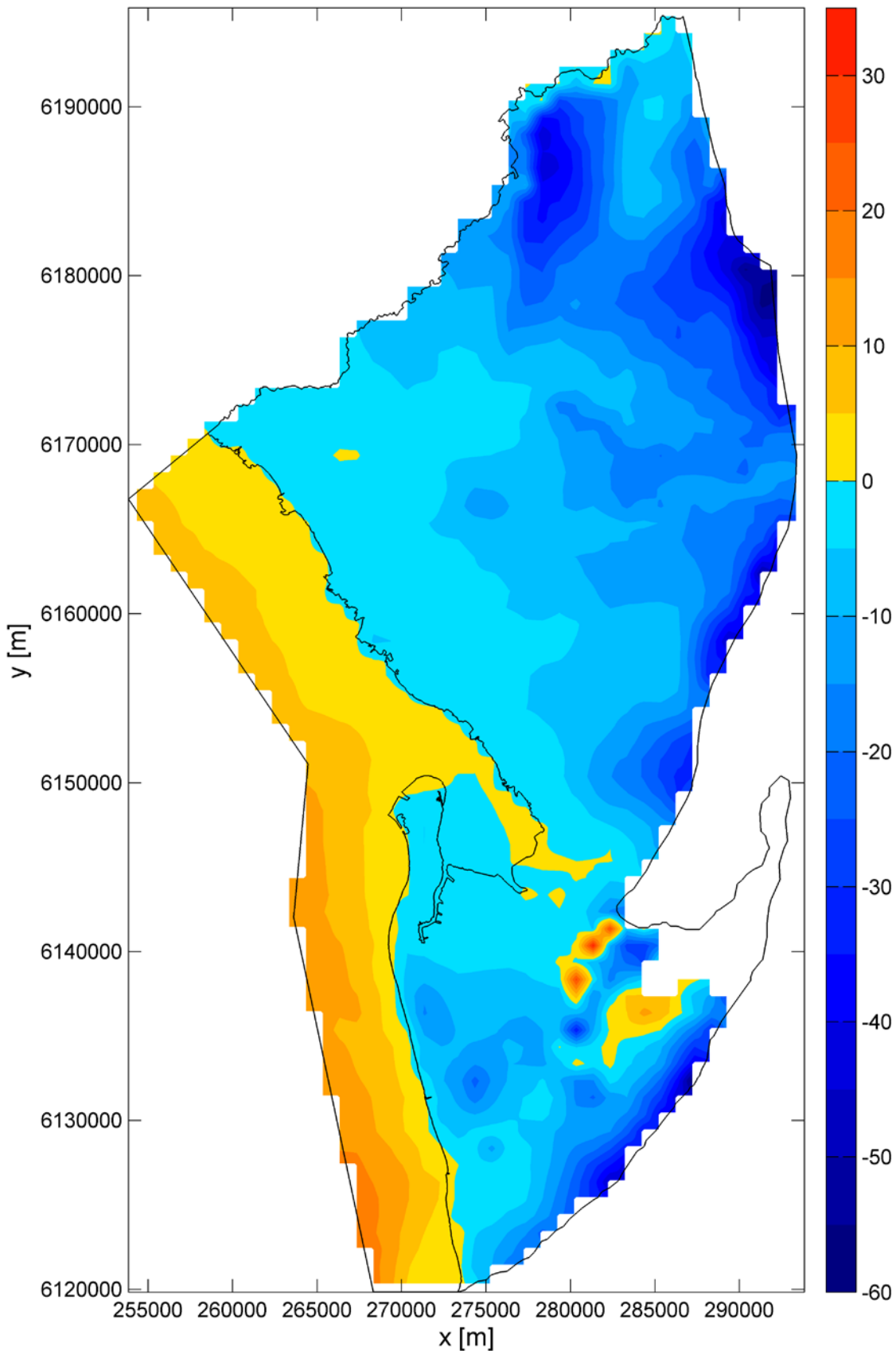
Apx Figure K.78 Hydraulic head minus topography in the first layer, October 2012

Hydraulic head minus topography in first layer [m]



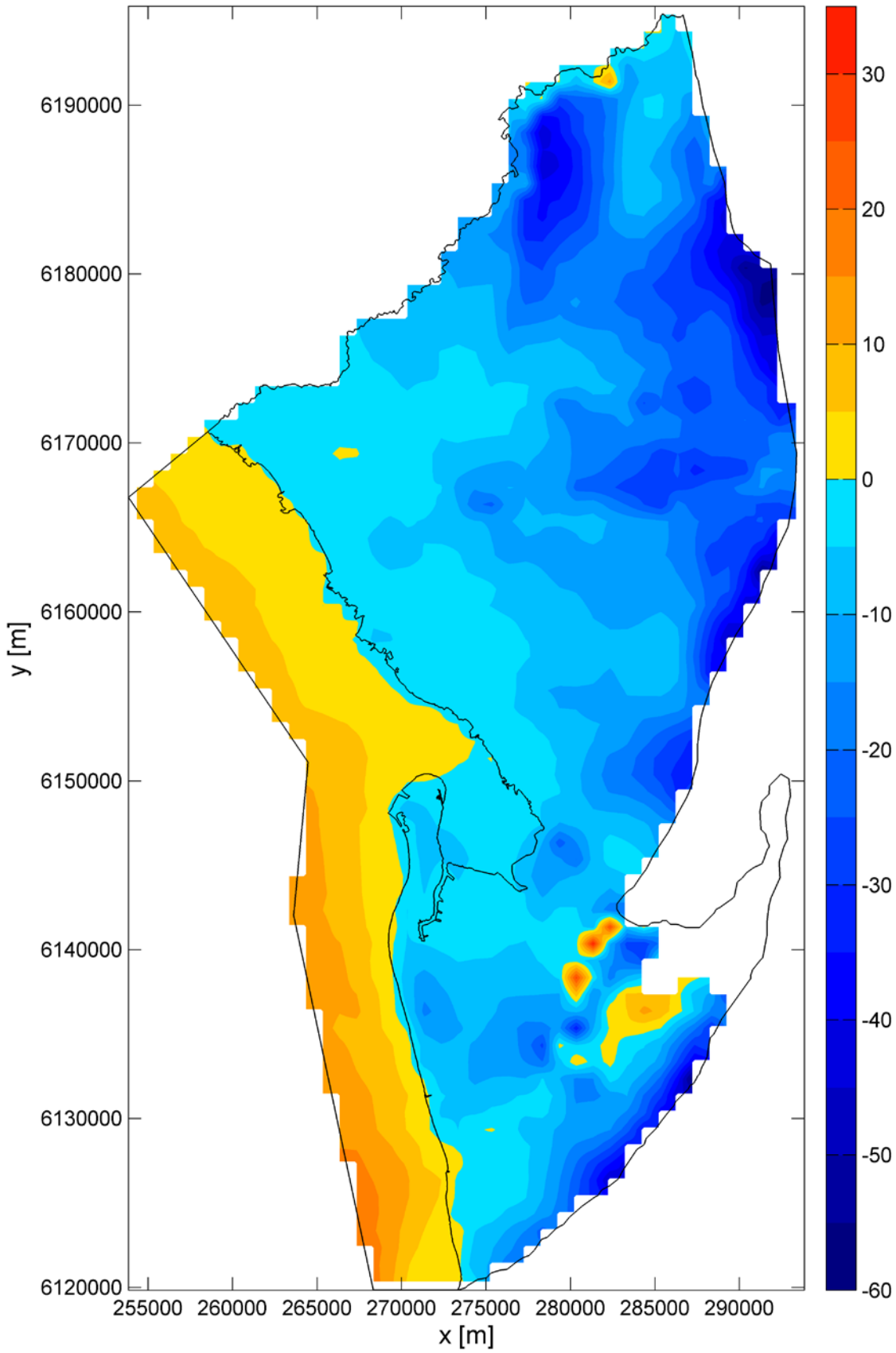
Apx Figure K.79 Hydraulic head minus topography in the first layer, April 2013

Hydraulic head minus topography in T1 [m]



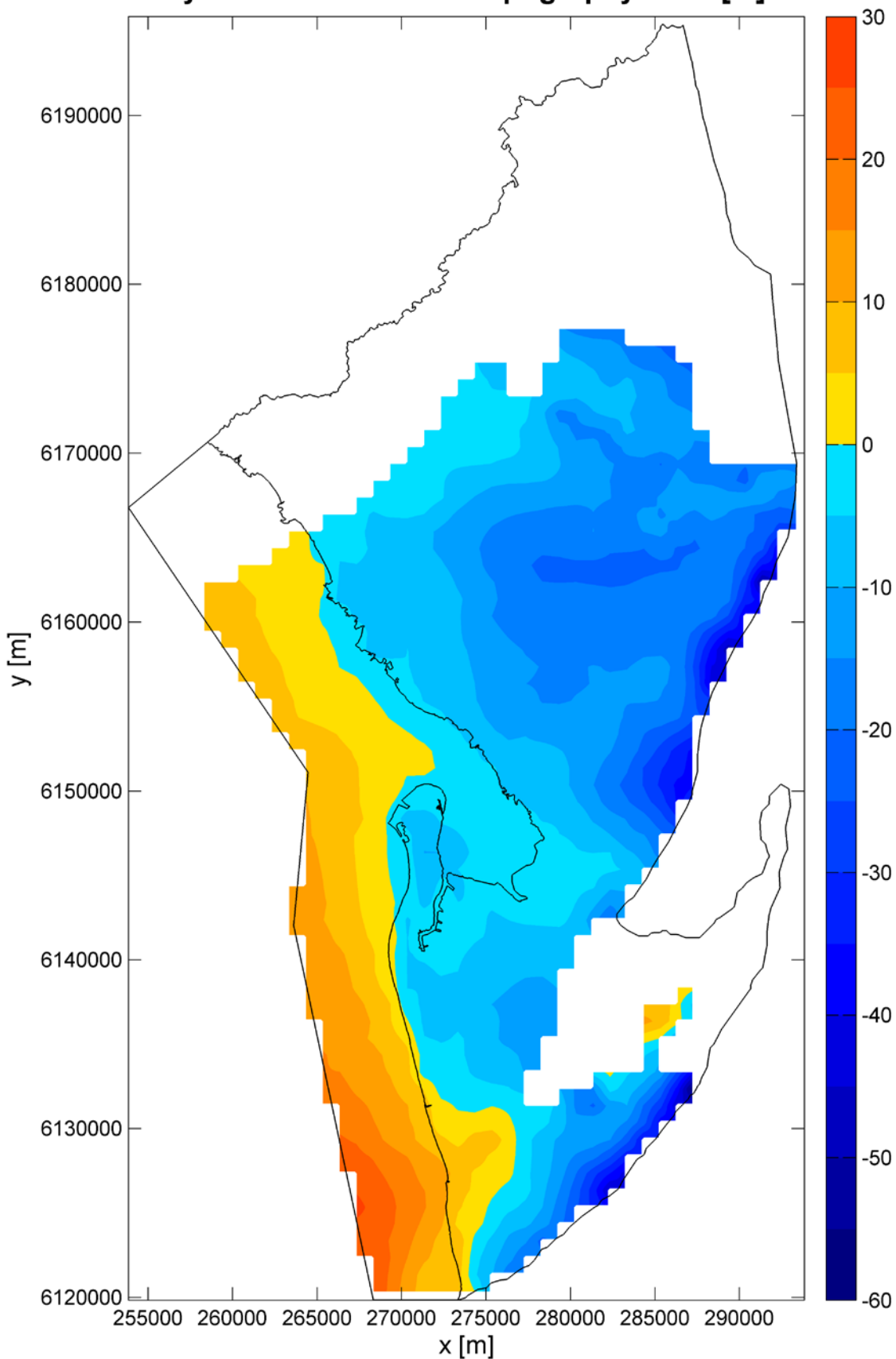
Apx Figure K.80 Hydraulic head minus topography in the T1 aquifer, October 2012

Hydraulic head minus topography in T1 [m]



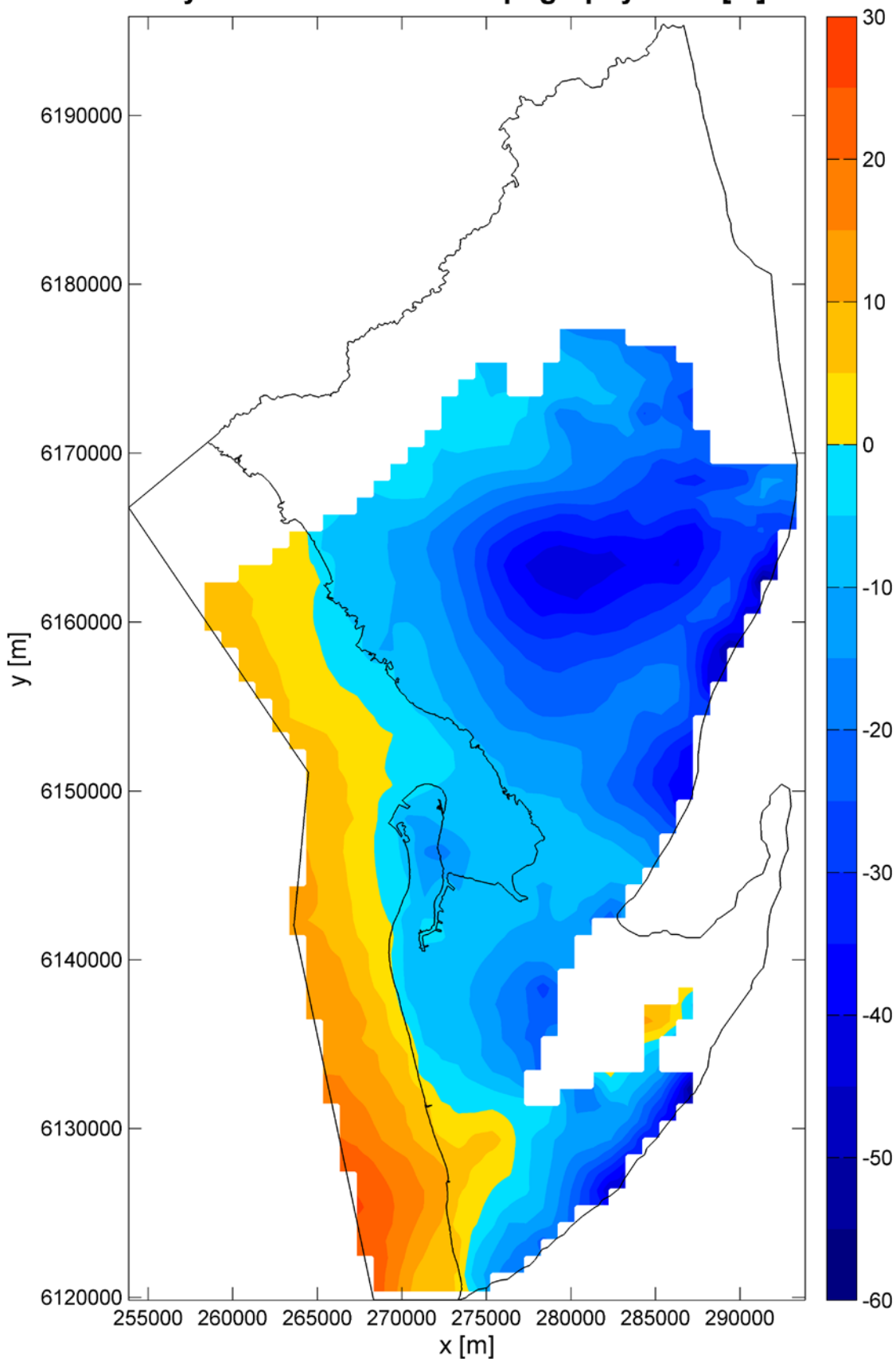
Apx Figure K.81 Hydraulic head minus topography in the T1 aquifer, April 2013

Hydraulic head minus topography in T2 [m]



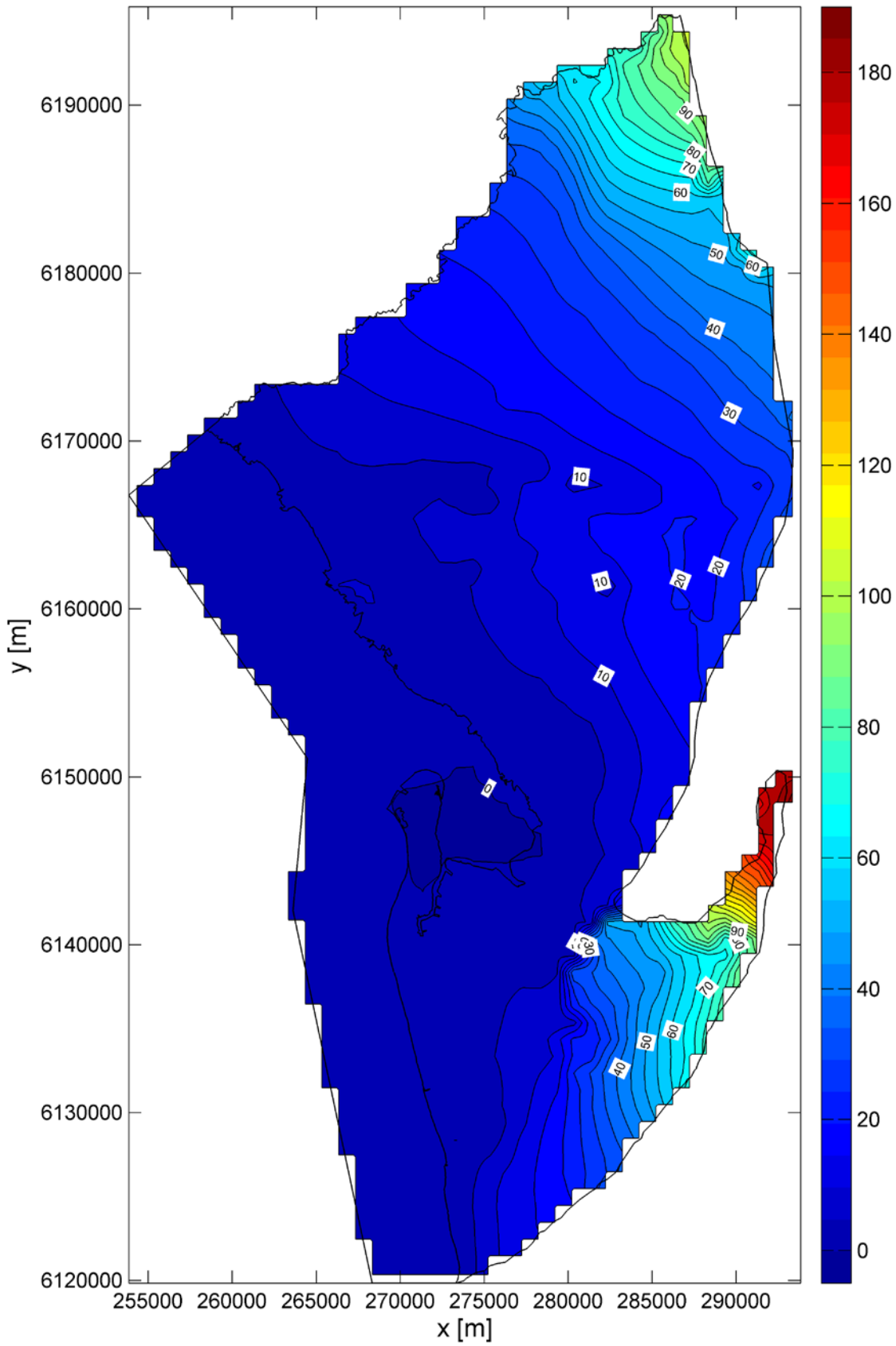
Apx Figure K.82 Hydraulic head minus topography contours in the T2 aquifer, October 2012

Hydraulic head minus topography in T2 [m]



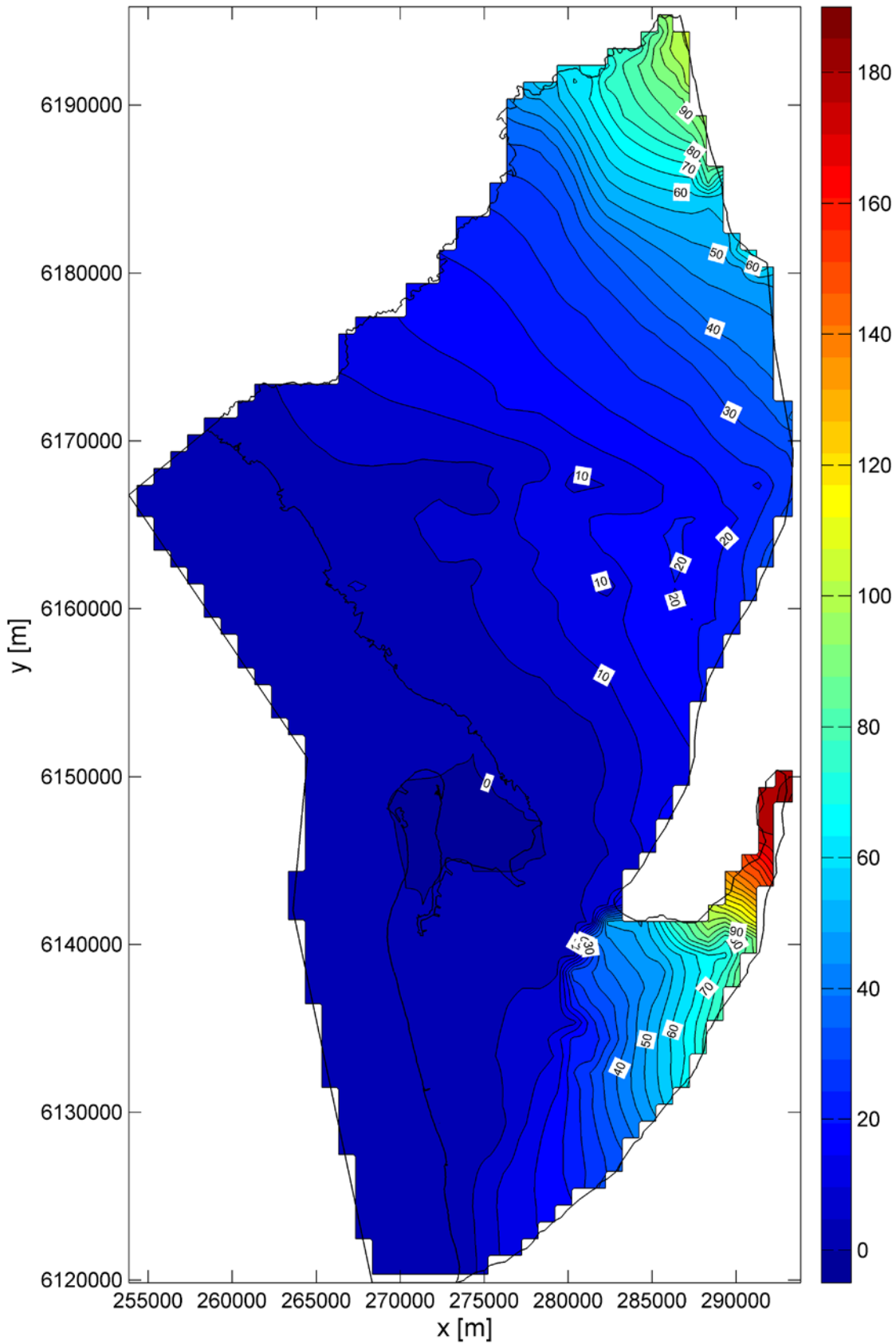
Apx Figure K.83 Hydraulic head minus topography contours in the T2 aquifer, April 2013

Hydraulic head contours in first layer [m AHD]



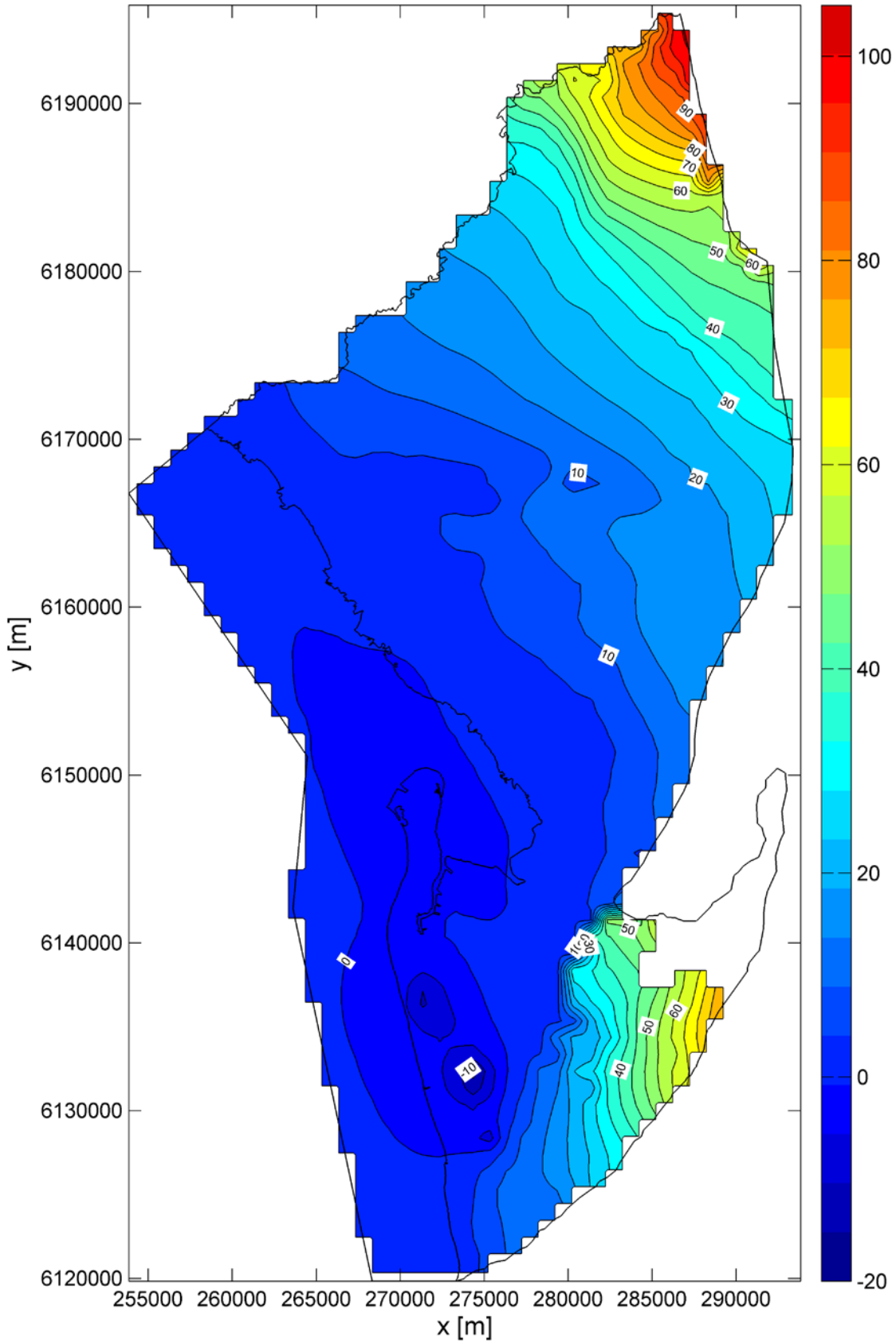
Apx Figure K.84 Simulated head contours in the first layer, October 2012

Hydraulic head contours in first layer [m AHD]



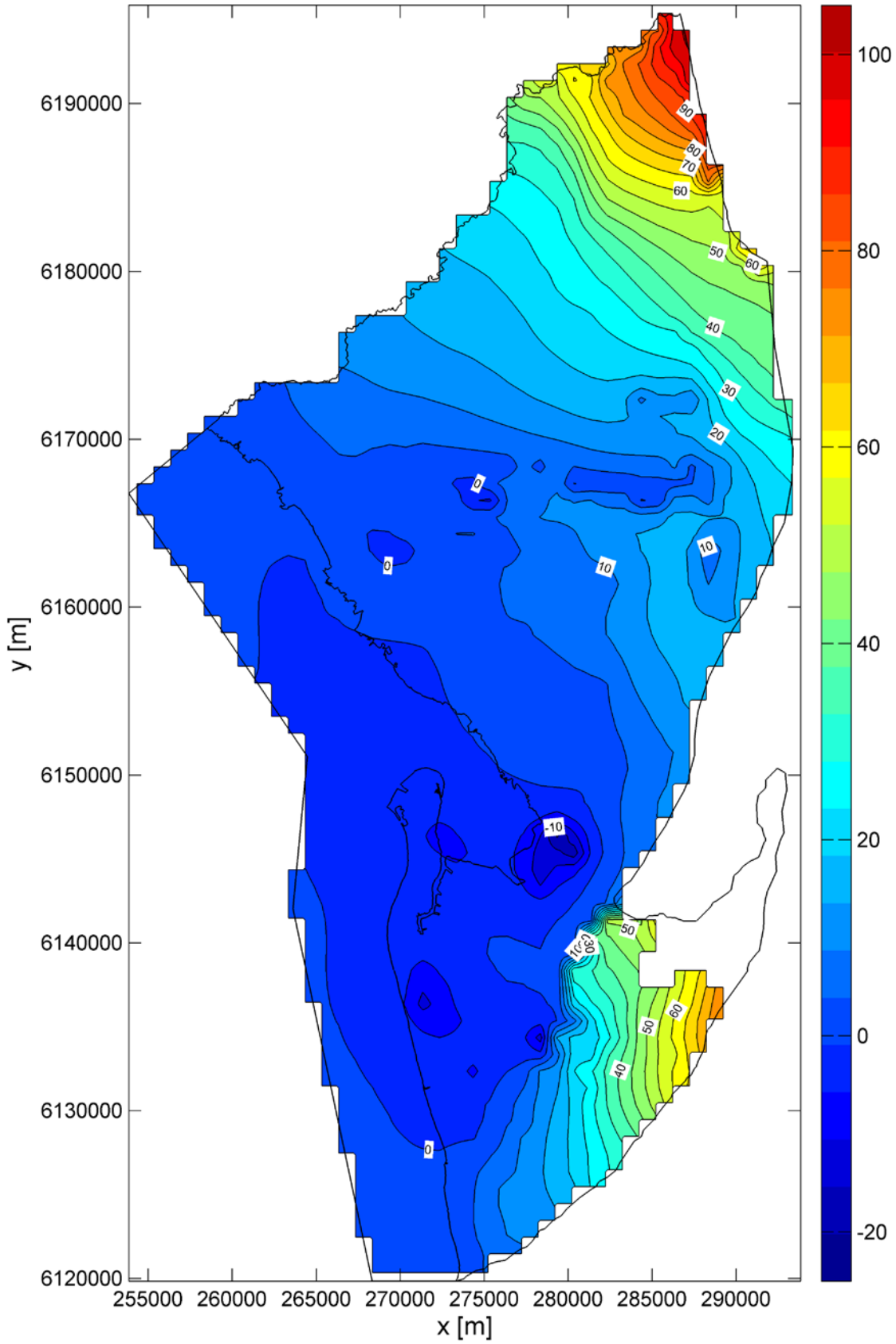
Apx Figure K.85 Simulated head contours in the first layer, April 2013

Hydraulic head contours in T1 [m AHD]



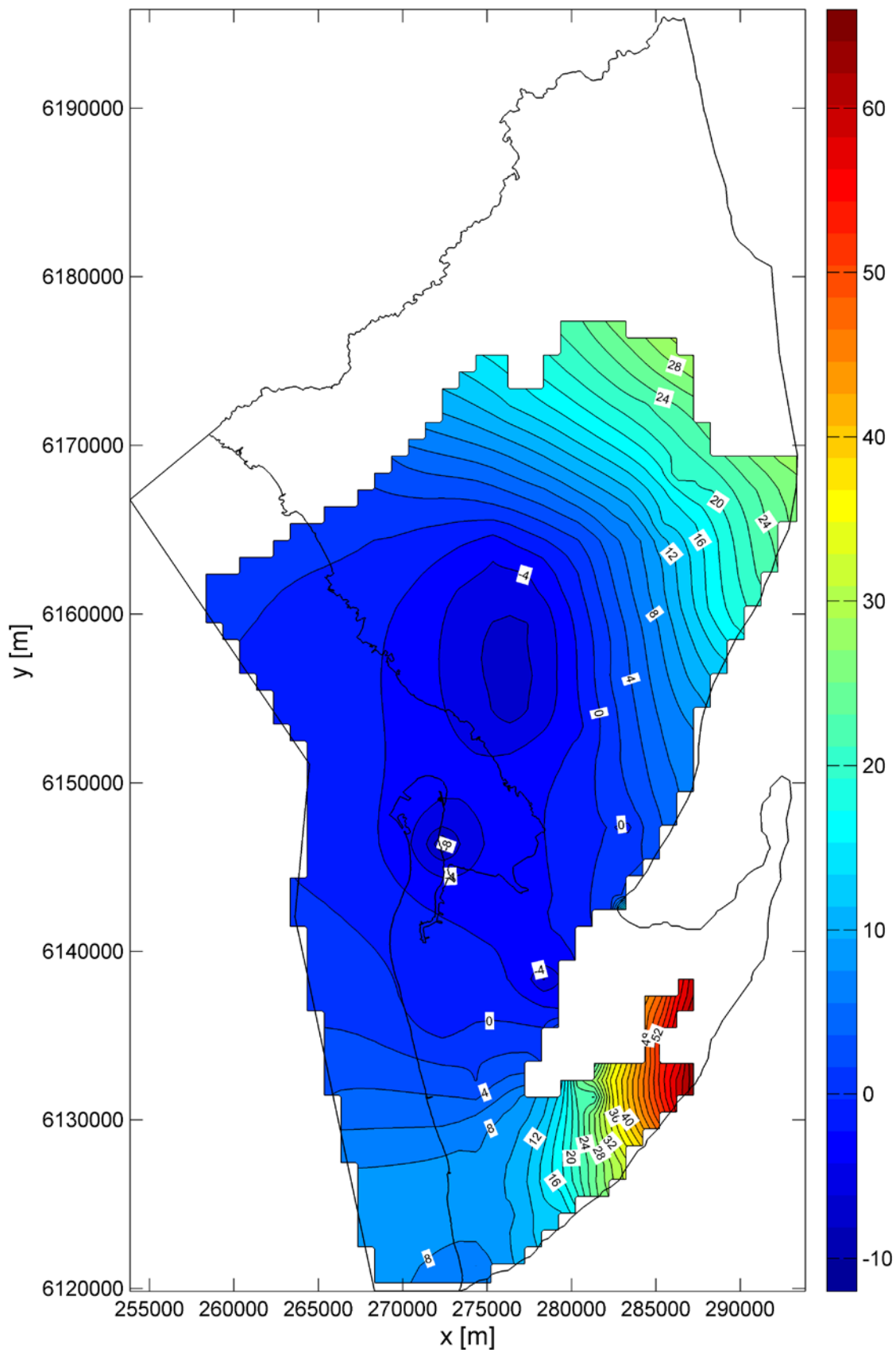
Apx Figure K.86 Simulated head contours in the T1 aquifer, October 2012

Hydraulic head contours in T1 [m AHD]



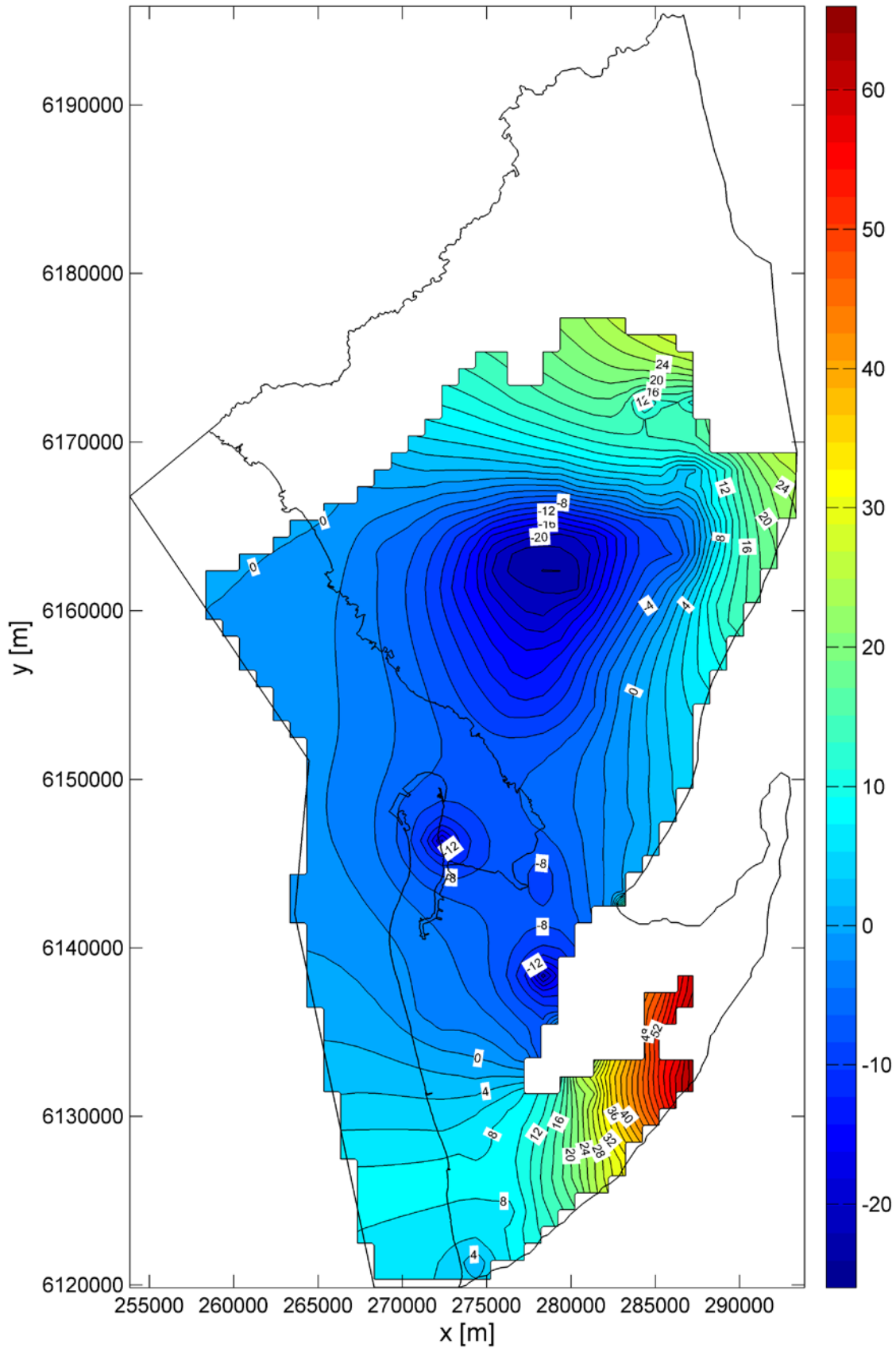
Apx Figure K.87 Simulated head contours in the T1 aquifer, April 2013

Hydraulic head contours in T2 [m AHD]

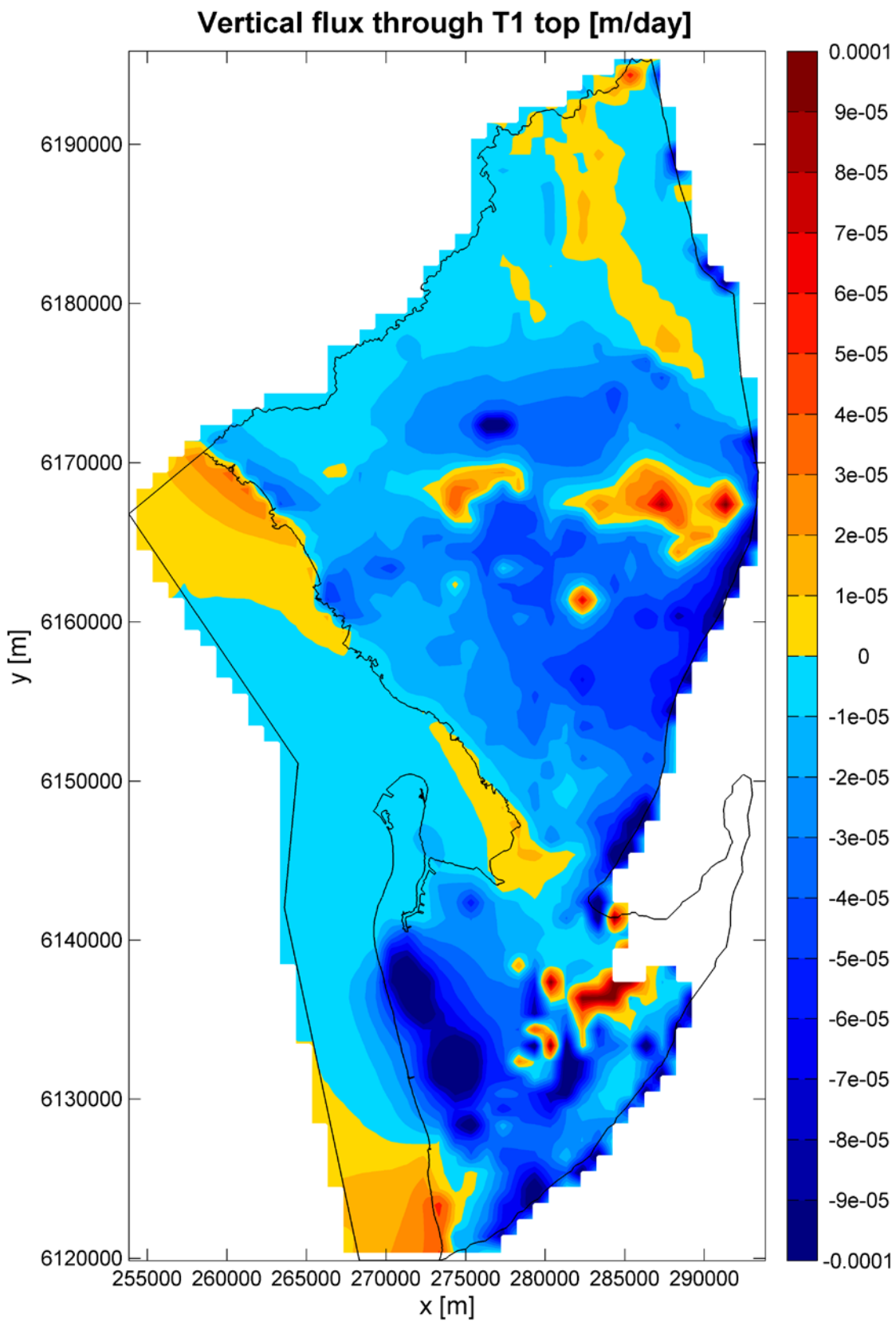


Apx Figure K.88 Simulated head contours in the T2 aquifer, October 2012

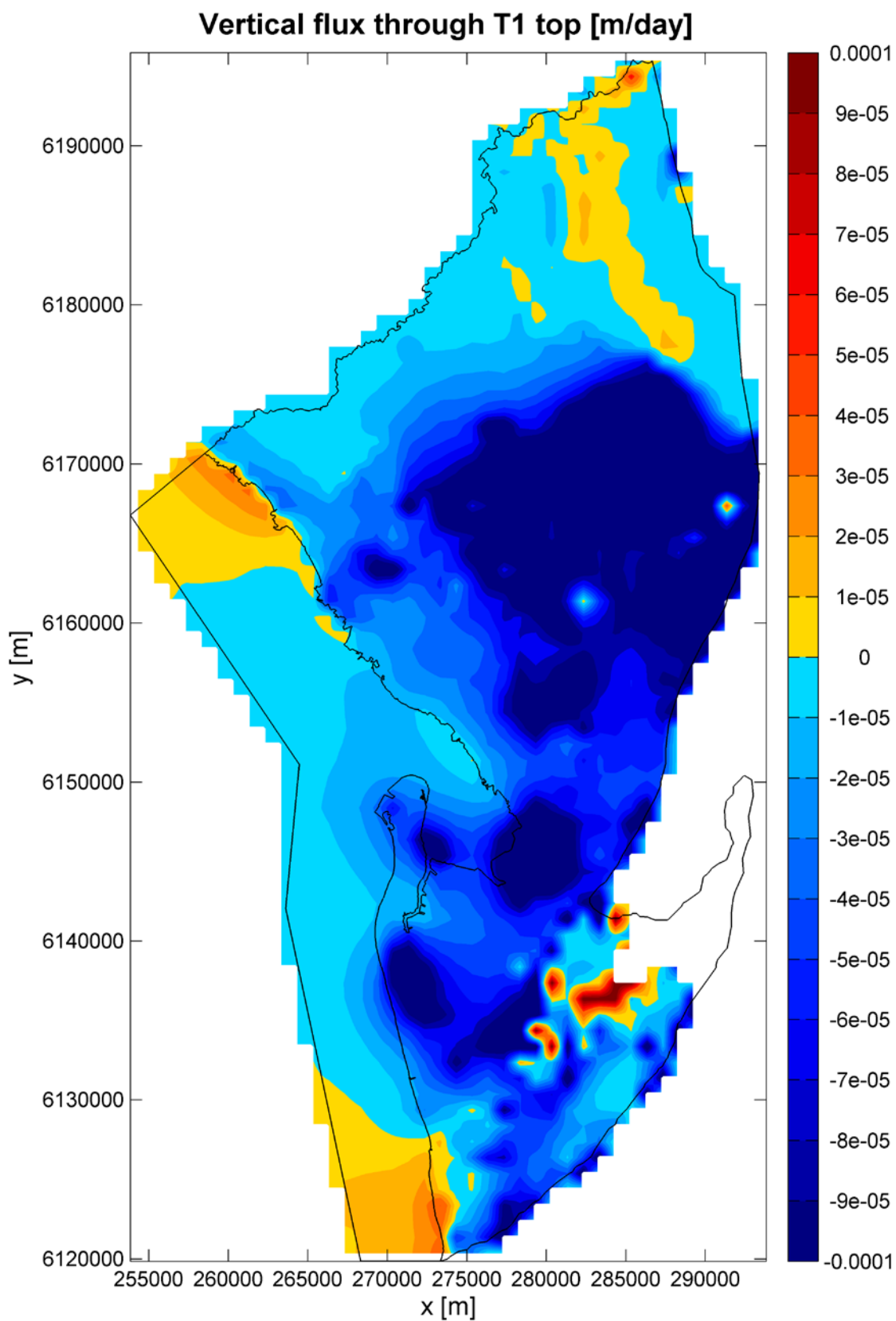
Hydraulic head contours in T2 [m AHD]



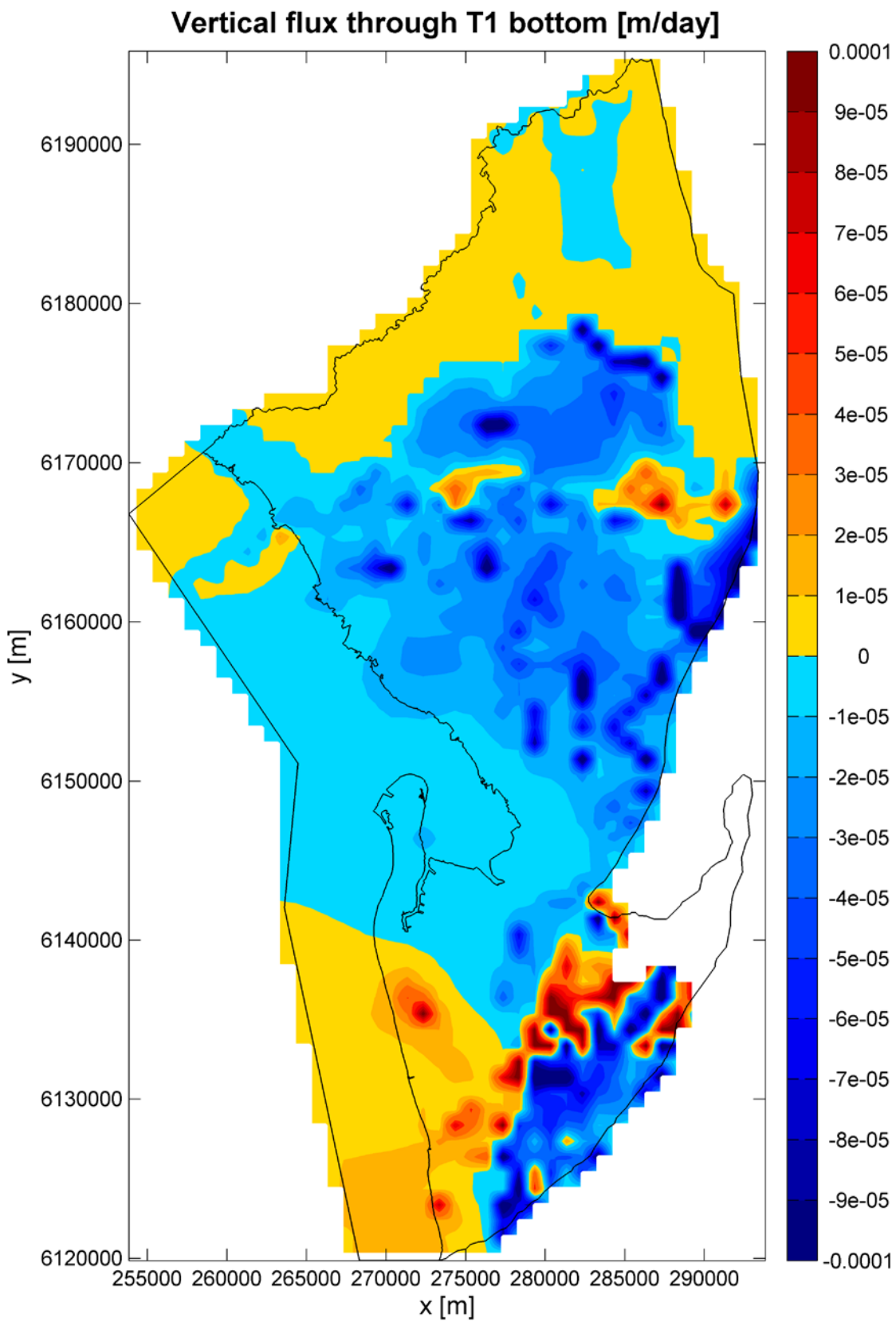
Apx Figure K.89 Simulated head contours in the T2 aquifer, April 2013



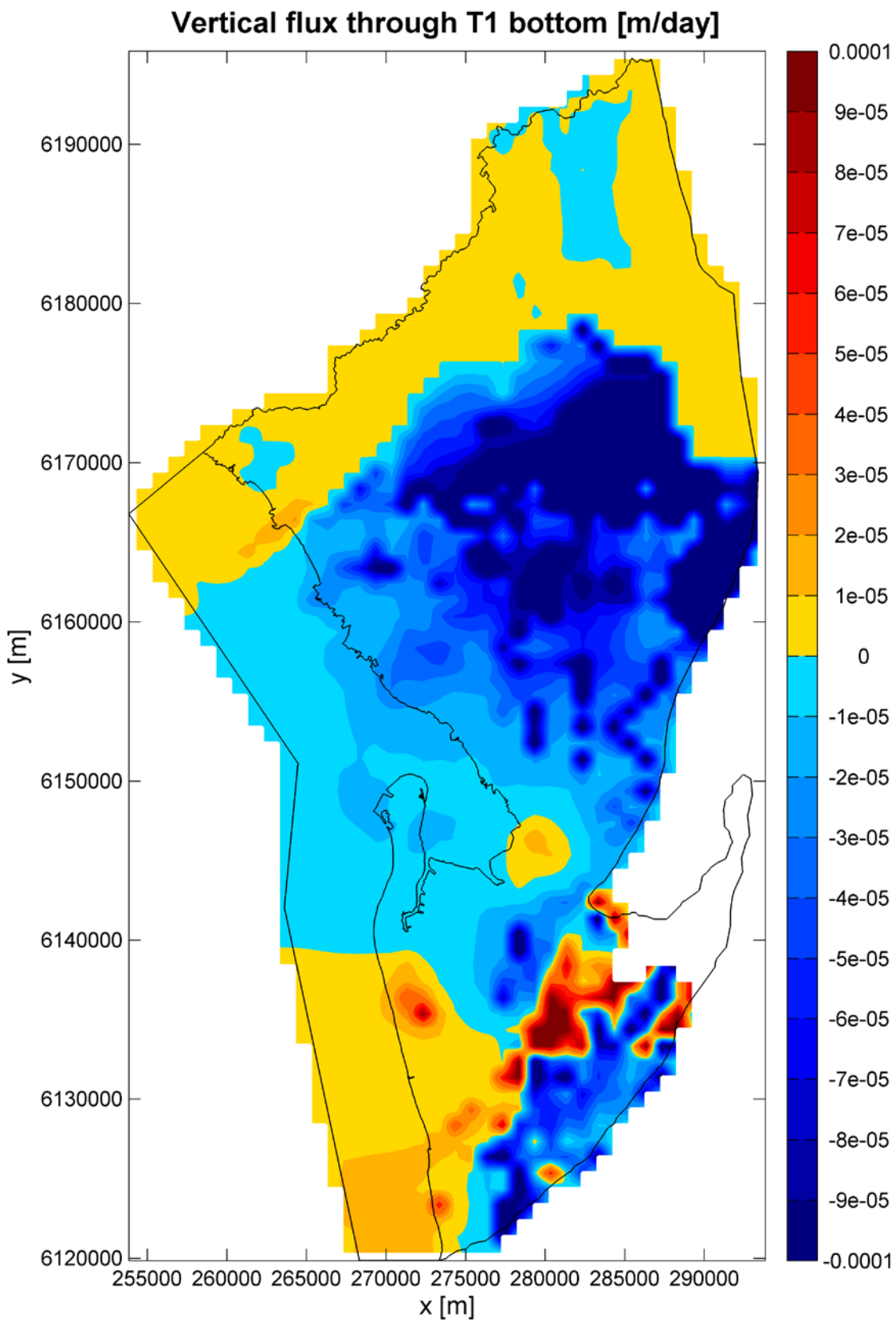
Apx Figure K.90 Simulated vertical flux through the top of the T1 aquifer in October 2012



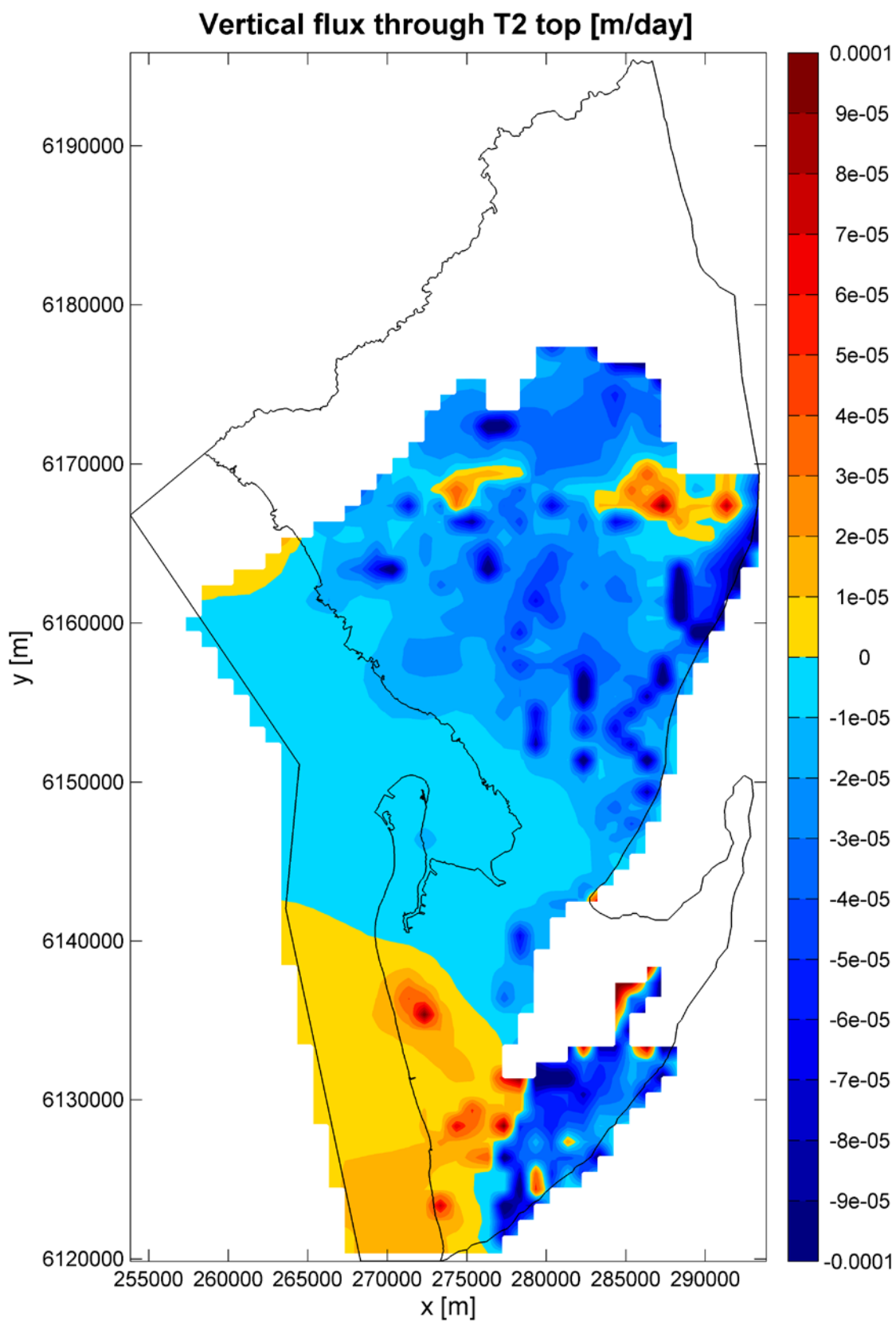
Apx Figure K.91 Simulated vertical flux through the top of the T1 aquifer in April 2013



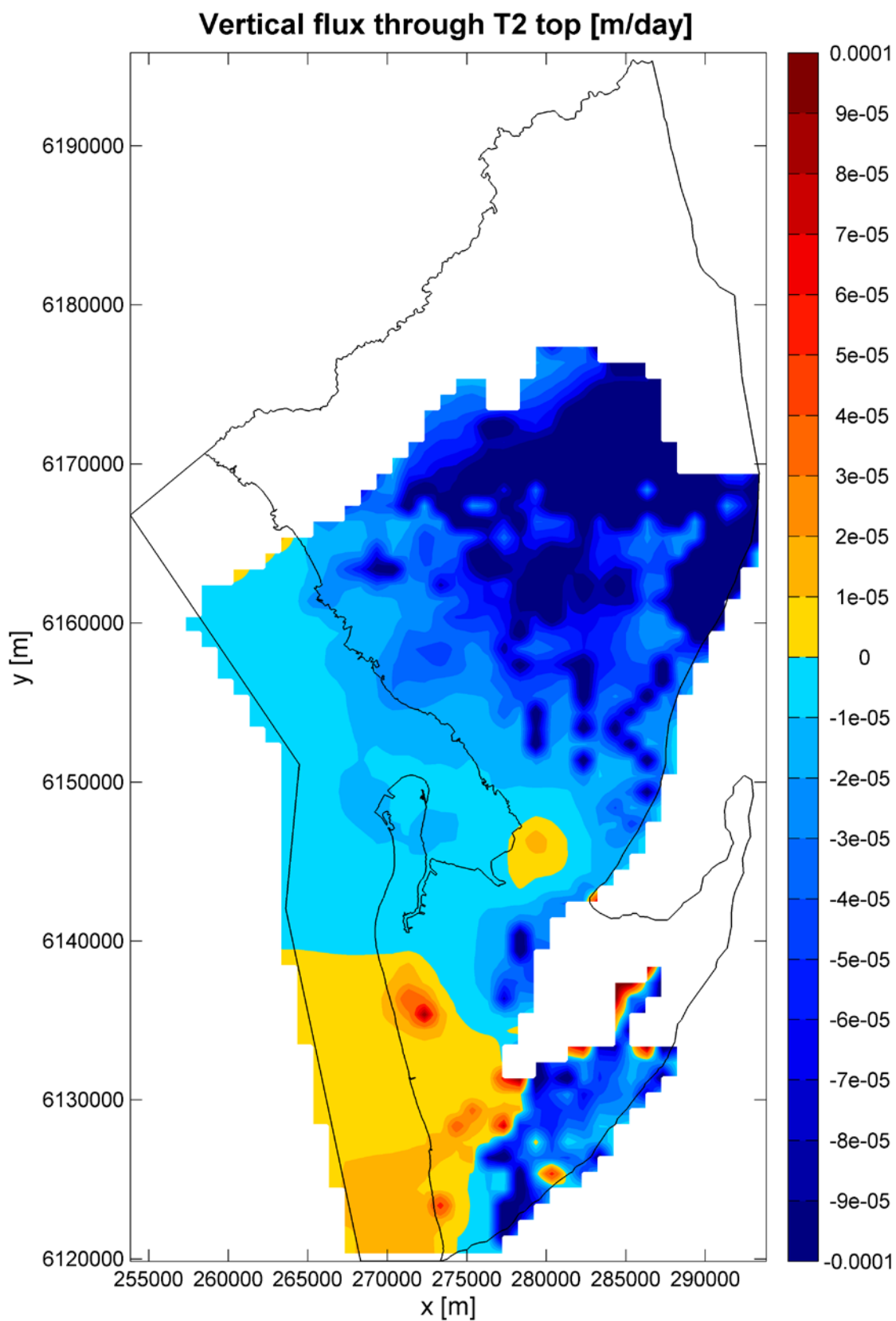
Apx Figure K.92 Simulated vertical flux through the bottom of the T1 aquifer in October 2012



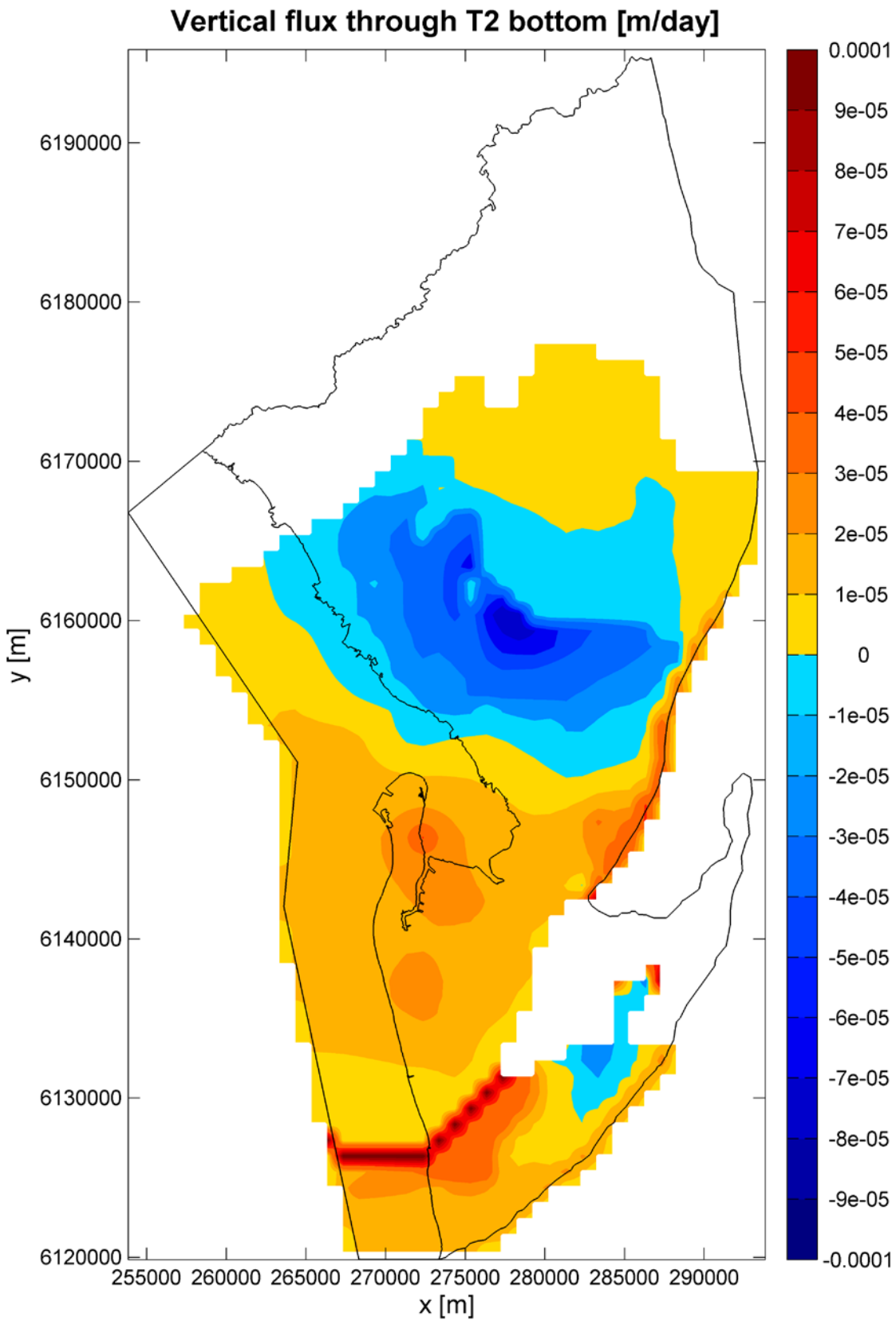
Apx Figure K.93 Simulated vertical flux through the bottom of the T1 aquifer in April 2013



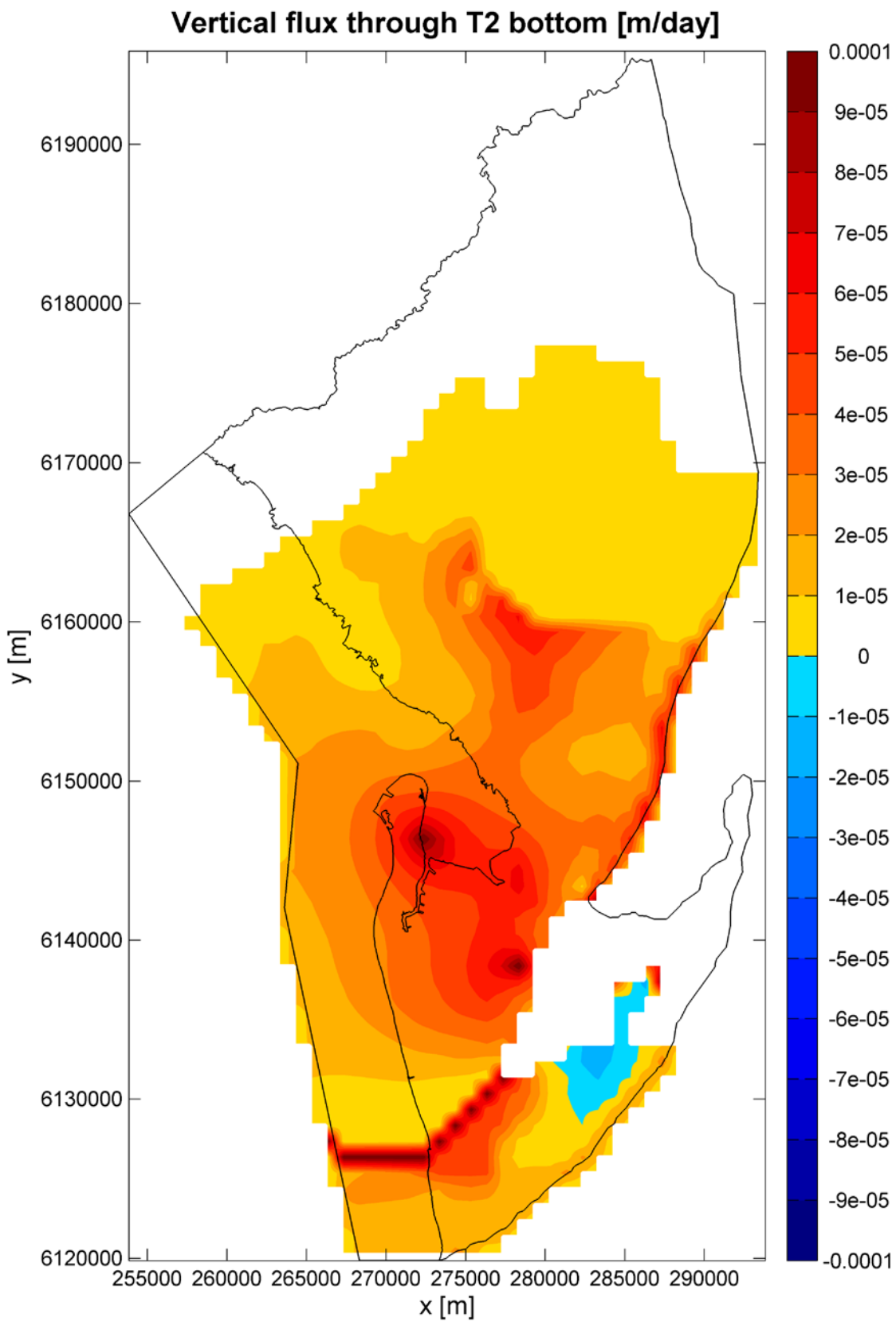
Apx Figure K.94 Simulated vertical flux through the top of the T2 aquifer in October 2012



Apx Figure K.95 Simulated vertical flux through the top of the T2 aquifer in April 2013



Apx Figure K.96 Simulated vertical flux through the bottom of the T2 aquifer in October 2012



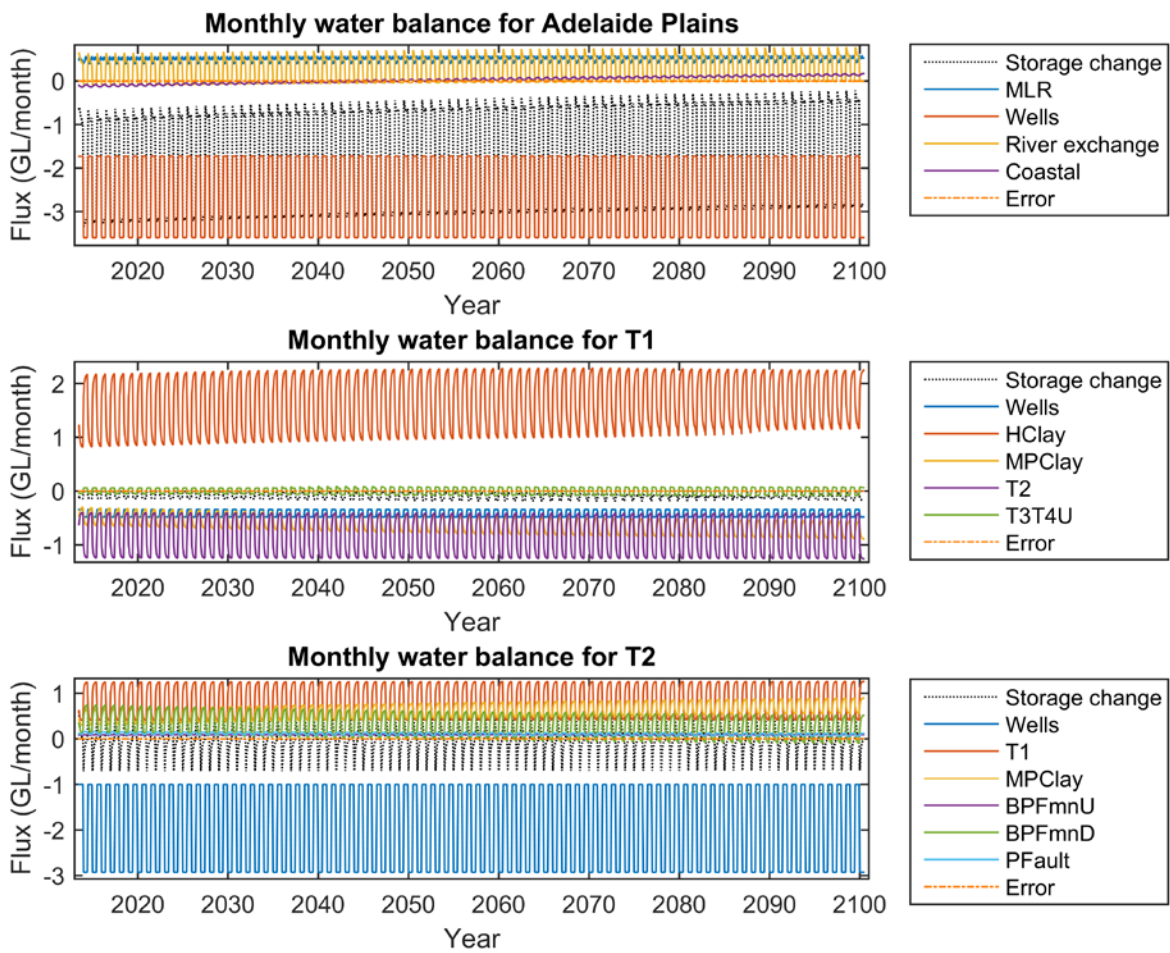
Apx Figure K.97 Simulated vertical flux through the bottom of the T2 aquifer in April 2013

Future scenarios (2013–2100)

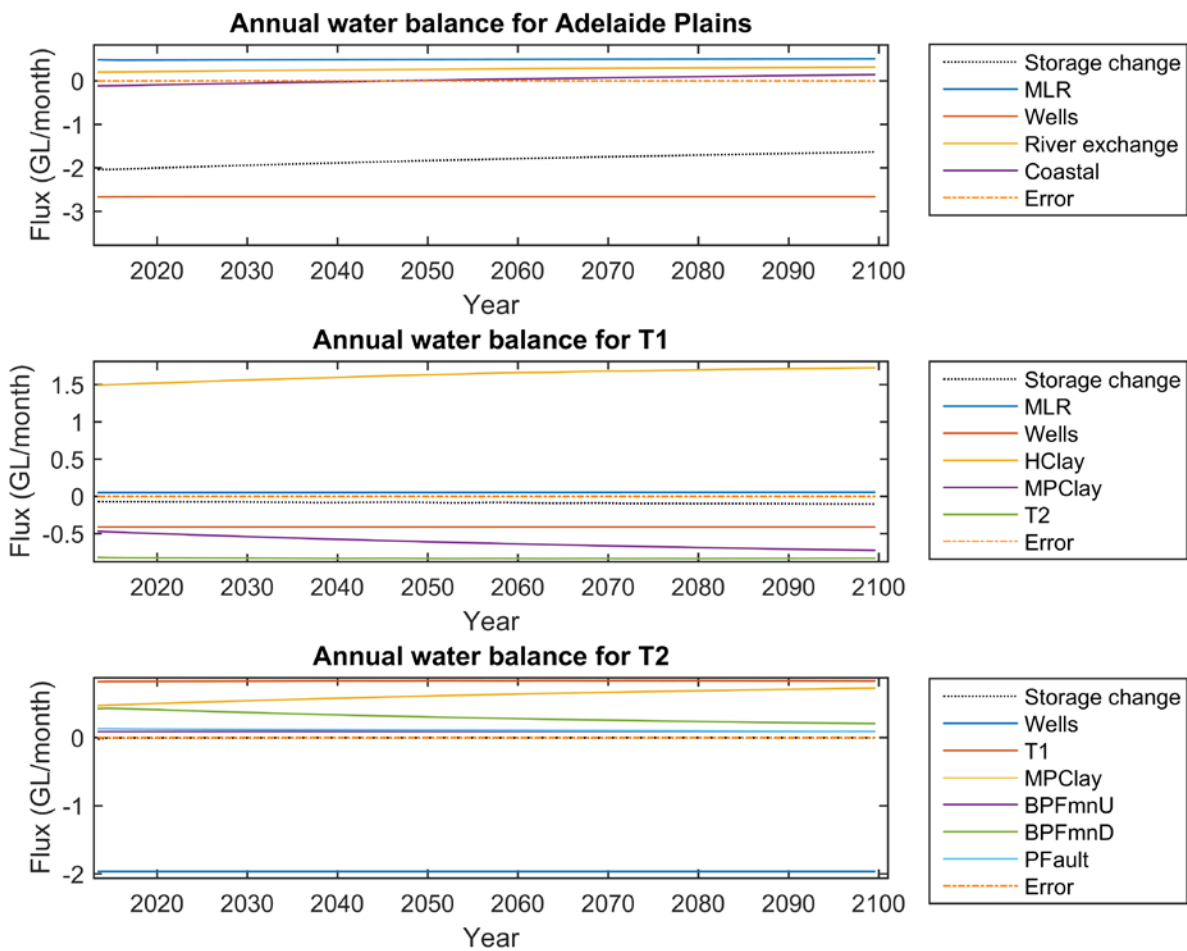
The base case for the future is presented first as the benchmark to which all other scenarios are compared to elucidate the impacts of the stresses on the system. In each of the scenario analyses the decadal water balance is presented for 2020–2030 and 2040–2050. The temporal water balance at monthly and annual time scales is presented for the overall budget and the T1 and T2 aquifer. Also, maps of head, head minus topography, head minus top of layer, and vertical flux are presented for the end of winter in 2049 and the end of summer 2050.

Base case

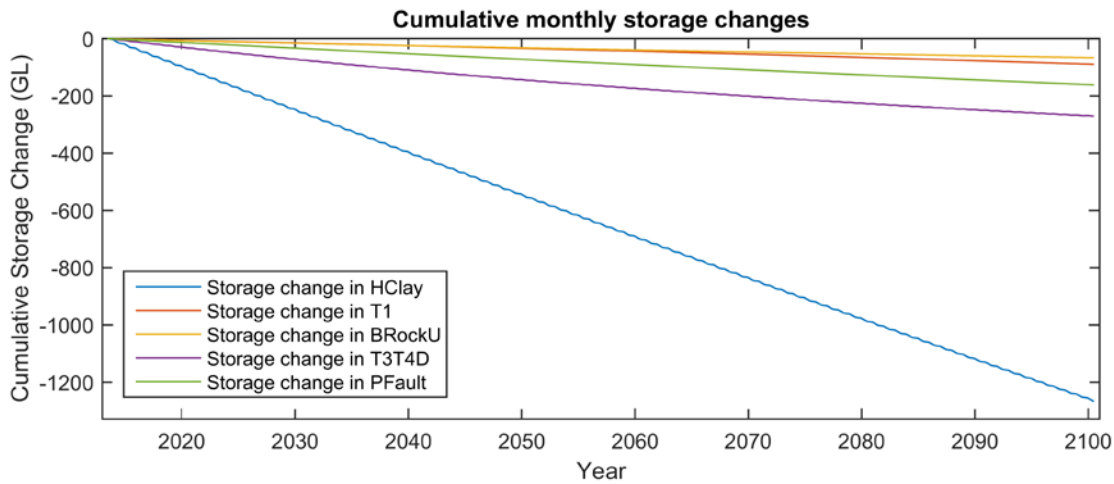
The base case future scenario shows that when the current rate of pumping is used, with the same monthly dynamics of 2012, the system continues to behave in the same manner as seen at the end of the development period. The temporal dynamics are shown in Apx Figure K.98 with the trends more apparent in the annual water balances (Apx Figure K.99). Overall it is clear that absolute values of the rate of change of storage are decreasing with time (which is indicated by the line for storage change having a positive gradient below the zero line) as there is less storage to draw from over time, which creates a greater pull from the head dependent boundaries, in particular at the coast. Internally it is apparent that the T1 aquifer is drawing more water from the Hindmarsh Clay but at the same time is also losing more water through the Munno Para Clay through to the T2 aquifer. The T2 aquifer's pumping supply is sourced from overlying aquifers when it no longer can pull from the Blanche Point formation. The cumulative change in storage in Apx Figure K.100 shows that the loss of storage to the system is quite large (850 GL yr^{-1} when summed across all zones) by 2050 and that there is no sign of this trend in storage loss changing rapidly at the end of simulation in 2100 despite the continual decrease in the absolute rate of change of storage. The decadal flux matrices at 2030 and 2050 (Apx Table K.19 and Apx Table K.20) show a system under continued stress starting to demand more of the head dependent MLR, stream and coastal boundaries to supplement storage losses and increase the inflow to the system and meet pumping demands. The decrease in hydraulic head is apparent in the Hindmarsh Clay, T1 aquifer, and T2 aquifer in Apx Figure K.101, Apx Figure K.102, and Apx Figure K.103.



Apx Figure K.98 Monthly water balance components for the whole model domain (top), T1 aquifer (middle) and T2 aquifer (bottom), for the base case scenario (2013–2100)



Apx Figure K.99 Annual water balance components for the whole model domain (top), T1 aquifer (middle) and T2 aquifer (bottom), for the base case scenario (2013–2100)



Apx Figure K.100 Cumulative changes in storage for the Hindmarsh Clay, T1 aquifer, Bedrock, T3 and T4 aquifers and Para Fault, for the base case scenario (2013–2100)

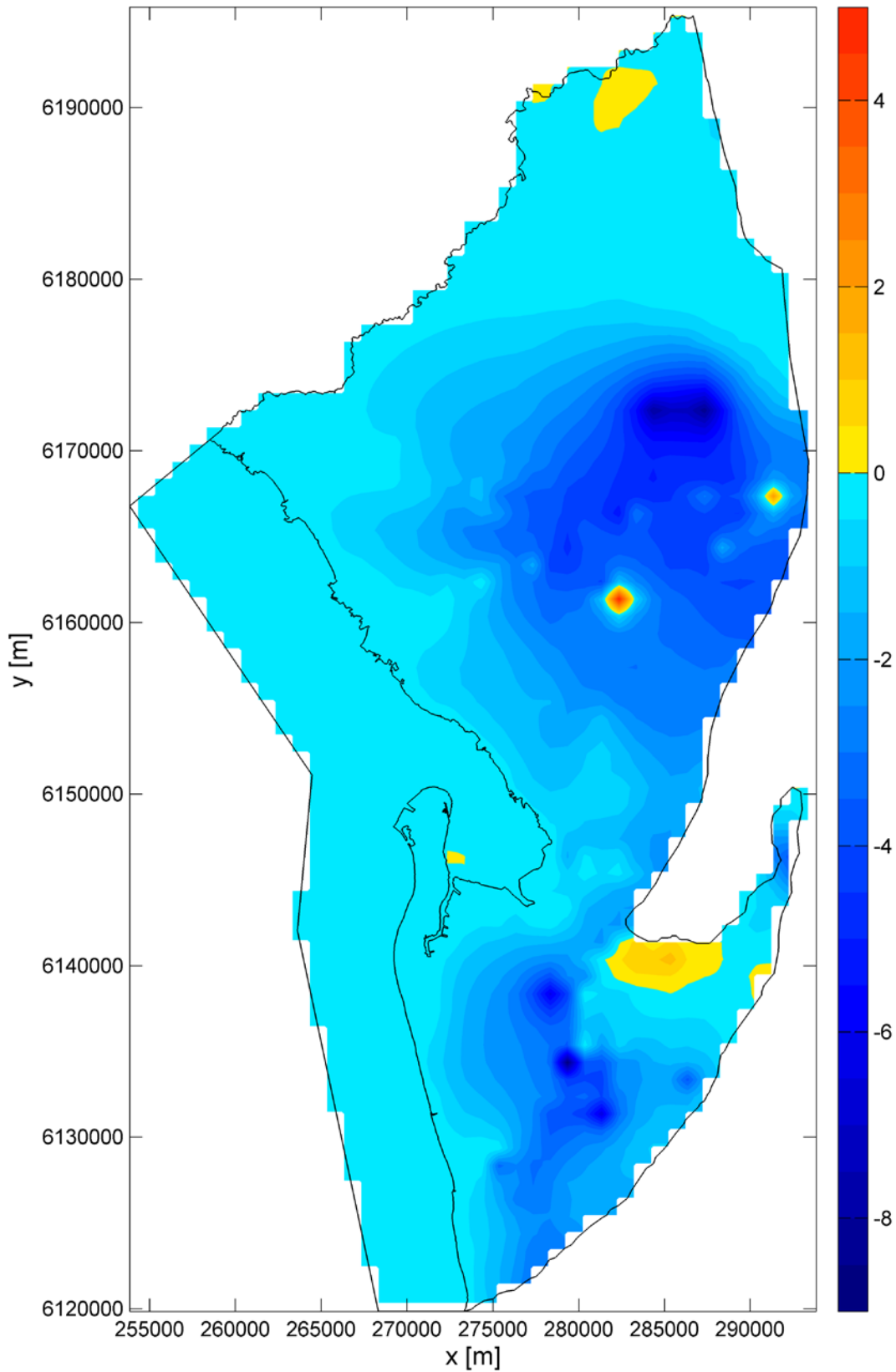
Apx Table K.19 Decadal (2020–2030) average annual flux matrix for water balance components of the base case scenario. An additional row of rate of change in storage for all zones is appended to the matrix. The same display threshold and colour scheme as for Apx Table K.14 apply

Yr 2030	Hclay	UTSand	T1	MPClay	T2	BPFmnU	T3T4U	BedrockU	BPFmnD	T3T4D	BedrockD	Pfault	MLR	Wells	Streams	Coast	Recharge
Hclay			20.13											1.04	0.73	1.79	
UTSand			0.14					1.53							3.75		
T1	1.61	0.14		6.64	10.87		0.36	0.19		0.02				4.94			
MPClay			0.42		6.65												
T2		0.21	0.93	0.42		0.06			0.61					23.96			
BPFmnU					1.13		0.08	0.03									
T3T4U			0.42			0.79		0.17							1.72		
BedrockU		2.52	0.66			0.19	2.48					0.03		0.68			
BPFmnD					5.31					0.54							
T3T4D			0.03						4.98								
BedrockD			0.02						0.03	0.06			0.06				
Pfault			0.53		1.46									0.06			
MLR	0.37	0.04	0.63		0.38	0.18		3.74	0.21	0.14	0.13	0.03					
Wells	0.07				0.30												
Streams	4.97	2.19															
Coast	0.92																
Recharge	0.62	0.02															
Storage change	-15.14	0.29	0.87		0.09		0.17	0.90	0.01	4.24	0.05	1.99					

Apx Table K.20 Decadal (2040–2050) average annual flux matrix for water balance components of the base case scenario. An additional row of rate of change in storage for all zones is appended to the matrix. The same display threshold and colour scheme as for Apx Table K.14 apply

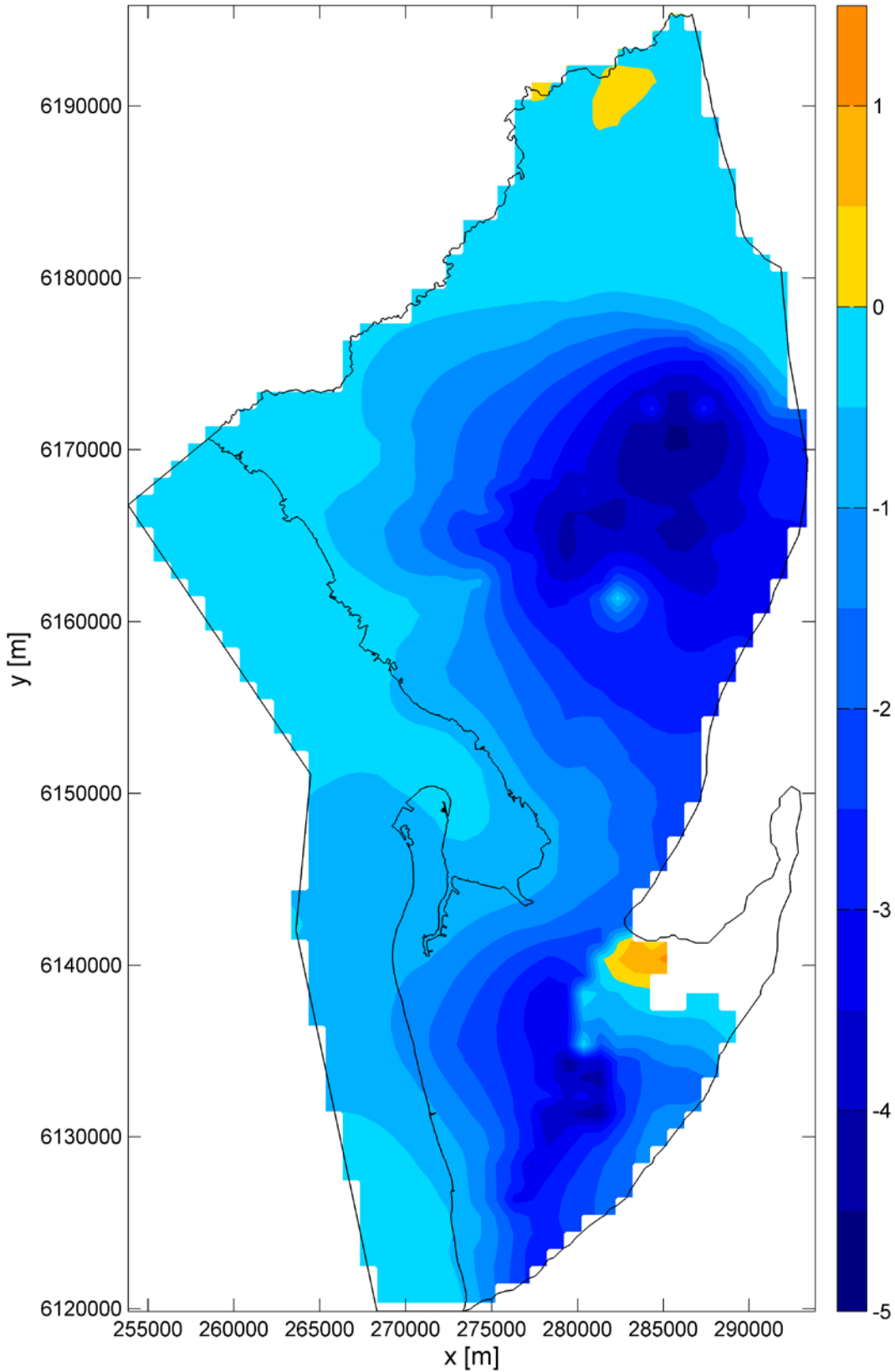
Yr 2050	Hclay	UTSand	T1	MPClay	T2	BPFmnU	T3T4U	BedrockU	BPFmnD	T3T4D	BedrockD	Pfault	MLR	Wells	Streams	Coast	Recharge
Hclay			20.90											1.04	0.64	1.47	
UTSand			0.14					1.50							3.70		
T1	1.47	0.13		7.41	11.04		0.45	0.21		0.02				4.94			
MPClay			0.30		7.42												
T2		0.21	1.02	0.30		0.06			0.63					23.96			
BPFmnU					1.14		0.08	0.03									
T3T4U			0.45			0.80		0.17							1.72		
BedrockU		2.49	0.65			0.19	2.43					0.03		0.68			
BPFmnD					4.47					0.55							
T3T4D			0.03						4.13								
BedrockD			0.02						0.03	0.05			0.06				
Pfault			0.58		1.35									0.06			
MLR	0.37	0.04	0.64		0.39	0.18		3.79	0.22	0.15	0.13	0.03					
Wells	0.07				0.30												
Streams	5.22	2.19															
Coast	1.44																
Recharge	0.62	0.02															
Storage change	-14.86	0.26	0.95		0.07		0.16	0.78		3.39	0.04	1.93					

Hydraulic head change in first layer between 2013 and 2050



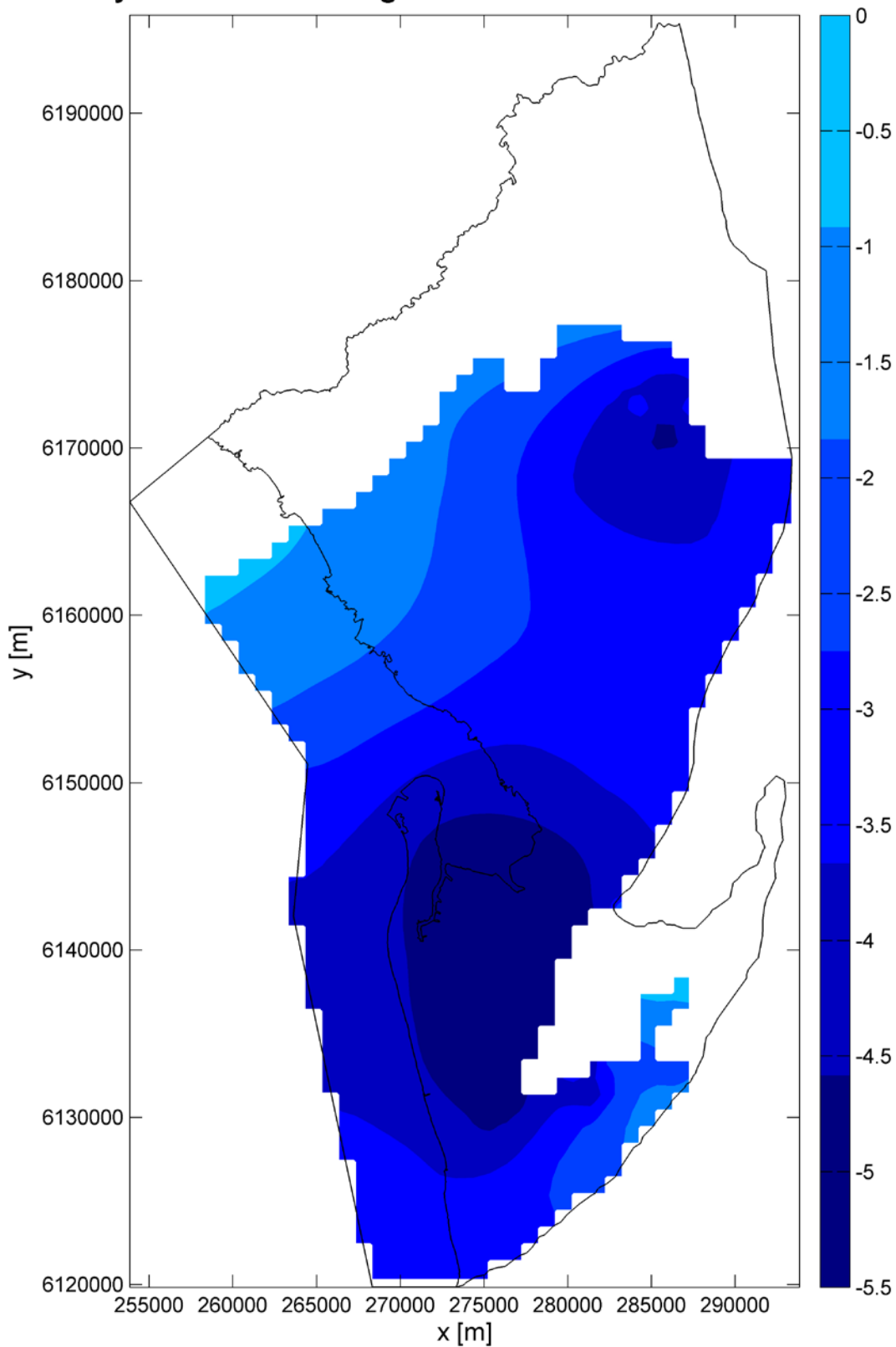
Apx Figure K.101 Hydraulic head change in the first layer between 2013 and 2050 for the base case scenario

Hydraulic head change in T1 between 2013 and 2050



Apx Figure K.102 Hydraulic head change in the T1 aquifer between 2013 and 2050 for the base case scenario.

Hydraulic head change in T2 between 2013 and 2050



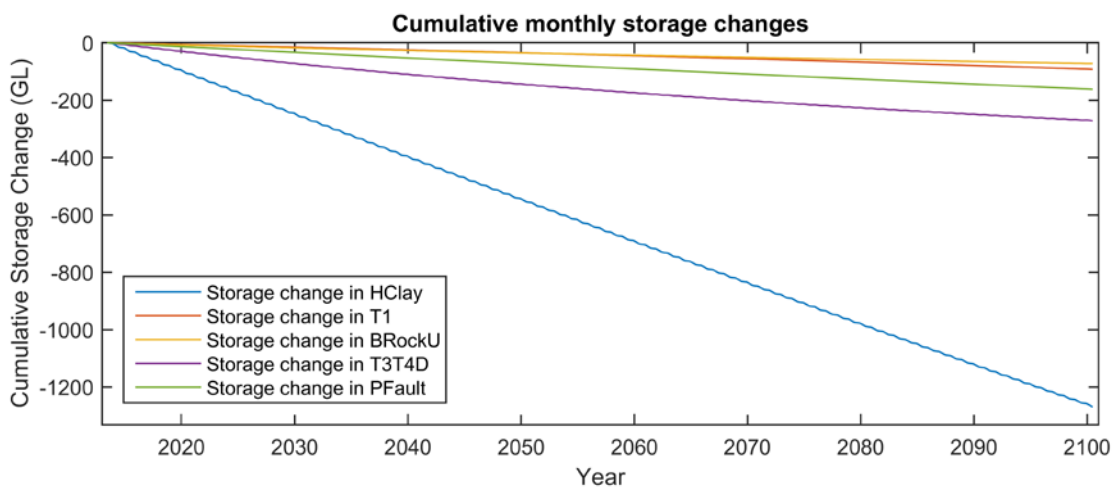
Apx Figure K.103 Hydraulic head change in the T2 aquifer between 2013 and 2050 for the base case scenario

RCP4.5

The first of the climate change scenarios RCP4.5 shows similar behaviour to the base case scenario. Storage changes are equivalent as seen in the cumulative changes (Apx Figure K.104).

The decadal flux matrices for 2030 and 2050 are shown in Apx Table K.21 and Apx Table K.22. These flux matrices demonstrate only small changes to the system dynamics between these periods, with an average decrease in the rate of change of storage and a small increase in the boundaries contribution to the system. The difference between the base case and the RCP4.5 scenarios with respect to the decadal average flux matrix from 2050 is shown in Apx Table K.23. This shows very little difference between these scenarios which is as expected in this model given the small contribution that areal recharge gives to the system. The main changes are a small increase in recharge of 0.16 GL yr⁻¹, and a reduction of 0.34 GL yr⁻¹ lateral inflow from the MLR. The final row shows that there is a small decrease in the rate of storage depletion of 0.17 GL yr⁻¹.

The changes in hydraulic head between 2013 and 2050 in the first layer (Apx Figure K.105), T1 (Apx Figure K.106) and T2 (Apx Figure K.107) aquifers shows the same patterns as in the base case with no discernible differences.



Apx Figure K.104 Cumulative changes in storage for the Hindmarsh Clay, T1 aquifer, Bedrock, T3 and T4 aquifers and Para Fault, for the RCP4.5 scenario (2013–2100)

Apx Table K.21 Decadal (2020–2030) average annual flux matrix for water balance components of the RCP4.5 scenario. An additional row of rate of change in storage for all zones is appended to the matrix. The same display threshold and colour scheme as for Apx Table K.14 apply

Yr 2030	Hclay	UTSand	T1	MPClay	T2	BPFmnU	T3T4U	BedrockU	BPFmnD	T3T4D	BedrockD	Pfault	MLR	Wells	Streams	Coast	Recharge
Hclay			20.18											1.04	0.73	1.82	
UTSand			0.14					1.57							3.72		
T1	1.60	0.14		6.65	10.89		0.36	0.19		0.02				4.94			
MPClay			0.42		6.66												
T2		0.21	0.93	0.41		0.06			0.61					23.96			
BPFmnU					1.12		0.08	0.03									
T3T4U			0.42			0.79		0.17						1.72			
BedrockU		2.47	0.64			0.19	2.47					0.03		0.68			
BPFmnD					5.31					0.54							
T3T4D			0.03						4.99								
BedrockD			0.02						0.03	0.06			0.02				
Pfault			0.53		1.46									0.06			
MLR	0.35	0.04	0.60		0.36	0.17		3.52	0.20	0.14	0.08	0.02					
Wells	0.07				0.30												
Streams	4.96	2.20															
Coast	0.86																
Recharge	0.79	0.03															
Storage change	-15.16	-0.34	-0.89		-0.09		-0.18	-1.00	-0.01	-4.26	-0.05	-1.99					

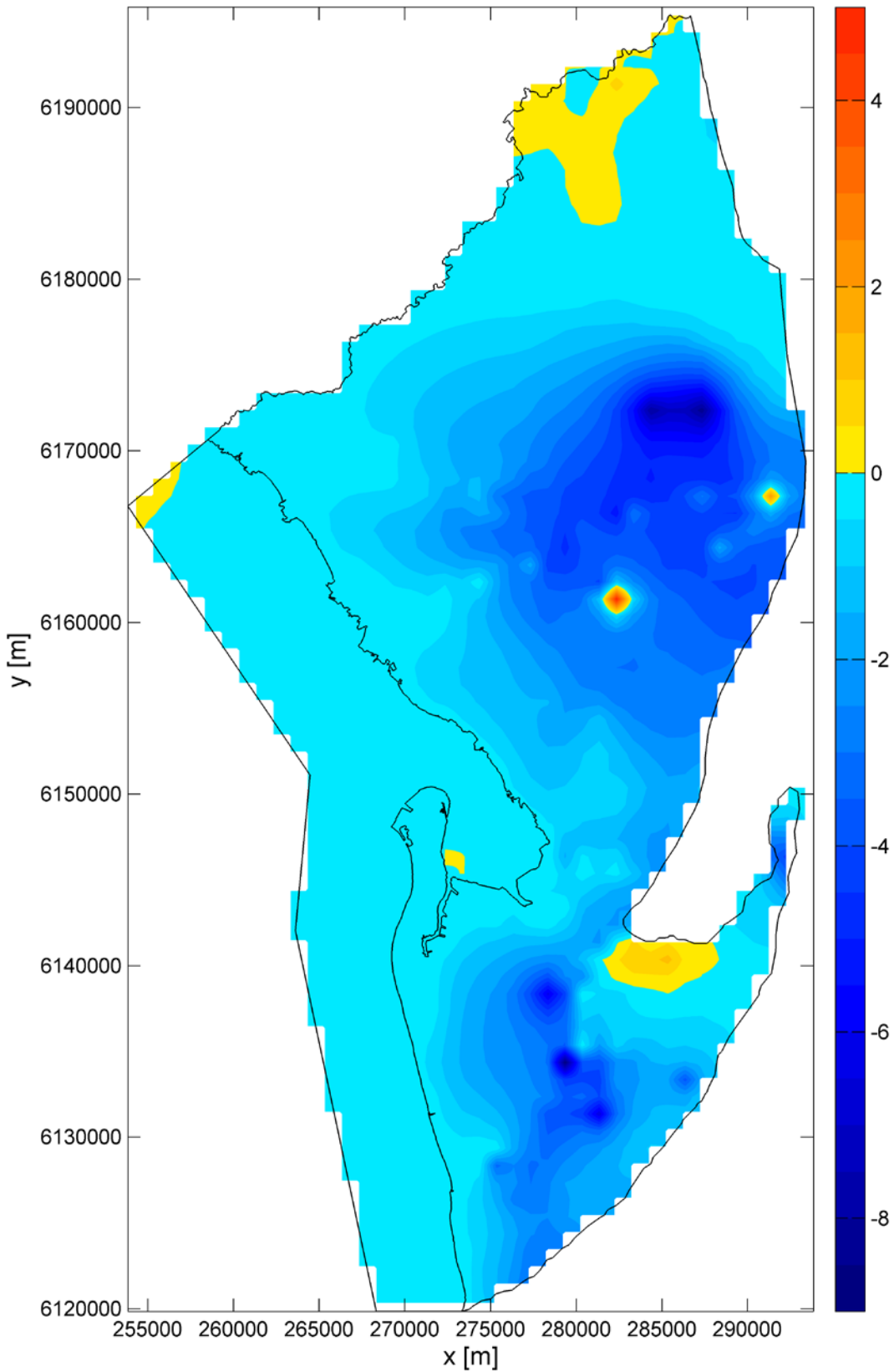
Apx Table K.22 Decadal (2040–2050) average annual flux matrix for water balance components of the RCP4.5 scenario. An additional row of rate of change in storage for all zones is appended to the matrix. The same display threshold and colour scheme as for Apx Table K.14 apply

Yr 2050	Hclay	UTSand	T1	MPClay	T2	BPFmnU	T3T4U	BedrockU	BPFmnD	T3T4D	BedrockD	Pfault	MLR	Wells	Streams	Coast	Recharge
Hclay			20.96											1.04	0.63	1.49	
UTSand			0.14					1.54							3.66		
T1	1.46	0.13		7.42	11.05		0.46	0.22		0.02				4.94			
MPClay			0.30		7.44												
T2		0.21	1.02	0.30		0.06			0.63						23.96		
BPFmnU					1.13		0.08	0.03									
T3T4U			0.45			0.80		0.16							1.72		
BedrockU		2.43	0.63			0.19	2.41					0.03		0.68			
BPFmnD					4.46					0.55							
T3T4D			0.03						4.14								
BedrockD			0.02						0.03	0.05			0.02				
Pfault			0.57		1.35									0.06			
MLR	0.36	0.04	0.61		0.37	0.18		3.59	0.21	0.14	0.08	0.02					
Wells	0.07				0.30												
Streams	5.21	2.22															
Coast	1.37																
Recharge	0.78	0.03															
Storage change	-14.88	-0.29	-0.98		-0.07		-0.17	-0.84		-3.40	-0.04	-1.93					

Apx Table K.23 Difference between base case and RCP4.5 in the decadal (2040–2050) average annual flux matrix. Values below 1×10^{-3} are not shown

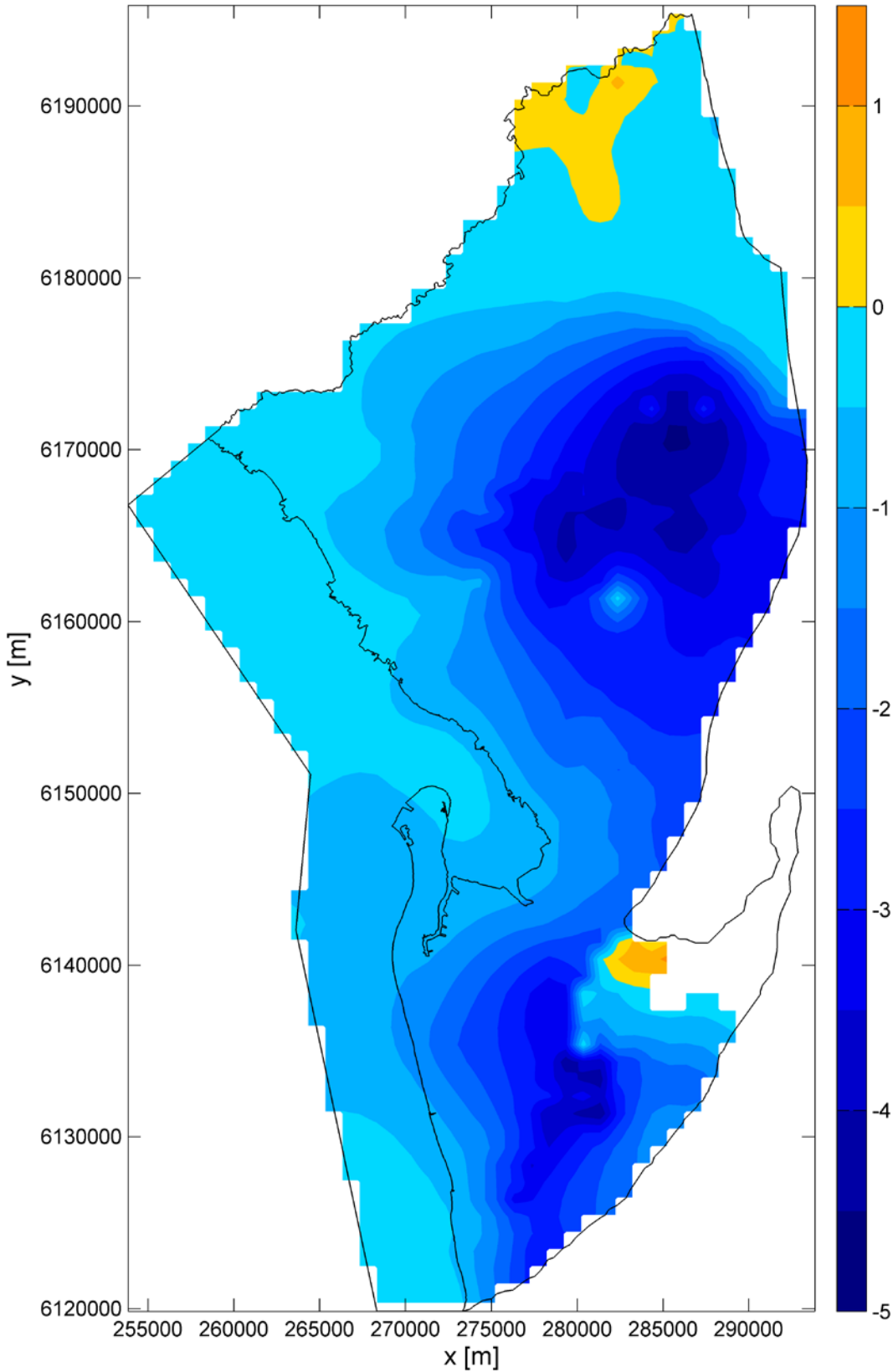
Yr 2050	Hclay	UTSand	T1	MPClay	T2	BPFmnU	T3T4U	BedrockU	BPFmnD	T3T4D	BedrockD	Pfault	MLR	Wells	Streams	Coast	Recharge
Hclay			0.06											0.00	-0.01	0.03	
UTSand			0.00					0.04							-0.04		
T1	-0.01	0.00		0.01	0.02		0.01	0.01		0.00				0.00			
MPClay			0.00		0.01												
T2		0.00	0.00	0.00		0.00			0.00					0.00			
BPFmnU					-0.01		0.00	0.00									
T3T4U			0.00			0.00		-0.01						0.00			
BedrockU		-0.06	-0.02			0.00	-0.02					0.00		0.00			
BPFmnD					-0.01					0.00							
T3T4D			0.00						0.00								
BedrockD			0.00						0.00	0.00							
Pfault			0.00		0.00									0.00			
MLR	-0.02	0.00	-0.03		-0.02	-0.01		-0.20	-0.01	-0.01	-0.04	0.00					
Wells	0.00				0.00												
Streams	-0.01	0.02															
Coast	-0.07																
Recharge	0.16	0.00															
Storage change	-0.02	-0.04	-0.03		0.00		-0.01	-0.06		-0.01	0.00	0.00					

Hydraulic head change in first layer between 2013 and 2050



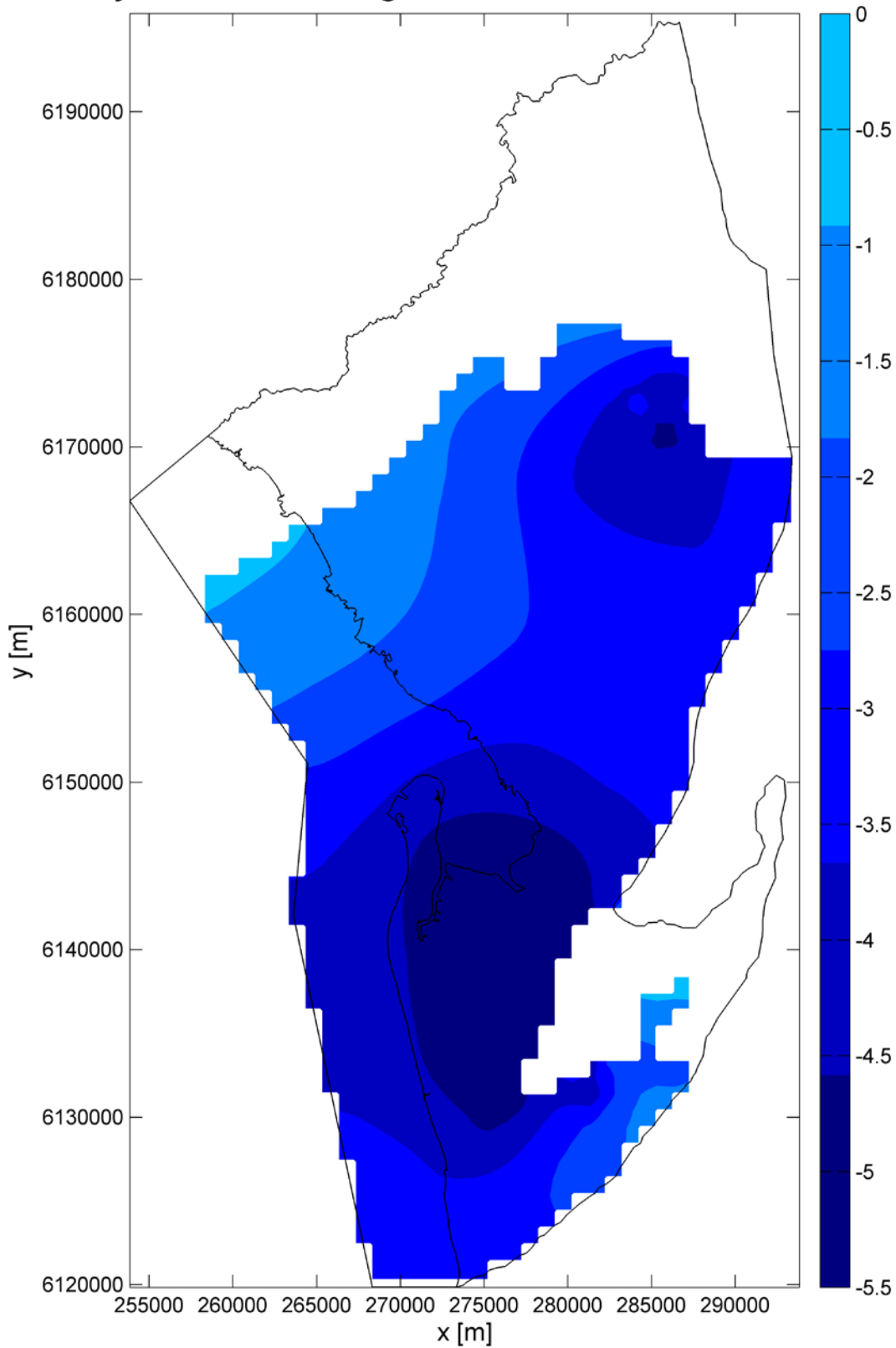
Apx Figure K.105 Hydraulic head change in the first layer between 2013 and 2050 for the RCP4.5 scenario

Hydraulic head change in T1 between 2013 and 2050



Apx Figure K.106 Hydraulic head change in the T1 aquifer between 2013 and 2050 for the RCP4.5 scenario

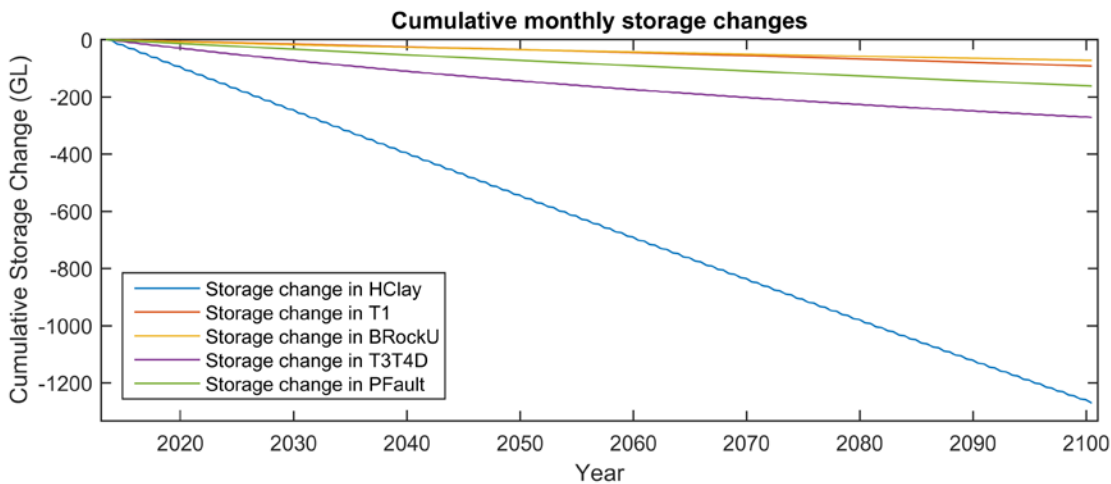
Hydraulic head change in T2 between 2013 and 2050



Apx Figure K.107 Hydraulic head change in the T2 aquifer between 2013 and 2050 for the RCP4.5 scenario

RCP8.5

The RCP8.5 scenario considers a higher emissions future which results in less rainfall to the Adelaide Plains compared to the RCP4.5 scenario. The cumulative change in storage is presented in Apx Figure K.108 and shows the same decreases in storage as was seen in the base case. The decadal flux matrices at 2030 and 2050 are shown in Apx Table K.24 and Apx Table K.25. A comparison with the base case for the decadal flux matrix at 2050 in Apx Table K.26 shows only marginal differences in the fluxes and rates of change in storage. The main changes are similar to RCP4.5 with a small increase in recharge of 0.13 GL yr^{-1} , and a reduction of 0.33 GL yr^{-1} lateral inflow from the MLR. The final row also shows that there is a small decrease in the rate of storage depletion of 0.19 GL yr^{-1} . Similarly the changes in head between 2013 and 2050 for the first layer (Apx Figure K.109), T1 aquifer (Apx Figure K.110) and T2 aquifer (Apx Figure K.111) have little difference as compared to the base case.



Apx Figure K.108 Cumulative changes in storage for the Hindmarsh Clay, T1 aquifer, Bedrock, T3 and T4 aquifers and Para Fault, for the RCP8.5 scenario (2013–2100)

ApX Table K.24 Decadal (2020–2030) average annual flux matrix for water balance components of the RCP8.5 scenario. An additional row of rate of change in storage for all zones is appended to the matrix. The same display threshold and colour scheme as for ApX Table K.14 apply

Yr 2030	Hclay	UTSand	T1	MPClay	T2	BPFmnU	T3T4U	BedrockU	BPFmnD	T3T4D	BedrockD	Pfault	MLR	Wells	Streams	Coast	Recharge
Hclay			20.18											1.04	0.73	1.83	
UTSand			0.14					1.56							3.72		
T1	1.60	0.14		6.65	10.89		0.36	0.19		0.02				4.94			
MPClay			0.42		6.66												
T2		0.21	0.93	0.41		0.06			0.61					23.96			
BPFmnU					1.12		0.08	0.03									
T3T4U			0.42			0.79		0.17						1.72			
BedrockU		2.48	0.64			0.19	2.47					0.03		0.68			
BPFmnD					5.31					0.54							
T3T4D			0.03						4.99								
BedrockD			0.02						0.03	0.06			0.03				
Pfault			0.53		1.46									0.06			
MLR	0.35	0.04	0.60		0.37	0.17		3.56	0.20	0.14	0.08	0.02					
Wells	0.07				0.30												
Streams	4.96	2.19															
Coast	0.85																
Recharge	0.81	0.03															
Storage change	-15.14	-0.34	-0.89		-0.09		-0.18	-0.99	-0.01	-4.26	-0.05	-1.99					

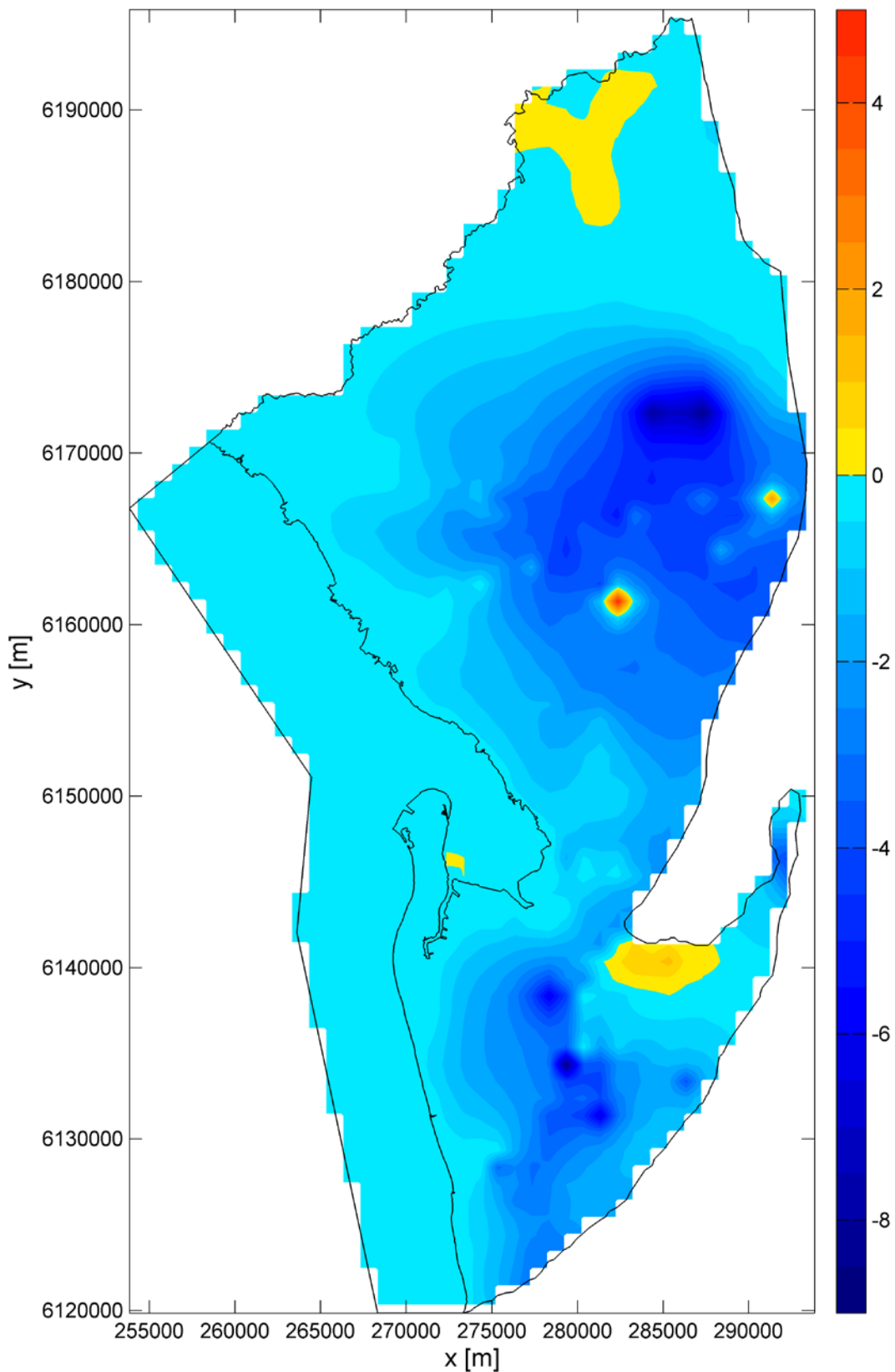
ApX Table K.25 Decadal (2040–2050) average annual flux matrix for water balance components of the RCP8.5 scenario. An additional row of rate of change in storage for all zones is appended to the matrix. The same display threshold and colour scheme as for ApX Table K.14 apply

Yr 2050	Hclay	UTSand	T1	MPClay	T2	BPFmnU	T3T4U	BedrockU	BPFmnD	T3T4D	BedrockD	Pfault	MLR	Wells	Streams	Coast	Recharge
Hclay			20.95											1.04	0.63	1.49	
UTSand			0.14					1.54							3.67		
T1	1.46	0.13		7.42	11.05		0.46	0.21		0.02				4.94			
MPClay			0.30		7.44												
T2		0.21	1.02	0.30		0.06			0.63					23.96			
BPFmnU					1.13		0.08	0.03									
T3T4U			0.45			0.80		0.16						1.72			
BedrockU		2.43	0.63			0.19	2.41					0.03		0.68			
BPFmnD					4.46					0.55							
T3T4D			0.03						4.14								
BedrockD			0.02						0.03	0.05			0.03				
Pfault			0.57		1.35									0.06			
MLR	0.36	0.04	0.61		0.37	0.18		3.60	0.21	0.14	0.08	0.02					
Wells	0.07				0.30												
Streams	5.22	2.21															
Coast	1.37																
Recharge	0.75	0.02															
Storage change	-14.90	-0.29	-0.98		-0.07		-0.17	-0.84		-3.40	-0.04	-1.93					

ApX Table K.26 Difference between base case and RCP8.5 in the decadal (2040–2050) average annual flux matrix. Values below 1x10⁻³ are not shown

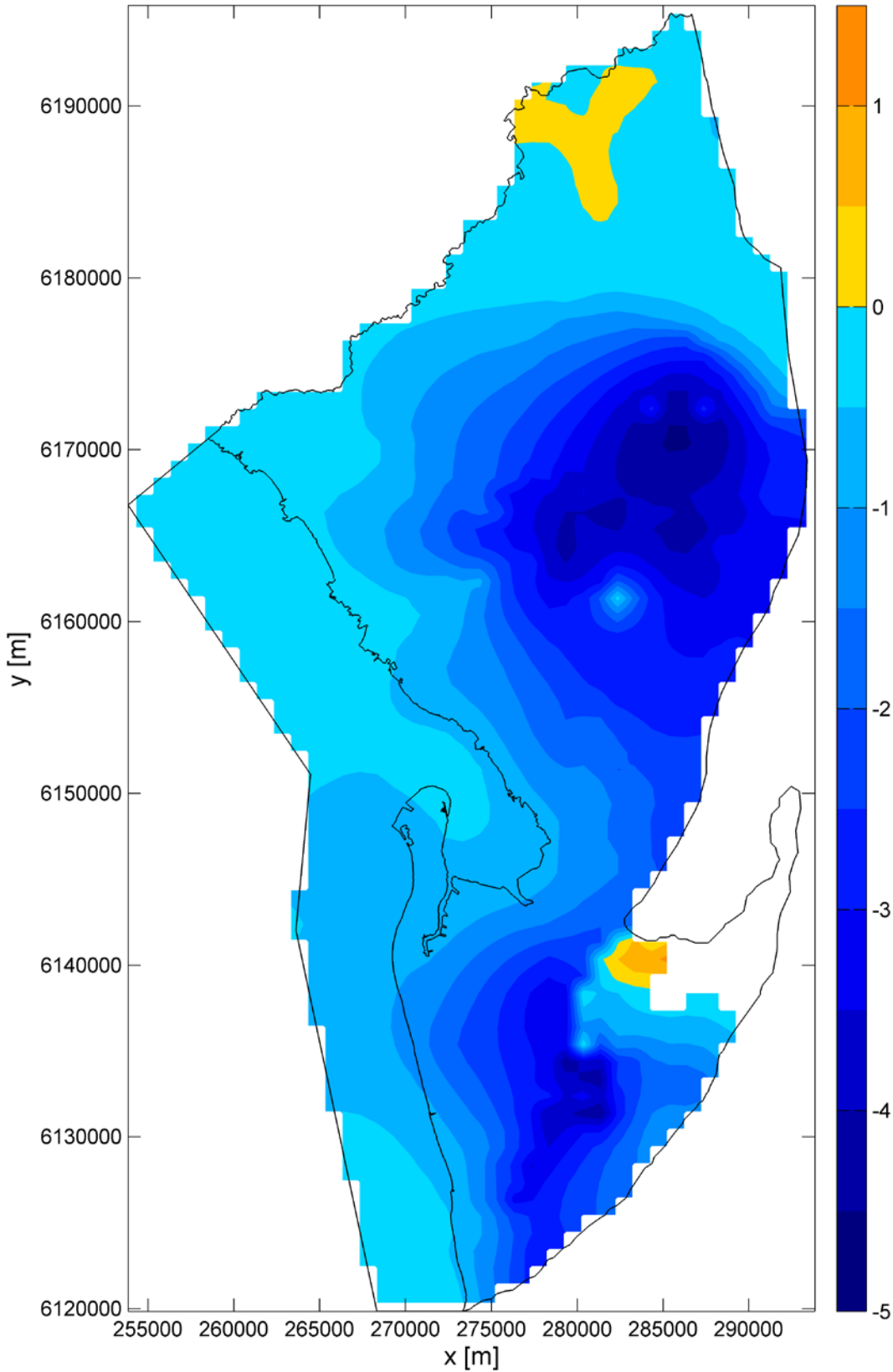
Yr 2050	Hclay	UTSand	T1	MPClay	T2	BPFmnU	T3T4U	BedrockU	BPFmnD	T3T4D	BedrockD	Pfault	MLR	Wells	Streams	Coast	Recharge
Hclay			0.05											0.00		0.02	
UTSand			0.00					0.03							-0.01		
T1	-0.01	0.00		0.01	0.02		0.01	0.01		0.00				0.00			
MPClay			0.00		0.01												
T2		0.00	0.00	0.00		0.00			0.00					0.00			
BPFmnU					-0.01		0.00	0.00									
T3T4U			0.00			0.00		0.00						0.00			
BedrockU		-0.06	-0.02			0.00	-0.02					0.00		0.00			
BPFmnD					-0.01					0.00							
T3T4D			0.00						0.00								
BedrockD			0.00						0.00	0.00			-0.03				
Pfault			0.00		0.00									0.00			
MLR	-0.02	0.00	-0.03		-0.02	-0.01		-0.19	-0.01	-0.01	-0.04	0.00					
Wells	0.00				0.00												
Streams	-0.01	0.02															
Coast	-0.06																
Recharge	0.13	0.00															
Storage change	-0.04	-0.03	-0.03		0.00		-0.01	-0.06		-0.01	-0.01	0.00					

Hydraulic head change in first layer between 2013 and 2050



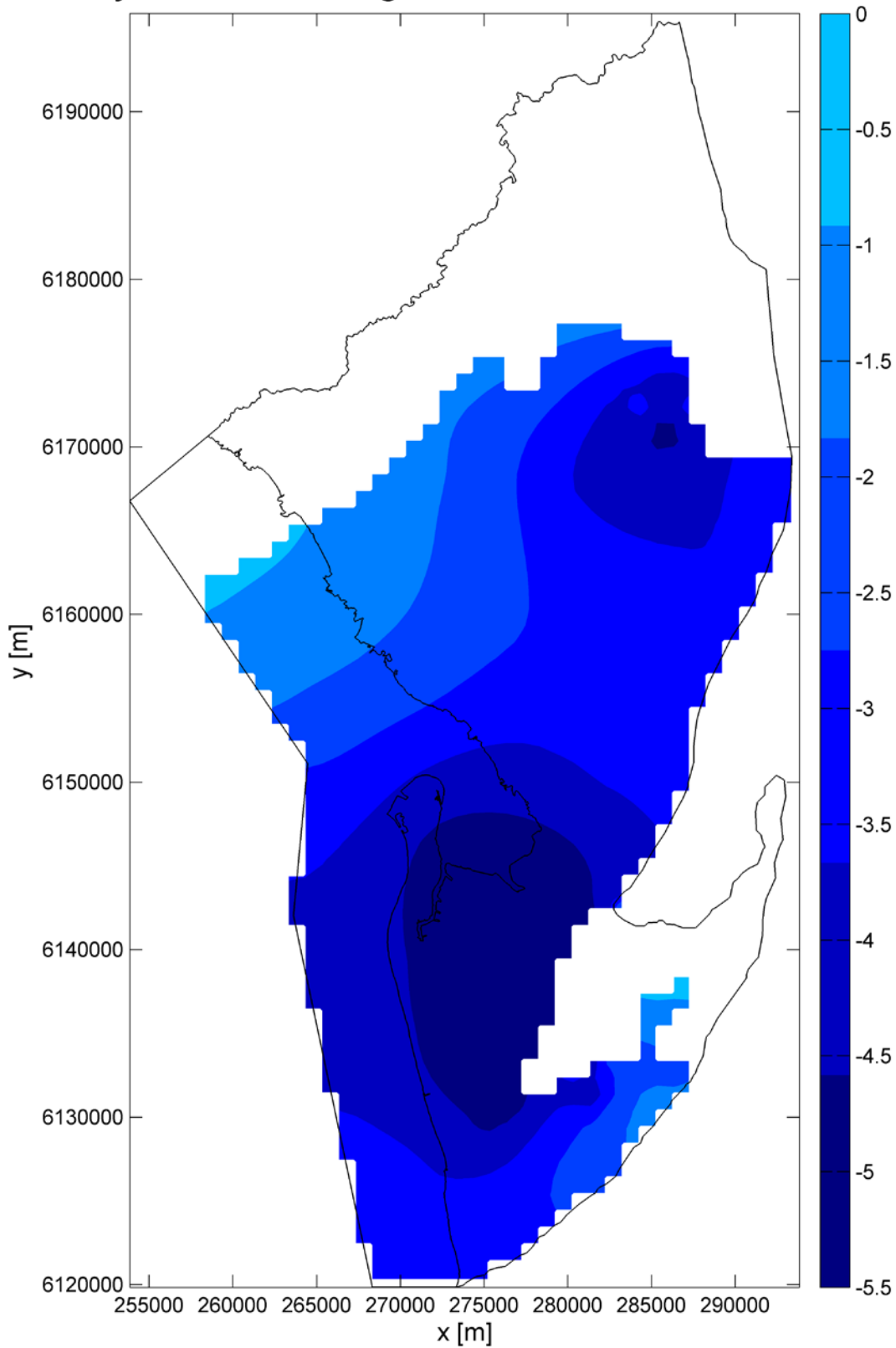
Apx Figure K.109 Hydraulic head change in the first layer between 2013 and 2050 for the RCP8.5 scenario

Hydraulic head change in T1 between 2013 and 2050



Apx Figure K.110 Hydraulic head change in the T1 aquifer between 2013 and 2050 for the RCP8.5 scenario

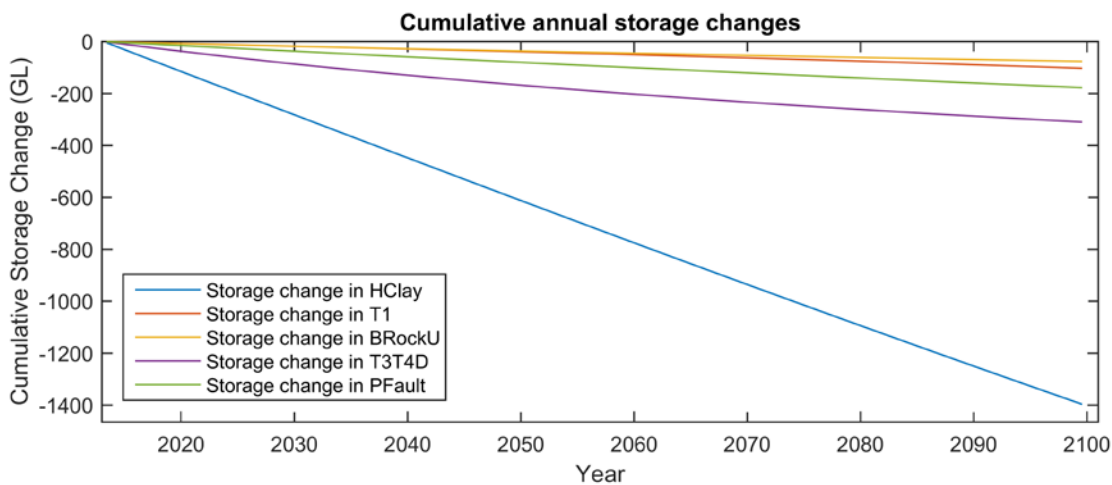
Hydraulic head change in T2 between 2013 and 2050



Apx Figure K.111 Hydraulic head change in the T2 aquifer between 2013 and 2050 for the RCP8.5 scenario

Increased Pumping

This scenario assesses the effect of pumping at rates that correspond to the full allocation of groundwater. The cumulative change in storage is presented in Apx Figure K.112. This shows that by the year 2100 there is an extra 135 GL removed from storage in the Hindmarsh Clay when compared to the base case. The decadal flux matrices for 2030 and 2050 are shown in Apx Table K.27 and Apx Table K.28. The comparison for the decadal flux matrix for 2050 to the base case is shown in Apx Table K.29. The first notable difference is the pumping which has increased 10%. The Hindmarsh Clay is losing 1.66 GL yr⁻¹ more from storage than in the base case. Also the flow downwards from the Hindmarsh Clay to the T1 has increased, as has the downward flow both directly and across the Munno Para Clay from the T1 aquifer to the T2 aquifer. The changes in hydraulic head between 2013 and 2050 are shown for the first layer (Apx Figure K.113), the T1 aquifer (Apx Figure K.114) and the T2 aquifer (Apx Figure K.115). In comparison to the base case the patterns are similar but the magnitude of the changes has increased.



Apx Figure K.112 Cumulative changes in storage for the the Hindmarsh Clay, T1 aquifer, Bedrock, T3 and T4 aquifers and Para Fault, for the Increased pumping scenario (2013–2100)

Apx Table K.27 Decadal (2020–2030) average annual flux matrix for water balance components of the Increased Pumping scenario. An additional row of rate of change in storage for all zones is appended to the matrix. The same display threshold and colour scheme as for Apx Table K.14 apply

Yr 2030	Hclay	UTSand	T1	MPClay	T2	BPFmnU	T3T4U	BedrockU	BPFmnD	T3T4D	BedrockD	Pfault	MLR	Wells	Streams	Coast	Recharge
Hclay			21.92											1.15	0.70	1.70	
UTSand			0.14					1.55							3.74		
T1	1.52	0.14		7.26	11.76		0.43	0.19		0.02				5.43			
MPClay			0.40		7.27												
T2		0.21	0.92	0.39		0.06			0.63					26.35			
BPFmnU					1.14		0.08	0.03									
T3T4U			0.41				0.80	0.17						1.89			
BedrockU		2.51	0.66			0.19	2.58					0.03		0.75			
BPFmnD					6.03												
T3T4D			0.04						5.69								
BedrockD			0.02						0.03	0.06			0.06				
Pfault			0.58		1.60									0.06			
MLR	0.37	0.04	0.63		0.38	0.18		3.74	0.21	0.15	0.13	0.03					
Wells	0.07				0.30												
Streams	5.03	2.19															
Coast	1.10																
Recharge	0.62	0.02															
Storage change	-16.75	-0.32	-1.05		-0.08		-0.18	-1.03	-0.01	-4.94	-0.05	-2.19					

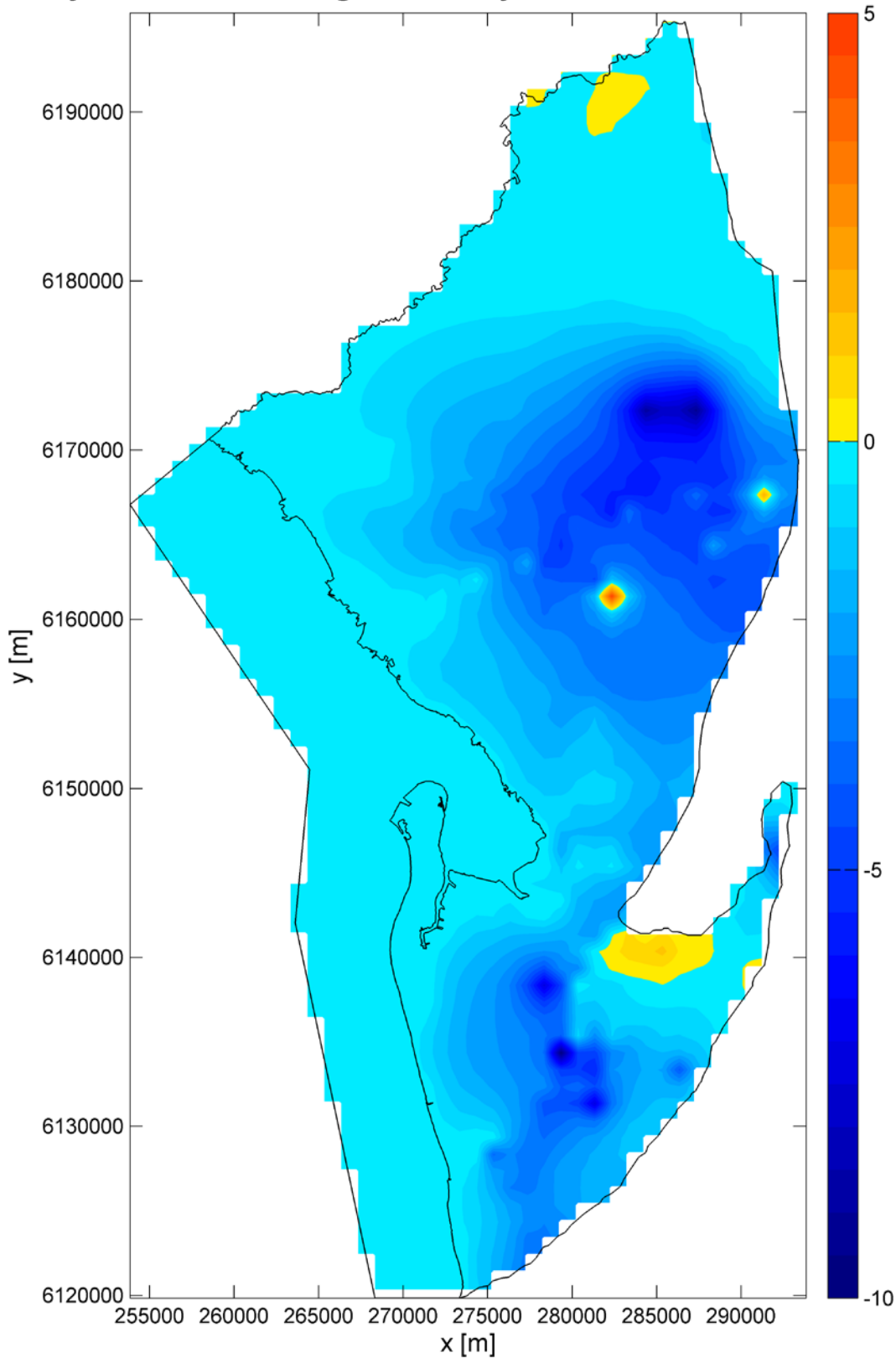
ApX Table K.28 Decadal (2040–2050) average annual flux matrix for water balance components of the Increased Pumping scenario. An additional row of rate of change in storage for all zones is appended to the matrix. The same display threshold and colour scheme as for ApX Table K.14 apply

Yr 2050	Hclay	UTSand	T1	MPClay	T2	BPFmnU	T3T4U	BedrockU	BPFmnD	T3T4D	BedrockD	Pfault	MLR	Wells	Streams	Coast	Recharge
Hclay			22.95											1.14	0.62	1.35	
UTSand			0.14					1.53							3.69		
T1	1.40	0.13		8.20	12.06		0.56	0.22		0.02				5.43			
MPClay			0.28		8.22												
T2		0.21	1.13	0.27		0.07			0.67					26.35			
BPFmnU					1.15		0.08	0.03									
T3T4U			0.50			0.82		0.15						1.89			
BedrockU		2.47	0.65			0.19	2.51					0.03		0.75			
BPFmnD					5.02						0.59						
T3T4D			0.04						4.67								
BedrockD			0.02						0.03	0.06			0.06				
Pfault			0.63		1.48									0.06			
MLR	0.37	0.04	0.64		0.39	0.18		3.80	0.22	0.15	0.13	0.03					
Wells	0.07				0.30												
Streams	5.36	2.20															
Coast	1.73																
Recharge	0.62	0.02															
Storage change	-16.52	-0.28	-1.06		-0.08		-0.19	-0.88	-0.01	-3.88	-0.05	-2.12					

ApX Table K.29 Difference between base case and increased pumping in the decadal (2040–2050) average annual flux matrix. Values below 1×10^{-3} are not shown

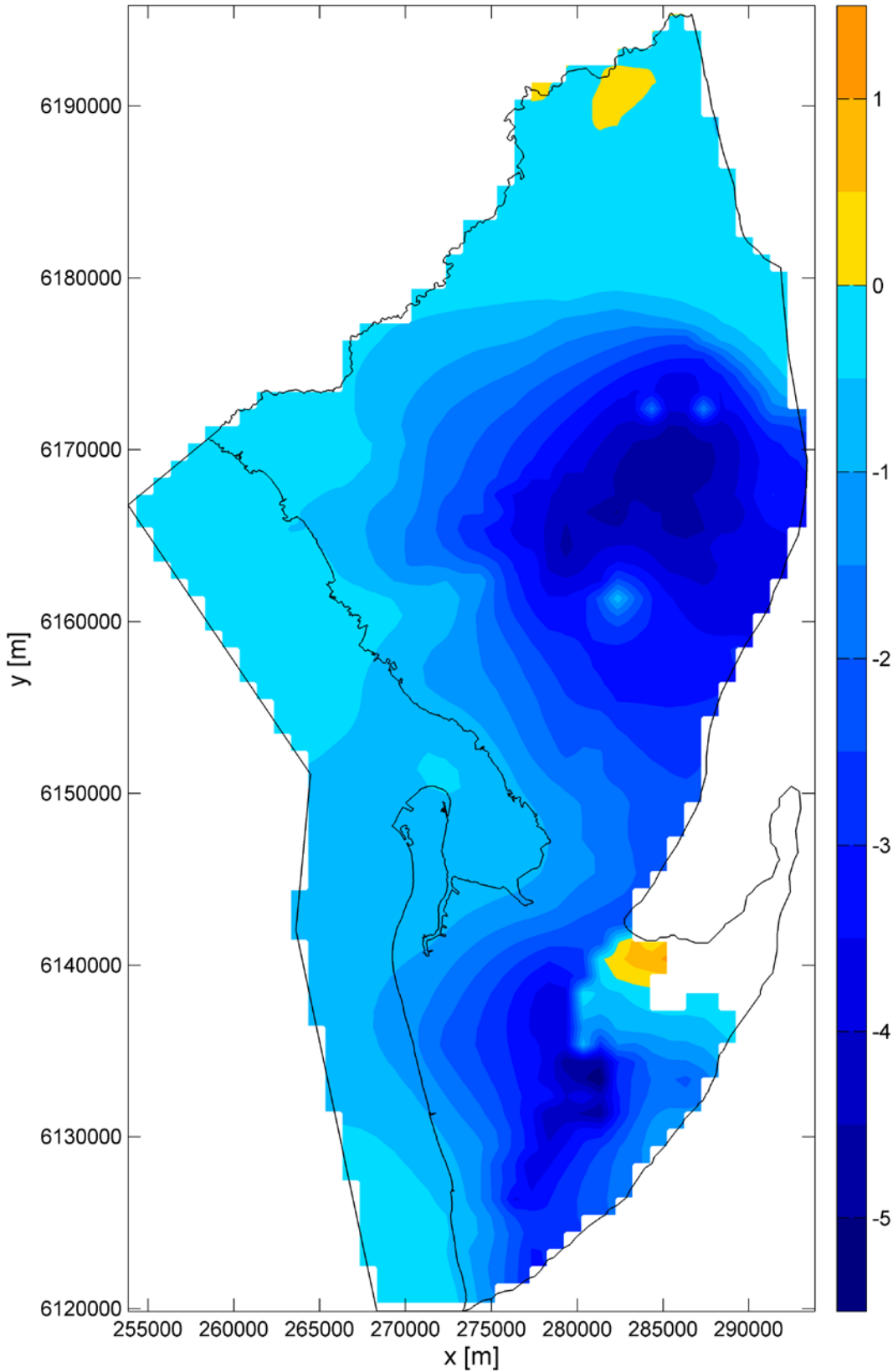
Yr 2050	Hclay	UTSand	T1	MPClay	T2	BPFmnU	T3T4U	BedrockU	BPFmnD	T3T4D	BedrockD	Pfault	MLR	Wells	Streams	Coast	Recharge
Hclay			2.05											0.10	-0.02	-0.11	
UTSand			0.00					0.02							-0.01		
T1	-0.07	0.00		0.79	1.02		0.11	0.01		0.00				0.49			
MPClay			-0.03		0.79												
T2		0.00	0.11	-0.03		0.00			0.04					2.39			
BPFmnU					0.01		0.00	0.00									
T3T4U			0.05			0.01		-0.02						0.17			
BedrockU		-0.02	0.00			0.00	0.08					0.00		0.07			
BPFmnD					0.55					0.04							
T3T4D			0.00						0.54								
BedrockD			0.00						0.00	0.00			0.00				
Pfault			0.06		0.13									0.01			
MLR	0.00	0.00	0.00		0.00	0.00		0.01	0.00	0.00	0.00	0.00					
Wells	0.00				0.00												
Streams	0.13	0.01															
Coast	0.29																
Recharge	0.00	0.00															
Storage change	-1.66	-0.02	-0.11		-0.01		-0.03	-0.10		-0.50	-0.01	-0.19					

Hydraulic head change in first layer between 2013 and 2050



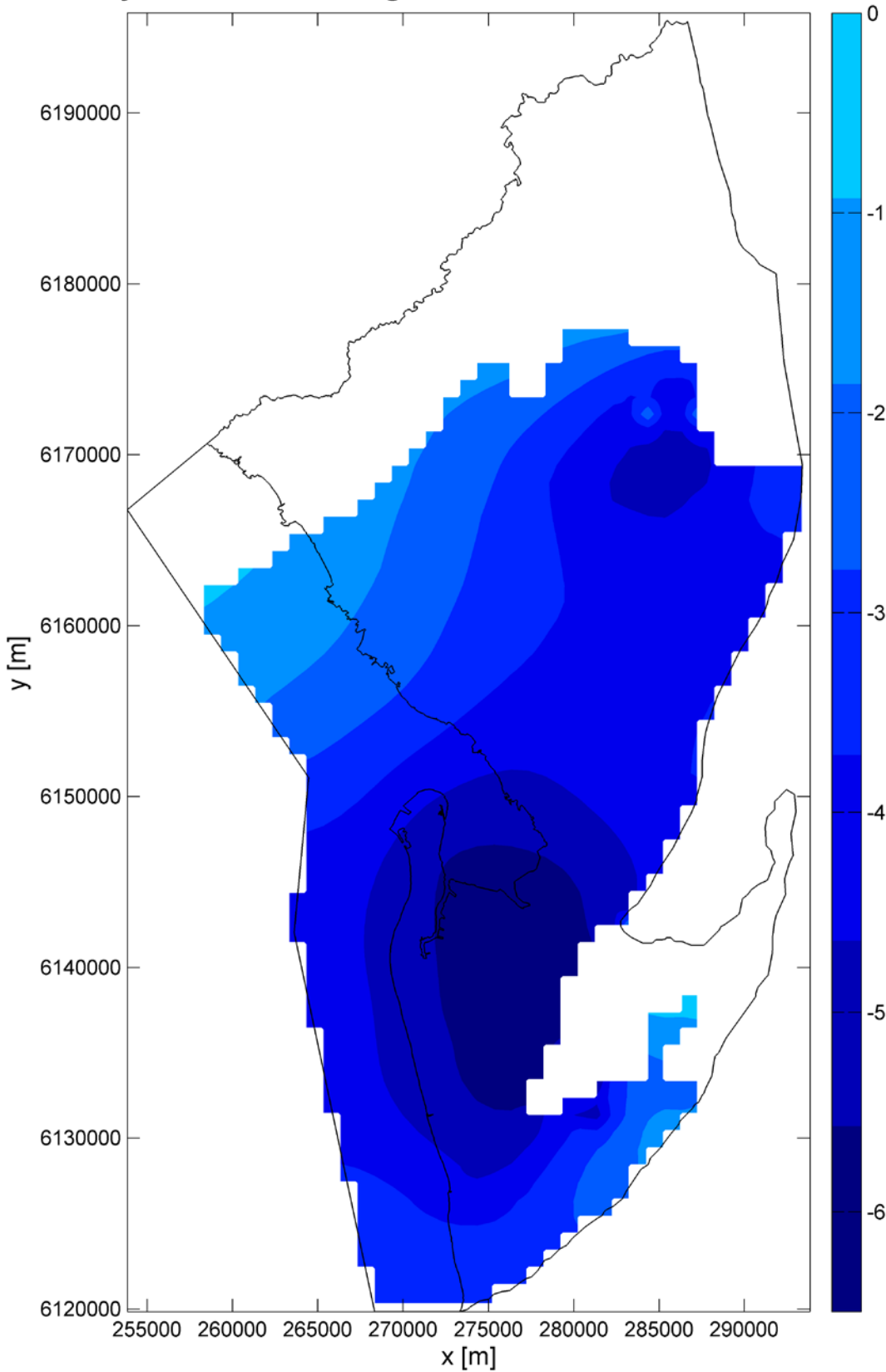
Apx Figure K.113 Hydraulic head change in the first layer between 2013 and 2050 for the Increased pumping scenario

Hydraulic head change in T1 between 2013 and 2050



Apx Figure K.114 Hydraulic head change in the T1 aquifer between 2013 and 2050 for the Increased pumping scenario

Hydraulic head change in T2 between 2013 and 2050



Apx Figure K.115 Hydraulic head change in the T2 aquifer between 2013 and 2050 for the Increased pumping scenario

Decreased Pumping

This scenario assessed the effect of reduced stress on the system due to 10% less pumping than in 2012/2013. The decadal flux matrices for 2030 and 2050 are shown in Apx Table K.30 and Apx Table K.31 respectively. The comparison to the base case for the decadal flux matrix is shown in Apx Table K.32. Of interest is the near linear response of the system between an increase of 10% and decrease of 10% in pumping with the key changes the rate of change of storage in the Hindmarsh Clay (increased by 1.64 GL yr⁻¹) and the decrease in flux from the Hindmarsh Clay to the T1 aquifer (-2.01 GL yr⁻¹). The head changes in the first layer (Apx Figure K.116), T1 (Apx Figure K.117) aquifer and T2 aquifer (Apx Figure K.118) similarly show less change from 2013 to 2050 when compared to the base case.

Apx Table K.30 Decadal (2020–2030) average annual flux matrix for water balance components of the Decreased Pumping scenario. The same display threshold and colour scheme as for Apx Table K.14 apply

Yr 2030	Hclay	UTSand	T1	MPClay	T2	BPFmnU	T3T4U	BedrockU	BPFmnD	T3T4D	BedrockD	Pfault	MLR	Wells	Streams	Coast	Recharge
Hclay			18.33											0.94	0.78	1.89	
UTSand			0.14					1.51							3.75		
T1	1.71	0.14		6.03	10.01		0.32	0.19		0.02				4.44			
MPClay			0.44		6.04												
T2		0.21	0.95	0.44		0.06			0.61					21.58			
BPFmnU					1.11		0.08	0.03									
T3T4U			0.44			0.78		0.17						1.55			
BedrockU		2.53	0.66			0.19	2.38							0.61			
BPFmnD					4.60						0.54						
T3T4D			0.03						4.29								
BedrockD			0.02						0.03	0.05			0.06				
Pfault			0.48		1.32									0.05			
MLR	0.37	0.04	0.63		0.38	0.18		3.73	0.21	0.14	0.13	0.03					
Wells	0.07				0.30												
Streams	4.90	2.18															
Coast	0.75																
Recharge	0.62	0.02															
Storage change	-13.52	-0.27	-0.75		-0.08		-0.16	-0.78		-3.55	-0.04	-1.79					

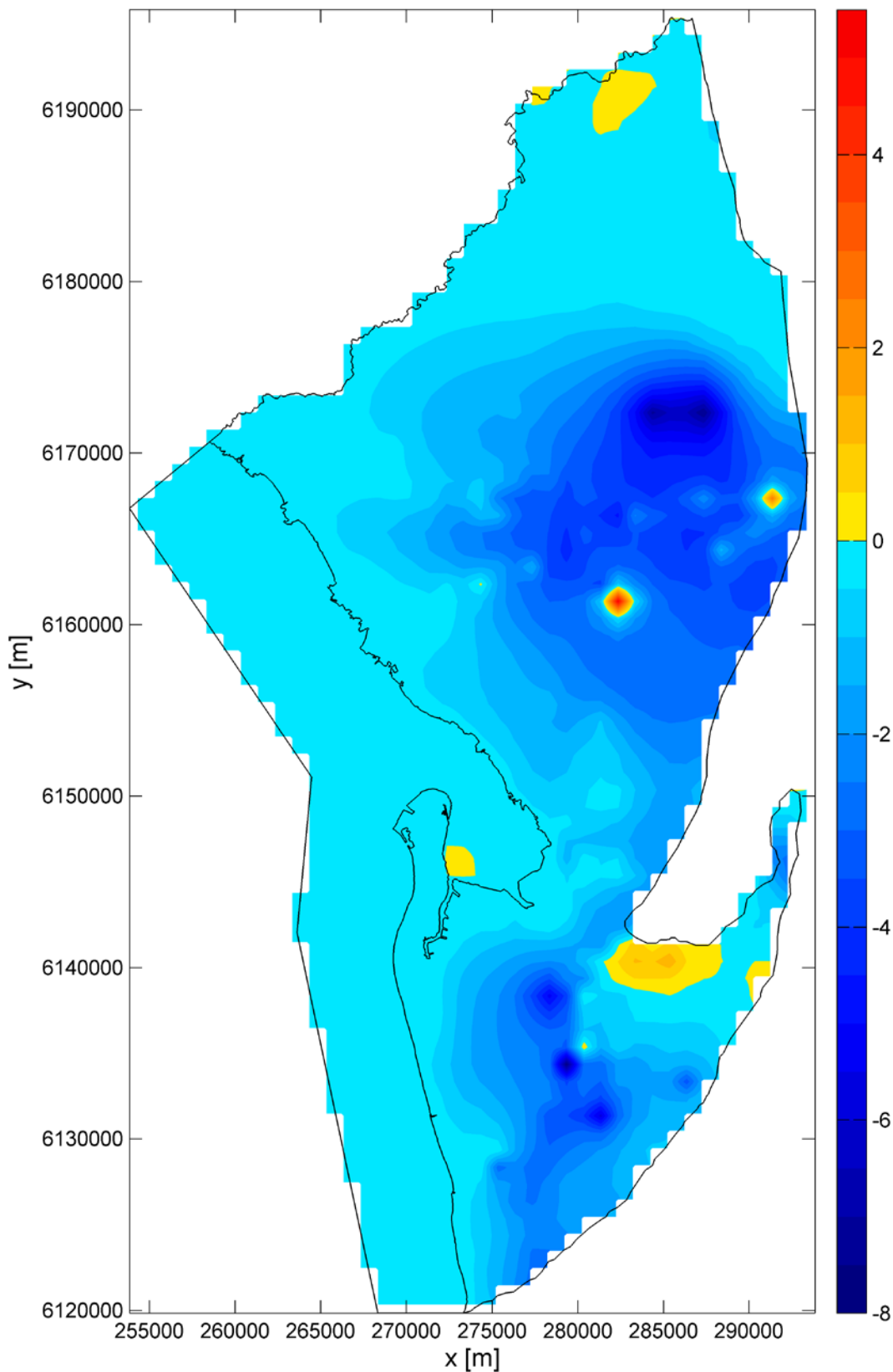
Apx Table K.31 Decadal (2040–2050) average annual flux matrix for water balance components of the Decreased Pumping scenario. The same display threshold and colour scheme as for Apx Table K.14 apply

Yr 2050	Hclay	UTSand	T1	MPClay	T2	BPFmnU	T3T4U	BedrockU	BPFmnD	T3T4D	BedrockD	Pfault	MLR	Wells	Streams	Coast	Recharge
Hclay			18.89											0.93	0.69	1.60	
UTSand			0.14					1.48							3.71		
T1	1.57	0.13		6.62	10.04		0.31	0.20		0.02				4.44			
MPClay			0.33		6.63												
T2		0.21	0.93	0.33		0.06			0.59					21.58			
BPFmnU					1.13		0.08	0.03									
T3T4U			0.38			0.79		0.19						1.55			
BedrockU		2.51	0.66			0.19	2.36					0.03		0.61			
BPFmnD					3.93					0.52							
T3T4D			0.03						3.60								
BedrockD			0.02						0.03	0.05			0.06				
Pfault			0.51		1.22									0.05			
MLR	0.37	0.04	0.64		0.39	0.18		3.78	0.21	0.15	0.13	0.03					
Wells	0.07				0.30												
Streams	5.10	2.19															
Coast	1.16																
Recharge	0.62	0.02															
Storage change	-13.22	-0.24	-0.81		-0.07		-0.15	-0.68		-2.89	-0.03	-1.73					

Apx Table K.32 Difference between base case and decreased pumping in the decadal (2040–2050) average annual flux matrix. Values below 1×10^{-3} are not shown

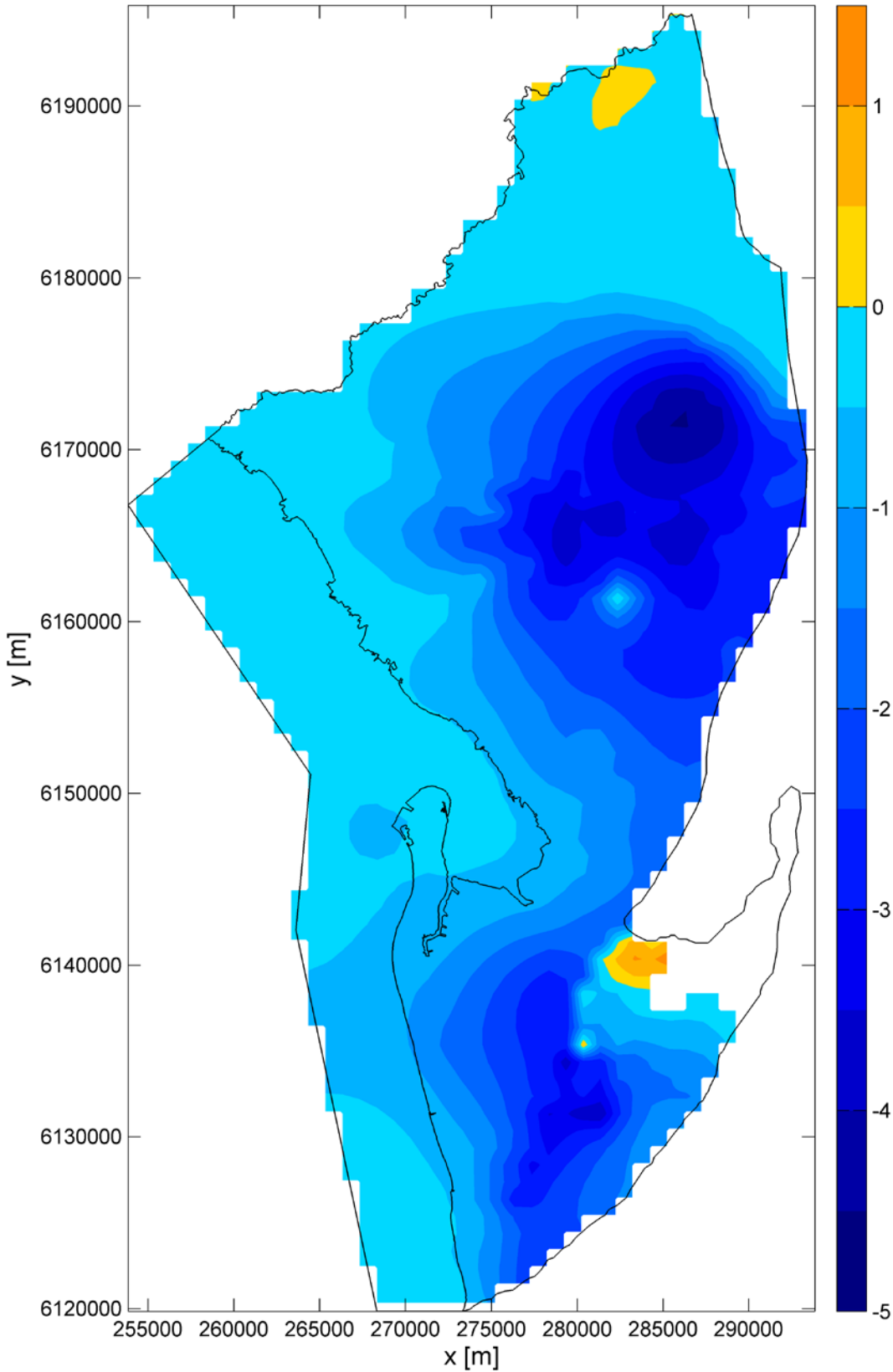
Yr 2050	Hclay	UTSand	T1	MPClay	T2	BPFmnU	T3T4U	BedrockU	BPFmnD	T3T4D	BedrockD	Pfault	MLR	Wells	Streams	Coast	Recharge
Hclay			-2.01											-0.10	0.05	0.13	
UTSand			0.00					-0.02							0.01		
T1	0.10	0.00		-0.79	-1.00		-0.14	-0.01		0.00				-0.49			
MPClay			0.03		-0.79												
T2		0.00	-0.09	0.03		0.00			-0.04					-2.39			
BPFmnU					-0.01		0.00	0.00									
T3T4U			-0.06			-0.01		0.02						-0.17			
BedrockU		0.02	0.00			0.00	-0.07					0.00		-0.07			
BPFmnD					-0.55					-0.03							
T3T4D			0.00						-0.53								
BedrockD			0.00						0.00	0.00			0.00				
Pfault			-0.07		-0.13									-0.01			
MLR	0.00	0.00	0.00		0.00	0.00		-0.01	0.00	0.00	0.00	0.00					
Wells	0.00				0.00												
Streams	-0.12	-0.01															
Coast	-0.27																
Recharge	0.00	0.00															
Storage change	1.64	0.02	0.14		0.00		0.01	0.10		0.50	0.01	0.20					

Hydraulic head change in first layer between 2013 and 2050



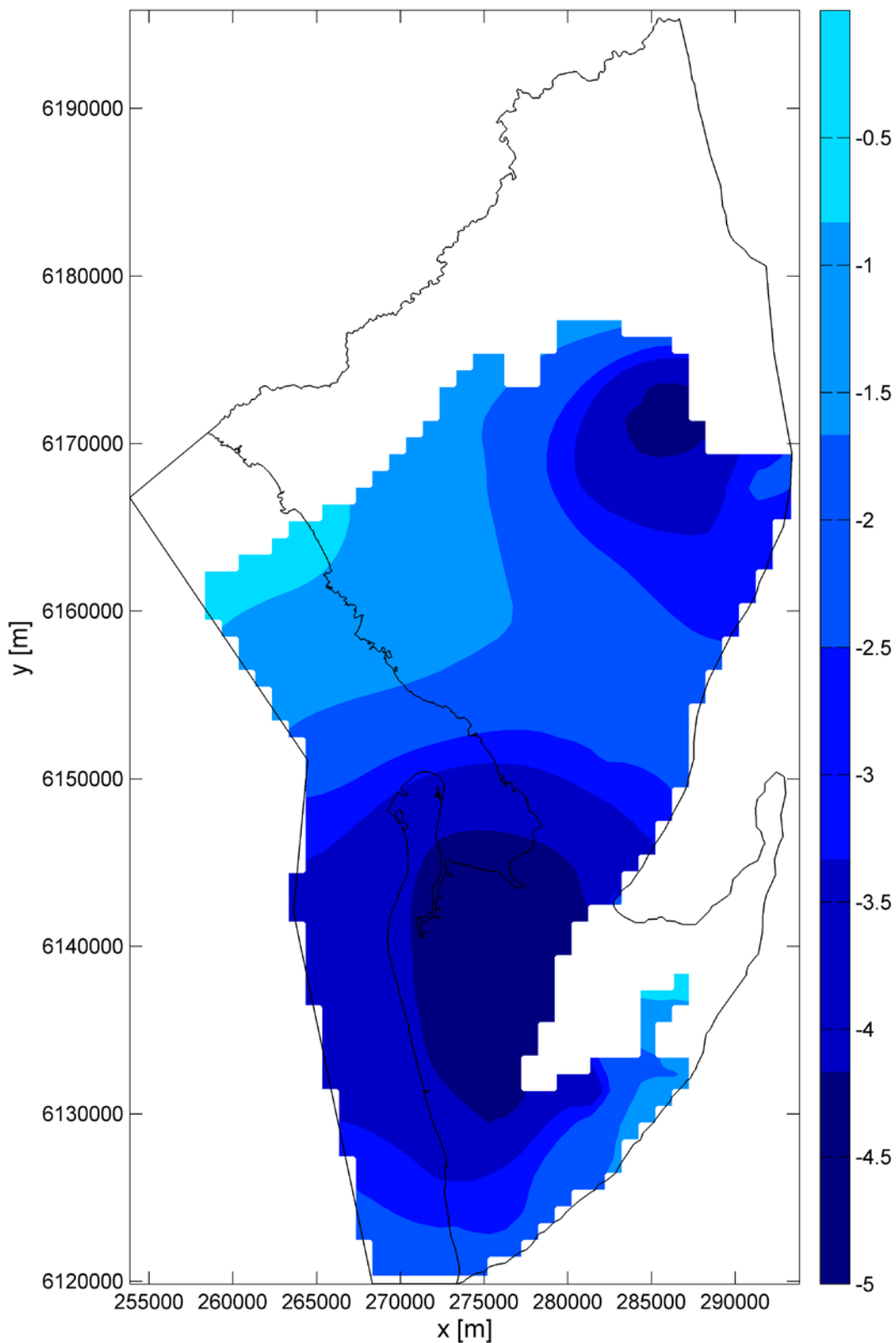
Apx Figure K.116 Hydraulic head change in the first layer between 2013 and 2050 for the Decreased pumping scenario

Hydraulic head change in T1 between 2013 and 2050



Apx Figure K.117 Hydraulic head change in the T1 aquifer between 2013 and 2050 for the Decreased pumping scenario

Hydraulic head change in T2 between 2013 and 2050



Apx Figure K.118 Hydraulic head change in the T2 aquifer between 2013 and 2050 for the Decreased pumping scenario

Increased MAR

The increase in MAR has the effect of increasing heads at the locations of injection and increases recharge to the Adelaide Plains until the recovery efficiency reaches 100%. The decadal water balances for 2030 and 2050 are shown in Apx Table K.33 and Apx Table K.34 respectively. When compared to the base case (Apx Table K.35) this shows decreases in the fluxes from the Hindmarsh Clay down to the T1 (from 20.13 to 17.96 GL yr⁻¹) and the absolute rate of change of storage in the Hindmarsh Clay decreases by almost 3 GL yr⁻¹. Notable changes are an increase in the discharge to the coast, less recharge to the groundwater system from the streams and a slight reduction in recharge from the MLR. The spatial maps of hydraulic head minus topography for the T1 and T2 aquifers immediately after injection are shown in Apx Figure K.119 and Apx Figure K.120 respectively. The resulting generation of extensive artesian conditions north of Adelaide in these aquifers is clear, although it should be noted that this doesn't persist for longer than 2 months after which time the extraction coupled with other pumping wells lowers the heads.

Apx Table K.33 Decadal (2020–2030) average annual flux matrix for water balance components of the Increased MAR. The same display threshold and colour scheme as for Apx Table K.14 apply

Yr 2030	Hclay	UTSand	T1	MPClay	T2	BPFmnU	T3T4U	BedrockU	BPFmnD	T3T4D	BedrockD	Pfault	MLR	Wells	Streams	Coast	Recharge
Hclay			17.96											1.02	0.79	2.00	
UTSand			0.14					1.50							3.78		
T1	2.84	0.14		5.55	10.13		0.31	0.19		0.02				4.64			
MPClay			0.68		5.61												
T2		0.21	1.67	0.72		0.06			1.94			0.11		23.86			
BPFmnU					1.10		0.08	0.03									
T3T4U			0.45			0.77		0.17						1.55			
BedrockU		2.56	0.66			0.19	2.39					0.03		0.68			
BPFmnD					5.03						1.82						
T3T4D			0.03						4.66								
BedrockD			0.02						0.03	0.05			0.06				
Pfault			0.47											0.05			
MLR	0.37	0.04	0.62		0.37	0.18		3.73	0.20	0.14	0.13	0.03					
Wells	0.23		0.44		4.93			0.16									
Streams	4.85	2.18															
Coast			0.63														
Recharge		0.62	0.02														
Storage change	-12.25	-0.26	-0.69		-0.09		-0.15	-0.74		-2.66	-0.03	-1.65					

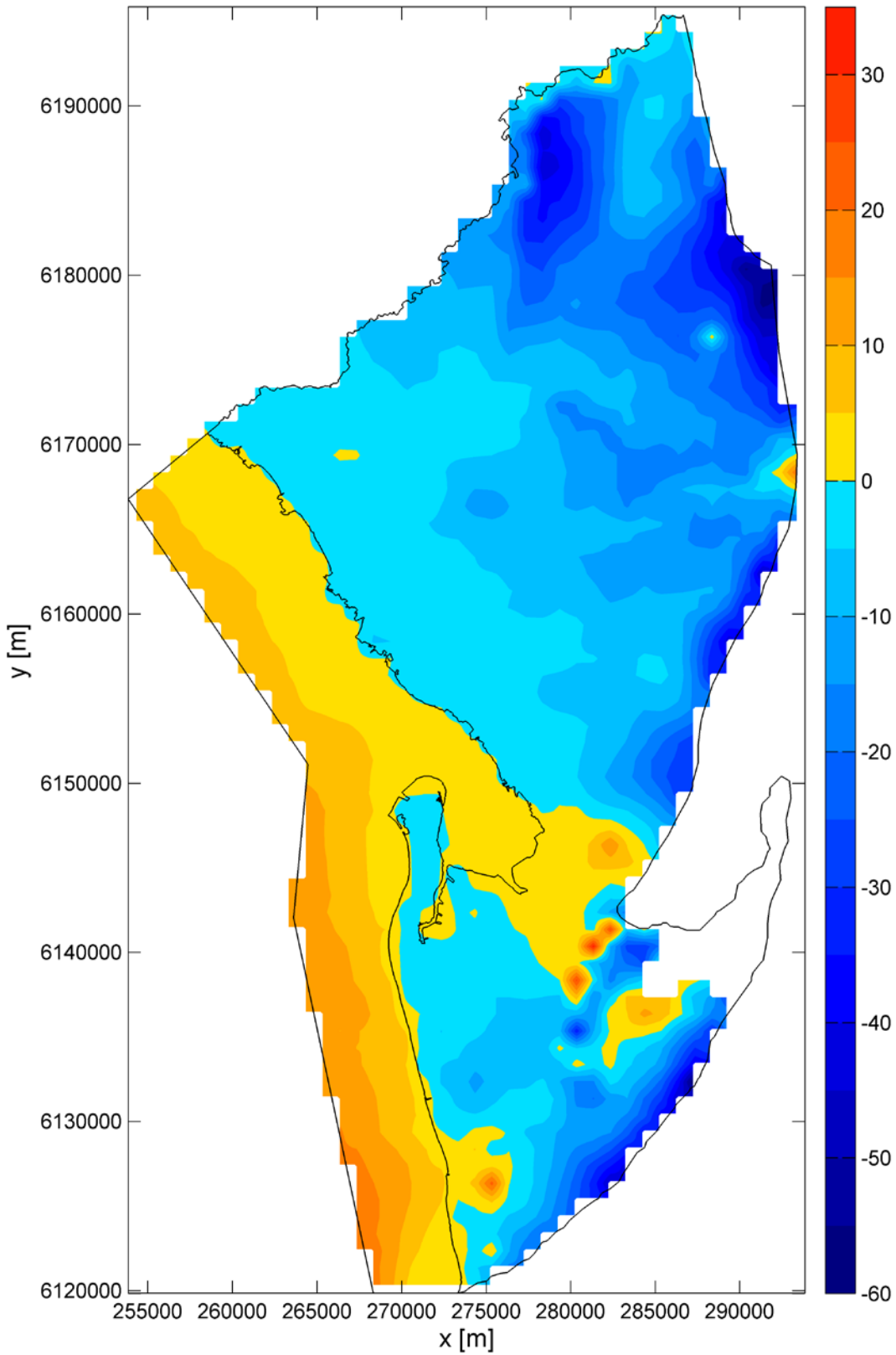
Apx Table K.34 Decadal (2040–2050) average annual flux matrix for water balance components of the Increased MAR scenario. The same display threshold and colour scheme as for Apx Table K.14 apply

Yr 2050	Hclay	UTSand	T1	MPClay	T2	BPFmnU	T3T4U	BedrockU	BPFmnD	T3T4D	BedrockD	Pfault	MLR	Wells	Streams	Coast	Recharge
Hclay			18.66											0.93	0.69	1.65	
UTSand			0.14					1.48							3.72		
T1	1.60	0.13		6.37	10.01		0.31	0.20		0.02				4.44			
MPClay			0.35		6.39												
T2		0.21	0.95	0.34		0.06			0.56					21.58			
BPFmnU					1.12		0.08	0.03									
T3T4U			0.39			0.79		0.19						1.55			
BedrockU		2.51	0.66			0.19	2.36					0.03		0.61			
BPFmnD					4.20						0.49						
T3T4D			0.03						3.88								
BedrockD			0.02						0.03	0.05			0.06				
Pfault			0.50											0.05			
MLR	0.37	0.04	0.63		0.38	0.18		3.77	0.21	0.15	0.13	0.03					
Wells	0.07				0.30												
Streams	5.06	2.19															
Coast			1.06														
Recharge		0.62	0.02														
Storage change	-13.15	-0.24	-0.78		-0.07		-0.15	-0.68		-3.20	-0.03	-1.72					

Apx Table K.35 Difference between base case and increased MAR in the decadal (2040–2050) average annual flux matrix. Values below 1×10^{-3} are not shown

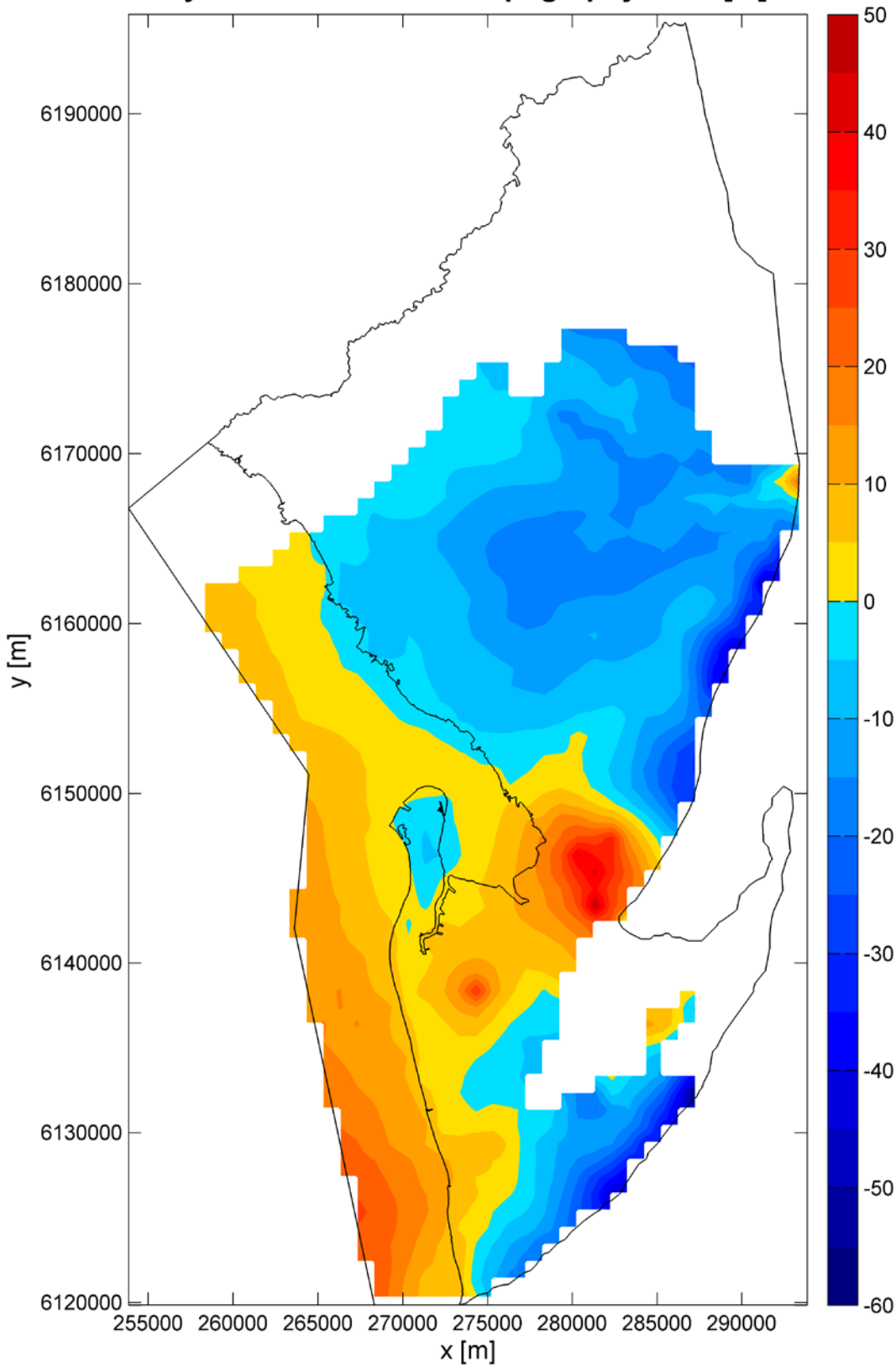
Yr 2050	Hclay	UTSand	T1	MPClay	T2	BPFmnU	T3T4U	BedrockU	BPFmnD	T3T4D	BedrockD	Pfault	MLR	Wells	Streams	Coast	Recharge
Hclay			-2.25												-0.10	0.05	0.18
UTSand			0.00					-0.02							0.02		
T1	0.13	0.00		-1.04	-1.03		-0.14	-0.01		0.00				-0.49			
MPClay			0.04		-1.04												
T2		0.00	-0.07	0.04		0.00			-0.07					-2.39			
BPFmnU					-0.02		0.00	0.00									
T3T4U			-0.06			-0.02		0.02						-0.17			
BedrockU		0.02	0.01			0.00	-0.07					0.00		-0.07			
BPFmnD					-0.27					-0.06							
T3T4D			0.00						-0.25								
BedrockD			0.00						0.00	0.00			0.00				
Pfault			-0.07		-0.13									-0.01			
MLR	0.00	0.00	0.00		-0.01	0.00		-0.01	-0.01	0.00	0.00	0.00					
Wells	0.00				0.00												
Streams	-0.16	-0.01															
Coast	-0.37																
Recharge	0.00	0.00															
Storage change	1.71	0.02	0.17		0.00		0.01	0.09		0.19	0.01	0.20					

Hydraulic head minus topography in T1 [m]



Apx Figure K.119 Hydraulic head minus topography in the T1 aquifer immediately after injection has ceased, August 2013

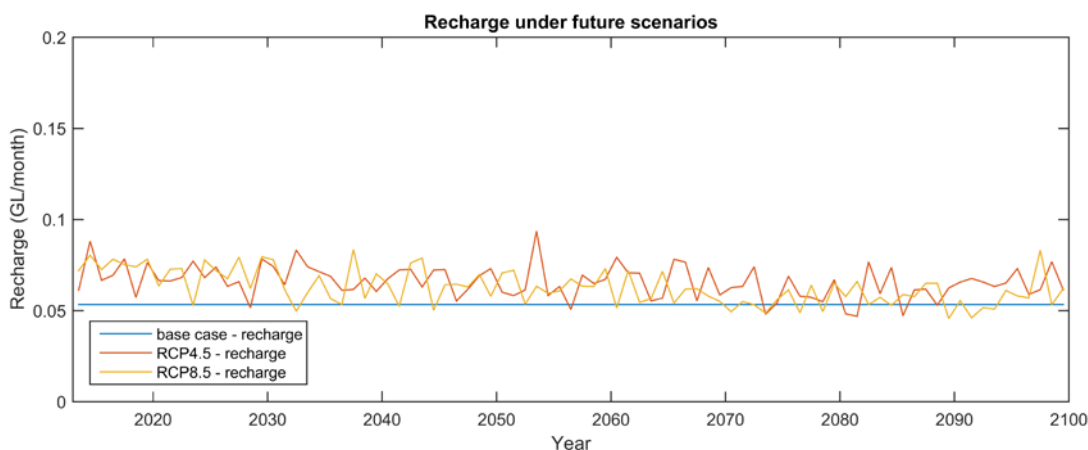
Hydraulic head minus topography in T2 [m]



Apx Figure K.120 Hydraulic head minus topography in the T2 aquifer immediately after injection has ceased, August 2013

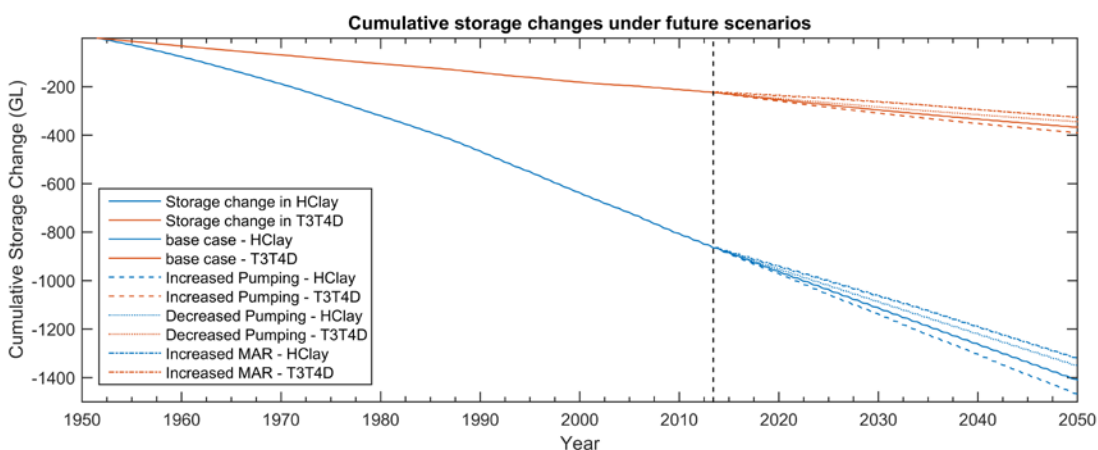
Comparison of future scenarios

The alternative climate scenarios of RCP4.5 and RCP8.5 were not significantly different from the base case (Apx Figure K.121) due to the small influence of areal recharge on the system. Furthermore, the actual changes in rainfall shown for these particular emissions scenarios under the particular GCM show only small change in the recharge for the future period as compared to the base-case (for which recharge is based on the 10 yr monthly averages from 2002–2012), which is actually higher than the base case. The reason for this is the choice of 2002–2012 as the average which contained part of the millennium drought and hence was below longer term average rainfall.



Apx Figure K.121 Areal recharge to the Adelaide Plains input to the model for the base case, RCP4.5 and RCP8.5

A comparison of the cumulative storage change under future scenarios, which are shown after the vertical dashed line at 2013 in Apx Figure K.122, demonstrate that system behaviour has predictable dynamics, i.e. increased pumping further increases storage loss, whereas decreased pumping and also the increased MAR reduces the storage loss compared to the base case. The most important aspect to observe is the continued decrease in storage across all of the scenarios.



Apx Figure K.122 Comparison of cumulative storage change between base case, increased pumping, decreased pumping and increased MAR future scenarios in the Hindmarsh Clay, and T3 and T4 aquifers (most significantly affected)

K.4.5 UNCERTAINTY AROUND MODEL PREDICTIONS

Unfortunately, time did not allow for a comprehensive predictive uncertainty analysis to be conducted during this project. However, insights can be gained from the calibration performance analysis on the one hand and on the parameter uncertainty analysis on the other hand, as discussed hereafter.

Uncertainty on predictions that are of same nature as the data comprising the calibration dataset can be expected to be of the same order as the level of misfit. I.e., errors on historical hydraulic head predictions can be expected to be on the order of RMS, which is 8.60 m on average for absolute hydraulic heads (Apx Table K.13). For future predictions, the accuracy also depends on probability of future stresses. Similarly, on the basis of RMS, errors on Cl predictions can be expected to be on the order of 1410 mg L⁻¹ and errors on ¹⁴C predictions can be expected to be on the order of 22 pmC.

For predictions that are not of same type as the data comprising the dataset (e.g., fluxes), a qualitative assessment of the uncertainty can be obtained from the parameter uncertainty analysis. For example, the hydraulic conductivity of the eastern boundary conductance is shown to be known with certainty. Therefore, a relatively small uncertainty can be expected on the flow from the MLR. In contrast, the 95 % confidence interval of the hydraulic conductivity of the ocean boundary conductance ranges from about 5 times smaller to 5 times larger than the calibrated value. Therefore, the flux through the ocean floor could easily be 5 times smaller or 5 times larger than predicted with the calibrated model.

Large caution is nevertheless needed in the interpretation of any uncertainty analysis performed or that will be performed on the basis of the current model. The model uses a low parameterisation that consists of large zones of uniform material properties. Such a simplification of reality has important implications on the capabilities of the model to be used for uncertainty analysis (Moore *et al.* 2006). Indeed, predictions may depend on local variations of the material properties. This is the case of solute transport predictions, but also of hydraulic head and water balance component predictions (even if the latter should be less affected than the former). Using large zones of uniform material properties implies that the parameters are quite constrained by the calibration dataset, because the model has only a limited flexibility. This is reflected in the identifiability analysis, which revealed that a large number of parameters are completely identifiable, even if they show quite a low sensitivity, for a number of them. This is because the availability of data in only a small area of a zone suffices to constrain the whole zone when the latter consists of one parameter only. Large identifiability implies relatively small parameter uncertainty, and consequently it can be expected that prediction uncertainties will be small. Therefore, using a model with a low parameterisation as in this study will necessarily imply relatively small estimated uncertainties on model predictions. However, these uncertainty estimates are unreliable as a consequence of the oversimplification of the system. Also note that other potential structural/conceptual errors such as the errors implied by the use of a coarse grid resolution (amongst others but this one is outstanding) are not captured when performing parameter-based uncertainty analysis.

K.5 Conclusions and recommendations

K.5.1 TECHNICAL ACHIEVEMENTS

A new modelling platform was developed for simulating groundwater flow and transport in the Adelaide Plains. The model domain extends from the major faults at the foothill of the Mount Lofty Ranges (MLR) in the south and west, up to 5 km offshore in the east and it is bounded by the Light River in the north. Improvements to the previous modelling platform as mentioned in introduction were achieved, the most important of which are:

- The stronger physical basis onto which the implementation of the boundary conditions relies. For the flow model, this mainly concerns the systematic determination of hydraulic heads and conductances used for general head boundaries (in both eastern and coastal boundaries) and for groundwater-surface water exchanges (section K.3.5). For the Cl transport model this concerns the concentration of the recharge, infiltrated surface water and the inflow from the MLR (section K.3.7).
- The revision of the hydrostratigraphy, with the two key differences with the previous platform being: (i) the T1 and T2 aquifers are considered continuous across Para fault; (ii) layers below the T2 aquifer are included. The first of these modifications was based on the conclusions of Zulfic *et al.* (2008), which were confirmed by recent reinterpretation of geological data by DEWNR. The second finds justification in that upward leakage from layers below the T2 aquifer could be significant both in terms of water quantity and salinity, especially where the T2 aquifer is heavily pumped. The modelling results suggest that upward leakage into T2 is indeed significant.
- The sensitivity analysis of a number of structural elements of the model: grid resolution, time-step resolution and initial condition for the transient flow model.
- The collation of a larger dataset for calibration. The current dataset includes:
 - All hydraulic head data of the WaterConnect database (51,912 hydraulic head data from 4,791 wells), spanning a wide range of water levels distributed over most of the model domain.
 - A large number of Cl concentrations (1,067 chloride data from 766 wells and 19,018 EC-derived Cl data from 4,545 wells). All Cl and EC data from the WaterConnect database were used.
 - An expanded ¹⁴C dataset (68 ¹⁴C data from 68 wells). This includes both data from this project and from previous studies (see Appendix E).

However, compatibility issues between MODFLOW-NWT and MT3DMS precluded the effective use of Cl and ¹⁴C for calibration. Results of forward Cl transport and ¹⁴C transport runs were nevertheless compared to the measurements, and the dataset is readily available for re-calibration of the model once the technical issue is resolved.

- Automatic calibration was achieved with PEST (on the basis of hydraulic head data only). In doing this, some of the most advanced techniques offered in PEST were adopted such as Tikhonov regularisation and singular value decomposition. Furthermore, a weighting scheme was used that integrates measurement errors and that accommodates the different scales and density distributions of the data. The SRMS for hydraulic heads (2.99 %; Apx Table K.13) is significantly smaller than in the previous modelling platform (6.77–7.79 % at given stress periods (Georgiou *et al.* 2011)).
- The extensive assessment of the calibration performance using relevant indicators. This included the analysis of weighted residuals for the entire model and for different aquifers independently, both spatially and temporally, as well as the calculation of a number of performance statistics. This assessment allowed identification of strengths and weaknesses of the model (see below).
- The rigorous analysis of parameters sensitivity, parameters identifiability and parameters uncertainty.
- The model was built using a script based approach, facilitating modifications.

K.5.2 MODEL PREDICTIONS

The water balance and flow mechanisms were analysed on the basis of the new model. However, given the limitations of the model (summarized in the next section), a large uncertainty surrounds these results. The description below is hence subject to verification and refinement in future works.

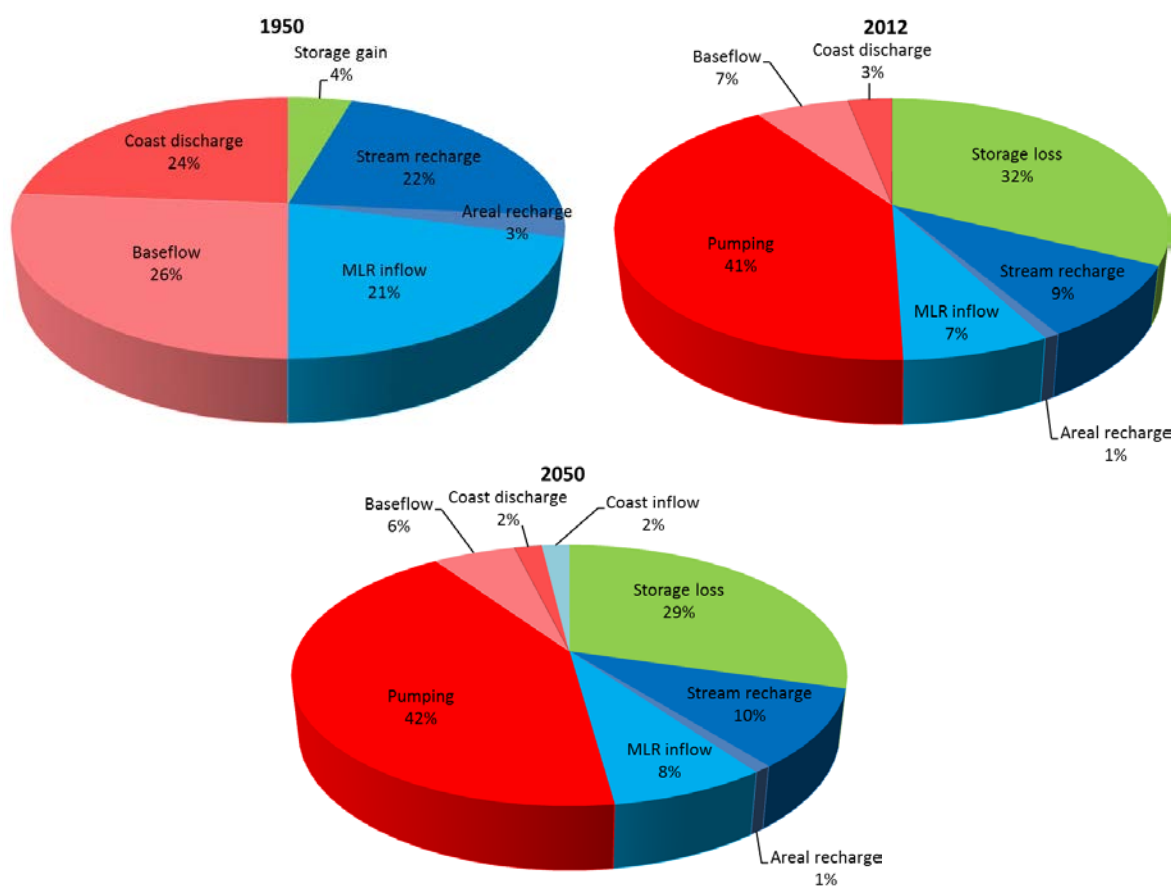
Under dynamic pre-development conditions (Apx Table K.15), the average downward flow from the Quaternary sediments into the T1 aquifer is estimated to be 3.47 GL yr⁻¹. Of this flow, a maximum of 0.32 GL yr⁻¹ originates from the MLR via lateral flow into the Quaternary sediments, i.e., at least 3.15 GL yr⁻¹ (the remaining part) originates from infiltration in the Plains (mostly from river leakage as diffuse recharge is 10 times less than river leakage). Such a downward flow is supported by historical hydraulic head data showing downward gradient towards the eastern boundary of the modelled region and by the freshwater plumes existing in the Tertiary aquifers that show a certain alignment with major streams. It is also in line with the findings from Green *et al.* (2010) who suggested that focused river leakage near the fault zone might be a significant contributor to the Tertiary aquifers. The total lateral flux from the MLR into the Plains is estimated to be 5.11 GL yr⁻¹. Of this flux, 0.32 GL yr⁻¹ flows into the Quaternary sediments whereas 0.55 and 0.30 GL yr⁻¹ flows directly into the T1 and T2 aquifers, respectively, and the remaining part (4.26 GL yr⁻¹) first flows deeper (mostly through the Bedrock in the Golden Grove Embayment; 3.37 GL yr⁻¹) before flowing upward. Namely, in the Golden Grove Embayment a significant amount of water flows from the Bedrock upward into UTSand (2.71 GL yr⁻¹), the T3T4 aquifer (1.51 GL yr⁻¹) and the T1 aquifer (0.74 GL yr⁻¹). The latter groundwater pathway is significant and does not seem to have been recognised as such before. Hence, this constitutes a major difference between the current results and previous understanding and this warrants further investigation to confirm or deny this modelling outcome. After recharge occurs from the streams and MLR, the water flows towards the coast and upward. There is a large flux from the T2 aquifer to the T1 aquifer through the Munno Para Clay (2.88 GL yr⁻¹) but also a significant component of direct flow from the T1 aquifer to the T2 aquifer (1.37 GL yr⁻¹). The T1 aquifer then discharges into the Hindmarsh Clay (6.62 GL yr⁻¹) and the outflow from the Hindmarsh Clay to the sea is 5.81 GL yr⁻¹.

The model predictions show clear changes between the past, present, and future conditions of the groundwater system (Apx Figure K.123). Prior to pumping, the behaviour of the system is quite stable with inflow and outflows well balanced (although the model initial condition induces an unrealistic – albeit relatively small – storage decrease). Simulation of the development period reveals a greatly disturbed balance and shows that groundwater extraction has caused a large loss of groundwater from storage with storage depletion equating to 64 % of the inflows (32 % of the sum of all water balance components in the pie chart). In other words, the overall water balance shows that extraction is much larger than natural inflows. For a business-as-usual predictive scenario, storage loss can be seen to be slowly decreasing in the future. Other sources make up for this reduction. Stream recharge and MLR inflows contribute more to the system, and the change in coastal exchanges (which notably switch from net outflow to net inflow around 2050) make up for the most of the reduction. Note that there is no direct field-based evidence of river reaches changing from average gaining to average losing and this could be the object of further work (subject to data availability).

The low calibrated value of specific storage for both the T1 and T2 aquifers implies that increased pumping draws the head down in these aquifers without the capacity to release large quantities of water per unit change in head. This induces large downward head gradients between the Hindmarsh Clay and T1 aquifer and between the T1 and T2 aquifers. Even though the hydraulic conductivity of Munno Para Clay is quite low in the calibrated model, this large hydraulic gradient between the T1 and T2 aquifers allows significant flow across Munno Para Clay. While the T1 and T2 aquifers are seemingly not overstressed based on the relatively small cumulative change in storage for these units, the depletion of the Hindmarsh Clay is indicative of the stress imposed on the system as a whole. The other units surrounding the T1 and T2 aquifers seem to be compensating for the pumping. In particular the confining Hindmarsh Clay provide most of the storage, i.e. is most heavily depleted. Such a relationship is not unusual, as low-permeability sediments tend to be volumetrically dominant and more storative than confined aquifers (Konikow *et al.* 2007). However, the Hindmarsh Clay has an upper limit as to how much water it can release from storage

to supply the pumping demands in the T1 and T2 aquifers. Once this limit reached, the decrease in heads reverses the gradient to the coast and induces encroachment of seawater into the system.

The increased inflow from streams and from the MLR in the current model supposes that these have an unlimited storage, which in reality would be limited. The MLR is poorly understood with respect to how much water it stores and its storage dynamics. If the contributions of stream and MLR boundaries to the system are overestimated, the encroachment of sea water into the system and the ongoing storage depletion can be underestimated. Furthermore, seawater intrusion is not the only risk posed to water quality in the heavily pumped T1 and T2 aquifers. The release of storage and subsequent upward flow from the saline T3 and T4 aquifers to the T2 is also of concern; however, further work should be undertaken to seek field-based evidence of this process, e.g. by analysing salinity trends in the areas of T2 where greater leakage is expected. The release of storage and subsequent downward flow from the relatively saline Hindmarsh Clay into the T1 aquifer is subject of similar concern and calls for more field-based analysis.



Apx Figure K.123 Decadal average water balance components as a percentage of the total balance for pre-development (in 1950), development (in 2012) and future (base-case in 2050) periods. Red coloured pieces of the pie indicate flow out of the system, blue pieces indicate flow into the system, and green indicates storage changes (either gain or loss)

The scenario analyses allowed quantification of the degree to which different future scenarios might impact on the Adelaide Plains groundwater system. A common thread across all scenarios considered was the gross imbalance between extraction and inflows of the system. For all the variations of the amount of rainfall, pumping and MAR considered, the fact remained that storage will continually be depleted, with similar consequences on groundwater circulations.

In setting up the scenario analyses for the base-case, climate change, modified pumping and increased MAR, a series of assumptions were made that are likely to have impacted the results. These assumptions were not able to be explicitly tested and so quantifying the impacts was not possible. However, the assumptions made and possible influences on the modelling results are detailed below in Apx Table K.36.

Apx Table K.36 Scenarios summary for Adelaide Plains groundwater modelling

SCENARIO	ASSUMPTION/LIMITATION	POSSIBLE INFLUENCE ON RESULTS
Base case	Selection of average rainfall for the base case subjective.	The selection of distributed rainfall as being the 10-year monthly average based on the development model (1950–2013) recharge spatiotemporal input, means that rainfall is low compared to the longer term average as it captures a major drought period. As the contribution of areal recharge is low compared to other components, this is not deemed a significant concern.
Climate change	Only one GCM was used and the 100 realisations for this one GCM were averaged to give a single spatiotemporal rainfall series for each of the two emission scenarios RCP4.5 and RCP8.5.	This does not account for the variability of rainfall predictions. However, as the model shows that these scenarios were not particularly sensitive to the degree of change in the average recharge amount, this was not deemed important.
	Rivers boundaries are unchanged. Reduced rainfall will lead to a change in the hydrologic response of the waterways within the APMLR areas. Not only will the total volumes change but the flow duration curves for these waterways will likely be different	As with the above, the rainfall-runoff dynamics will change and therefore the heads in the streams and their extent are also likely to change which will influence the degree of surface water-groundwater exchange.
	Simplified representation of changes in the MLR	The linking of spatially averaged rainfall to the plains is used to drive variation in the eastern boundary head. The lack of a storage component in this boundary allows it to provide an infinite supply of water and would likely counteract any significant pumping stress applied to the system as the reducing heads near the boundary will just drive more flow into the model domain.
Increased pumping	Assuming that all users will evenly increase their usage. Uniform increases across the board are unlikely with particular industries probably changing their usage according not only to quantity but quality as well.	This is clearly not correct as some users are already at allocation in their usage whereas some are far from it. This will modify where changes in the pumping takes place both in location and in which aquifer, which will likely influence the water balances and long-term changes in storage for the system.
Increased MAR	River boundaries are unchanged. Reduction in runoff to sea due to stormwater capture in wetlands for MAR schemes	Increased capture of stormwater, particularly at the top of catchments will cause reductions in available water for downstream flow. This will result in decreased heads in the streams and their extents and will modify the SW-GW interactions.
	Distribution of schemes not exact	In some cases for schemes that are under investigation, an exact location of pumping/injection wells is not yet known. The effect of this is deemed insignificant as the error in the location should be less than the grid size of the model and hence it effectively will act in the same place even if the input co-ordinates are changed
	Uniform increases to existing MAR	This is the same problem as for increased pumping above.

Improved data management would allow for more accurate scenarios with respect to the pumping and MAR, but this also requires a better understanding of user behaviour / management rules under different climates. There are a number of analyses that could be done in the future to improve on the work presented. It is recommended that the following be applied:

- Development of an up-to-date, consistent and consolidated register for pumping wells across the model domain.
- Development of an up-to-date, consistent and consolidated register of existing, planned and decommissioned MAR schemes.

K.5.3 MODEL CAPABILITIES AND LIMITATIONS

The current modelling platform is viewed as an ongoing effort towards achievement of regional-scale predictions of hydraulic heads, fluxes, Cl and ¹⁴C. It should not be expected to provide locally accurate predictions. This is reflected in the calculated RMS which has been calculated for local observations of hydraulic heads, Cl and ¹⁴C. On this basis, the local accuracy on modelled hydraulic heads, Cl and ¹⁴C can be expected to be on average on the order of 8.60 m, 1410 mg L⁻¹ and 22 pmC, respectively (Apx Table K.13). Unfortunately, local accuracy on flux predictions cannot be obtained in this way as no flux observations were used to compare with the model results.

The RMS only reflects the comparison of model results with local measurements. In contrast, the SRMS gives an idea of how well the model is capable of representing the variability of a given data type at the scale of the model, and is therefore a better measure of the suitability of the model to serve its purpose. The calculated SRMS for hydraulic heads, Cl concentrations and ¹⁴C activities is 2.99 %, 28.28 % and 24.05 %, respectively (Apx Table K.13). In view of these and assuming that the variability of a given data type is dominated by regional-scale variability (as opposed to local-scale variability), the model could be deemed suitable for regional-scale prediction of hydraulic head but not for Cl and ¹⁴C.

The suitability of the current model to predict groundwater fluxes is difficult to assess as no flux observations were used to compare with the model results. As discussed in section K.4.5, parameter uncertainty analysis could give some hints on the uncertainty surrounding flux estimates but a reliable estimation of uncertainty cannot be achieved solely on this basis. Predictive uncertainty on flux estimates using the current model could be performed as a next step, but this still would not capture the uncertainty induced by potential structural/conceptual errors (such as the absence of intra-zone heterogeneity or the coarse grid resolution). The lack of capacity to estimate uncertainty on flux predictions is considered to be a major limitation of the current model.

A number of results in this study indicate that the current model might contain significant structural/conceptual errors which could compromise the capacity of the model to provide reliable future predictions (with mostly unknown consequences which will be prediction-dependent):

- The influence of grid resolution on the simulation results is indicative of structural error. This was shown to affect not only groundwater-surface water interactions but also the flow across the MLR boundary.
- The initial condition was shown to influence the results as a dynamic equilibrium is not reached at the end of the pre-development period. This may bias the results, although this bias is insignificant for the development period as pumping effects largely surpass this artefact.
- A number of parameters deviated significantly from their preferred value during calibration. While some values can find reasonable justification, some others seem rather unlikely or would require further investigation to be deemed plausible. The most concerning of these (given their importance for the dynamics of the main aquifers) are K_H in the T1 aquifer and S_S in the T1 and T2 aquifers.
- Strong biases are observed in the weighted residuals of the calibration dataset. These generally indicate that both the spatial and temporal variability are underestimated by the model, and also that some areas have a systematic bias towards either low or high values.

K.5.4 RECOMMENDATIONS

Key recommendations for future improvements of the modelling platform are listed below.

Data

1. Estimates of historical pumping and MAR are quite rough. Calibration results suggest that pumping rates might be globally underestimated (potentially caused by non-consideration of non-licensed pumping wells) and that the inter-annual variability is poorly represented. Pumping and MAR rates constitute perhaps the most important dataset as at this stage they are the only fluxes that drive the calibration through their specification in the transient model. Hence, this is viewed as a crucial area of improvement. Note that this was already mentioned in Georgiou *et al.* (2011).
2. Current estimates of aquifer properties (both hydraulic conductivity and storage coefficients) have a poor spatial representation in the T1 and T2 aquifers and are essentially inexistent in deep aquifers. The current calibrated values of K_H in the T1 aquifer and S_S in the T1 and T2 aquifers are quite different from existing estimates and so new aquifer tests are recommended, especially in the Golden Grove Embayment.
3. Current results suggest that a significant groundwater pathway is through the Bedrock west of the Eden-Burnside Fault receiving water from the MLR and releasing water upward to the sedimentary aquifers in the Golden Grove Embayment. Verification of this outcome should be sought by performing new data analysis including field work as little data is available in the deep aquifers.
4. Monitoring data (both hydraulic head and salinity) are also largely lacking in the northern part of the model. New monitoring wells should target not only the Plains but also the MLR in order to improve the boundary conditions. Note that this was already mentioned in Georgiou *et al.* (2011).
5. Given the suggested importance of groundwater-surface water interactions, the model would benefit from incorporating more accurate river level information including temporal variability. Note that this was already mentioned in Georgiou *et al.* (2011). Field work could also be undertaken to estimate riverbed bottom and thickness.
6. The spatiotemporal characterisation of groundwater-surface water exchanges should be extended (see Appendix D). Specifically, measurements should aim to quantify both intra and inter-annual fluctuations of the exchange rates and should target surface water features that are poorly documented so far such as Dry Creek, Cobbler Creek, Smith Creek, Light River, lakes and farm dams.
7. The salinity of surface water features should also be characterized as this would enhance the reliability of the Cl transport model not only for predictions but also in its capacity to inform calibration. Note that this was already mentioned in Georgiou *et al.* (2011).
8. Recharge estimates should be refined, potentially by using remote sensing products for estimating actual evapotranspiration and/or by improving recharge modelling.

Model structure

9. The model would benefit from using a finer grid to allow better resolution of structural and surface water features and therefore to improve the accuracy of the results. In this work the model was calibrated only on a uniform 1,000 m resolution grid and a sensitivity analysis revealed that the results are sensitive to grid resolution. More research is warranted to achieve a grid-resolution-independent model. Until such research is available, the model should be recalibrated to be used at a finer resolution.
10. Although the adopted hydrostratigraphy is more comprehensive than in Georgiou *et al.* (2011), further refinements could be considered. Namely, recent findings suggest that T1 is inexistent in the northeast part of the domain.
11. Intra-zone heterogeneity should be considered, at least for hydraulic conductivity (using for example the pilot points approach), as the use of large zones of piecewise constancy has been identified as the most likely reason for the misfit in mean hydraulic heads (i.e. temporal mean in each well). In addition to allowing achievement of a better fit, this should also provide a more appropriate basis for reliable predictive uncertainty analysis.

12. Different coastal conceptualizations should be tested. Indeed, the model results indicate that seawater intrusion is occurring in response to pumping. Since the actual distance up to which groundwater is fresh offshore is unknown, testing the sensitivity to the position of the offshore boundary seems important. Tests could also be carried out where inflow is allowed across the lateral offshore boundary.
13. Given the importance of groundwater-surface water interaction suggested by the model results, upgrading the model to an integrated (surface-subsurface) model could be considered.

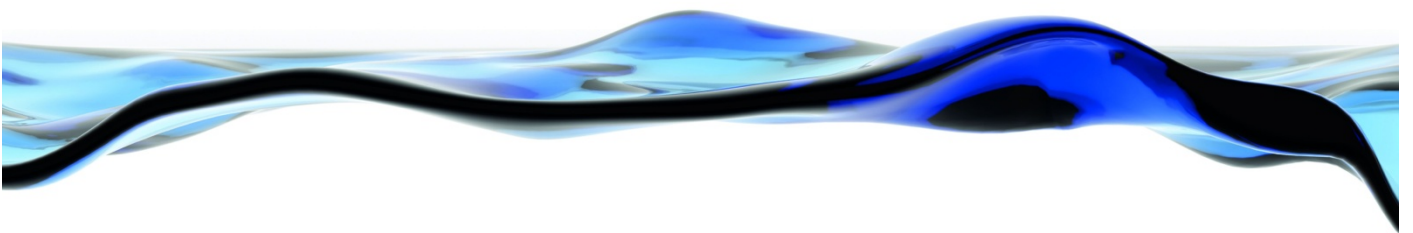
Calibration and uncertainty analysis

14. The model should be re-calibrated using Cl and ^{14}C once compatibility issues between MODFLOW-NWT and MT3DMS are resolved. Transport results should also be analysed in detail.
15. Independent flux estimates should be included in the calibration dataset – river leakage in particular (see above).
16. Predictive uncertainty analysis should be performed to help decision-makers to assess the reliability of the model predictions.

K.6 References

- Barnett B, Townley LR, et al. (2012) 'Australian groundwater modelling guidelines.' National Water Commission, Canberra.
- Bense VF, Gleeson T, Loveless SE, Bour O, Scibek J (2013) Fault zone hydrogeology. *Earth-Science Reviews* 127, 171-192.
- Bresciani E, Ordens CM, Werner AD, Batelaan O, Guan H, Post VEA (2014) Spatial variability of chloride deposition in a vegetated coastal area: Implications for groundwater recharge estimation. *Journal of Hydrology* 519, Part A, 1177-1191.
- Charles SP, Fu G (2015) 'Statistically Downscaled Climate Change Projections for South Australia.' Goyder Institute for Water Research, Technical Report Series No. 15/1, Adelaide, South Australia.
- Clark ID, Fritz P (1997) 'Environmental Isotopes in Hydrogeology.' (CRC Press)
- Cook PG, Bohlke JK (2000) Determining timescales for groundwater flow and solute transport. In 'Environmental Tracers in Subsurface Hydrology'. (Eds PG Cook and AL Herczeg) pp. 1-30. (Kluwer: Boston)
- Crosbie RS, Jolly ID, Leaney FW, Petheram C (2010) Can the dataset of field based recharge estimates in Australia be used to predict recharge in data-poor areas? *Hydrol. Earth Syst. Sci.* 14, 2023-2038.
- de Marsily G (1986) 'Quantitative hydrogeology: groundwater hydrology for engineers.' (Academic Press)
- Doherty J (2013) 'Manual and Addendum for PEST: Model-Independent Parameter Estimation.' (Watermark Numerical Computing: Brisbane, Australia)
- Doherty J, Hunt RJ (2010a) 'Approaches to highly parameterized inversion—A guide to using PEST for groundwater-model calibration.' U.S.G.S., 2010–5169.
- Doherty J, Hunt RJ, Tonkin M (2010b) 'Approaches to highly parameterized inversion—A guide to using PEST for model-parameter and predictive-uncertainty analysis.' U.S.G.S., 2010–5211.
- Eriksson E, Khunakasem V (1969) Chloride concentration in groundwater, recharge rate and rate of deposition of chloride in the Israel Coastal Plain. *Journal of Hydrology* 7, 178-197.
- Georgiou J, Stadter M, Purczel C (2011) 'Adelaide Plains groundwater flow and solute transport model.'
- Gerges NZ (1999) The Geology and Hydrogeology of the Adelaide Metropolitan Area Volume 1 & Volume 2. PhD thesis, Flinders University.
- Gerges NZ (2001) 'Northern Adelaide Plains groundwater review.' Department for Water Resources, DWR Report 2001/013, Adelaide.
- Gerges NZ (2006) 'Overview of the hydrogeology of the Adelaide metropolitan area.' Department of Water, Land and Biodiversity Conservation, DWLBC Report 2006/10, South Australia.
- Green G, Watt E, Alcoe D, Costar A, Mortimer L (2010) 'Groundwater flow across regional scale faults.' Government of South Australia, through Department for Water, DFW Technical Report 2010/15, Adelaide.
- Guan H, Love AJ, Simmons CT, Hutson J, Ding Z (2010) Catchment conceptualisation for examining applicability of chloride mass balance method in an area with historical forest clearance. *Hydrol. Earth Syst. Sci.* 14, 1233-1245.
- Guo W, Langevin CD (2002) 'User's Guide to SEAWAT: A Computer Program for Simulation of Three-Dimensional Variable-Density Ground-Water Flow.' U.S. Geological Survey, 6-A7.
- Hill MC, Tiedeman CR (2007) 'Effective groundwater model calibration: With analysis of data, sensitivities, predictions and uncertainty.' (John Wiley & Sons, Inc.: New York)

- Hunt RJ, Feinstein DT (2012) MODFLOW-NWT: Robust Handling of Dry Cells Using a Newton Formulation of MODFLOW-2005. *Ground Water* 50, 659-663.
- Hunt RJ, Luchette J, Schreuder WA, Rumbaugh JO, Doherty J, Tonkin MJ, Rumbaugh DB (2010) Using a Cloud to Replenish Parched Groundwater Modeling Efforts. *Ground Water* 48, 360-365.
- Hutton JT (1976) Chloride in rainwater in relation to distance from ocean. *Search* 7, 207-208.
- Jeffrey SJ, Carter JO, Moodie KB, Beswick AR (2001) Using spatial interpolation to construct a comprehensive archive of Australian climate data. *Environmental Modelling & Software* 16, 309-330.
- Jeuken B (2006) 'Tertiary aquifers of the Adelaide Coastal Plains groundwater model – Transient model set-up and calibration report.' Resource & Environmental Management Pty Ltd.
- Knowling MJ, Werner AD, Herckenrath D (2015) Quantifying climate and pumping contributions to aquifer depletion using a highly parameterised groundwater model: Uley South Basin (South Australia). *Journal of Hydrology* 523, 515-530.
- Konikow LF, Neuzil CE (2007) A method to estimate groundwater depletion from confining layers. *Water Resources Research* 43, n/a-n/a.
- Martin R (2011) 'Estimating Non-Licensed Groundwater Use Across the Adelaide Plains PWA.' Australian Groundwater Technologies, Report no 1079-10-AAA.
- Moore C, Doherty J (2006) The cost of uniqueness in groundwater model calibration. *Advances in Water Resources* 29, 605-623.
- Niswonger RG, Panday S, Ibaraki M (2011) MODFLOW-NWT, a Newton formulation for MODFLOW-2005. *U.S. Geological Survey Techniques and Methods* 6, 44.
- Ordens C, Werner A, Post VA, Hutson J, Simmons C, Irvine B (2012) Groundwater recharge to a sedimentary aquifer in the topographically closed Uley South Basin, South Australia. *Hydrogeology Journal* 20, 61-72.
- Pritchard J, Richardson S (2006) 'Northern Adelaide Plains – Water Balance.' Resource & Environmental Management Pty Ltd.
- REM (2006a) 'Tertiary Aquifers of the Adelaide Coastal Plains Groundwater Model: Steady-state Model Set-up and Calibration Report.' Resources and Environmental Management, Adelaide, South Australia.
- REM (2006b) 'Tertiary Aquifers of the Adelaide Coastal Plains Groundwater Model: Transient Model Set-up and Calibration Report.' Resources and Environmental Management, Adelaide, South Australia.
- Sanchez-Vila X, Guadagnini A, Carrera J (2006) Representative hydraulic conductivities in saturated groundwater flow. *Rev. Geophys.* 44, RG3002.
- Sanford W (2002) Recharge and groundwater models: an overview. *Hydrogeology Journal* 10, 110-120.
- Scanlon BR, Keese KE, Flint AL, Flint LE, Gaye CB, Edmunds WM, Simmers I (2006) Global synthesis of groundwater recharge in semiarid and arid regions. *Hydrological Processes* 20, 3335-3370.
- SKM (2009) 'Regional Groundwater Model Update.' Sinclair Knight Mertz, Adelaide.
- White JT, Doherty JE, Hughes JD (2014) Quantifying the predictive consequences of model error with linear subspace analysis. *Water Resources Research* 50, 1152-1173.
- Zheng C, Wang PP (1999) 'MT3DMS, A modular three-dimensional multi-species transport model for simulation of advection, dispersion and chemical reactions of contaminants in groundwater systems; documentation and user's guide.' U.S. Army Engineer Research and Development Center, Contract Report SERDP-99-1, Vicksburg, MS.
- Zulfic D, Osei-Bonsu K, Barnett SR (2008) 'Adelaide Metropolitan Area Groundwater Modelling Project. Volume 1 - Review of Hydrogeology, and Volume 2 - Numerical model development and prediction run.' Department of Water, Land and Biodiversity Conservation, DWLBC Report 2008/05, South Australia.



**Government
of South Australia**

Department of Environment,
Water and Natural Resources



**THE UNIVERSITY
of ADELAIDE**



**University of
South Australia**



**Flinders
UNIVERSITY**
ADELAIDE • AUSTRALIA

The Goyder Institute for Water Research is a partnership between the South Australian Government through the Department of Environment, Water and Natural Resources, CSIRO, Flinders University, the University of Adelaide and the University of South Australia.